# Geological controls on megathrust slip: the 2014 Pisagua, Chile, earthquake sequence as a natural laboratory

**DISSERTATION**

zur Erlangung des Doktorgrades an der

Mathematisch-Naturwissenschaftlichen Fakultät der

Christian-Albrechts-Universität zu Kiel

vorgelegt von

Bo Ma

Kiel, 2023

Erste Gutachterin: Prof. Dr. Heidrun Kopp

Zweiter Gutachter: Prof. Dr. Christian Berndt

Tag der mündlichen Prüfung: 31.01.2023

Zum Druck genehmigt: 31.01.2023

---

Der Dekan

## Erklärung

Hiermit erkläre ich, dass ich die vorliegende Doktorarbeit selbstständig und ohne Zuhilfenahme unerlaubter Hilfsmittel erstellt habe. Weder diese noch eine ähnliche Arbeit wurde an einer anderen Abteilung oder Hochschule im Rahmen eines Prüfungsverfahrens veröffentlicht oder zur Veröffentlichung vorgelegt. Ferner versichere ich, dass die Arbeit unter Einhaltung der Regeln guter wissenschaftlicher Praxis der Deutschen Forschungsgemeinschaft entstanden ist. Ich versichere, dass mir noch kein akademischer Titel entzogen wurde.

Ort, Datum Bo Ma

# Summary

Most subduction zones remain poorly resolved when it comes to the study of the precise location of the far offshore located updip limit of coseismic slip and its controlling parameters, which is an essential component of earthquake hazard assessment. The relative lack of seismicity on the updip limit, combined with laboratory friction studies, suggest the shallow fault is mostly velocity strengthening and likely to creep. This view is reinforced by geodetic inversions, which show low to zero coupling close to the trench. However, these locations are remote from the land; hence the models derived from terrestrial stations are not sufficiently well constrained. Moreover, the updip region can also be seismogenic, as demonstrated by tsunami earthquakes and shallow, slow slip events.

To better understand the controls on the updip limit, we analyze high-resolution seismic data to image an erosive margin with documented intense seismicity. Developing a high-resolution model of the seismic velocity and reflectivity of a region where we have exceptionally good knowledge of the temporal and spatial distribution of slip will provide new insights into these controls that can be transferred to studies of seismic slip and crustal structure elsewhere. These results will also have a significant impact on statistical forecasts of future earthquake activity, which can affect seismic hazard evaluation and mitigation plans.

The thesis is motivated by two themes, which are interrelated and addressed in a holistic seismic approach. One theme is mainly focused on the fluid-pressure variations revealed by the reflectivity of the seismic profiles along the updip limit to identify the shallow, velocity strengthening part of the plate boundary. Another theme is the study of the structure of the updip limit and the hanging upper plate caused by the subducting oceanic ridge.

The studies in the thesis will address the following scientific hypotheses: 1. Co-seismic slip propagation along-strike and along-dip are controlled by distinct rupture domains with potentially varying frictional properties; 2. The structural contact between the frontal prism and the framework rock in the overriding plate of the Iquique region defines the up-dip limit of the seismogenic zone and hence the potential size of tsunamigenic earthquakes; 3. Co-seismic slip distribution during the 2014 Iquique earthquake is controlled by abrupt variations in seafloor topography of the incoming oceanic plate. Slip termination is associated with the seafloor topography; 4. A low interseismic coupling factor and correlated

segmentation of seismogenic slip have been associated to structural and geometric heterogeneities in the incoming plate such as subducted seamounts.

The Northern Chilean margin is arguably an ideal place to understand the effect of crustal structure on the behaviour of continent-ocean subduction plate boundaries due to several recent large megathrust earthquakes yield detailed information on the history of slip on the plate boundary prior to, during and after the earthquake. Multichannel seismic data, especially for the shallowest part of the megathrust fault, displays clearly subsurface structure, providing a new perspective to help us understand the characteristics of the updip limit.

# Zusammenfassung

Für die meisten Subduktionszonen ist die genaue Kenntnis der Obergrenze der seismogenen Zone unzureichend, obwohl dies zusammen mit den kontrollierenden Parametern eine wesentliche Komponente zur Bewertung der Erdbebengefährdung darstellt. In Verbindung mit Laboruntersuchungen zur tektonischen Reibung deutet das relative Fehlen von Seismizität im flachen Bereich der Subduktionszone darauf hin, dass die Hauptverwerfung tektonischem Kriechen unterliegt.

Diese Ansicht wird durch geodätische Inversionen untermauert, die eine geringe bis keine Kopplung in der Nähe des Tiefseegrabens zeigen. Diese Lokationen liegen jedoch fernab der Küste, so dass die von terrestrischen Stationen abgeleiteten Modelle nicht ausreichend belastbar sind. Darüber hinaus kann die flache Subduktionszone durchaus seismogen sein, wie Tsunami-Erdbeben zeigen.

Um die Einflussfaktoren auf die Seismizitätsverteilung besser zu verstehen, analysieren wir hochauflösende seismische Daten eines erosiven Kontinentrandes mit dokumentierter intensiver Seismizität. Die Entwicklung eines hochauflösenden Modells der seismischen Geschwindigkeit und des Reflexionsvermögens einer Region, in der wir außergewöhnlich gute Kenntnisse über die zeitliche und räumliche Verteilung der Seismizität haben, wird neue Erkenntnisse über die Kontrollmechanismen liefern, die auf Studien anderer Systeme übertragen werden können.

Diese Arbeit ist durch zwei Themen motiviert, die miteinander verbunden sind und in einem ganzheitlichen seismischen Ansatz behandelt werden. Das eine Thema konzentriert sich hauptsächlich auf die Fluiddruckvariationen, die durch die Reflektivität der seismischen Profile entlang der Plattengrenze aufgedeckt werden. Ein weiteres Thema ist die Untersuchung der Struktur der Plattengrenze und der Oberplatte, die durch einen subduzierenden ozeanischen Rücken modifiziert werden.

Die Studien im Rahmen der Dissertation befassen sich mit den folgenden wissenschaftlichen Hypothesen: 1. Die ko-seismische Bruchausbreitung in lateraler Richtung sowie mit der Tiefe wird durch verschiedene Bruchbereiche mit potenziell unterschiedlichen Reibungseigenschaften gesteuert; 2. der strukturelle Kontakt zwischen akkretiertem Material und dem Grundgebirge in der Oberplatte der Iquique-Region definiert die Obergrenze der

seismogenen Zone und damit die potenzielle Größe eines tsunamogenen Erdbebens; 3. das Bruchverhalten des 2014 Iquique-Erdbebens wird durch die ausgeprägte Topographie des Meeresbodens der ozeanischen Platte beeinflußt; 4. ein niedriger interseismischer Kopplungsfaktor und damit einhergehende Segmentierung der seismogenen Zone stehen in Verbindung mit strukturellen und geometrischen Heterogenitäten in der ozeanischen Platte, wie z.B. subduzierten Seamounts.

Der nordchilenische Kontinentrand ist ein idealer Ort, um die Auswirkungen der Krustenstruktur auf das Verhalten der Subduktion zu verstehen, denn mehrere große Subduktionsbeben in jüngster Zeit liefern detaillierte Informationen über die Seismizität. Seismische Mehrkanaldaten bilden zudem detailliert die Struktur der Plattengrenze und des oberen Bereiches der seismogenen Zone ab.

# Contents

# Abbreviations

| | |
|---|---|
| **$M_W$** | Moment magnitude |
| **OBS** | Ocean Bottom Seismometer |
| **CMP** | Common Middle Point |
| **Myr** | million year |
| **MCS** | multichannel seismic |
| **UTC** | Universal Time Coordinated |
| **gCMT** | Global Centroid Moment Tensor |
| **CIP** | Common Image Point |
| **PSDM** | Pre-stack depth migration |

# 1 Motivation and Outline

## 1.1 Motivation

As a critical part of the Earth's recycling system, subduction zones are characterized by active seismicity and complex geological conditions. They outline much of the Pacific plate, producing many of the largest and most destructive earthquake records(Bilek, 2010). Assessing seismic hazards remains one of the most challenging scientific issues in Earth sciences, and growing evidence indicates that the behavior of earthquakes is associated with the structure and geometry of the subduction zones; thus, we should devote more attention to understanding the processes of the subduction margins.

The circum-Pacific convergent margins are the main region of the megathrust earthquakes in the world, accounting for more than 80% of the global earthquakes. In the 21st century, megathrust earthquakes with magnitude larger than 8.4 have occurred worldwide, including the 26 December 2004 Mw 9.0 Sumatra earthquake (Lay et al., 2005; Tilmann et al., 2010), the 28 March 2005 Mw 8.6 Nias earthquake (Tilmann et al., 2010), the 12 September 2007 Mw 8.4 Sumatra earthquake (Lorito et al., 2008), the 27 February 2010 Mw 8.8 Maule earthquake (Moreno et al., 2010; Vigny et al., 2011) and the 11 March 2011 Mw 9.0 Tohuku-Oki earthquake (Loveless and Meade, 2011). These earthquakes and their secondary hazards, such as the tsunami, have caused enormous civilian casualties and damage to property. Notably, the tsunami hazards caused by the 2004 Mw 9.0 Sumatra earthquake killed almost 30,000 people. Therefore, studying the megathrust earthquake, including the controlling factors on asperities and deformation along the subducting interface, can be useful in preventing disasters.

Studying megathrust earthquakes should be interrelated and may be best addressed in a holistic seismic approach. Multichannel seismic reflection analysis, as an advantageous method for imaging the subsurface, enables us to obtain information about its structure and composition and helps to understand the origin of the subsurface structure. Integrating multichannel seismic images with seismicity analysis (Soto et al., 2019; Petersen et al., 2021), slip models from geodetic and seismological data, including coseismic (Duputel et al., 2015), afterslip (Hoffmann et al., 2018) or interseismic coupling information (Schurr

et al., 2014), we can study the forearc structure on the Northern Chilean margin and the deformation of the forearc during the interseismic, coseismic and postseismic phase, including its along strike and downdip segmentation in a region where dense geophysical datasets from land observations are available for all phases of the seismic cycle. In detail, the study includes: a.) the seismotectonics of the study area, b.) the structure of the forearc, including the structure of the oceanic and overriding plate, c.) imaging of the internal structure of the forearc for both downdip and lateral changes, d.) the structural control on megathrust deformation during the coseismic, interseismic and postseismic phases of the seismic cycle.

## 1.2 Thesis outline

### 1.2.1 Stand-alone published/submitted articles

The thesis encompasses 8 chapters. Chapters 3-4 represent stand-alone articles published or submitted for publication of the individual aspects related to the structure of the Northern Chilean margin. Chapters 5-7 represent additional contributions to peer-reviewed articles. Finally, summarizations of the articles and an outlook on future challenges and recommendations for potential projects to improve our knowledge are given in chapter 8.

**Chapter 3** concentrates on the analysis of the plate boundary from the multichannel seismic profiles offshore the Northern Chilean margin. We document a spatial correspondence between the 2014 Iquique earthquake rupture area and the seismic reflectivity of the plate boundary. North and updip of the rupture area, a coherent, highly reflective plate boundary indicate excess fluid pressure, which may prevent the accumulation of elastic strain. In contrast, the rupture area is characterized by the absence of plate boundary reflectivity, which suggests low fluid pressure that result in stress accumulation and thus control the extent of earthquake rupture.

**Author contributions**: B.M. processed the seismic data with the support of D.K. B.M., J.G., D.L. and H.K. wrote the initial draft of the paper, which was critically revised by all co-authors. E.C.R. established the thermal model. I.G. and E.C.R. contributed to the discussion of the thermal models and implications of the findings. F.P., M.R., A.T., E.C.R. participated in cruise MGL1610 of *R/V Marcus G. Langseth*. E.C.R., A.T., M.R., and Y.X. contributed to the discussion of the seismic data. I.G., D.L., F.P. contributed to seismological topics.

Chapter 3 is published in Nature Communications as:

**Ma, B.**, Geersen, J., Lange, D., Klaeschen, D., Grevemeyer, I., Contreras-Reyes, E., Petersen, F., Riedel, M., Xia, Y., Tréhu, A. M., & Kopp, H. Megathrust reflectivity reveals the updip limit of the 2014 Iquique earthquake rupture. Nat Commun 13, 3969 (2022). https://doi.org/10.1038/s41467-022-31448-4

Inspired by the novel results of chapter 3, Chapter 4 maps structures related to ridge subduction under the marine forearc with unprecedented accuracy and resolution and evaluate their impact on the deformation of both the plate boundary and the upper plate. We show that significant ridge-related topography is currently subducting south of 20.5 °S and that the combined effect of horst and graben subduction with subduction of Iquique ridge-related thickened and elevated crust causes an upward bulging of the entire upper plate from the plate interface up to the seafloor as well as the presence of kilometer-scale anticlinal structures observed in multibeam bathymetric data that are approximately aligned with horsts seaward of the trench.

**Author contributions**: B.M. processed the seismic data with the support of D.K. B.M., J.G. and H.K. wrote the initial draft of the paper, which was critically revised by all co-authors. M.R., A.T., E.C.R. participated in cruise MGL1610 of *R/V Marcus G. Langseth*. M.R., Y.X. and D.L. contributed to the discussion of the seismic data.

Chapter 4 is submitted to Journal of South American Earth Sciences as: **Ma, B.**, Geersen, J., Klaeschen, D., Contreras-Reyes, E., Riedel, M., Xia, Y., Tréhu, A. M., & Kopp, H. (submitted). Impact of the Iquique Ridge on structure and deformation of the North Chilean subduction zone. Journal of South American Earth Sciences.

### 1.2.2 Additional contributions to peer-reviewed articles

In addition to the articles presented in this PhD thesis for the Northern Chilean margin, I contributed to the following complementary peer-reviewed articles during my PhD studies for the Northern Chilean and Java subduction zone:

**Chapter 5** focuses on the subduction erosion in the Northern Chilean margin through the aftershocks distribution of the 2014 Mw 8.1 Iquique earthquake by a long-term deployment of ocean bottom seismometers installed eight months after the mainshock. Together with the multichannel seismic data, the aftershock seismicity documents subduction erosion that removes mass from the base of the wedge and results in normal faulting in the upper plate.

**Author contributions**: DL, IG, EV, AT, HK designed the study. FP, DL, IG, HK, SB, ECR deployed and recovered the OBS. FP, MR, AT, ECR participated on MGL1610

cruise of *RV Marcus G. Langseth* during which the seismic reflection data was collected. FP processed the earthquake data and discussed the results with all co-authors. BM processed the multi-channel data with support of DK. FP produced the figures and wrote the paper supported by all co-authors. All co-authors contributed to the reviewing and editing of the paper.

Chapter 5 is published in Geophysical Research Letters as:

Petersen, F., Lange, D., **Ma, B.**, Grevemeyer, I., Geersen, J., Klaeschen, D., Contreras-Reyes, E., Barrientos, S., Tréhu, A. M., Vera, E., & Kopp, H. (2021). Relationship between subduction erosion and the up-dip limit of the 2014 mw 8.1 iquique earthquake. Geophysical Research Letters, 48, e2020GL092207(9), https://doi.org/10.1029/2020GL092207.

**Chapter 6** resolves a previously unrecognized shallow subducting seamount from a re-processes multichannel seismic profile crossing the 1994 Mw 7.8 Java tsunami earthquake rupture area. Pronounced back-thrusting at the landward slope of the forearc high and the formation of splay faults branching off the landward flank of the subducting seamount are observed. Furthermore, the location of the seamount in relation to the 1994 earthquake hypocentre and its co-seismic slip model suggests that the seamount acted as a seismic barrier to the up-dip co-seismic rupture propagation of this moderate-size earthquake.

**Author contributions**: YX and DK performed the computations and are responsible for the main processing. YX, JG, DK, BM, MR, MS, DL and HK helped to strengthen the overall scope and added to interpretational aspects and the discussion of the presented results. MS made the data available and was responsible for the navigation and geometry processing. YX, JG, and HK wrote the article, and all authors contributed equally to proofreading and final preparation of the paper.

Chapter 6 is published in Solid Earth as:

Xia, Y., Geersen, J., Klaeschen, D., **Ma, B.**, Lange, D., Riedel, M., Schnabel, M., and Kopp, H.: Marine forearc structure of eastern Java and its role in the 1994 Java tsunami earthquake, Solid Earth, 12, 2467–2477, https://doi.org/10.5194/se-12-2467-2021, 2021.

**Chapter 7** studies the marine forearc from four downdip multichannel seismic lines offshore from eastern Java margins to Lesser Sunda island. The detailed structure of the accretionary wedge complex and the structure of the megathrusts were analysed by MCS data and multi-beam bathymetry. Subducting seamounts with different scales are observed and compared to one MCS line without subducting seamount. We investigate the structural impact of subducting seamounts with different sizes and at different depths.

**Author contributions**: YX and DK performed the computations and are responsible for the main processing. HK helped to strengthen the overall scope and added to interpretational aspects and the discussion of the presented results. MS made the data available and was responsible for the navigation and geometry processing. YX wrote the article, and all authors contributed equally to the proofreading and final preparation of the manuscript.

Chapter 7 is submitted to Journal of Geophysical Research: Solid Earth.

**Chapter 8** summarizes the previous chapters' results and discussions and provides an outlook for potential research concerning yet un-fully solved plate interface and upper plate structures and suggestions for future geophysical surveys.

## References

Bilek, S. L. (2010). The role of subduction erosion on seismicity. *Geology*, *38*(5), 479–480, https://doi.org/10.1130/focus052010.1.

Duputel, Z., Jiang, J., Jolivet, R., Simons, M., Rivera, L., Ampuero, J. P., Riel, B., Owen, S. E., Moore, A. W., Samsonov, S. V., Culaciati, F. O., & Minson, S. E. (2015). The iquique earthquake sequence of april 2014: Bayesian modeling accounting for prediction uncertainty. *Geophysical Research Letters*, *42*(19), 7949–7957, https://doi.org/10.1002/2015gl065402.

Hoffmann, F., Metzger, S., Moreno, M., Deng, Z. G., Sippl, C., Ortega-Culaciati, F., & Oncken, O. (2018). Characterizing afterslip and ground displacement rate increase following the 2014 iquique-pisagua m-w 8.1 earthquake, northern chile. *Journal of Geophysical Research-Solid Earth*, *123*(5), 4171–4192, https://doi.org/10.1002/2017jb014970.

Lay, T., Kanamori, H., Ammon, C. J., Nettles, M., Ward, S. N., Aster, R. C., Beck, S. L., Bilek, S. L., Brudzinski, M. R., Butler, R., DeShon, H. R., Ekstrom, G., Satake, K., & Sipkin, S. (2005). The great sumatra-andaman earthquake of 26 december 2004. *Science*, *308*(5725), 1127–33, https://doi.org/10.1126/science.1112250.

Lorito, S., Romano, F., Piatanesi, A., & Boschi, E. (2008). Source process of the september 12, 2007, mw8.4 southern sumatra earthquake from tsunami tide gauge record inversion. *Geophysical Research Letters*, *35*(2), https://doi.org/10.1029/2007gl032661.

Loveless, J. P. & Meade, B. J. (2011). Spatial correlation of interseismic coupling and coseismic rupture extent of the 2011 mw= 9.0 tohoku-oki earthquake. *Geophysical Research Letters*, *38*(17), n/a–n/a, https://doi.org/10.1029/2011gl048561.

Moreno, M., Rosenau, M., & Oncken, O. (2010). 2010 maule earthquake slip correlates with pre-seismic locking of andean subduction zone. *Nature*, *467*(7312), 198–U84, https://doi.org/10.1038/nature09349.

Petersen, F., Lange, D., Ma, B., Grevemeyer, I., Geersen, J., Klaeschen, D., Contreras-Reyes, E., Barrientos, S., Tréhu, A. M., Vera, E., & Kopp, H. (2021). Relationship between subduction erosion and the up-dip limit of the 2014 mw 8.1 iquique earthquake. *Geophysical Research Letters*, *48*(9), e2020GL092207, https://doi.org/10.1029/2020gl092207.

Schurr, B., Asch, G., Hainzl, S., Bedford, J., Hoechner, A., Palo, M., Wang, R., Moreno, M., Bartsch, M., Zhang, Y., Oncken, O., Tilmann, F., Dahm, T., Victor, P., Barrientos, S., & Vilotte, J. P. (2014). Gradual unlocking of plate boundary controlled initiation of the 2014 iquique earthquake. *Nature*, *512*(7514), 299–302, https://doi.org/10.1038/nature13681.

Soto, H., Sippl, C., Schurr, B., Kummerow, J., Asch, G., Tilmann, F., Comte, D., Ruiz, S., & Oncken, O. (2019). Probing the northern chile megathrust with seismicity: The 2014 m8.1 iquique earthquake sequence. *Journal of Geophysical Research-Solid Earth*, *124*(12), 12935–12954, https://doi.org/10.1029/2019jb017794.

Tilmann, F. J., Craig, T. J., Grevemeyer, I., Suwargadi, B., Kopp, H., & Flueh, E. (2010). The updip seismic/aseismic transition of the sumatra megathrust illuminated by aftershocks of the 2004 aceh-andaman and 2005 nias events. *Geophysical Journal International*, *181*(3), 1261–1274, https://doi.org/10.1111/j.1365-246X.2010.04597.x.

Vigny, C., et al. (2011). The 2010 m-w 8.8 maule megathrust earthquake of central chile, monitored by gps. *Science*, *332*(6036), 1417–1421, https://doi.org/10.1126/science.1204132.

# 2 Introduction

## 2.1 Convergent erosive plate margins

Subduction zones are usually classified as either erosive, where the material is removed from the base of the overriding plate (Clift and Vannucchi, 2004; Vannucchi et al., 2013) and recycled back into the mantle (Stern, 2011), or accretionary margin, with material actively added to the overriding plate (Von Huene and Scholl, 1991). Margin erosion occurs at all convergent plate boundaries, even if they are accretionary margins (Stern, 2011). With topographic highs such as large seamount complexes associated with significant volumes of flanking sediments on oceanic plates, it may promote concurrent accretion and erosion over short distances along the trench (Clarke et al., 2018). As a typical erosive margin, it is generally composed of large seafloor slopes, high convergence rates, thin sediments cover, narrow front prisms and strong interplate coupling (Kopp et al., 2006; Kukowski and Oncken, 2006; von Huene and Ranero, 2003).

Most of the largest earthquakes are thrust events along the interface. During great earthquakes ($M_w > 8$) along the convergent plate boundaries, the shallow interface ruptures down to depths of up to 50 km (Oleskevich et al., 1999), while the rupture propagates along the margin. These events nucleate in the area of the so-called seismogenic zone (Fig. 2.1; Hyndman and Wang, 1993; Hyndman et al., 1997), a region where the properties of the plate interface are heterogeneous and is reflected by the complex pattern of coupling between the plates (Metois et al., 2013; Métois et al., 2016), coseismic slip distributions (Schurr et al., 2014) and afterslip related to postseismic deformation (Bedford et al., 2013).

In the shallow plate, the temperature and pressure are relatively low, and earthquakes occur along the interface or inside plates, mainly caused by the fracture of brittle rocks or unstable frictional slip along pre-existing faults under the mechanism of stick-slip (Brace and Byerlee, 1966). In late 2016 high-resolution seismic reflection and refraction data were acquired by the cruise MGL1610 of the *R/V Marcus G. Langseth* offshore Northern Chile. The study area is the region of the $M_w$ 8.1 Iquique earthquake (Schurr et al., 2014), which occurred on 1 April 2014 in Northern Chile, where the Integrated Plate Boundary

Observatory Chile (IPOC) is located onshore, and rich geophysical datasets during the inter-, co- and postseismic phase are available.

## 2.2 The role of the incoming plate along the erosive margins

### 2.2.1 The input sediment

The accretionary margins are typically characterized by thick sediments on the oceanic crust, which are scraped off the oceanic plate and incorporated into the accretionary wedges (Mannu et al., 2016). Previous studies suggested that thick trench sediments were a prerequisite for large earthquake (Ruff, 1989; Heuret et al., 2012; Brizzi et al., 2020), which allows ruptures to propagate for considerable distances along strike under uniform coupling and decreasing in megathrust dip results in a wider seismogenic zone along downdip. The subduction interfaces of large earthquakes tend to be relatively smooth due to thick sediments covering the interplate morphology (van Rijsingen et al., 2018). However, for the erosive margins, with little sediments on the oceanic crust, such as in northern Chile (Fig. 2.1; von Huene and Ranero, 2003), large earthquakes have occurred with an estimated moment magnitude of Mw ~8.8 in 1877, followed by an event of similar magnitude to the north in Peru in 1868 (Comte and Pardo, 1991). Instead of subducted sediment carried into plate interface, the critical factor of erosive margin for allowing rupture to propagate over a long distance is material eroded from the upper plate (Scherwath et al., 2009).

### 2.2.2 Bending faults

The bending of the incoming plate prior to subduction creates an extended stress field at the outer rise of the trench, resulting in the creation of normal faults. These bending-related normal faults may reactivate pre-existing cracks in the oceanic crust and also generate faults cutting deep into the lithosphere (Grevemeyer et al., 2005), leading to the formation of horst and graben structures adjacent to trenches (Von Huene and Scholl, 1991; Geersen et al., 2018).

The bending-related normal faults are detected regularly within ~75 km from the deformation front. Most often, these faults are 5 - 30 km long, with distances of 1 - 10 km between them and a gradual decrease in fault throws seaward (Masson, 1991). The deformation induced by the activities of bending-related normal faults markedly affects the distribution of outer-rise earthquakes (Christensen and Ruff, 1988; Jiao et al., 2000; Ranero et al., 2005) and the hydration of the oceanic crust (Ranero et al., 2003, 2005). Before subduction, the outer-rise normal faults act as pathways for water infiltration into the oceanic

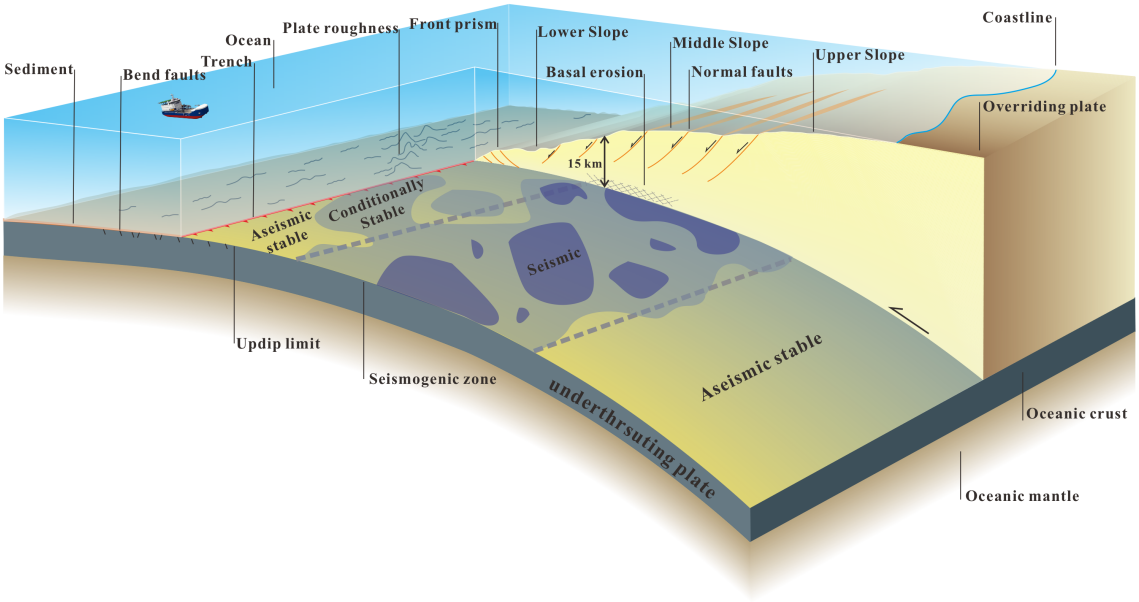


**Figure 2.1:** Sketch through the erosive convergent margin. Along-dip of the plate interface is separated as updip limit, seismogenic zone and downdip limit. Across-strike segmentation from the oceanic crust to the marine forearc encompassing the plate roughness, lower slope, middle slope and upper slope.

crust (Ranero et al., 2003; Grevemeyer et al., 2007), which cut through the crust and reach the upper mantle (Ranero et al., 2003). Hydration of the oceanic crust is assumed to cause earthquakes, especially at intermediate depths (70 - 300 km), where fluids from metamorphic dehydration reactions (Schmidt and Poli, 1998) are thought to increase the pore fluid pressure to weaken pre-existing faults and cause earthquakes. The numerical model indicates that the changes in stress and pressure of slab bending can induce fluid circulation through fault into the upper mantle (Faccenda et al., 2009, 2012).

The bending-related normal faults are also responsible for the shallow seismicity (Ranero et al., 2005; Lefeldt et al., 2009), which may generate considerable earthquakes seaward of the updip limit (Moscoso et al., 2011; Nishikawa and Ide, 2015) or produce destructive tsunamis (Satake and Tanioka, 1999). Through the normal faults in the plate interface, the expelled fluid from the oceanic crust migrated upward to the plate interface, leading to high pore fluid pressure and a lower degree of locking along the plate interface (Moreno et al., 2014). The volume of subduction fluid governs many tectonic processes, including seismic coupling (Scholz and Small, 1997; Saffer and Tobin, 2011) and arc magma genesis (Gaetani and Grove, 1998).

### 2.2.3 Oceanic Plate roughness

The high reliefs and seamount chains on oceanic crust (Hillier and Watts, 2007) are considered to influence the geometry and seismic coupling of the subduction interface (Lallemand et al., 1992; Scholz and Small, 1997; Agard et al., 2018). Scarps in the outer wedge of the marine forearc are viewed as direct evidence for the subducted seamounts (Ranero and von Huene, 2000). The subducting seamounts are considered to increase the crustal thickness (Kopp et al., 2004; Tang et al., 2013), which creates increased normal stress along the plate interface (Contreras-Reyes and Carrizo, 2011) and enhance seismic coupling (Scholz and Small, 1997).

Seamounts can localize seismicity, fault creep (Singh et al., 2011; Wang and Bilek, 2011), fluid flow (Spinelli and Harris, 2011), and large earthquakes (Scholz and Small, 1997). The influence of subducting seamounts on large earthquakes is still disputed (Watts et al., 2010; Wang and Bilek, 2011). Some authors suggest the subducting seamounts may increase the interseismic coupling and act as rigid asperities to rupture during an earthquake (Scholz and Small, 1997; Dominguez et al., 1998). Conversely, subducting seamounts are also associated with weak interplate coupling (Kelleher and Mccann, 1976; Mochizuki et al., 2008; Singh et al., 2011; Marcaillou et al., 2016), which is conducive to aseismic slip and relatively small earthquakes (Cummins et al., 2002; Mochizuki et al., 2008; Wang and Bilek, 2011).

Bathymetric highs subduction has also been thought to be related to tectonic erosion of the overriding forearc (Ranero and von Huene, 2000; Bangs et al., 2006). Geological and geophysical data show that the forearc of subduction zones experiences intense deformation during the subduction of aseismic oceanic ridges. Tectonic erosion associated with seamount subduction removes continental material at the front of the margin or along the base of the upper plate (von Huene et al., 1996) as they are capable of fracturing margin rocks (von Huene and Lallemand, 1990; Dominguez et al., 2000) and thin, possibly by hydrofracturing processes, the underside of the margin (Ranero and von Huene, 2000; von Huene et al., 2004).

## 2.3 The downdip segmentation along the plate interface

The subduction plate interface is a narrow tectonic activated zone between the subducting oceanic crust and the continental crust (Fig. 2.1), accounting for ~90% of the total seismic moment that has been globally released during the last century (Pacheco and Sykes, 1992). Specific parameters such as subduction rate, subducting plate age, subduction interface

thermal structure, or the presence of subducting sediment (Uyeda and Kanamori, 1979; Kanamori, 1986; Ruff, 1989; Scholz and Campos, 1995).

The plate interface is heterogeneous in different regions, with seismic rupture terminating at the seismic barrier where the slip deficit is reduced by many factors, such as physical properties changes of fault zone rocks (Saffer and Wallace, 2015; Ujiie et al., 2013), pore pressure anomalies (Kitajima and Saffer, 2012), and subducting high reliefs and its effect on the hanging wall plate (Wang and Bilek, 2011). The shallower part of subduction zones can be divided into two or three regions by their characteristic slip behavior, such as unstable, stable, and conditionally stable slip (Fig. 2.1; Bilek and Lay, 2002). The plate boundary fault creeps without seismic ruptures in the stable sliding zone (which we called 'Aseismic stable' in Fig. 2.1). In the unstable seismic region (called 'seismogenic zone'), megathrust earthquakes rupture the plate boundary fault, and coupling is strong on the plate boundary. The conditionally stable (called 'transition zone') is where intermittent slip events such as slow earthquakes occur. Coupling is relatively weak in the transition zone, and seismic studies reveal that slow slip events (SSEs), very-low-frequency earthquakes (VLFEs) and small repeating earthquakes are ubiquitously distributed, suggesting that the plate boundary is enriched in fluids and mostly creeping (Arai et al., 2016).

The subducting sediments largely influence the frictional properties along the plate interface in the accretionary wedge. Both clay-rich material and ocean-floor carbonates are frictionally weak under various conditions (Saffer, 2003). Fluid overpressure can weaken the megathrust by reducing the effective normal stress (Han et al., 2017). Sediments are therefore thought to lubricate the plate interface (Lamb and Davis, 2003), thereby facilitating rupture propagation and large slip at shallow depths, as unexpectedly observed during the 2011 Tohoku-Oki earthquake (Simons et al., 2011). For erosive margin, the generic subduction erosion mechanism induced by horst and graben structures originates from the high relief on the incoming sediment-starved oceanic crust, which increases friction along the plate interface and abrades the underside of the overlying plate (von Huene and Ranero, 2003; von Huene et al., 2004; Kukowski and Oncken, 2006). Critical parameters and boundary conditions to study wedge dynamics during the seismic cycle, such as taper geometries and frictional properties, can be inferred from seismic data. The frictional behavior of the megathrust is often suggested to be interrelated to structures of the overriding plate (Hicks et al., 2014) and to fluids (Moreno et al., 2014), which are capable of modifying and serpentinizing the overriding plate structure.

Subducting slabs are likely to contain large amounts of water along their upper interface, either as hydrous minerals or as free pore fluid (Peacock, 1990; Iwamori and Nakakuki, 2013). Material within an interface has a lower tensile strength when pressure increases. As a result of rheological weakening, aqueous fluids under pressurized percolation increase

the likelihood of fracturing and faulting (Duarte et al., 2015). As seismic imaging indicates, overpressure pore fluid near the active plate interface is associated with high *vp/vs* ratios (Petersen et al., 2021) or high electrical conductivity zones (Chesley et al., 2021). Dehydration reactions in the slab are also believed to trigger subduction-related seismicity via fluid release (Hacker et al., 2003; Faccenda et al., 2012). Stress perturbations, such as large earthquakes, are determined by the lithology and fluid pressure along the tectonic plate boundaries (Dieterich and Kilgore, 1994).

### 2.3.1 Updip limit

The shallow boundary between the seismogenic zone and transition zones corresponds to the updip edge of the rupture area of great earthquakes. The seaward side of the boundary is the updip limit, which constrains the potential size of these earthquakes (Fig. 2.1). Controls on the updip limit were suggested to be related to forearc structure and morphology (Tilmann et al., 2010; Wang and Hu, 2006), metamorphic processes (Moore and Saffer, 2001), or thermal properties (Moore and Saffer, 2001; Oleskevich et al., 1999). Geodetic inversions show that the plate interface coupling close to the trench is relatively low (Chlieh et al., 2008; Loveless et al., 2010b; Metois et al., 2013; Métois et al., 2016; Nocquet et al., 2017), consistent with the velocity-strengthening in the shallow-most region and therefore must creep under applied stress (Byrne et al., 1988; Marone, 1998; Wang and Hu, 2006).

The shallow parts of the plate interface can also be seismogenic, with earthquake ruptures that extend into the updip limit domain triggering potentially large tsunamis (Vannucchi et al., 2017; Kodaira et al., 2012; Simons et al., 2011). Shallow slow-slip events (Saffer and Wallace, 2015; Wallace et al., 2016, 2017) represent transient behaviors where the fault releases accumulated stress episodically, indicating partially unstable patches in the updip stable - conditionally stable region (Ito et al., 2007).

The updip limit of the seismogenic zone located at the temperature threshold of 100 - 150 °C, corresponding to a number of diagenetic to low-grade metamorphic and consolidation phenomena that can more comprehensively account for lithification and decreased fluid pressure ($P$) ratio ($\lambda^*$) that lead to mechanical changes (where $\lambda^* = [P_{\text{fluid}} - P_{\text{hydrostatic}}] / [P_{\text{lithostatic}} - P_{\text{hyrostatic}}]$) (Moore and Saffer, 2001). The updip limit appears to be thermally controlled, but the chemical and physical changes downdip that affect frictional properties of the material appear to be complex (Underwood, 2007). The shallowest, trenchward portion of subduction megathrusts are thought to be stable sliding, likely due to a combination of abundant weak velocity-strengthening clays and low effective stresses associated with elevated pore fluid pressure (Scholz, 1998; Moore and Saffer, 2001; Saffer and Tobin, 2011). A high fluid content along the shallow aseismic section of

the plate boundary in this temperature regime where compaction dewatering and clay-mineral diagenetic reactions are expected to release most of the water from the oceanic crust (Ma et al., 2022; Kameda et al., 2011) and in the subducting sediments (Saffer and Tobin, 2011).

### 2.3.2 Seismogenic zone

Great earthquakes occur in the seismogenic zone of the subduction plate interface (Fig. 2.1; Scholz and Campos, 2012). Generally, the seismogenic zone includes the area of the plate interface that can slip seismically during a large earthquake, and its regional extent is estimated based on the rupture zones of past earthquakes, present-locking, uplift/subsidence history, and/or megathrust temperature (Kanamori, 1986; Scholz, 1998; Scholz and Campos, 2012). Great thrust events are characterized by consistently updip, and downdip limits along strike and maximum depths of smaller thrust events (Tichelaar and Ruff, 1993; Hyndman et al., 1997; Oleskevich et al., 1999), and coseismic rupture limits and interseismic locked zones are well correlated based on geodetic data (Schurr et al., 2014).

Depending on slab dip, the seismogenic zone is generally at 10 and 35 km depth. Thermal structure and the temperature threshold range from 150 °C to 350 - 400 °C inferred from laboratory data for quartzofeldspathic rocks and found for a number of young subduction zones (Tichelaar and Ruff, 1991; Hyndman et al., 1997; Oleskevich et al., 1999). In this region, the plate interface is strongly coupled, and devastating megathrust earthquakes occur.

### 2.3.3 Downdip limit

The beneath boundary between the seismogenic zone and transition zones corresponds to the downdip edge of the rupture area of great earthquakes. As for the downdip limit, the critical change in composition has been observed at the thrust intersection with the forearc mantle, which is aseismic due to serpentinization (Peacock and Wang, 1999). This depth usually exceeds 40 km (Oleskevich et al., 1999), which is beyond the maximum depth of our seismic profiles (e.g., Fig. 3.2), and thus is not the major study in our thesis.

Similar to the updip limit (subsection 2.3.1) , downdip of the seismogenic zone, the megathrust transitions from stick-slip behavior to stable sliding (Fig. 2.1; Scholz, 1998). As indicated by laboratory data, the downdip limit for the seismogenic zone in many young hot subduction zones is at ~350 °C, while the transition zone between velocity weakening (seismic) and velocity strengthening (aseismic) happens between 350 °C - 450 °C (Hyndman et al., 1997).

### 2.3.4 Basal erosion

Subduction erosion has been identified as frontal erosion by the structural collapse of the marine forearc into the trench (Stern, 2011), and basal erosion, with abrading the base of the upper plate by oceanic topography (Hilde, 1983; Ranero and von Huene, 2000; Bangs et al., 2006) and hydrofracturing in the upper plate that dragged materials into the subduction channel (von Huene et al., 2004; Ranero et al., 2008). In particular, the role of the subduction channel (Cloos and Shreve, 1996) along the plate interface for erosive margins is not fully understood. One class of models suggests high friction along the plate interface, often related to the presence of subducted topographic features on the incoming plate, leading to the removal of material at the base of the overriding plate through abrasion (Bangs et al., 2006). Another class of models propose a weaker fault and suggests that subduction erosion occurs because of hydrofracturing of the upper plate, allowing upper plate material to enter the subduction zone. Thinning of the upper plate results in measurable subsidence, and fluid seeps along the normal faults in the upper prism (Ranero et al., 2008).

## 2.4 Structure and properties of the overriding continental plate

The convergent margin affects both the incoming and overriding plates. Upon approaching the continent, the lithosphere bends into the trench, resulting in a prominent bathymetric deformation. Oceanic plates are dominated by extensional faults, while the upper plates display widespread contractional structures, suggesting a near 90 ° rotation of the orientation of the principal stresses across the megathrust (Sallares and Ranero, 2019). Drilling and seismic surveys have previously examined the structure and lithology of the upper plate (Tsuru et al., 2000, 2002; von Huene and Ranero, 2003; Sallares and Ranero, 2005). During the last decade, high-resolution 2D velocity-depth models have provided a detailed picture of the inner structure and geometry of the Chilean marine forearc, from where petrophysical properties of the margin and fracturing and sediment compaction degrees have been inferred. Along the Chilean margin these 2D lines include the erosional margin off Antofagasta (~23 °S) and off Tocopilla (~22 °S) (Sallares and Ranero, 2005; Contreras-Reyes et al., 2012), the accretionary southern central Chile margin off Valparaiso (~33 °S) (Zelt et al., 1999), off Constitución (~34 °S) (Moscoso et al., 2011), off Isla de Chiloé (~43 °S) (Scherwath et al., 2009; Contreras-Reyes et al., 2010) and off Aysén (~44 °S and ~45 °S) (Scherwath et al., 2009). The motion and structure of the overriding plate may play a significant role in trench migration and slab geometry (Jarrard, 1986) and seismicity can also be diffuse or localized on the upper plate (Sippl et al., 2018). Their velocity-depth

models show wedge-shaped bodies of reduced velocities bounded landward by an abrupt horizontal increase of velocities suggesting a change in rock type. These features have been interpreted as a frontal accretionary prism composed of poorly consolidated sediment and its landward contact with the framework rock (continental basement made of paleo-accretionary complex or metamorphic basement) (i.e., Contreras-Reyes et al., 2010). In contrast, at the northern erosional margin, seismic velocities gradually decrease toward the trench, interpreted to be linked to hydrofracturing and erosional processes by Sallares and Ranero (2005). In this study, the authors image the margin structure of the Mejillones peninsula in northern Chile (23.5 °S) and derived a pronounced increase of porosity towards the frontal part of the margin based on reduced *vp* velocities close to the trench. They suggest that the frontal part of the margin is fluid-saturated and highly hydrated due to subduction erosion. This zone correlates with the aseismic shallow part of the Antofagasta 1995 earthquake.

### 2.4.1 Frontal prism

The frontal prism is a distinct morphological unit that is tectonically active as reflected in the disruption of the slope drainage system (Fig. 2.1; Ranero and von Huene, 2000; von Huene et al., 2004). As a result of seismic data and multibeam bathymetric images, the frontal prism spans five to fifteen kilometres at the bottom of the slope in the Middle America Trench (Weinrebe et al., 2003), in Peru (Kukowski et al., 2001), in Chile (von Huene and Ranero, 2003), and in northern Japan (Kobayashi et al., 1998). Located at the toe of the upper plate, this unit is a contractional structure composed of disaggregated material from the overlying plate (von Huene and Ranero, 2003). As previously hypothesized (Lallemand et al., 1994), tectonic thickening of slope sediment may be associated with erosion at the underside of the prism farther down the subduction zone. Thus the frontal prism is stabilized by the balance between addition and subtraction of mass (von Huene and Ranero, 2003). The frontal prism is characterized by a low-velocity zone in the erosive margins, with values between 2 km/s and 3 km/s.

### 2.4.2 Lower to middle slope

In non-accretionary margins, it has been suggested that most of the lower to the middle slope is above the velocity strengthening zone, which prevents stress accumulation, coseismic slip, and high extensional deformation (Wang and Hu, 2006; Geersen et al., 2018; Ma et al., 2022). In the lower to middle slope, highly fractured material generated a subduction channel that smoothes the interplate contact and facilitates aseismic slip (Noda et al., 2016). An important characteristic of the lower to the middle slope is its steepness

morphology, which can displace the water column vertically, thus contributing to tsunami formation (Tanioka and Satake, 1996). This has been evidenced to have increased the tsunami height from the Tohoku earthquake (Hooper et al., 2013). In the erosive margins such as Northern Chile, the velocity model shows a higher velocity zone (3 – 4.5 km/s) associated to a high fractured continental crust in this region compared to its seaward frontal prism (subsection 2.4.1; Petersen et al., 2021; Contreras-Reyes et al., 2012; Maksymowicz et al., 2018).

The pervasive seaward normal faults located in the lower to the middle slope are a prominent feature in the erosive margin (von Huene and Ranero, 2003; von Huene et al., 2004; Vannucchi et al., 2013; Sallares and Ranero, 2005). During subduction erosion, material from the base of the upper plate is removed through hydrofracturing, which has been implicated in the causative process for upper plate normal faulting (Adam and Reuther, 2000; Armijo and Thiele, 1990; von Huene and Ranero, 2003; von Huene et al., 2004). Coseismic and interseismic Coulomb Failure Stress Change (CFS) models have been used to investigate the relationship between upper plate fault activity and the subduction seismic cycle (Loveless et al., 2010a).

### 2.4.3 Upper slope

Due to lacking seismic reflection in the internal continental plate underneath the upper slope from multichannel seismic profiles (e.g., Fig. 3.2), thus this part is not a significant part of the thesis. Typically, various upper plate features such as transverse faults and forearc basins are observed along the South American Plate. These features are observed in subduction zones around the globe, and many suggestions that these link to the large earthquake occurrence (Scholz and Small, 1997; Song and Simons, 2003; Wells et al., 2003).

## 2.5 The 2014 Iquique earthquake sequence

Several large earthquakes in Northern Chile preceded the 2014 Iquique earthquake, including those in 1543, 1615, 1786 and 1877 (Comte and Pardo, 1991). Approximately 500 km of the northern Chile seismic gap were ruptured by the $M_w$ 8.1 earthquake of 1 April 2014 (Fig. 2.2, red star; Comte and Pardo, 1991; Ruiz and Madariaga, 2018). This seismic gap, between 18 and 23 °S, has not ruptured since 1877 ($M_w$ 8.6 Iquique earthquake), is capable of generating a $M_w$ ~9 earthquake (Kelleher, 1972). On 1 April 2014, an Mw 8.1 interplate thrust earthquake initiated in the northern portion of the 1877 seismic gap (19.642 °S, 70.817 °W, 23 : 46 : 46 UTC [U.S. Geological Survey (USGS) National Earthquake Information Center (NEIC): `http://earthquake.usgs.gov/regional/neic/`]). The global

centroid moment tensor (gCMT) solution for this event (http://www.globalcmt.org/CMTsearch.html) indicates an almost purely double-couple faulting geometry with strike 357 °, dip 18 °, and rake 109 ° at a centroid depth of 21.9 km and centroid location south of the hypocenter (19.77 °S, 70.98 °W), with a centroid time shift of 42.5 s and seismic moment of 1.69 × 1021 $Nm$ ($M_w$ 8.1) (Lay et al., 2014).

The mainshock was preceded by several months of seismic activity, with events M > 5 in August 2013 and January 2014 (Bedford et al., 2015). A large foreshock ($M_w$6.6, 16 March 2014) occurred in the upper plate (Cesca et al., 2016), and before the mainshock broke the asperity, the foreshock series migrated down onto the megathrust, where three events of M > 6 were recorded (An et al., 2014; Duputel et al., 2015; Gusman et al., 2015; Hayes et al., 2014; Herman et al., 2016; Lay et al., 2014; Liu et al., 2015; Meng et al., 2015; Ruiz et al., 2014; Schurr et al., 2014; Yagi et al., 2014). The mainshock was followed by a vigorous aftershock sequence, including an $M_w$7.6 event, the largest aftershock (02 : 43 : 14 UTC, 20.518 °S, 70.49,°W, centroid depth 31.3 km, 49 km southwest of Iquique), ~100 km south of the mainshock approximately 2 days later (Lay et al., 2014; Schurr et al., 2014).

The main $M_w$ 8.1 event occurred within a region of geodetically determined high interseismic coupling before the earthquake sequence (Duputel et al., 2015; Lay et al., 2014; Meng et al., 2015; Ruiz et al., 2014; Yagi et al., 2014) and exhibited a heterogeneous rupture with a complex moment-rate function (Duputel et al., 2015; Meng et al., 2015; Yagi et al., 2014). Distributed aseismic and seismic afterslip followed to the northeast and southwest of the main slip, respectively, in regions of lower interseismic coupling (Meng et al., 2015; Métois et al., 2016; Schurr et al., 2014; Shrivastava et al., 2019). A region of precursory slow slip surrounding and partially overlapping the eventual area of greatest coseismic slip has also been observed in this region (Meng et al., 2015; Ruiz et al., 2014; Schurr et al., 2020).

## 2.6 Geological setting of the Northern Chilean margin

In the Peru-Chile subduction margin, the Nazca Plate subducts obliquely beneath the South American Plate at a rate of approximately 6.6 cm/year (Angermann et al., 1999). Plate ages at the trench increase from the south to the north, reaching 52 Myr in the study area, where the Iquique Ridge subducts (Müller et al., 2008). Since at least the Jurassic period, the western edge of South America has been formed by subduction (Ramos, 2009). As a result of this subduction process, the oceanic Nazca plate flexes in the forearc region, causing high tensional stresses and the formation of horsts and grabens with a vertical displacement of up to 500 metres (Ranero et al., 2006; Contreras-Reyes et al., 2012; Geersen et al., 2018). Across the Nazca plate, the bathymetry is relatively rough, with prominent

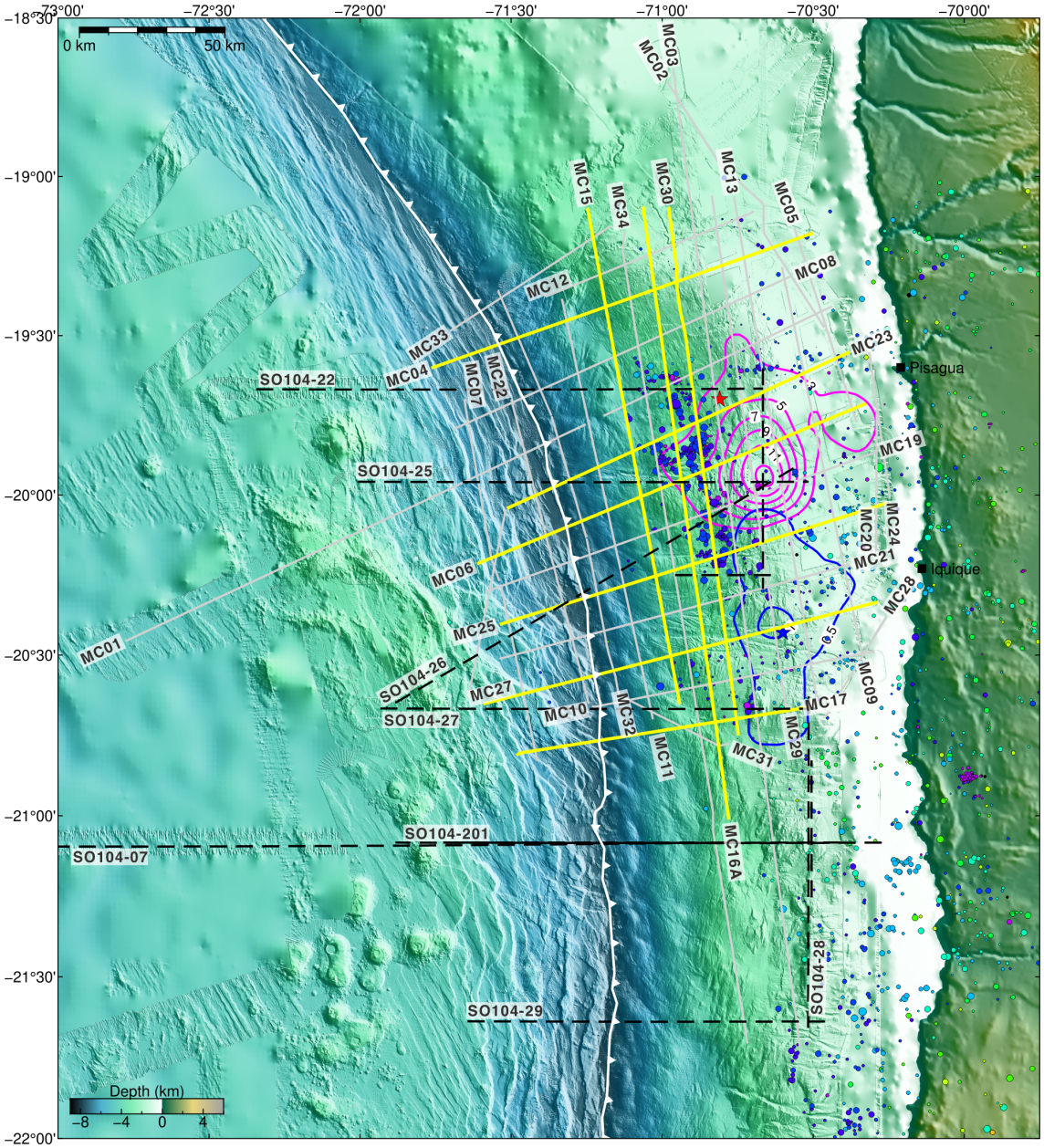


**Figure 2.2:** Overview map of the erosional margin of Northern Chile in the region affected by the 2014 Iquique earthquake. The hypocenter (star) and slip contour lines (in meters) of the 2014 Iquique Mw 8.1 mainshock (magenta) and Mw 7.7 aftershock (blue) are from (Duputel et al., 2015). Black dashed lines indicate the locations of the MCS lines acquired before the 2014 Iquique earthquake, while the gray and yellow lines represent the MCS lines acquired after the 2014 Iquique earthquake. The yellow MCS lines means the profiles in chapter 3 and 4. The white dashed lines show the depth of the plate interface estimated from the seismic reflection data. The colored circles according to the color bar (see Fig. 3.1) are aftershocks (December 2014 until October 2016) from the 2014 Iquique earthquake recorded by ocean bottom seismometers indicated as green and orange triangles (Petersen et al., 2021). All symbols as Fig. 3.1.

bathymetric ridges, seamounts, and incoming faults (Contreras-Reyes et al., 2015; Geersen et al., 2018). The faulting fabric on the oceanic crust offshore Northern Chilean margin consists of both the preexisting spreading fabric oriented 30 ° obliquely to the margin and normal faults parallel the margin just before entering the trenches (Contreras-Reyes and Carrizo, 2011; Geersen et al., 2018). As incoming plate enters subduction zones, the horst-and-graben structures exhibit some large offsets (Boneh et al., 2019). These features complicate the incoming plate in this region, further complex the subsurface conditions.

The most prominent feature on the oceanic crust is the SW-NE subduction Iquique Ridge. The on-axis Foundation hotspot is assumed to be the origin of the Iquique Ridge (Bello-González et al., 2018). It is characterized by a broad swell >1100 km long and up to 250 km wide, averaging >500 m high with multiple ridge sections and discrete 1 – 1.5 km high seamounts (Geersen et al., 2018). As the ridge enters the subduction zone at 18 ° and 20 °S, the trench is ~1 km shallower than to the north and south (Geersen et al., 2018). Subducting oceanic ridges have been identified as a major control on the historical distribution of earthquakes along the Chilean margin (Contreras-Reyes and Carrizo, 2011). Based on this finding, Geersen et al. (2015) delimits the ruptured area and shows that subducted seamounts are likely to be further responsible for reduced plate-coupling in the shallow subduction zone and a lowly coupled region around 20.5 °S.

Subduction or collision of high-relief oceanic features has also been observed offshore in north-central Chile, where the Juan Fernandez Ridge subducts beneath the South American Plate (Contreras-Reyes et al., 2014, 2015; Von Huene et al., 1997; Becerra et al., 2017). The results demonstrate the subduction erosion processes caused by the quasi-stationary collision of the Juan Fernandez Ridge with the continental South American Plate. Offshore Peru, the Nazca Ridge subducts beneath the South American Plate. Using MCS data and bathymetric data, Krabbenhöft et al. (2004) provide evidence for subduction erosion processes temporarily enhanced here by the Nazca Ridge subduction.

The northern Chilean margin is also a typical erosive margin, which has undergone subduction erosion since at least the Jurassic, inferred from the eastward migration of the volcanic arc (Rutland, 1971; Stern, 2011) as well as the long-term arcward retreat of the trench, crustal thinning and subsidence of the outer forearc (Kukowski and Oncken, 2006; Contreras-Reyes, 2018). Several wedge-shaped bodies of reduced velocities were discovered off northern Chile, which has been interpreted as the toe of fluid-saturated margins that are disaggregated by fracturing as a result of subduction erosion (Sallares and Ranero, 2005; Contreras-Reyes et al., 2012; Reginato et al., 2020; Petersen et al., 2021).

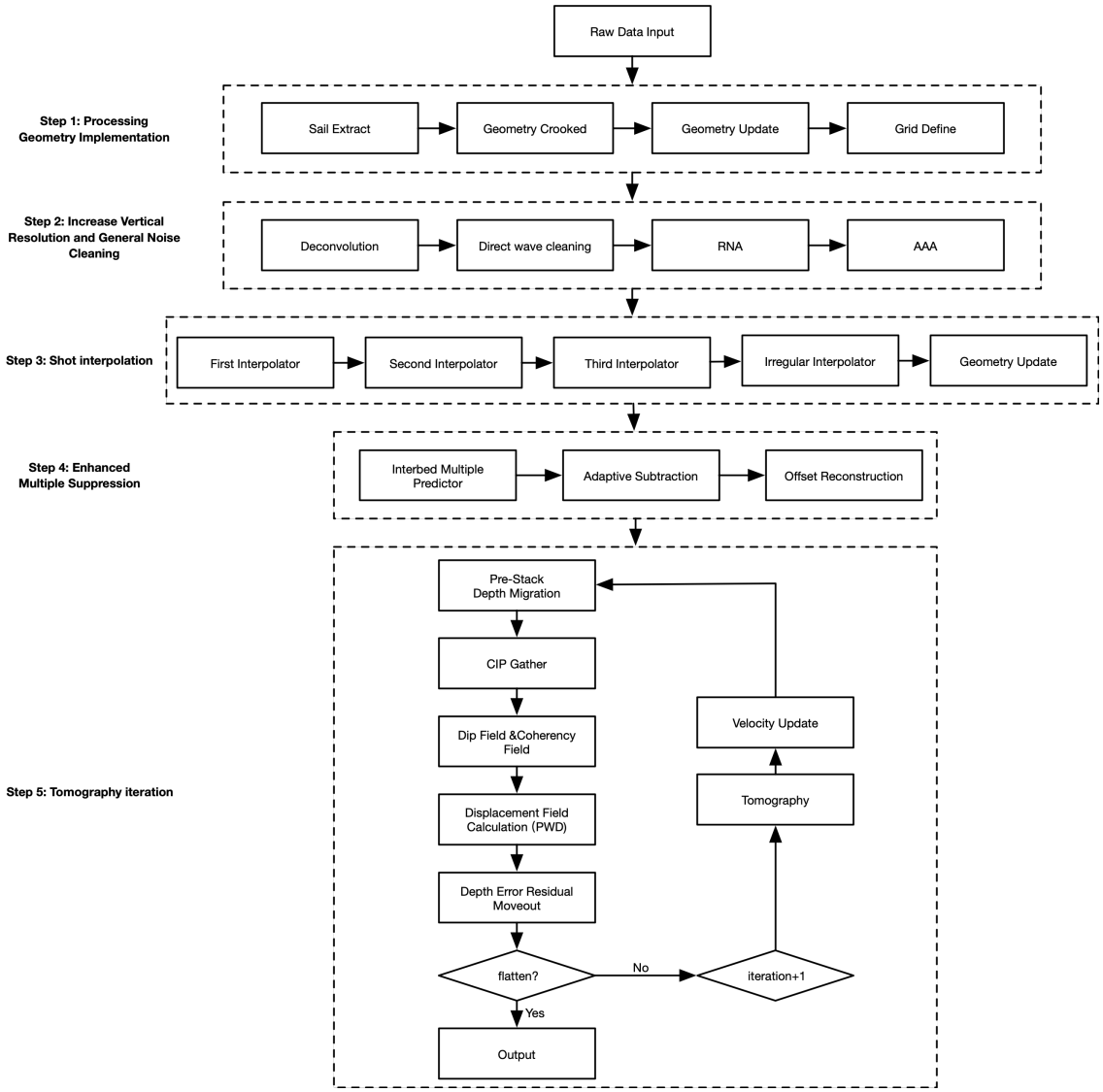


**Figure 2.3:** Overview of the processing sequence.

## 2.7 Reflection seismic data

Seismic multichannel reflection data used in this study were acquired in 2016 during the MGL1610 cruise of *R/V Marcus G. Langseth* offshore Northern Chile (https://www.rvdata.us/search/cruise/MGL1610). Seismic signals were generated with a source of 6600 cubic inches (108.15 liters), provided by four strings of 10 air-guns each. Data were recorded with an 8 km long streamer towed by *R/V Marcus G. Langseth*. The source was towed at 12 m depth below the water surface, and the record length was 16 s. The shots were acquired using a shot interval of 125 m to avoid interference from previous shots on ocean bottom seismometer data that were being acquired simultaneously. Surface-related multiple prediction, anomalous amplitude noise attenuation and adaptive filter

are effective methods to attenuate multiples in our 2D seismic data, the detail of the de-multiple could be found in chapter 3 (Fig. 2.3, step 1 - 4). After that, we update the *vp* model to get the accurate depth based on residual move-out analysis of reflectors in common image point (CIP) gathers through the tomography iteration, the detail of the iteration process could be found in chapter 4 (Fig. 2.3, step 5). Accurate subsurface velocity models are crucial for geological interpretations based on seismic depth images. The pre-stack depth migration (PSDM) profiles in the previous study with a preliminary P-wave velocity model (Ma et al., 2022) may result in 1 - 2 km mismatch in depth, which should not be applied in studying the subsurface structure. Although the primary may lead to some depth error, it does not influence the study of reflectivity along the plate interface described in chapter 3. The most critical part for the tomography iteration is the depth error estimation, in which to calculate the residual move-out for the reflector in the CIP gathers. After several iterations, an accurate subsurface vp field is produced and the depth of the reflectors is more precise, which could be applied in the study of internal structure, such as the subduction Iquique Ridge and its influence on the plate interface and hanging upper plate described in chapter 4.

## References

Adam, J. & Reuther, C. D. (2000). Crustal dynamics and active fault mechanics during subduction erosion. application of frictional wedge analysis on to the north chilean forearc. *Tectonophysics*, *321*(3), 297–325, https://doi.org/10.1016/s0040-1951(00)00074-3.

Agard, P., Plunder, A., Angiboust, S., Bonnet, G., & Ruh, J. (2018). The subduction plate interface: rock record and mechanical coupling (from long to short timescales). *Lithos*, *320*, 537–566, https://doi.org/10.1016/j.lithos.2018.09.029.

An, C., Sepulveda, I., & Liu, P. L. F. (2014). Tsunami source and its validation of the 2014 iquique, chile, earthquake. *Geophysical Research Letters*, *41*(11), 3988–3994, https://doi.org/10.1002/2014gl060567.

Angermann, D., Klotz, J., & Reigber, C. (1999). Space-geodetic estimation of the nazca-south america euler vector. *Earth and Planetary Science Letters*, *171*(3), 329–334, https://doi.org/10.1016/S0012-821x(99)00173-9.

Arai, R., Takahashi, T., Kodaira, S., Kaiho, Y., Nakanishi, A., Fujie, G., Nakamura, Y., Yamamoto, Y., Ishihara, Y., Miura, S., & Kaneda, Y. (2016). Structure of the tsunamigenic plate boundary and low-frequency earthquakes in the southern ryukyu trench. *Nature Communications*, *7*, https://doi.org/10.1038/ncomms12255.

Armijo, R. & Thiele, R. (1990). Active faulting in northern chile: ramp stacking and lateral decoupling along a subduction plate boundary? *Earth and Planetary Science Letters*, *98*(1), 40–61, https://doi.org/10.1016/0012-821x(90)90087-e.

Bangs, N. L. B., Gulick, S. P. S., & Shipley, T. H. (2006). Seamount subduction erosion in the nankai trough and its potential impact on the seismogenic zone. *Geology*, *34*(8), 701–704, https://doi.org/10.1130/G22451.1.

Becerra, J., Arriagada, C., Contreras-Reyes, E., Bascunan, S., De Pascale, G. P., Reichert, C., Diaz-Naveas, J., & Cornejo, N. (2017). Gravitational deformation and inherited structural control on slope morphology in the subduction zone of north-central chile (ca. 29-33 degrees s). *Basin Research*, *29*(6), 798–815, https://doi.org/10.1111/bre.12205.

Bedford, J., Moreno, M., Baez, J. C., Lange, D., Tilmann, F., Rosenau, M., Heidbach, O., Oncken, O., Bartsch, M., Rietbrock, A., Tassara, A., Bevis, M., & Vigny, C. (2013). A high-resolution, time-variable afterslip model for the 2010 maule mw = 8.8, chile megathrust earthquake. *Earth and Planetary Science Letters*, *383*, 26–36, https://doi.org/10.1016/j.epsl.2013.09.020.

Bedford, J., Moreno, M., Schurr, B., Bartsch, M., & Oncken, O. (2015). Investigating the final seismic swarm before the iquique-pisagua 2014 m-w 8.1 by comparison of continuous gps and seismic foreshock data. *Geophysical Research Letters*, *42*(10), 3820–3828, https://doi.org/10.1002/2015gl063953.

Bello-González, J. P., Contreras-Reyes, E., & Arriagada, C. (2018). Predicted path for hotspot tracks off south america since paleocene times: Tectonic implications of ridge-trench collision along the andean margin. *Gondwana Research*, *64*(september), 216–234, https://doi.org/10.1016/j.gr.2018.07.008.

Bilek, S. L. & Lay, T. (2002). Tsunami earthquakes possibly widespread manifestations of frictional conditional stability. *Geophysical Research Letters*, *29*(14), 18–1, https://doi.org/10.1029/2002gl015215.

Boneh, Y., Schottenfels, E., Kwong, K., van Zelst, I., Tong, X. Y., Eimer, M., Miller, M. S., Moresi, L., Warren, J. M., Wiens, D. A., Billen, M., Naliboff, J., & Zhan, Z. W. (2019). Intermediate-depth earthquakes controlled by incoming plate hydration along bending-related faults. *Geophysical Research Letters*, *46*(7), 3688–3697, https://doi.org/10.1029/2018gl081585.

Brace, W. F. & Byerlee, J. D. (1966). Stick-slip as a mechanism for earthquakes. *Science*, *153*(3739), 990–2, https://doi.org/10.1126/science.153.3739.990.

Brizzi, S., Zelst, I., Funiciello, F., Corbi, F., & Dinther, Y. (2020). How sediment thickness influences subduction dynamics and seismicity. *Journal of Geophysical Research: Solid Earth*, *125*(8), https://doi.org/10.1029/2019jb018964.

Byrne, D. E., Davis, D. M., & Sykes, L. R. (1988). Loci and maximum size of thrust earthquakes and the mechanics of the shallow region of subduction zones. *Tectonics*, *7*(4), 833–857, https://doi.org/10.1029/TC007i004p00833.

Cesca, S., Grigoli, F., Heimann, S., Dahm, T., Kriegerowski, M., Sobiesiak, M., Tassara, C., & Olcay, M. (2016). The mw 8.1 2014 iquique, chile, seismic sequence: A tale of foreshocks and aftershocks. *Geophys. J. Int.*, *204*(3), 1766–1780, https://doi.org/10.1093/gji/ggv544.

Chesley, C., Naif, S., Key, K., & Bassett, D. (2021). Fluid-rich subducting topography generates anomalous forearc porosity. *Nature*, *595*(7866), 255–260, https://doi.org/10.1038/s41586-021-03619-8.

Chlieh, M., Avouac, J. P., Sieh, K., Natawidjaja, D. H., & Galetzka, J. (2008). Heterogeneous coupling of the sumatran megathrust constrained by geodetic and paleogeodetic measurements. *Journal of Geophysical Research-Solid Earth*, *113*(B5), https://doi.org/10.1029/2007jb004981.

Christensen, D. H. & Ruff, L. J. (1988). Seismic coupling and outer rise earthquakes. *Journal of Geophysical Research: Solid Earth*, *93*(B11), 13421–13444, https://doi.org/10.1029/JB093iB11p13421.

Clarke, A. P., Vannucchi, P., & Morgan, J. (2018). Seamount chain-subduction zone interactions: Implications for accretionary and erosive subduction zone behavior. *Geology*, *46*(4), 367–370, https://doi.org/10.1130/G40063.1.

Clift, P. & Vannucchi, P. (2004). Controls on tectonic accretion versus erosion in subduction zones: Implications for the origin and recycling of the continental crust. *Reviews of Geophysics*, *42*(2), https://doi.org/10.1029/2003rg000127.

Cloos, M. & Shreve, R. L. (1996). Shear-zone thickness and the seismicity of chilean- and marianas-type subduction zones. *Geology*, *24*(2), 107–110, https://doi.org/10.1130/0091-7613(1996)024<0107:Sztats>2.3.Co;2.

Comte, D. & Pardo, M. (1991). Reappraisal of great historical earthquakes in the northern chile and southern peru seismic gaps. *Nat. hazards*, *4*(1), 23–44, https://doi.org/10.1007/BF00126557.

Contreras-Reyes, E. (2018). *Structure and tectonics of the Chilean convergent margin from wide-angle seismic studies: a review*, (pp. 3–29). Springer.

Contreras-Reyes, E., Becerra, J., Kopp, H., Reichert, C., & Diaz-Naveas, J. (2014). Seismic structure of the north-central chilean convergent margin: Subduction erosion of a paleomagmatic arc. *Geophysical Research Letters*, *41*(5), 1523–1529, https://doi.org/10.1002/2013gl058729.

Contreras-Reyes, E. & Carrizo, D. (2011). Control of high oceanic features and subduction channel on earthquake ruptures along the chile-peru subduction zone. *Physics of the Earth and Planetary Interiors*, *186*(1-2), 49–58, https://doi.org/10.1016/j.pepi.2011.03.002.

Contreras-Reyes, E., Flueh, E. R., & Grevemeyer, I. (2010). Tectonic control on sediment accretion and subduction off south central chile: Implications for coseismic rupture processes of the 1960 and 2010 megathrust earthquakes. *Tectonics*, *29*(6), https://doi.org/10.1029/2010tc002734.

Contreras-Reyes, E., Jara, J., Grevemeyer, I., Ruiz, S., & Carrizo, D. (2012). Abrupt change in the dip of the subducting plate beneath north chile. *Nature Geoscience*, *5*(5), 342–345, https://doi.org/10.1038/Ngeo1447.

Contreras-Reyes, E., Ruiz, J. A., Becerra, J., Kopp, H., Reichert, C., Maksymowicz, A., & Arriagada, C. (2015). Structure and tectonics of the central chilean margin (31 degrees-33 degrees s): implications for subduction erosion and shallow crustal seismicity. *Geophysical Journal International*, *203*(2), 776–791, https://doi.org/10.1093/gji/ggv309.

Cummins, P. R., Baba, T., Kodaira, S., & Kaneda, Y. (2002). The 1946 nankai earthquake and segmentation of the nankai trough. *Physics of the Earth and Planetary Interiors*, *132*(1-3), 75–87, https://doi.org/10.1016/S0031-9201(02)00045-6.

Dieterich, J. H. & Kilgore, B. D. (1994). Direct observation of frictional contacts: New insights for state-dependent properties. *Pure and Applied Geophysics*, *143*(1), 283–302, https://doi.org/10.1007/BF00874332.

Dominguez, S., Lallemand, S. E., Malavieille, J., & von Huene, R. (1998). Upper plate deformation associated with seamount subduction. *Tectonophysics*, *293*(3-4), 207–224, https://doi.org/10.1016/S0040-1951(98)00086-9.

Dominguez, S., Malavieille, J., & Lallemand, S. E. (2000). Deformation of accretionary wedges in response to seamount subduction: Insights from sandbox experiments. *Tectonics*, *19*(1), 182–196, https://doi.org/10.1029/1999tc900055.

Duarte, J. C., Schellart, W. P., & Cruden, A. R. (2015). How weak is the subduction zone interface? *GEOPHYSICAL RESEARCH LETTERS*, *42*(8), 2664–2673, https://doi.org/10.1002/2014GL062876.

Duputel, Z., Jiang, J., Jolivet, R., Simons, M., Rivera, L., Ampuero, J. P., Riel, B., Owen, S. E., Moore, A. W., Samsonov, S. V., Culaciati, F. O., & Minson, S. E. (2015). The iquique earthquake sequence of april 2014: Bayesian modeling accounting for prediction uncertainty. *Geophysical Research Letters*, *42*(19), 7949–7957, https://doi.org/10.1002/2015gl065402.

Faccenda, M., Gerya, T. V., & Burlini, L. (2009). Deep slab hydration induced by bending-related variations in tectonic pressure. *Nature Geoscience*, *2*(11), 790–793, https://doi.org/10.1038/Ngeo656.

Faccenda, M., Gerya, T. V., Mancktelow, N. S., & Moresi, L. (2012). Fluid flow during slab unbending and dehydration: Implications for intermediate-depth seismicity, slab weakening and deep water recycling. *Geochemistry Geophysics Geosystems*, *13*, https://doi.org/10.1029/2011gc003860.

Gaetani, G. A. & Grove, T. L. (1998). The influence of water on melting of mantle peridotite. *Contributions to Mineralogy and Petrology*, *131*(4), 323–346, https://doi.org//10.1007/s004100050396.

Geersen, J., Ranero, C. R., Barckhausen, U., & Reichert, C. (2015). Subducting seamounts control interplate coupling and seismic rupture in the 2014 iquique earthquake area. *Nat Commun*, *6*, 8267, https://doi.org/10.1038/ncomms9267.

Geersen, J., Ranero, C. R., Klaucke, I., Behrmann, J. H., Kopp, H., Trehu, A. M., Contreras-Reyes, E., Barckhausen, U., & Reichert, C. (2018). Active tectonics of the north chilean marine forearc and adjacent oceanic nazca plate. *Tectonics*, *37*(11), 4194–4211, https://doi.org/10.1029/2018tc005087.

Grevemeyer, I., Kaul, N., Diaz-Naveas, J. L., Villinger, H. W., Ranero, C. R., & Reichert, C. (2005). Heat flow and bending-related faulting at subduction trenches: Case studies offshore of nicaragua and central chile. *Earth and Planetary Science Letters*, *236*(1-2), 238–248, https://doi.org/10.1016/j.epsl.2005.04.048.

Grevemeyer, I., Ranero, C. R., Flueh, E. R., Klaschen, D., & Bialas, J. (2007). Passive and active seismological study of bending-related faulting and mantle serpentinization at the middle america trench. *Earth and Planetary Science Letters*, *258*(3-4), 528–542, https://doi.org/10.1016/j.epsl.2007.04.013.

Gusman, A. R., Murotani, S., Satake, K., Heidarzadeh, M., Gunawan, E., Watada, S., & Schurr, B. (2015). Fault slip distribution of the 2014 iquique, chile, earthquake estimated from ocean-wide tsunami waveforms and gps data. *Geophysical Research Letters*, *42*(4), 1053–1060, https://doi.org/10.1002/2014gl062604.

Hacker, B. R., Abers, G. A., & Peacock, S. M. (2003). Subduction factory 1. theoretical mineralogy, densities, seismic wave speeds, and h2o contents. *Journal of Geophysical Research: Solid Earth*, *108*(B1), https://doi.org/10.1029/2001jb001127.

Han, S. S., Bangs, N. L., Carbotte, S. M., Saffer, D. M., & Gibson, J. C. (2017). Links between sediment consolidation and cascadia megathrust slip behaviour. *Nature Geoscience*, *10*(12), 954–+, https://doi.org/10.1038/s41561-017-0007-2.

Hayes, G. P., Herman, M. W., Barnhart, W. D., Furlong, K. P., Riquelme, S., Benz, H. M., Bergman, E., Barrientos, S., Earle, P. S., & Samsonov, S. (2014). Continuing megathrust earthquake potential in chile after the 2014 iquique earthquake. *Nature*, *512*(7514), 295–8, https://doi.org/10.1038/nature13677.

Herman, M. W., Furlong, K. P., Hayes, G. P., & Benz, H. M. (2016). Foreshock triggering of the 1 april 2014 mw 8.2 iquique, chile, earthquake. *Earth and Planetary Science Letters*, *447*(April 2014), 119–129, https://doi.org/10.1016/j.epsl.2016.04.020.

Heuret, A., Conrad, C. P., Funiciello, F., Lallemand, S., & Sandri, L. (2012). Relation between subduction megathrust earthquakes, trench sediment thickness and upper plate strain. *Geophysical Research Letters*, *39*(5), https://doi.org/10.1029/2011gl050712.

Hicks, S. P., Rietbrock, A., Ryder, I. M. A., Lee, C. S., & Miller, M. (2014). Anatomy of a megathrust: The 2010 m8.8 maule, chile earthquake rupture zone imaged using seismic tomography. *Earth and Planetary Science Letters*, *405*, 142–155, https://doi.org/10.1016/j.epsl.2014.08.028.

Hilde, T. W. C. (1983). Sediment subduction versus accretion around the pacific. *Tectonophysics*, *99*(2-4), 381–397, https://doi.org/10.1016/0040-1951(83)90114-2.

Hillier, J. K. & Watts, A. B. (2007). Global distribution of seamounts from ship-track bathymetry data. *Geophysical Research Letters*, *34*(13), https://doi.org/10.1029/2007gl029874.

Hooper, A., Pietrzak, J., Simons, W., Cui, H., Riva, R., Naeije, M., van Scheltinga, A. T., Schrama, E., Stelling, G., & Socquet, A. (2013). Importance of horizontal seafloor motion on tsunami height for the 2011 mw= 9.0 tohoku-oki earthquake. *Earth and Planetary Science Letters*, *361*, 469–479, https://doi.org/10.1016/j.epsl.2012.11.013.

Hyndman, R. D. & Wang, K. (1993). Thermal constraints on the zone of major thrust earthquake failure - the cascadia subduction zone. *Journal of Geophysical Research-Solid Earth*, *98*(B2), 2039–2060, https://doi.org/10.1029/92jb02279.

Hyndman, R. D., Yamano, M., & Oleskevich, D. A. (1997). The seismogenic zone of subduction thrust faults. *Island Arc*, *6*(3), 244–260, https://doi.org/10.1111/j.1440-1738.1997.tb00175.x.

Ito, Y., Obara, K., Shiomi, K., Sekine, S., & Hirose, H. (2007). Slow earthquakes coincident with episodic tremors and slow slip events. *Science*, *315*(5811), 503–506, https://doi.org/10.1126/science.1134454.

Iwamori, H. & Nakakuki, T. (2013). Fluid processes in subduction zones and water transport to the deep mantle. *Physics and chemistry of the deep Earth*, (pp. 372–391)., https://doi.org/10.1002/9781118529492.ch13.

Jarrard, R. D. (1986). Terrane motion by strike-slip faulting of forearc slivers. *Geology*, *14*(9), 780–783, https://doi.org/10.1130/0091-7613(1986)14<780:TMBSFO>2.0.CO;2.

Jiao, W. J., Silver, P. G., Fei, Y. W., & Prewitt, C. T. (2000). Do intermediate- and deep-focus earthquakes occur on preexisting weak zones? an examination of the tonga subduction zone. *Journal of Geophysical Research-Solid Earth*, *105*(B12), 28125–28138, https://doi.org/10.1029/2000jb900314.

Kameda, J., Yamaguchi, A., Saito, S., Sakuma, H., Kawamura, K., & Kimura, G. (2011). A new source of water in seismogenic subduction zones. *Geophysical Research Letters*, *38*, L22306, https://doi.org/10.1029/2011gl048883.

Kanamori, H. (1986). Rupture process of subduction-zone earthquakes. *Annual Review of Earth and Planetary Sciences*, *14*(1), 293–322, https://doi.org/10.1146/annurev.ea.14.050186.001453.

Kelleher, J. & Mccann, W. (1976). Buoyant zones, great earthquakes, and unstable boundaries of subduction. *Journal of Geophysical Research*, *81*(26), 4885–4896, https://doi.org/DOI 10.1029/JB081i026p04885.

Kelleher, J. A. (1972). Rupture zones of large south-american earthquakes and some predictions. *Journal of Geophysical Research*, *77*(11), 2087, https://doi.org/DOI 10.1029/JB077i011p02087.

Kitajima, H. & Saffer, D. M. (2012). Elevated pore pressure and anomalously low stress in regions of low frequency earthquakes along the nankai trough subduction megathrust. *Geophysical Research Letters*, *39*, https://doi.org/10.1029/2012gl053793.

Kobayashi, K., Nakanishi, M., Tamaki, K., & Ogawa, Y. (1998). Outer slope faulting associated with the western kuril and japan trenches. *Geophysical Journal International*, *134*, 356–372, https://doi.org/10.1046/j.1365-246x.1998.00569.x.

Kodaira, S., No, T., Nakamura, Y., Fujiwara, T., Kaiho, Y., Miura, S., Takahashi, N., Kaneda, Y., & Taira, A. (2012). Coseismic fault rupture at the trench axis during the 2011 tohoku-oki earthquake. *Nature Geoscience*, *5*(9), 646–650, https://doi.org/10.1038/Ngeo1547.

Kopp, H., Flueh, E. R., Papenberg, C., & Klaeschen, D. (2004). Seismic investigations of the o'higgins seamount group and juan fernandez ridge: Aseismic ridge emplacement and lithosphere hydration. *Tectonics*, *23*(2), 1–21, https://doi.org/10.1029/2003tc001590.

Kopp, H., Flueh, E. R., Petersen, C. J., Weinrebe, W., Wittwer, A., & Scientists, M. (2006). The java margin revisited: Evidence for subduction erosion off java. *Earth and Planetary Science Letters*, *242*(1-2), 130–142, https://doi.org/10.1016/j.epsl.2005.11.036.

Krabbenhöft, A., Bialas, J., Kopp, H., Kukowski, N., & Hübscher, C. (2004). Crustal structure of the peruvian continental margin from wide-angle seismic studies. *Geophysical Journal International*, *159*(2), 749–764, https://doi.org/10.1111/j.1365-246X.2004.02425.x.

Kukowski, N. & Oncken, O. (2006). Subduction erosion — the "normal" mode of fore-arc material transfer along the chilean margin? *The Andes*, (pp. 217–236)., https://doi.org/10.1007/978-3-540-48684-8_10.

Kukowski, N., Schillhorn, T., Huhn, K., von Rad, U., Husen, S., & Flueh, E. R. (2001). Morphotectonics and mechanics of the central makran accretionary wedge off pakistan. *Marine Geology*, *173*(1-4), 1–19, https://doi.org/10.1016/S0025-3227(00)00167-5.

Lallemand, S. E., Malavieille, J., & Calassou, S. (1992). Effects of oceanic ridge subduction on accretionary wedges - experimental modeling and marine observations. *Tectonics*, *11*(6), 1301–1313, https://doi.org/10.1029/92tc00637.

Lallemand, S. E., Schnürle, P., & Malavieille, J. (1994). Coulomb theory applied to accretionary and nonaccretionary wedges: Possible causes for tectonic erosion and/or frontal accretion. *Journal of Geophysical Research: Solid Earth*, *99*(B6), 12033–12055, https://doi.org/10.1029/94JB00124.

Lamb, S. & Davis, P. (2003). Cenozoic climate change as a possible cause for the rise of the andes. *Nature*, *425*(6960), 792–7, https://doi.org/10.1038/nature02049.

Lay, T., Yue, H., Brodsky, E. E., & An, C. (2014). The 1 april 2014 iquique, chile, mw 8.1 earthquake rupture sequence. *Geophysical Research Letters*, *7*(April), 1–8, https://doi.org/10.1002/2014GL060238.Received.

Lefeldt, M., Grevemeyer, I., Goßler, J., & Bialas, J. (2009). Intraplate seismicity and related mantle hydration at the nicaraguan trench outer rise. *Geophysical Journal International*, *178*(2), 742–752, https://doi.org/10.1111/j.1365-246X.2009.04167.x.

Liu, C. L., Zheng, Y., Wang, R. J., & Xiong, X. (2015). Kinematic rupture process of the 2014 chile m-w 8.1 earthquake constrained by strong-motion, gps static offsets and teleseismic data. *Geophysical Journal International*, *202*(2), 1137–1145, https://doi.org/10.1093/gji/ggv214.

Loveless, J. P., Allmendinger, R. W., Pritchard, M. E., & González, G. (2010a). Normal and reverse faulting driven by the subduction zone earthquake cycle in the northern chilean fore arc. *Tectonics*, https://doi.org/10.1029/2009TC002465.

Loveless, J. P., Pritchard, M. E., & Kukowski, N. (2010b). Testing mechanisms of subduction zone segmentation and seismogenesis with slip distributions from recent andean earthquakes. *Tectonophysics*, *495*(1-2), 15–33, https://doi.org/10.1016/j.tecto.2009.05.008.

Ma, B., Geersen, J., Lange, D., Klaeschen, D., Grevemeyer, I., Contreras-Reyes, E., Petersen, F., Riedel, M., Xia, Y., Trehu, A. M., & Kopp, H. (2022). Megathrust reflectivity reveals the updip limit of the 2014 iquique earthquake rupture. *Nat Commun*, *13*(1), 3969, https://doi.org/10.1038/s41467-022-31448-4.

Maksymowicz, A., Ruiz, J., Vera, E., Contreras-Reyes, E., Ruiz, S., Arraigada, C., Bonvalot, S., & Bascunan, S. (2018). Heterogeneous structure of the northern chile marine forearc and its implications for megathrust earthquakes. *Geophysical Journal International*, *215*(2), 1080–1097, https://doi.org/10.1093/gji/ggy325.

Mannu, U., Ueda, K., Willett, S. D., Gerya, T. V., & Strasser, M. (2016). Impact of sedimentation on evolution of accretionary wedges: Insights from high-resolution thermomechanical modeling. *Tectonics*, *35*(12), 2828–2846, https://doi.org/10.1002/2016tc004239.

Marcaillou, B., Collot, J. Y., Ribodetti, A., d'Acremont, E., Mahamat, A. A., & Alvarado, A. (2016). Seamount subduction at the north-ecuadorian convergent margin: Effects on structures, inter-seismic coupling and seismogenesis. *Earth and Planetary Science Letters*, *433*, 146–158, https://doi.org/10.1016/j.epsl.2015.10.043.

Marone, C. (1998). Laboratory-derived friction laws and their application to seismic faulting. *Annual Review of Earth and Planetary Sciences*, *26*(1), 643–696, https://doi.org/10.1146/annurev.earth.26.1.643.

Masson, D. G. (1991). Fault patterns at outer trench walls. *Marine Geophysical Researches*, *13*(3), 209–225, https://doi.org/10.1007/Bf00369150.

Meng, L. S., Huang, H., Burgmann, R., Ampuero, J. P., & Strader, A. (2015). Dual megathrust slip behaviors of the 2014 iquique earthquake sequence. *Earth and Planetary Science Letters*, *411*, 177–187, https://doi.org/10.1016/j.epsl.2014.11.041.

Metois, M., Socquet, A., Vigny, C., Carrizo, D., Peyrat, S., Delorme, A., Maureira, E., Valderas-Bermejo, M. C., & Ortega, I. (2013). Revisiting the north chile seismic gap segmentation using gps-derived interseismic coupling. *Geophysical Journal International*, *194*(3), 1283–1294, https://doi.org/10.1093/gji/ggt183.

Mochizuki, K., Yamada, T., Shinohara, M., Yamanaka, Y., & Kanazawa, T. (2008). Weak interplate coupling by seamounts and repeating m approximately 7 earthquakes. *Science*, *321*(5893), 1194–7, https://doi.org/10.1126/science.1160250.

Moore, J. C. & Saffer, D. (2001). Updip limit of the seismogenic zone beneath the accretionary prism of southwest japan: An effect of diagenetic to low-grade metamorphic processes and increasing effective stress. *Geology*, *29*(2), 183–186, https://doi.org/10.1130/0091-7613(2001)029<0183:Ulotsz>2.0.Co;2.

Moreno, M., Haberland, C., Oncken, O., Rietbrock, A., Angiboust, S., & Heidbach, O. (2014). Locking of the chile subduction zone controlled by fluid pressure before the 2010 earthquake. *Nature Geoscience*, *7*(4), 292–296, https://doi.org/10.1038/ngeo2102.

Moscoso, E., Grevemeyer, I., Contreras-Reyes, E., Flueh, E. R., Dzierma, Y., Rabbel, W., & Thorwart, M. (2011). Revealing the deep structure and rupture plane of the 2010 maule, chile earthquake (mw=8.8) using wide angle seismic data. *Earth and Planetary Science Letters*, *307*(1-2), 147–155, https://doi.org/10.1016/j.epsl.2011.04.025.

Métois, M., Vigny, C., & Socquet, A. (2016). Interseismic coupling, megathrust earthquakes and seismic swarms along the chilean subduction zone (38°–18°s). *Pure and Applied Geophysics*, *173*(5), 1431–1449, https://doi.org/10.1007/s00024-016-1280-5.

Müller, R. D., Sdrolias, M., Gaina, C., & Roest, W. R. (2008). Age, spreading rates, and spreading asymmetry of the world's ocean crust. *Geochemistry, Geophysics, Geosystems*, *9*(4), https://doi.org/10.1029/2007gc001743.

Nishikawa, T. & Ide, S. (2015). Background seismicity rate at subduction zones linked to slab-bending-related hydration. *Geophysical Research Letters*, *42*(17), 7081–7089, https://doi.org/10.1002/2015gl064578.

Nocquet, J. M., Jarrin, P., Vallee, M., Mothes, P. A., Grandin, R., Rolandone, F., Delouis, B., Yepes, H., Font, Y., Fuentes, D., Regnier, M., Laurendeau, A., Cisneros, D., Hernandez, S., Sladen, A., Singaucho, J. C., Mora, H., Gomez, J., Montes, L., & Charvis, P. (2017). Supercycle at the ecuadorian subduction zone revealed after the 2016 pedernales earthquake. *Nature Geoscience*, *10*(2), 145–+, https://doi.org/10.1038/Ngeo2864.

Noda, A., Tanaka, H., Ikeda, M., Onishi, K., & Nishizaka, N. (2016). Dynamic rupture simulations of the median tectonic line in southwest japan: Rupture propagations and macroscopic source parameters. In *AGU Fall Meeting Abstracts*, volume 2016 (pp. S13A–2544).

Oleskevich, D. A., Hyndman, R. D., & Wang, K. (1999). The updip and downdip limits to great subduction earthquakes: Thermal and structural models of cascadia, south alaska, sw japan, and chile. *Journal of Geophysical Research-Solid Earth*, *104*(B7), 14965–14991, https://doi.org/10.1029/1999jb900060.

Pacheco, J. F. & Sykes, L. R. (1992). Seismic moment catalog of large shallow earthquakes, 1900 to 1989. *Bulletin of the Seismological Society of America*, *82*(3), 1306–1349, https://doi.org/10.1785/BSSA0820031306.

Peacock, S. A. (1990). Fluid processes in subduction zones. *Science*, *248*(4953), 329–337, https://doi.org/10.1126/science.248.4953.329.

Peacock, S. M. & Wang, K. (1999). Seismic consequences of warm versus cool subduction metamorphism: Examples from southwest and northeast japan. *Science*, *286*(5441), 937–939, https://doi.org/10.1126/science.286.5441.937.

Petersen, F., Lange, D., Ma, B., Grevemeyer, I., Geersen, J., Klaeschen, D., Contreras-Reyes, E., Barrientos, S., Tréhu, A. M., Vera, E., & Kopp, H. (2021). Relationship between subduction erosion and the up-dip limit of the 2014 mw 8.1 iquique earthquake. *Geophysical Research Letters*, *48*(9), e2020GL092207, https://doi.org/10.1029/2020gl092207.

Ramos, V. A. (2009). Anatomy and global context of the andes: Main geologic features and the andean orogenic cycle. *Backbone of the Americas: Shallow subduction, plateau uplift, and ridge and terrane collision*, *204*, 31–65, https://doi.org/10.1130/MEM204.

Ranero, C. R., Grevemeyer, I., Sahling, H., Barckhausen, U., Hensen, C., Wallmann, K., Weinrebe, W., Vannucchi, P., von Huene, R., & McIntosh, K. (2008). Hydrogeological system of erosional convergent margins and its influence on tectonics and interplate seismogenesis. *Geochemistry, Geophysics, Geosystems*, *9*(3), Q03S04, https://doi.org/10.1029/2007gc001679.

Ranero, C. R., Morgan, J. P., McIntosh, K., & Reichert, C. (2003). Bending-related faulting and mantle serpentinization at the middle america trench. *Nature*, *425*(6956), 367–73, https://doi.org/10.1038/nature01961.

Ranero, C. R., Villasenor, A., Morgan, J. P., & Weinrebe, W. (2005). Relationship between bend-faulting at trenches and intermediate-depth seismicity. *Geochemistry Geophysics Geosystems*, *6*(12), https://doi.org/10.1029/2005gc000997.

Ranero, C. R. & von Huene, R. (2000). Subduction erosion along the middle america convergent margin. *Nature*, *404*(6779), 748–52, https://doi.org/10.1038/35008046.

Ranero, C. R., von Huene, R., Weinrebe, W., & Reichert, C. (2006). *Tectonic processes along the Chile convergent margin*, (pp. 91–121). Springer.

Reginato, G., Vera, E., Contreras-Reyes, E., Trehu, A. M., Maksymowicz, A., Bello-Gonzalez, J. P., & Gonzalez, F. (2020). Seismic structure and tectonics of the continental wedge overlying the source region of the iquique mw8.1 2014 earthquake. *Tectonophysics*, *796*, https://doi.org/10.1016/j.tecto.2020.228629.

Ruff, L. J. (1989). *Do trench sediments affect great earthquake occurrence in subduction zones?*, (pp. 263–282). Springer.

Ruiz, S. & Madariaga, R. (2018). Historical and recent large megathrust earthquakes in chile. *Tectonophysics*, *733*, 37–56, https://doi.org/10.1016/j.tecto.2018.01.015.

Ruiz, S., Metois, M., Fuenzalida, A., Ruiz, J., Leyton, F., Grandin, R., Vigny, C., Madariaga, R., & Campos, J. (2014). Intense foreshocks and a slow slip event preceded the 2014 iquique mw 8.1 earthquake. *Science*, *345*(6201), 1165–9, https://doi.org/10.1126/science.1256074.

Rutland, R. W. R. (1971). Andean orogeny and ocean floor spreading. *Nature*, *233*(5317), 252, https://doi.org/10.1038/233252a0.

Saffer, D. M. (2003). Pore pressure development and progressive dewatering in underthrust sediments at the costa rican subduction margin: Comparison with northern barbados and nankai. *Journal of Geophysical Research-Solid Earth*, *108*(B5), https://doi.org/10.1029/2002jb001787.

Saffer, D. M. & Tobin, H. J. (2011). Hydrogeology and mechanics of subduction zone forearcs: Fluid flow and pore pressure. *Annual Review of Earth and Planetary Sciences*, *39*, 157–186, https://doi.org/10.1146/annurev-earth-040610-133408.

Saffer, D. M. & Wallace, L. M. (2015). The frictional, hydrologic, metamorphic and thermal habitat of shallow slow earthquakes. *Nature Geoscience*, *8*(8), 594–600, https://doi.org/10.1038/Ngeo2490.

Sallares, V. & Ranero, C. R. (2005). Structure and tectonics of the erosional convergent margin off antofagasta, north chile (23 degrees 30 ' s). *Journal of Geophysical Research-Solid Earth*, *110*(B6), https://doi.org/10.1029/2004jb003418.

Sallares, V. & Ranero, C. R. (2019). Upper-plate rigidity determines depth-varying rupture behaviour of megathrust earthquakes. *Nature*, *576*(7785), 96–+, https://doi.org/10.1038/s41586-019-1784-0.

Satake, K. & Tanioka, Y. (1999). Sources of tsunami and tsunamigenic earthquakes in subduction zones. *Pure and Applied Geophysics*, *154*(3), 467–483, https://doi.org/10.1029/2003jb002521.

Scherwath, M., Contreras-Reyes, E., Flueh, E. R., Grevemeyer, I., Krabbenhoeft, A., Papenberg, C., Petersen, C. J., & Weinrebe, R. W. (2009). Deep lithospheric structures along the southern central chile margin from wide-angle p-wave modelling. *Geophysical Journal International*, *179*(1), 579–600, https://doi.org/10.1111/j.1365-246X.2009.04298.x.

Schmidt, M. W. & Poli, S. (1998). Experimentally based water budgets for dehydrating slabs and consequences for arc magma generation. *Earth and Planetary Science Letters*, *163*(1-4), 361–379, https://doi.org/10.1016/S0012-821x(98)00142-3.

Scholz, C. H. (1998). Earthquakes and friction laws. *Nature*, *391*(6662), 37–42, https://doi.org/10.1038/34097.

Scholz, C. H. & Campos, J. (1995). On the mechanism of seismic decoupling and back-arc spreading at subduction zones. *Journal of Geophysical Research-Solid Earth*, *100*(B11), 22103–22115, https://doi.org/10.1029/95jb01869.

Scholz, C. H. & Campos, J. (2012). The seismic coupling of subduction zones revisited. *Journal of Geophysical Research-Solid Earth*, *117*(5), 1–22, https://doi.org/10.1029/2011jb009003.

Scholz, C. H. & Small, C. (1997). The effect of seamount subduction on seismic coupling. *Geology*, *25*(6), 487–490, https://doi.org/10.1130/0091-7613(1997)025<0487:Teosso>2.3.Co;2.

Schurr, B., Asch, G., Hainzl, S., Bedford, J., Hoechner, A., Palo, M., Wang, R., Moreno, M., Bartsch, M., Zhang, Y., Oncken, O., Tilmann, F., Dahm, T., Victor, P., Barrientos, S., & Vilotte, J. P. (2014). Gradual unlocking of plate boundary controlled initiation of the 2014 iquique earthquake. *Nature*, *512*(7514), 299–302, https://doi.org/10.1038/nature13681.

Schurr, B., Moreno, M., Tréhu, A. M., Bedford, J., Kummerow, J., Li, S., & Oncken, O. (2020). Forming a mogi doughnut in the years prior to and immediately before the 2014 m8.1 iquique, northern chile, earthquake. *Geophysical Research Letters*, *47*(16), e2020GL088351, https://doi.org/10.1029/2020gl088351.

Shrivastava, M. N., Gonzalez, G., Moreno, M., Soto, H., Schurr, B., Salazar, P., & Baez, J. C. (2019). Earthquake segmentation in northern chile correlates with curved plate geometry. *Scientific Reports*, *9*(1), 4403, https://doi.org/10.1038/s41598-019-40282-6.

Simons, M., Minson, S. E., Sladen, A., Ortega, F., Jiang, J., Owen, S. E., Meng, L., Ampuero, J. P., Wei, S., Chu, R., Helmberger, D. V., Kanamori, H., Hetland, E., Moore, A. W., & Webb, F. H. (2011). The 2011 magnitude 9.0 tohoku-oki earthquake: mosaicking the megathrust from seconds to centuries. *Science*, *332*(6036), 1421–5, https://doi.org/10.1126/science.1206731.

Singh, S. C., Hananto, N., Mukti, M., Robinson, D. P., Das, S., Chauhan, A., Carton, H., Gratacos, B., Midnet, S., Djajadihardja, Y., & Harjono, H. (2011). Aseismic zone and earthquake segmentation associated with a deep subducted seamount in sumatra. *Nature Geoscience*, *4*(5), 308–311, https://doi.org/10.1038/Ngeo1119.

Sippl, C., Schurr, B., Asch, G., & Kummerow, J. (2018). Seismicity structure of the northern chile forearc from > 100,000 double-difference relocated hypocenters. *Journal of Geophysical Research-Solid Earth*, *123*(5), 4063–4087, https://doi.org/10.1002/2017jb015384.

Song, T. R. & Simons, M. (2003). Large trench-parallel gravity variations predict seismogenic behavior in subduction zones. *Science*, *301*(5633), 630–3, https://doi.org/10.1126/science.1085557.

Spinelli, G. & Harris, R. (2011). Thermal effects of hydrothermal circulation and seamount subduction: Temperatures in the nankai trough seismogenic zone experiment transect, japan. *Geochemistry, Geophysics, Geosystems*, *12*(12), https://doi.org/10.1029/2011GC003727.

Stern, C. R. (2011). Subduction erosion: Rates, mechanisms, and its role in arc magmatism and the evolution of the continental crust and mantle. *Gondwana Research*, *20*(2-3), 284–308, https://doi.org/10.1016/j.gr.2011.03.006.

Tang, G. Y., Barton, P. J., McNeill, L. C., Henstock, T. J., Tilmann, F., Dean, S. M., Jusuf, M. D., Djajadihardja, Y. S., Permana, H., Klingelhoefer, F., & Kopp, H. (2013). 3-d active source tomography around simeulue island offshore sumatra: Thick crustal zone responsible for earthquake segment boundary. *Geophysical Research Letters*, *40*(1), 48–53, https://doi.org/10.1029/2012gl054148.

Tanioka, Y. & Satake, K. (1996). Fault parameters of the 1896 sanriku tsunami earthquake estimated from tsunami numerical modeling. *Geophysical Research Letters*, *23*(13), 1549–1552, https://doi.org/10.1029/96gl01479.

Tichelaar, B. W. & Ruff, L. J. (1991). Seismic coupling along the chilean subduction zone. *Journal of Geophysical Research-Solid Earth and Planets*, *96*(B7), 11997–12022, https://doi.org/10.1029/91jb00200.

Tichelaar, B. W. & Ruff, L. J. (1993). Depth of seismic coupling along subduction zones. *Journal of Geophysical Research-Solid Earth*, *98*(B2), 2017–2037, https://doi.org/10.1029/92jb02045.

Tilmann, F. J., Craig, T. J., Grevemeyer, I., Suwargadi, B., Kopp, H., & Flueh, E. (2010). The updip seismic/aseismic transition of the sumatra megathrust illuminated by aftershocks of the 2004 aceh-andaman and 2005 nias events. *Geophysical Journal International*, *181*(3), 1261–1274, https://doi.org/10.1111/j.1365-246X.2010.04597.x.

Tsuru, T., Park, J. O., Miura, S., Kodaira, S., Kido, Y., & Hayashi, T. (2002). Along-arc structural variation of the plate boundary at the japan trench margin: Implication of interplate coupling. *Journal of Geophysical Research-Solid Earth*, *107*(B12), https://doi.org/10.1029/2001jb001664.

Tsuru, T., Park, J. O., Takahashi, N., Kodaira, S., Kido, Y., Kaneda, Y., & Kono, Y. (2000). Tectonic features of the japan trench convergent margin off sanriku, northeastern japan, revealed by multichannel seismic reflection data. *Journal of Geophysical Research-Solid Earth*, *105*(B7), 16403–16413, https://doi.org/10.1029/2000jb900132.

Ujiie, K., Tanaka, H., Saito, T., Tsutsumi, A., Mori, J. J., Kameda, J., Brodsky, E. E., Chester, F. M., Eguchi, N., Toczko, S., Expedition, & Scientists, T. (2013). Low coseismic shear stress on the tohoku-oki megathrust determined from laboratory experiments. *Science*, *342*(6163), 1211–4, https://doi.org/10.1126/science.1243485.

Underwood, M. B. (2007). *Sediment Inputs to Subduction Zones: Why Lithostratigraphy and Clay Mineralogy Matter*, (pp. 42–85). Columbia University Press.

Uyeda, S. & Kanamori, H. (1979). Back-arc opening and the mode of subduction. *Journal of Geophysical Research*, *84*(Nb3), 1049–1061, https://doi.org/10.1029/JB084iB03p01049.

van Rijsingen, E., Lallemand, S., Peyret, M., Arcay, D., Heuret, A., Funiciello, F., & Corbi, F. (2018). How subduction interface roughness influences the occurrence of large interplate earthquakes. *GEOCHEMISTRY GEOPHYSICS GEOSYSTEMS*, *19*(8), 2342–2370, https://doi.org/10.1029/2018GC007618.

Vannucchi, P., Sak, P. B., Morgan, J. P., Ohkushi, K., Ujiie, K., & Scie, I. E. . S. (2013). Rapid pulses of uplift, subsidence, and subduction erosion offshore central america: Implications for building the rock record of convergent margins. *Geology*, *41*(9), 995–998, https://doi.org/10.1130/G34355.1.

Vannucchi, P., Spagnuolo, E., Aretusini, S., Di Toro, G., Ujiie, K., Tsutsumi, A., & Nielsen, S. (2017). Past seismic slip-to-the-trench recorded in central america megathrust. *Nature Geoscience*, *10*(12), 935–940, https://doi.org/10.1038/s41561-017-0013-4.

Von Huene, R., Corvalán, J., Flueh, E. R., Hinz, K., Korstgard, J., Ranero, C. R., & Weinrebe, W. (1997). Tectonic control of the subducting juan fernández ridge on the andean margin near valparaiso, chile. *Tectonics*, *16*(3), 474–488, https://doi.org/10.1029/96TC03703.

von Huene, R. & Lallemand, S. (1990). Tectonic erosion along the japan and peru convergent margins. *Geological Society of America Bulletin*, *102*(6), 704–720, https://doi.org/10.1130/0016-7606(1990)102<0704:TEATJA>2.3.CO;2.

von Huene, R., Pecher, I. A., & Gutscher, M. (1996). Development of the accretionary prism along peru and material flux after subduction of nazca ridge. *Tectonics*, *15*(1), 19–33, https://doi.org/10.1029/95TC02618.

von Huene, R. & Ranero, C. R. (2003). Subduction erosion and basal friction along the sediment-starved convergent margin off antofagasta, chile. *Journal of Geophysical Research-Solid Earth*, *108*(B2), https://doi.org/10.1029/2001jb001569.

von Huene, R., Ranero, C. R., & Vannucchi, P. (2004). Generic model of subduction erosion. *Geology*, *32*(10), 913–916, https://doi.org/10.1130/G20563.1.

Von Huene, R. & Scholl, D. W. (1991). Observations at convergent margins concerning sediment subduction, subduction erosion, and the growth of continental-crust. *Reviews of Geophysics*, *29*(3), 279–316, https://doi.org/10.1029/91rg00969.

Wallace, L. M., Kaneko, Y., Hreinsdottir, S., Hamling, I., Peng, Z. G., Bartlow, N., D'Anastasio, E., & Fry, B. (2017). Large-scale dynamic triggering of shallow slow slip enhanced by overlying sedimentary wedge. *Nature Geoscience*, *10*(10), 765–+, https://doi.org/10.1038/Ngeo3021.

Wallace, L. M., Webb, S. C., Ito, Y., Mochizuki, K., Hino, R., Henrys, S., Schwartz, S. Y., & Sheehan, A. F. (2016). Slow slip near the trench at the hikurangi subduction zone, new zealand. *Science*, *352*(6286), 701–704, https://doi.org/10.1126/science.aaf2349.

Wang, K. L. & Bilek, S. L. (2011). Do subducting seamounts generate or stop large earthquakes? *Geology*, *39*(9), 819–822, https://doi.org/10.1130/G31856.1.

Wang, K. L. & Hu, Y. (2006). Accretionary prisms in subduction earthquake cycles: The theory of dynamic coulomb wedge. *Journal of Geophysical Research-Solid Earth*, *111*(B6), https://doi.org/10.1029/2005jb004094.

Watts, A. B., Koppers, A. A., & Robinson, D. P. (2010). Seamount subduction and earthquakes. *Oceanography*, *23*(1), 166–173, https://doi.org/10.5670/oceanog.2010.68.

Weinrebe, R. W., Ranero, C., Masson, D., Huguen, D., Klaucke, I., Sahling, H., Hühnerbach, V., Flueh, E. R., & Bohrmann, G. (2003). Mehrskalige kartierung des konvergenten kontinentalrandes vor costa rica-erste ergebnisse der fahrt so163 mit fs sonne.

Wells, R. E., Blakely, R. J., Sugiyama, Y., Scholl, D. W., & Dinterman, P. A. (2003). Basin-centered asperities in great subduction zone earthquakes: A link between slip, subsidence, and subduction erosion? *Journal of Geophysical Research: Solid Earth*, *108*(B10), https://doi.org/10.1029/2002JB002072.

Yagi, Y., Okuwaki, R., Enescu, B., Hirano, S., Yamagami, Y., Endo, S., & Komoro, T. (2014). Rupture process of the 2014 iquique chile earthquake in relation with the foreshock activity. *Geophysical Research Letters*, *41*(12), 4201–4206, https://doi.org/10.1002/2014gl060274.

Zelt, C. A., Hojka, A. M., Flueh, E. R., & McIntosh, K. D. (1999). 3d simultaneous seismic refraction and reflection tomography of wide-angle data from the central chilean margin. *Geophysical Research Letters*, *26*(16), 2577–2580, https://doi.org/10.1029/1999gl900545.

# 3 Megathrust reflectivity reveals the updip limit of the 2014 Iquique earthquake rupture

**Bo Ma**[1], Jacob Geersen[1,2], Dietrich Lange[1], Dirk Klaeschen[1], Ingo Grevemeyer[1], Eduardo Contreras-Reyes[3], Florian Petersen[1], Michael Riedel[1], Yueyang Xia[1], Anne M. Tréhu[4] and Heidrun Kopp[1,2]

1) GEOMAR Helmholtz Centre for Ocean Research Kiel, Kiel, Germany.

2) Institute of Geosciences, Kiel University, Kiel, Germany.

3) Departamento de Geofísica, Facultad de Ciencias Físicas y Matemáticas, Universidad de Chile, Santiago, Chile.

4) Oregon State University, College of Earth, Ocean, and Atmospheric Sciences, Corvallis, USA

Published in **NATURE COMMUNICATIONS**, July 2022.

DOI: 10.1038/s41467-022-31448-4

## Abstract

The updip limit of seismic rupture during a megathrust earthquake exerts a major control on the size of the resulting tsunami. Offshore Northern Chile, the 2014 Mw 8.1 Iquique earthquake ruptured the plate boundary between 19.5 °- 21 °S. Rupture terminated under the mid-continental slope and did not propagate updip to the trench. Here, we use state-of-the-art seismic reflection data to investigate the tectonic setting associated with the apparent updip arrest of rupture propagation at 15 km depth during the Iquique earthquake. We document a spatial correspondence between the rupture area and the seismic reflectivity of the plate boundary. North and updip of the rupture area, a coherent, highly reflective plate boundary indicates excess fluid pressure, which may prevent the accumulation of elastic strain. In contrast, the rupture area is characterized by the absence of plate boundary reflectivity, which suggests low fluid pressure that results in stress accumulation and thus controls the extent of earthquake rupture. Generalizing these results, seismic reflection data can provide insights into the physical state of the shallow plate boundary and help to assess the potential for future shallow rupture in the absence of direct measurements of interplate deformation from most outermost forearc slopes.

## 3.1 Introduction

Megathrust earthquakes result from the sudden failure of the plate boundary in a region where elastic strain has accumulated prior to the event. Fluid pressure is a critical parameter that determines the physical nature of the megathrust and therefore exerts a main control on where and how seismic moment is released (Hubbert and Rubey, 1959; Saffer and Tobin, 2011). Pore fluid pressure in excess of hydrostatic pressure diminishes fault strength (Hubbert and Rubey, 1959) and enables a wide spectrum of transient, predominantly slow, earthquake phenomena especially along shallow subduction zone plate boundaries (Saffer and Wallace, 2015). The key processes that release water in shallow subduction zones, and thus control fluid pressure, are compaction dewatering and clay and opal dehydration reactions in subducting sediments and the upper oceanic basement (Moore and Saffer, 2001; Ranero et al., 2008; Kameda et al., 2011; Saffer and Tobin, 2011). These processes take place under low temperatures and low confining pressures (Kastner et al., 1991; Hüpers and Kopf, 2012), so excess pore pressures are expected in areas of low overburden, such as the shallow plate-boundary. Seismic reflection data are sensitive to the high acoustic impedance contrast generated by fluids and thus seismic reflection studies have proven powerful to investigate spatial variations in plate boundary fluid pressure, at least in a qualitative manner (Shipley et al., 1994; Moore et al., 1998; Bangs et al., 1999; Ranero et al., 2008; Spinelli and Wang, 2008; Tobin and Saffer, 2009; Bell et al.,

2010; Bangs et al., 2015). For the erosive convergent margin of Central America, Ranero et al. (2008) suggested a high fluid content along the shallow aseismic section of the plate boundary (also compare Bangs et al., 2015; Edwards et al., 2018) in a temperature regime where compaction dewatering and clay-mineral diagenetic reactions are expected to release most of the water in the subducting sediments (Saffer and Tobin, 2011). The authors further described a rapid decrease in fluid content where temperatures exceed ~150 °C, which corresponds to the transition from aseismic sliding at shallow depth to stick-slip sliding in the seismogenic zone.

On 1 April 2014, the $M_w$ 8.1 Iquique earthquake ruptured the plate boundary between 19.5 °- 21 °S along the erosive continental margin of Northern Chile (Hayes et al., 2014; Ruiz et al., 2014; Schurr et al., 2014, 2020). Seismic rupture did not break updip to the trench but terminated under the mid-continental slope (Fig. 3.1). Aftershocks of the 2014 Iquique earthquake concentrated around the updip limit of seismic rupture with little activity towards the trench (Sippl et al., 2018; Petersen et al., 2021).

In this work, we use high-resolution multichannel seismic reflection profiles in a grid layout covering the 2014 Iquique mainshock and aftershock region as well as the surrounding forearc not affected by seismic rupture (Fig. 3.1). The seismic reflectivity variations along the plate boundary elucidate the spatial variation in megathrust fluid pressure.

## 3.2 Correspondence between plate boundary reflectivity and rupture area of the 2014 Iquique earthquake

Pre-stack depth migrated seismic reflection profiles with a total length of 912 km cover the Northern Chilean marine forearc in the region that ruptured during the 2014 Iquique earthquake and the adjacent un-ruptured forearc (Fig. 3.1). The shallow plate boundary underneath the lower continental slope is visible as a prominent seismic reflection on all profiles. At greater depth, the reflectivity shows a high degree of variation in the dip direction and along strike. Along the northernmost line MC04, located to the north of the 2014 Iquique rupture where only sparse aftershocks occur (Fig. 3.1; Petersen et al., 2021), the plate boundary is imaged as a band of strong, albeit discontinuous, reflectivity from the trench to at least 103 km landward of the deformation front (Figs. 3.1 and 3.2a, yellow lines and arrows), where it is at a depth of about 35 km. Between profile kilometers 0 - 35 km, the plate boundary is imaged with a high degree of lateral coherency from the deformation front adjacent to the trench axis to a depth of around 15 km on all profiles (Figs. 3.1 and 3.2b-d, yellow lines and arrows). South of MC04, however, plate boundary reflectivity drops suddenly and is below the background noise level more than 30 - 35 km east of the trench.

The down-dip variations in plate boundary reflectivity are also seen on lines parallel to the trench (MC15, MC16A and MC30; Fig. 3.3) which image the lower continental slope with increasing distance from the deformation front (Fig. 3.1). The intersections of the

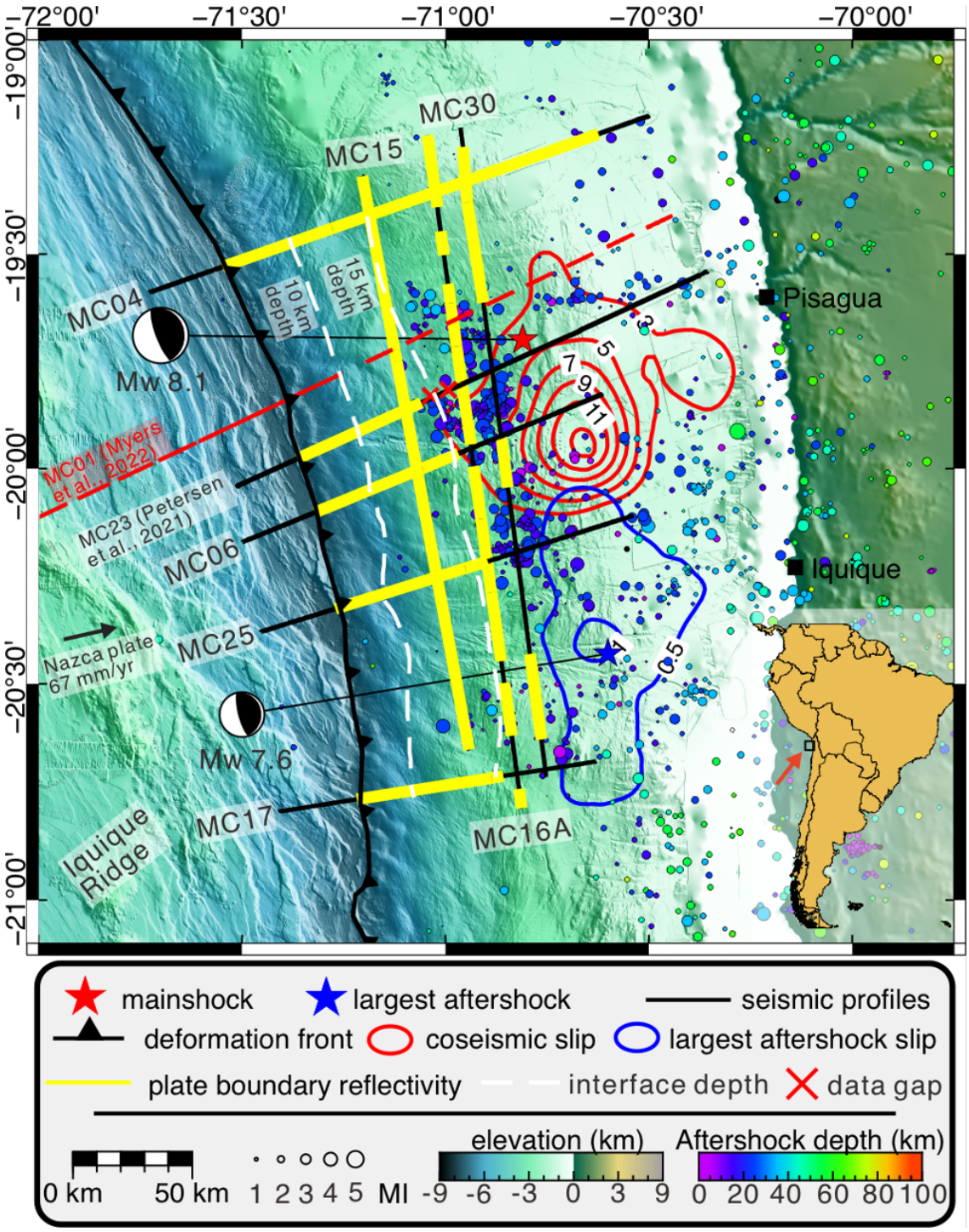


**Figure 3.1:** Overview map of the erosional margin of Northern Chile in the region affected by the 2014 Iquique earthquake (Caption next page).

trench-parallel lines with the dip lines provide an independent verification of the reflection character of the plate boundary at the crossing points. Along strike line MC15 which is located closest to the trench, a highly coherent plate boundary reflection is observed along the entire line at a depth of 11.5 - 16 km (Fig. 3.1, yellow line; Fig. 3.3a, yellow arrows). Strike line MC16A, located ~16 km farther downdip, shows intermittent high reflectivity on the plate boundary between profile kilometers 0 - 6, 20 - 33, 38 - 88, 94 - 137,145 - 150 and 157 - 175 km (Fig. 3.3b). Elsewhere, the reflectivity is moderate or even absent. Again, the reflectivity pattern matches the reflectivity of the dip lines, as evidenced at the cross points and intersections with MC25 and MC04 (coherent plate boundary reflection) as well as MC06 and MC17 (weak or absent plate boundary reflection). Only ~8 km farther landward, strike line MC30 shows a completely different pattern of plate boundary reflectivity. Here the plate boundary is located at depths between 17 - 21 km (Fig. 3.3c). Along line MC30, the plate boundary reflection is absent or very weak, except around the intersection with MC04, which is consistent with the reflection signal on MC04 at the corresponding depth.

We use an analytical thermal model by following the approach (England, 2018) to calculate the temperature as a function of depth at the interplate fault zone (see details in the Supporting Information). Thermal constraints (Kellner, 2007) reveal the temperature structure along the plate boundary from the trench axis downwards. The lower limit of the coherent and highly reflective plate boundary around 15 km depths corresponds to a temperature of 100 - 150 °C (Fig. 3.2). Further down-dip, plate boundary reflectivity decreases remarkably rapid in the rupture area of the 2014 Iquique earthquake and its main aftershock. Most noticeable, it also stands in sharp contrast to the region immediately north of the rupture zone (MC04), where a moderate plate boundary reflection is observed to a depth of 35 km, corresponding to a temperature well above 300 °C.

**Figure 3.1:** Overview map of the erosional margin of Northern Chile in the region affected by the 2014 Iquique earthquake. The hypocenter (star) and slip contour lines (in meters) of the 2014 Iquique $M_w$ 8.1 mainshock and $M_w$ 7.7 aftershock (Duputel et al., 2015) are shown as red and blue, respectively. Black lines indicate the locations of the seismic lines used in this study with yellow regions indicating a coherent plate boundary reflection. The location of MC23 (Petersen et al., 2021) has been added in the overview map, where the same color is used for the plate boundary reflectivity. The white dashed lines show the depth of the plate interface estimated from the seismic reflection data. The colored circles according to the color bar are aftershocks (December 2014 until October 2016) from the 2014 Iquique earthquake recorded by ocean bottom seismometers indicated as green and orange triangles (Petersen et al., 2021). Seafloor bathymetry (Geersen et al., 2011) combined with GEBCO_2019 bathymetry (`www.gebco.net`), SRTM topography (Farr et al., 2007). The convergence of the Nazca and South America plate indicated by a black arrow (Angermann et al., 1999). The location of the seismic line defining the structure of the incoming plate (Myers et al., 2022) is shown by a red dashed line.

Storch et al. (2021) observed down-dip variations in plate boundary reflectivity over short (5 - 10 km scale) distances. The maximum depth extent of reflectivity in their data is consistent with our observations. The seismic data used (Storch et al., 2021) were recorded in 1995 with a significantly shorter streamer and thus lack resolution at larger depths (>16 km) compared to data from our seismic campaign and did not resolve the dramatic decrease in reflectivity in the region of the 2014 rupture.

## 3.3 Impact of fluid pressure on the 2014 Iquique earthquake rupture

A striking observation is the spatial correlation between the reflection character of the plate boundary and the rupture areas of the 2014 Iquique Mw 8.1 earthquake and the Mw 7.7 aftershock, and the aftershock distribution (Fig. 3.1). Updip of both rupture areas, a highly reflective plate boundary is coherently imaged on all seismic lines. Subduction zone plate boundaries that are imaged as coherent high reflections in seismic data are usually interpreted as high porosity and fluid rich fault zones (Bangs et al., 1999; Spinelli and Wang, 2008; Bangs et al., 2015). In many subduction zones, some of which have been targeted by scientific ocean drilling (Northern Barbados, Costa Rica, Nankai Trough, Hikurangi), such coherent, high reflectivity corresponds to the shallow region of the plate boundary that does not nucleate giant earthquakes (Shipley et al., 1994; Moore et al., 1998; Bangs et al., 1999; Ranero et al., 2008; Spinelli and Wang, 2008; Tobin and Saffer, 2009; Bell et al., 2010; Bangs et al., 2015). Advances in seafloor geodesy, in concert with scientific drilling of shallow plate boundaries and numerical modelling, have further proven that these regions can host a wide spectrum of slow earthquake phenomena with event durations up to some years (Saffer and Wallace, 2015; Araki et al., 2017). For example, on the Nankai margin, recurring slow-slip events along the high-reflective shallow plate boundary, accommodate 30-55% of the plate convergence (Araki et al., 2017).

Along the erosive Central American margin, Ranero et al. (2008) observed a highly reflective shallow plate boundary (also compare to Bangs et al., 2015; Edwards et al., 2018). In their conceptual model, the high reflectivity is mainly caused by dehydration of sedimentary smectite clays at temperatures below 150 °C. The released fluids reduce the strength of the shallow plate boundary and migrate upwards through an upper plate dissected by large normal faults. Off Northern Chile, the shallow plate boundary is also highly reflective and the outermost part of the marine forearc is similarly fractured by long-term subduction erosion (Petersen et al., 2021) and the subduction of excess lower plate topography due to the Iquique Ridge (Geersen et al., 2015). The small volume of trench fill along the Northern Chilean margin (Fig. 3.2 and 3.12, also compare to Geersen et al., 2018), however, makes it questionable whether subducting sediments are a significant source of fluids.

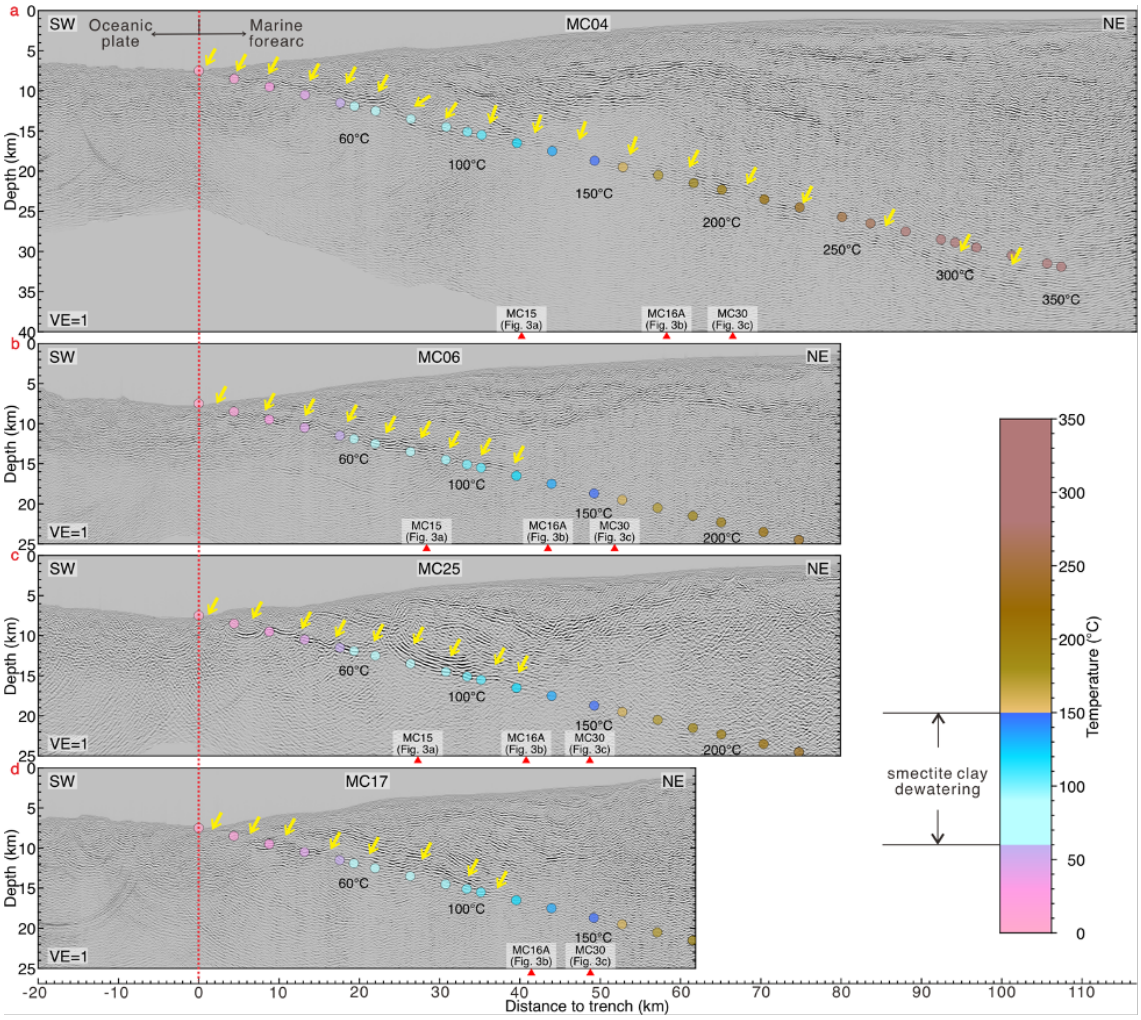


**Figure 3.2:** Pre-stack depth migrated section of seismic dip-lines. Yellow arrows indicate a coherent plate boundary reflection. The vertical red dashed line denotes the location of the deformation front. The red arrows specify the intersections with the strike lines. Temperatures are shown as colored dots according to the color bar. The approximate depth range of smectite clay dehydration is based on (Saffer and Tobin, 2011; Kastner et al., 1991; Bekins et al., 1994; Spinelli and Saffer, 2004; Underwood, 2007). **a**. seismic line MC04. **b**. seismic line MC06. **c**. seismic line MC25. **d**. seismic line MC17.

If smectite clay accounts for 50% of the bulk sediment, as observed in other subduction zones with typical deep-water pelagic and hemipelagic environments of mudstones such as the Nankai Trough, Cascadia, Barbados Ridge, Costa Rica (Underwood, 2007; Vannucchi et al., 2017), this would correspond to 8-10 wt% of water (~15 - 20 vol%). Considering that the thickness of sediments that rest on the igneous oceanic basement is generally less than 200 m (and often even less than 100 m) along the Northern Chilean margin (Fig. 3.12, red dots of error bar and yellow solid lines in (a) - (d)), water release from mineral dehydration within the subducting sediment must be quite limited, even when considering high smectite clay concentrations.

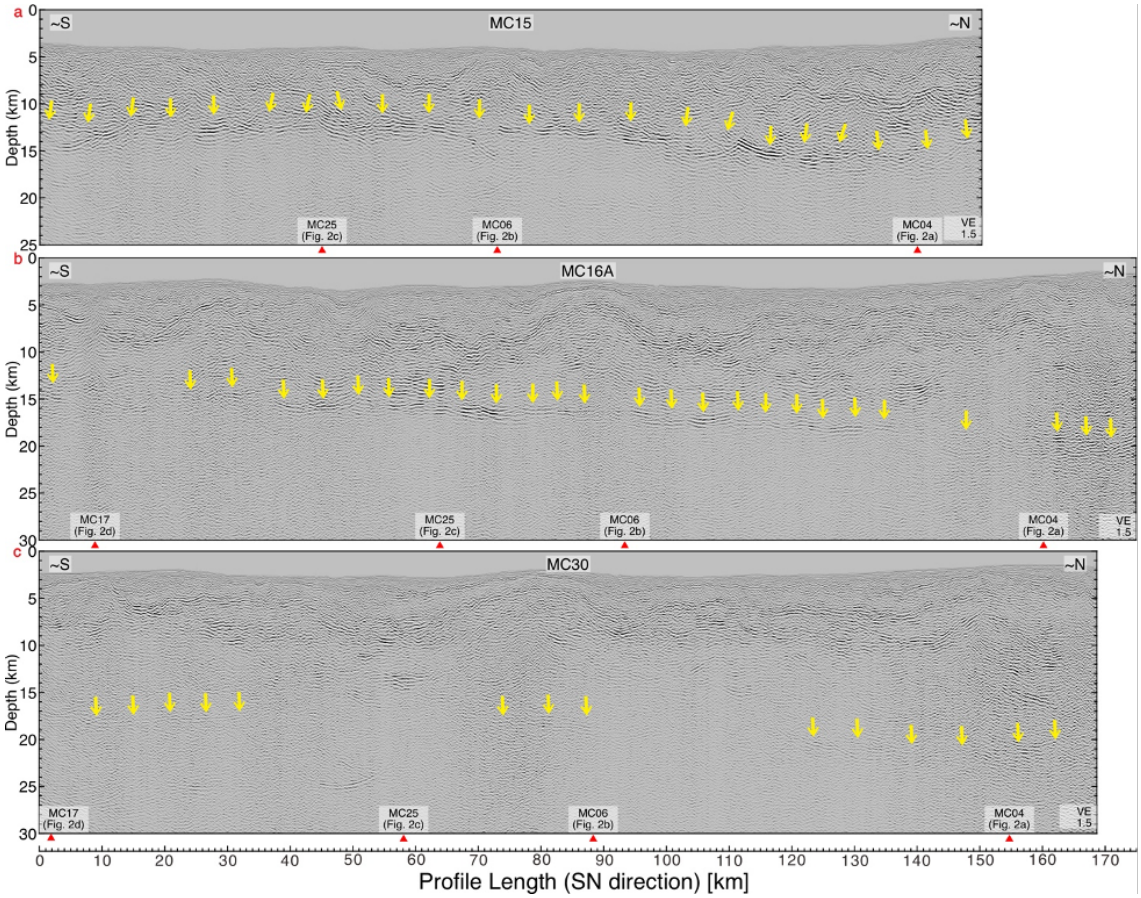


**Figure 3.3:** Pre-stack depth migrated sections of seismic strike-lines. Yellow arrows indicate a coherent plate boundary reflection. The red arrows specify the intersections with the dip lines. **a**. seismic line MC15. **b**. seismic line MC16A. **c**. seismic line MC30. All symbols as in Fig. 3.2.

Recent deep-ocean drilling campaigns targeting the oceanic plates offshore Costa Rica and Nankai recovered oceanic basalts with smectite concentrations up to 40 vol% (`http://publications.iodp.org/proceedings/344/104/104_.htm`; Kameda et al., 2011). In both cases, the smectite clay was formed as an alteration product during the basalt interaction with sea water. Dehydration of weathered clay-bearing basalt within the uppermost oceanic basement is generally less well studied and understood compared to dehydration reactions within the subducting sediments (Saffer and Tobin, 2011; Kastner et al., 1991; Bekins et al., 1994; Spinelli and Underwood, 2004; Underwood, 2007), or metamorphic reactions that release fluids from the deeper sections of the oceanic crust and the upper mantle at temperatures $> 300\,°C$ (Schmidt and Poli, 1998; Peacock and Wang, 1999; Kuwatani et al., 2011). However, similar to what is happening in the subducting sediments, dehydration of the subducting weathered basalt may initiate between the $60\,°$ and $150\,°C$ isotherms (Kameda et al., 2011; Jarrard, 2003; Saffer and Tobin, 2011; Bekins et al., 1994; Bethke, 1986). For the fossil margin complex of the Shimanto Belt (south-

west Japan), the smectite to chlorite conversion within the uppermost oceanic basement is discussed as a major source of water (Kameda et al., 2011; Hashimoto et al., 2012). Furthermore, the high *vp/vs* ratio derived from a recent local earthquake tomography using ocean bottom seismometers (Petersen et al., 2021) is indicative of hydration of the oceanic crust underneath the lower forearc. To calculate the total amount of water that could be liberated from the scarce subducting sediments and the subducting weathered oceanic basement, one would need to know the exact composition of the sediments as well as the depth extent and degree of weathering of the clay-bearing basalts.

Although the incoming oceanic crust off northern Chile has not been drilled, recent seismic data suggest that the upper crustal velocity of the incoming plate beneath the outer rise is anomalously low, suggesting presence of mineral hydration and/or pervasive fluid-filled cracks to a depth of ~5 km (Myers et al., 2022). We conclude that the coherent highly reflective shallow plate boundary off Northern Chile, which behaved aseismic during the 2014 Iquique earthquake, is fluid-rich, and that the source of the fluid is intergranular and fracture porosity in seismic layer 2A (Anderson et al., 1976; Jarrard, 2003; Kameda et al., 2011) of the oceanic crust and mineral bound water released through dehydration of the weathered clay-bearing oceanic basalt. This may promote reduced coupling as suggested by Moreno et al. (2014) for the southern boundary of the 2010 Maule earthquake. Furthermore, the high fluid pressures and the low effective stresses may promote strain release during slow and aseismic events that occur at shorter intervals compared to large megathrust earthquakes. While observed along the Nankai (Araki et al., 2017), Hikurangi (Wallace et al., 2016), and Costa Rica (Davis et al., 2015) margins, such slow and shallow earthquake phenomena have not been resolved off Northern Chile, where Global Navigation Satellite System-Acoustic (GNSS-A) seafloor observations and borehole observatories are lacking.

Farther downdip, into the seismogenic portion of the 2014 Iquique earthquake, the coherent reflectivity of the plate boundary diminishes rapidly where the plate boundary slipped in 2014 but not immediately to the north of the 2014 rupture zone (Fig. 3.1). For the Central American margin and elsewhere, similar observations are usually explained by a reduction in fluid pressure and/or thinning of the fault zone to a thickness that lies below the resolution of seismic reflection data (Tobin and Saffer, 2009; Bangs et al., 2015). The well-drained region farther downdip promotes the build-up of elastic strain over decadal to centennial timescales that was released during the 2014 Iquique earthquake. In particular, the three strike lines that sample the region seaward of the updip limit, the updip limit itself, and the region just below the updip limit, demonstrate the turnover from the coherent, strong reflective shallow plate boundary that did not rupture to the non-reflective plate boundary within the 2014 Iquique earthquake rupture area. While seismic resolution is a function of energy penetration with depth, profile MC04 (Fig. 3.2a) documents suffi-

cient resolution of our data set to image the plate boundary to a depth of ~35 km. While in general the reflection intensity decreases with increasing depth due to intrinsic attenuation and the viscoelastic material behavior of the subsurface (Bormann et al., 2012), the very rapid and rigorous disappearance of the plate boundary reflection over a very short depth range along-strike, in conjunction with the temperature isotherms increasing to beyond 150 °C precludes a seismic imaging problem.

For the Antofagasta Mw 8.0 earthquake, Husen and Kissling (2001) compared upper plate seismic velocities from before and after the earthquake and suggested that seismic rupture enabled fluids to migrate upwards from the plate boundary into the upper plate. Such a process could reduce plate boundary reflectivity during the early postseismic phase and would thus provide a possible explanation for the observed low reflectivity within the 2014 Iquique rupture area. In general, there is little information on transient changes of reflectivity during a seismic cycle. Prior to the 2014 Iquique earthquake Storch et al. (2021) observed high plate boundary reflectivity down to a depth of 16 km. This indicates that the shallow plate boundary remains fluid rich throughout the seismic cycle. Since plate boundary reflectivity at the depths of the seismogenic zone is not resolved prior to the 2014 Iquique earthquake (Storch et al., 2021), we cannot conclude whether it was altered by the 2014 Iquique earthquake. However, as the updip end of seismicity, which correlates to the updip extent of the 2014 Iquique rupture, is stable in space throughout the seismic cycle, as also observed for the Sumatran (Tilmann et al., 2010) and the South Chilean margin (Lange et al., 2018), we presume that the reflectivity may also not change significantly over time. Although the ultimate reason for the higher plate boundary fluid content at depths beyond 15 km to the north of the 2014 Iquique earthquake remains enigmatic, our seismic reflection data clearly suggest a hydrogeological control on the updip extent and likely also the along-strike extent of seismic rupture along the erosive Northern Chilean continental margin.

## 3.4 Implications for assessing the hazard of shallow earthquake rupture

The updip extent of seismic rupture during a plate boundary earthquake exerts a major influence on the magnitude of the associated tsunami. Models using only land geodetic measurements, however, cannot resolve whether the shallowest part of a plate boundary is locked over a time period that is long enough to accumulate sufficient elastic energy to nucleate a large earthquake (Métois et al., 2016; Almeida et al., 2018; Kosari et al., 2020; Lindsey et al., 2021). Alternatively, the shallow plate boundary may also creep at plate convergence rates or release energy during frequent slow-slip events, low-frequency earthquakes, or episodic tremor and slip (Saffer and Wallace, 2015; Yokota and Ishikawa, 2020).

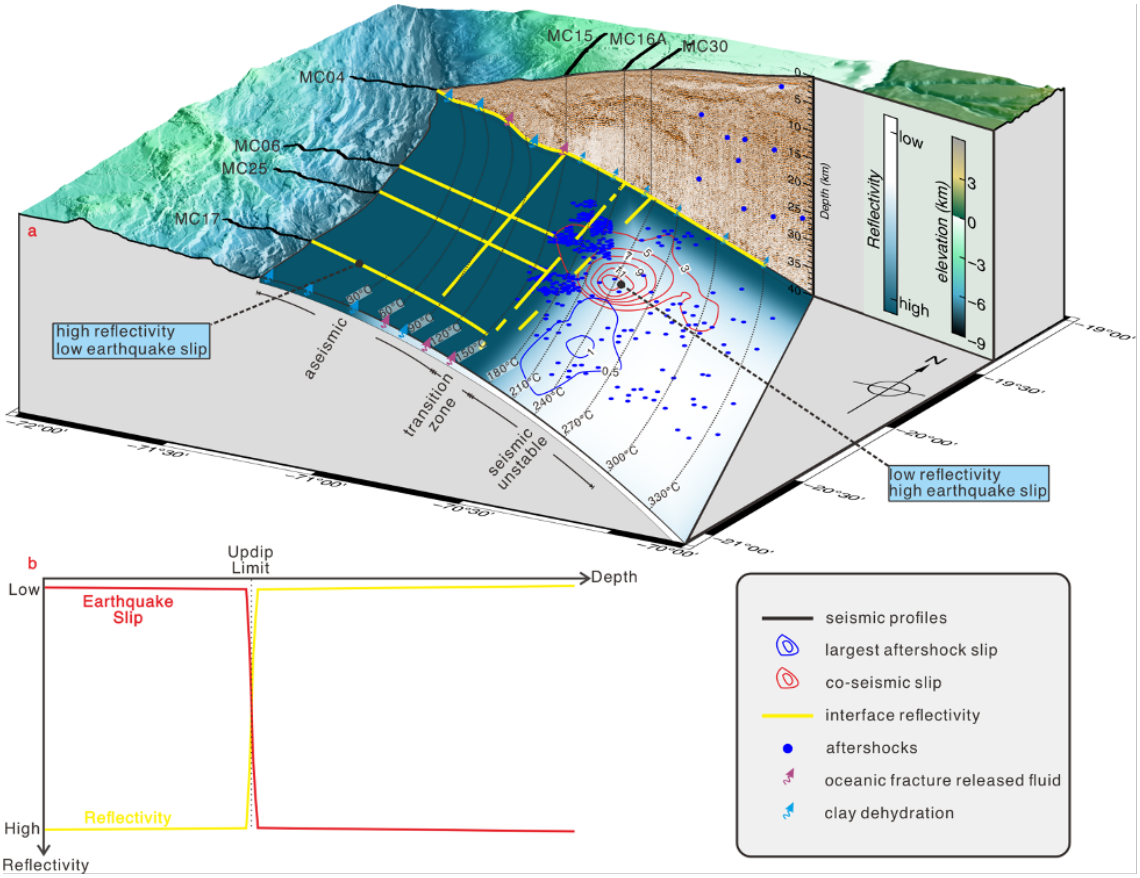


**Figure 3.4:** Conceptual model of the seismotectonic and hydrogeological setting in the region of the 2014 Iquique Mw 8.1 earthquake. **a**. Dehydration of weathered clay-bearing basalt (green arrows) and fluid release from intergranular and fracture porosity in layer 2A (red arrows) results in a fluid rich shallow plate boundary. **b**. Schematic trends in seismic reflectivity (yellow) and earthquake slip (red) with increasing depth along the plate boundary.

For the 2014 Iquique earthquake, we show that seismic reflectivity of the plate boundary is spatially related to the rupture area, with coherent, high reflectivity in the shallow aseismic regions that did not rupture and weak to absent reflectivity farther downdip within the rupture area (Fig. 3.4). This does not exclude the possibility that earthquake rupture arising from the downdip seismogenic zone may propagate into and through the shallow plate boundary, as it has been observed and inferred from other margins (Vannucchi et al., 2017; Kodaira et al., 2012; Maksymowicz et al., 2017).

Seismic reflection data, which are sensitive to fluid-pressure variations, can help to identify the shallow, velocity strengthening part of the plate boundary that may not nucleate a large earthquake and that may accumulate and release strain in a different manner and at different timescales (intervals), compared to the non-reflective seismogenic zone located further downdip. This knowledge may provide crucial, but often missing, information

towards a comprehensive evaluation of seismic and tsunami hazard along active margins, especially close to the trench where land-based geodetic and seismological studies lack resolution and offshore geodetic data are sparse or missing, but where the hazard of tsunami and tsunamigenic earthquakes is greatest.

## Methods

**Multichannel seismic reflection data.** Seismic multichannel reflection data used in this study were acquired in 2016 during the MGL1610 cruise of *R/V Marcus G. Langseth* offshore Northern Chile (https://www.rvdata.us/search/cruise/MGL1610). Seismic signals were generated with a source of 6600 cubic inches (108.15 liters), provided by four strings of 10 air-guns each. Data were recorded with an 8 km long streamer towed by *R/V Marcus G. Langseth*. The source was towed at 12 m depth below the water surface, and the record length was 16 s. The shots were acquired using a shot interval of 125 m to avoid interference from previous shots on ocean bottom seismometer data that were being acquired simultaneously. Surface-related multiple prediction, anomalous amplitude noise attenuation and adaptive filter are effective methods to attenuate multiples in our 2D seismic data. The plate boundary could be observed as a low frequency response of the seismic record. After that, pre-stack depth migration was applied to the sections with the aim to reveal more structural details. See Supplementary Methods for more information.

**Thermal modelling**. We calculated the thermal state along the plate interface megathrust fault using an analytical solutions (England, 2018) and compared the result to a two-dimensional thermal model for northern Chile (Kellner, 2007) that incorporates corner flow in the mantle wedge. See Supplementary Methods for detailed information on the thermal modelling.

## Data Availability

The multichannel seismic raw data is archived in https://www.marine-geo.org/tools/entry/MGL1610 and https://www.rvdata.us/search/cruise/MGL1610. Aftershocks (Petersen et al., 2021) can be accessed via https://doi.pangaea.de/10.1594/PANGAEA.929899. Multibeam data(Geersen et al., 2018) can be accessed via https://doi.pangaea.de/10.1594/PANGAEA.893034. We thank K. Davenport for providing a preliminary version of an unpublished 3D vp model. Figures were generated using GMT (Wessel et al., 2019).

## Code Available

The thermal model (England, 2018) with varying effective coefficient of basal friction values as MATLAB source code and thermal field file (Kellner, 2007) are available at Zenodo: https://doi.org/10.5281/zenodo.6536567.

## Acknowledgments

B. Ma acknowledges funding from the China Scholarship Council (grant 201706400073). The authors gratefully acknowledge the acquisition of the MCS data and bathymetric data during cruise MGL1610 of the *R/V Marcus G. Langseth* in 2016 (United States National Science Foundation grant OCE-1459368 to Oregon State University). EC-R thanks the support of the ANID/FONDECYT grant 1210101.

## Competing Interests statement

The authors declare no competing interests.

## References

Almeida, R., Lindsey, E. O., Bradley, K., Hubbard, J., Mallick, R., & Hill, E. M. (2018). Can the updip limit of frictional locking on megathrusts be detected geodetically? quantifying the effect of stress shadows on near-trench coupling. *Geophysical Research Letters*, *45*(10), 4754–4763, https://doi.org/10.1029/2018gl077785.

Anderson, R. N., Uyeda, S., & Miyashiro, A. (1976). Geophysical and geochemical constraints at converging plate boundaries .1. dehydration in downgoing slab. *Geophysical Journal of the Royal Astronomical Society*, *44*(2), 333–357, https://doi.org/10.1111/j.1365-246X.1976.tb03660.x.

Angermann, D., Klotz, J., & Reigber, C. (1999). Space-geodetic estimation of the nazca-south america euler vector. *Earth and Planetary Science Letters*, *171*(3), 329–334, https://doi.org/10.1016/S0012-821x(99)00173-9.

Araki, E., Saffer, D. M., Kopf, A. J., Wallace, L. M., Kimura, T., Machida, Y., Ide, S., Davis, E., & Scientist, E. . S. (2017). Recurring and triggered slow-slip events near the trench at the nankai trough subduction megathrust. *Science*, *356*(6343), 1157–1160, https://doi.org/10.1126/science.aan3120.

Bangs, N. L., McIntosh, K. D., Silver, E. A., Kluesner, J. W., & Ranero, C. R. (2015). Fluid accumulation along the costa rica subduction thrust and development of the seismogenic zone. *Journal of Geophysical Research-Solid Earth*, *120*(1), 67–86, https://doi.org/10.1002/2014jb011265.

Bangs, N. L., Shipley, T. H., Moore, J. C., & Moore, G. F. (1999). Fluid accumulation and channeling along the northern barbados ridge decollement thrust. *Journal of Geophysical Research-Solid Earth*, *104*(B9), 20399–20414, https://doi.org/10.1029/1999jb900133.

Bekins, B., Mccaffrey, A. M., & Dreiss, S. J. (1994). Influence of kinetics on the smectite to illite transition in the barbados accretionary prism. *Journal of Geophysical Research-Solid Earth*, *99*(B9), 18147–18158, https://doi.org/10.1029/94jb01187.

Bell, R., Sutherland, R., Barker, D. H. N., Henrys, S., Bannister, S., Wallace, L., & Beavan, J. (2010). Seismic reflection character of the hikurangi subduction interface, new zealand, in the region of repeated gisborne slow slip events. *Geophysical Journal International*, *180*(1), 34–48, https://doi.org/10.1111/j.1365-246X.2009.04401.x.

Bethke, C. M. (1986). Inverse hydrologic analysis of the distribution and origin of gulf coast-type geopressured zones. *Journal of Geophysical Research-Solid Earth and Planets*, *91*(B6), 6535–6545, https://doi.org/10.1029/JB091iB06p06535.

Bormann, P., Engdahl, E. R., & Kind, R. (2012). *Seismic Wave Propagation and Earth models*, (pp. 1–105).

Cabrera, L., Ruiz, S., Poli, P., Contreras-Reyes, E., Osses, A., & Mancini, R. (2021). Northern chile intermediate-depth earthquakes controlled by plate hydration. *Geophysical Journal International*, *226*(1), 78–90, https://doi.org/10.1093/gji/ggaa565.

Davis, E. E., Villinger, H., & Sun, T. (2015). Slow and delayed deformation and uplift of the outermost subduction prism following ets and seismogenic slip events beneath nicoya peninsula, costa rica. *Earth and Planetary Science Letters*, *410*, 117–127, https://doi.org/10.1016/j.epsl.2014.11.015.

Duputel, Z., Jiang, J., Jolivet, R., Simons, M., Rivera, L., Ampuero, J. P., Riel, B., Owen, S. E., Moore, A. W., Samsonov, S. V., Culaciati, F. O., & Minson, S. E. (2015). The iquique earthquake sequence of april 2014: Bayesian modeling accounting for prediction uncertainty. *Geophysical Research Letters*, *42*(19), 7949–7957, https://doi.org/10.1002/2015gl065402.

Edwards, J. H., Kluesner, J. W., Silver, E. A., Brodsky, E. E., Brothers, D. S., Bangs, N. L., Kirkpatrick, J. D., Wood, R., & Okamoto, K. (2018). Corrugated megathrust revealed offshore from costa rica. *Nature Geoscience*, *11*(3), 197–202, https://doi.org/10.1038/s41561-018-0061-4.

England, P. (2018). On shear stresses, temperatures, and the maximum magnitudes of earthquakes at convergent plate boundaries. *Journal of Geophysical Research-Solid Earth*, *123*(8), 7165–7202, https://doi.org/10.1029/2018jb015907.

Farr, T. G., Rosen, P. A., Caro, E., Crippen, R., Duren, R., Hensley, S., Kobrick, M., Paller, M., Rodriguez, E., Roth, L., Seal, D., Shaffer, S., Shimada, J., Umland, J., Werner, M., Oskin, M., Burbank, D., & Alsdorf, D. (2007). The shuttle radar topography mission. *Reviews of Geophysics*, *45*(2), RG2004, https://doi.org/10.1029/2005rg000183.

Gao, X. & Wang, K. (2014). Strength of stick-slip and creeping subduction megathrusts from heat flow observations. *Science*, *345*(6200), 1038–41, https://doi.org/10.1126/science.1255487.

Geersen, J., Behrmann, J. H., Volker, D., Krastel, S., Ranero, C. R., Diaz-Naveas, J., & Weinrebe, W. (2011). Active tectonics of the south chilean marine fore arc (35 degrees s-40 degrees s). *Tectonics*, *30*(3), https://doi.org/10.1029/2010tc002777.

Geersen, J., Ranero, C. R., Barckhausen, U., & Reichert, C. (2015). Subducting seamounts control interplate coupling and seismic rupture in the 2014 iquique earthquake area. *Nat Commun*, *6*, 8267, https://doi.org/10.1038/ncomms9267.

Geersen, J., Ranero, C. R., Klaucke, I., Behrmann, J. H., Kopp, H., Trehu, A. M., Contreras-Reyes, E., Barckhausen, U., & Reichert, C. (2018). Active tectonics of the north chilean marine forearc and adjacent oceanic nazca plate. *Tectonics*, *37*(11), 4194–4211, https://doi.org/10.1029/2018tc005087.

Grevemeyer, I., Diaz-Naveas, J. L., Ranero, C. R., Villinger, H. W., & Sci, O. D. P. L. . (2003). Heat flow over the descending nazca plate in central chile, 32 degrees s to 41 degrees s: observations from odp leg 202 and the occurrence of natural gas hydrates. *Earth and Planetary Science Letters*, *213*(3-4), 285–298, https://doi.org/10.1016/S0012-821x(03)00303-0.

Hashimoto, Y., Eida, M., Kirikawa, T., Iida, R., Takagi, M., Furuya, N., Nikaizo, A., Kikuchi, T., & Yoshimitsu, T. (2012). Large amount of fluid migration around shallow seismogenic depth preserved in tectonic melange: Yokonami melange, the cretaceous shimanto belt, kochi, southwest japan. *Island Arc*, *21*(1), 53–64, https://doi.org/10.1111/j.1440-1738.2011.00806.x.

Hayes, G. P., Herman, M. W., Barnhart, W. D., Furlong, K. P., Riquelme, S., Benz, H. M., Bergman, E., Barrientos, S., Earle, P. S., & Samsonov, S. (2014). Continuing megathrust earthquake potential in chile after the 2014 iquique earthquake. *Nature*, *512*(7514), 295–8, https://doi.org/10.1038/nature13677.

Hubbert, M. K. & Rubey, W. W. (1959). Role of fluid pressure in mechanics of overthrust faulting: 1. mechanics of fluid-filled porous solids and its application to overthrust faulting. *Geological Society of America Bulletin*, *70*(2), 115–166, https://doi.org/10.1130/0016-7606(1959)70[115:ROFPIM]2.0.CO;2.

Husen, S. & Kissling, E. (2001). Postseismic fluid flow after the large subduction earthquake of antofagasta, chile. *Geology*, *29*(9), 847–850, https://doi.org/10.1130/0091-7613(2001)029<0847:Pffatl>2.0.Co;2.

Hyndman, R. D. & Wang, K. (1993). Thermal constraints on the zone of major thrust earthquake failure - the cascadia subduction zone. *Journal of Geophysical Research-Solid Earth*, *98*(B2), 2039–2060, https://doi.org/10.1029/92jb02279.

Hyndman, R. D., Wang, K., Yuan, T., & Spence, G. D. (1993). Tectonic sediment thickening, fluid expulsion, and the thermal regime of subduction zone accretionary prisms - the cascadia margin off vancouver-island. *Journal of Geophysical Research-Solid Earth*, *98*(B12), 21865–21876, https://doi.org/10.1029/93jb02391.

Hüpers, A. & Kopf, A. J. (2012). Effect of smectite dehydration on pore water geochemistry in the shallow subduction zone: An experimental approach. *Geochemistry, Geophysics, Geosystems*, *13*(10), Q0AD26, https://doi.org/10.1029/2012gc004212.

Jarrard, R. D. (2003). Subduction fluxes of water, carbon dioxide, chlorine, and potassium. *Geochemistry Geophysics Geosystems*, *4*, 8905, https://doi.org/10.1029/2002gc000392.

Kameda, J., Yamaguchi, A., Saito, S., Sakuma, H., Kawamura, K., & Kimura, G. (2011). A new source of water in seismogenic subduction zones. *Geophysical Research Letters*, *38*, L22306, https://doi.org/10.1029/2011gl048883.

Kastner, M., Elderfield, H., & Martin, J. B. (1991). Fluids in convergent margins - what do we know about their composition, origin, role in diagenesis and importance for oceanic chemical fluxes. *Philosophical Transactions of the Royal Society of London Series a-Mathematical Physical and Engineering Sciences*, *335*(1638), 243–259, https://doi.org/10.1098/rsta.1991.0045.

Kellner, A. (2007). *Different styles of deformation of the fore-arc wedge along the Chilean convergent margin: Insights from 3D numerical experiments*. Thesis.

Kodaira, S., No, T., Nakamura, Y., Fujiwara, T., Kaiho, Y., Miura, S., Takahashi, N., Kaneda, Y., & Taira, A. (2012). Coseismic fault rupture at the trench axis during the 2011 tohoku-oki earthquake. *Nature Geoscience*, *5*(9), 646–650, https://doi.org/10.1038/Ngeo1547.

Kosari, E., Rosenau, M., Bedford, J., Rudolf, M., & Oncken, O. (2020). On the relationship between offshore geodetic coverage and slip model uncertainty: Analog megathrust earthquake case studies. *Geophysical Research Letters*, *47*(15), e2020GL088266, https://doi.org/10.1029/2020GL088266.

Kuwatani, T., Okamoto, A., & Toriumi, M. (2011). Thermodynamic forward modeling of progressive dehydration reactions during subduction of oceanic crust under greenschist facies conditions. *Earth and Planetary Science Letters*, *307*(1-2), 9–18, https://doi.org/10.1016/j.epsl.2011.01.027.

Lange, D., Ruiz, J., Carrasco, S., & Manriquez, P. (2018). The chiloe m-w 7.6 earthquake of 2016 december 25 in southern chile and its relation to the m(w )9.5 1960 valdivia earthquake. *Geophysical Journal International*, *213*(1), 210–221, https://doi.org/10.1093/gji/ggx514.

Lindsey, E. O., Mallick, R., Hubbard, J. A., Bradley, K. E., Almeida, R. V., Moore, J. D. P., Burgmann, R., & Hill, E. M. (2021). Slip rate deficit and earthquake potential on shallow megathrusts. *Nature Geoscience*, *14*(5), 321–326, https://doi.org/10.1038/s41561-021-00736-x.

Maksymowicz, A., Chadwell, C. D., Ruiz, J., Trehu, A. M., Contreras-Reyes, E., Weinrebe, W., Diaz-Naveas, J., Gibson, J. C., Lonsdale, P., & Tryon, M. D. (2017). Coseismic seafloor deformation in the trench region during the mw8.8 maule megathrust earthquake. *Sci Rep*, *7*, 45918, https://doi.org/10.1038/srep45918.

McCaffrey, R., Wallace, L. M., & Beavan, J. (2008). Slow slip and frictional transition at low temperature at the hikurangi subduction zone. *Nature Geoscience*, *1*(5), 316–320, https://doi.org/10.1038/ngeo178.

Molnar, P. & England, P. (1990). Temperatures, heat-flux, and frictional stress near major thrust faults. *Journal of Geophysical Research-Solid Earth and Planets*, *95*(B4), 4833–4856, https://doi.org/10.1029/JB095iB04p04833.

Molnar, P. & England, P. (1995). Temperatures in zones of steady-state underthrusting of young oceanic lithosphere. *Earth and Planetary Science Letters*, *131*(1-2), 57–70, https://doi.org/10.1016/0012-821x(94)00253-U.

Moore, J. C., Klaus, A., Bangs, N. L., Bekins, B., Bucker, C. J., Bruckmann, W., Erickson, S. N., Hansen, O., Horton, T., Ireland, P., Major, C. O., Moore, G. F., Peacock, S., Saito, S., Screaton, E. J., Shimeld, J. W., Stauffer, P. H., Taymaz, T., Teas, P. A., & Tokunaga, T. (1998). Consolidation patterns during initiation and evolution of a plate-boundary decollement zone: Northern barbados accretionary prism. *Geology*, *26*(9), 811–814, https://doi.org/10.1130/0091-7613(1998)026<0811:CPDIAE>2.3.CO;2.

Moore, J. C. & Saffer, D. (2001). Updip limit of the seismogenic zone beneath the accretionary prism of southwest japan: An effect of diagenetic to low-grade metamorphic processes and increasing effective stress. *Geology*, *29*(2), 183–186, https://doi.org/10.1130/0091-7613(2001)029<0183:Ulotsz>2.0.Co;2.

Moreno, M., Haberland, C., Oncken, O., Rietbrock, A., Angiboust, S., & Heidbach, O. (2014). Locking of the chile subduction zone controlled by fluid pressure before the 2010 earthquake. *Nature Geoscience*, *7*(4), 292–296, https://doi.org/10.1038/ngeo2102.

Myers, E. K., Roland, E. C., Trehu, A. M., Davenport, K., & Grp, P. (2022). Crustal structure of the incoming iquique ridge offshore northern chile. *Journal of Geophysical Research-Solid Earth*, *127*(2), https://doi.org/10.1029/2021JB023169.

Métois, M., Vigny, C., & Socquet, A. (2016). Interseismic coupling, megathrust earthquakes and seismic swarms along the chilean subduction zone (38°–18°s). *Pure and Applied Geophysics*, *173*(5), 1431–1449, https://doi.org/10.1007/s00024-016-1280-5.

Müller, R. D., Sdrolias, M., Gaina, C., & Roest, W. R. (2008). Age, spreading rates, and spreading asymmetry of the world's ocean crust. *Geochemistry, Geophysics, Geosystems*, *9*(4), https://doi.org/10.1029/2007gc001743.

Oncken, O., et al. (2003). Seismic imaging of a convergent continental margin and plateau in the central andes (andean continental research project 1996 (ancorp' 96)). *Journal of Geophysical Research-Solid Earth*, *108*(B7), https://doi.org/10.1029/2002jb001771.

Peacock, S. M. & Wang, K. (1999). Seismic consequences of warm versus cool subduction metamorphism: Examples from southwest and northeast japan. *Science*, *286*(5441), 937–939, https://doi.org/10.1126/science.286.5441.937.

Petersen, F., Lange, D., Ma, B., Grevemeyer, I., Geersen, J., Klaeschen, D., Contreras-Reyes, E., Barrientos, S., Tréhu, A. M., Vera, E., & Kopp, H. (2021). Relationship between subduction erosion and the up-dip limit of the 2014 mw 8.1 iquique earthquake. *Geophysical Research Letters*, *48*(9), e2020GL092207, https://doi.org/10.1029/2020gl092207.

Peyrat, S., Madariaga, R., Buforn, E., Campos, J., Asch, G., & Vilotte, J. P. (2010). Kinematic rupture process of the 2007 tocopilla earthquake and its main aftershocks from teleseismic and strong-motion data. *Geophysical Journal International*, *182*(3), 1411–1430, https://doi.org/10.1111/j.1365-246X.2010.04685.x.

Ranero, C. R., Grevemeyer, I., Sahling, H., Barckhausen, U., Hensen, C., Wallmann, K., Weinrebe, W., Vannucchi, P., von Huene, R., & McIntosh, K. (2008). Hydrogeological system of erosional convergent margins and its influence on tectonics and interplate seismogenesis. *Geochemistry, Geophysics, Geosystems*, *9*(3), Q03S04, https://doi.org/10.1029/2007gc001679.

Rotman, H. M. M. & Spinelli, G. A. (2014). Remarkably consistent thermal state of the south central chile subduction zone from 36 degrees s to 45 degrees s. *Journal of Geophysical Research-Solid Earth*, *119*(4), 3503–3516, https://doi.org/10.1002/2013jb010811.

Ruiz, S., Metois, M., Fuenzalida, A., Ruiz, J., Leyton, F., Grandin, R., Vigny, C., Madariaga, R., & Campos, J. (2014). Intense foreshocks and a slow slip event preceded the 2014 iquique mw 8.1 earthquake. *Science*, *345*(6201), 1165–9, https://doi.org/10.1126/science.1256074.

Saffer, D. M. & Tobin, H. J. (2011). Hydrogeology and mechanics of subduction zone forearcs: Fluid flow and pore pressure. *Annual Review of Earth and Planetary Sciences*, *39*, 157–186, https://doi.org/10.1146/annurev-earth-040610-133408.

Saffer, D. M. & Wallace, L. M. (2015). The frictional, hydrologic, metamorphic and thermal habitat of shallow slow earthquakes. *Nature Geoscience*, *8*(8), 594–600, https://doi.org/10.1038/Ngeo2490.

Schmidt, M. W. & Poli, S. (1998). Experimentally based water budgets for dehydrating slabs and consequences for arc magma generation. *Earth and Planetary Science Letters*, *163*(1-4), 361–379, https://doi.org/10.1016/S0012-821x(98)00142-3.

Scholz, C. H. (1988). The brittle-plastic transition and the depth of seismic faulting. *Geologische Rundschau*, *77*(1), 319–328, https://doi.org/10.1007/Bf01848693.

Schurr, B., Asch, G., Hainzl, S., Bedford, J., Hoechner, A., Palo, M., Wang, R., Moreno, M., Bartsch, M., Zhang, Y., Oncken, O., Tilmann, F., Dahm, T., Victor, P., Barrientos, S., & Vilotte, J. P. (2014). Gradual unlocking of plate boundary controlled initiation of the 2014 iquique earthquake. *Nature*, *512*(7514), 299–302, https://doi.org/10.1038/nature13681.

Schurr, B., Moreno, M., Tréhu, A. M., Bedford, J., Kummerow, J., Li, S., & Oncken, O. (2020). Forming a mogi doughnut in the years prior to and immediately before the 2014 m8.1 iquique, northern chile, earthquake. *Geophysical Research Letters*, *47*(16), e2020GL088351, https://doi.org/10.1029/2020gl088351.

Shipley, T. H., Moore, G. F., Bangs, N. L., Moore, J. C., & Stoffa, P. L. (1994). Seismically inferred dilatancy distribution, northern barbados ridge decollement - implications for fluid migration and fault strength. *Geology*, *22*(5), 411–414, https://doi.org/10.1130/0091-7613(1994)022<0411:Siddnb>2.3.Co;2.

Sippl, C., Schurr, B., Asch, G., & Kummerow, J. (2018). Seismicity structure of the northern chile forearc from > 100,000 double-difference relocated hypocenters. *Journal of Geophysical Research-Solid Earth*, *123*(5), 4063–4087, https://doi.org/10.1002/2017jb015384.

Spinelli, G. A. & Saffer, D. M. (2004). Along-strike variations in underthrust sediment dewatering on the nicoya margin, costa rica related to the updip limit of seismicity. *Geophysical Research Letters*, *31*(4), L04613, https://doi.org/10.1029/2003gl018863.

Spinelli, G. A. & Underwood, M. B. (2004). Character of sediments entering the costa rica subduction zone: Implications for partitioning of water along the plate interface. *Island Arc*, *13*(3), 432–451, https://doi.org/10.1111/j.1440-1738.2004.00436.x.

Spinelli, G. A. & Wang, K. (2008). Effects of fluid circulation in subducting crust on nankai margin seismogenic zone temperatures. *Geology*, *36*(11), 887–890, https://doi.org/10.1130/G25145a.1.

Springer, M. & Forster, A. (1998). Heat-flow density across the central andean subduction zone. *Tectonophysics*, *291*(1-4), 123–139, https://doi.org/10.1016/S0040-1951(98)00035-3.

Storch, I., Buske, S., Victor, P., & Oncken, O. (2021). Seismic images of the northern chilean subduction zone at 19 degrees 40 ' s, prior to the 2014 iquique earthquake. *Geophysical Journal International*, *225*(2), 1048–1061, https://doi.org/10.1093/gji/ggab035.

Tichelaar, B. W. & Ruff, L. J. (1991). Seismic coupling along the chilean subduction zone. *Journal of Geophysical Research-Solid Earth and Planets*, *96*(B7), 11997–12022, https://doi.org/10.1029/91jb00200.

Tichelaar, B. W. & Ruff, L. J. (1993). Depth of seismic coupling along subduction zones. *Journal of Geophysical Research-Solid Earth*, *98*(B2), 2017–2037, https://doi.org/10.1029/92jb02045.

Tilmann, F. J., Craig, T. J., Grevemeyer, I., Suwargadi, B., Kopp, H., & Flueh, E. (2010). The updip seismic/aseismic transition of the sumatra megathrust illuminated by aftershocks of the 2004 aceh-andaman and 2005 nias events. *Geophysical Journal International*, *181*(3), 1261–1274, https://doi.org/10.1111/j.1365-246X.2010.04597.x.

Tobin, H. J. & Saffer, D. M. (2009). Elevated fluid pressure and extreme mechanical weakness of a plate boundary thrust, nankai trough subduction zone. *Geology*, *37*(8), 679–682, https://doi.org/10.1130/G25752a.1.

Underwood, M. B. (2007). *Sediment Inputs to Subduction Zones: Why Lithostratigraphy and Clay Mineralogy Matter*, (pp. 42–85). Columbia University Press.

Vannucchi, P., Spagnuolo, E., Aretusini, S., Di Toro, G., Ujiie, K., Tsutsumi, A., & Nielsen, S. (2017). Past seismic slip-to-the-trench recorded in central america megathrust. *Nature Geoscience*, *10*(12), 935–940, https://doi.org/10.1038/s41561-017-0013-4.

Völker, D., Grevemeyer, I., Stipp, M., Wang, K., & He, J. (2011). Thermal control of the seismogenic zone of southern central chile. *Journal of Geophysical Research*, *116*(B10), B10305, https://doi.org/10.1029/2011jb008247.

Wallace, L. M., Webb, S. C., Ito, Y., Mochizuki, K., Hino, R., Henrys, S., Schwartz, S. Y., & Sheehan, A. F. (2016). Slow slip near the trench at the hikurangi subduction zone, new zealand. *Science*, *352*(6286), 701–704, https://doi.org/10.1126/science.aaf2349.

Wessel, P., Luis, J. F., Uieda, L., Scharroo, R., Wobbe, F., Smith, W. H. F., & Tian, D. (2019). The generic mapping tools version 6. *Geochemistry, Geophysics, Geosystems*, *20*(11), 5556–5564, https://doi.org/10.1029/2019gc008515.

Yokota, Y. & Ishikawa, T. (2020). Shallow slow slip events along the nankai trough detected by gnss-a. *Science Advances*, *6*(3), https://doi.org/10.1126/sciadv.aay5786.

# Supporting Information

## 1. Seismic Processing

Seismic data processing was conducted with the Schlumberger OMEGA2 software. Here we present the processing sequences and the corresponding results in terms of seismic line MC04. The same processing strategy is used for all profiles to eliminate the possibility that differences in reflectivity are due to differences in processing. An overview of the processing scheme is shown below (Fig. 3.5). The main seismic processing included four steps:

### A. Step1: Processing Geometry Implementation

In this step, the seismic data are exposed to a series of pre-processing modules of the Schlumberger OMEGA2 software, including sail extract module, geometry crooked module, geometry update module and grid define module, aiming to implement the processing geometry. In particular, the sail extract module is used to merge the geometry survey file information with the seismic traces. The geometry crooked module analyses the location of detectors, sources, and midpoints and projects them onto a smooth 2-D crooked common-mid-point (CMP) profile. Subsequently, the geometry update module and the grid define module were used to update the seismic trace header literals to the new processing grid. These pre-processing steps prepare the seismic data set for further analysis. Seismic shooting was conducted at an interval of 125 m to avoid interference from the previous shot on large offset OBS data. Due to the large shot interval, the original CMP gathers are imaged with prominent spatial aliasing. The aliasing has serious effects on the performance of multichannel data analysis processes such as f-k filtering. Because of spatial aliasing, these processes can perceive events with steep dips at high frequencies as different from what they are and, hence, do not treat them properly.

### B. Step2: Increase Vertical Resolution and General Noise Cleaning

In this step, four modules were used to increase the vertical resolution and clean the general noise. In particular, the deconvolution module is applied to compress the basic wavelet, thus increasing temporal resolution. The direct wave cleaning module was employed in shallow seafloor areas to enhance near-surface wide-angle reflections. Attenuation of random noise (RNA) was applied by a predictive deconvolution in the fx-domain. The anomalous amplitude attenuation (AAA) removed high amplitude events such as marine swell, rig and ship noise by transforming the seismic data into frequency bands and applying a spatial median filter. These pre-processing steps yield CMP gathers (Fig. 3.6a) which will be interpolated in the next step.

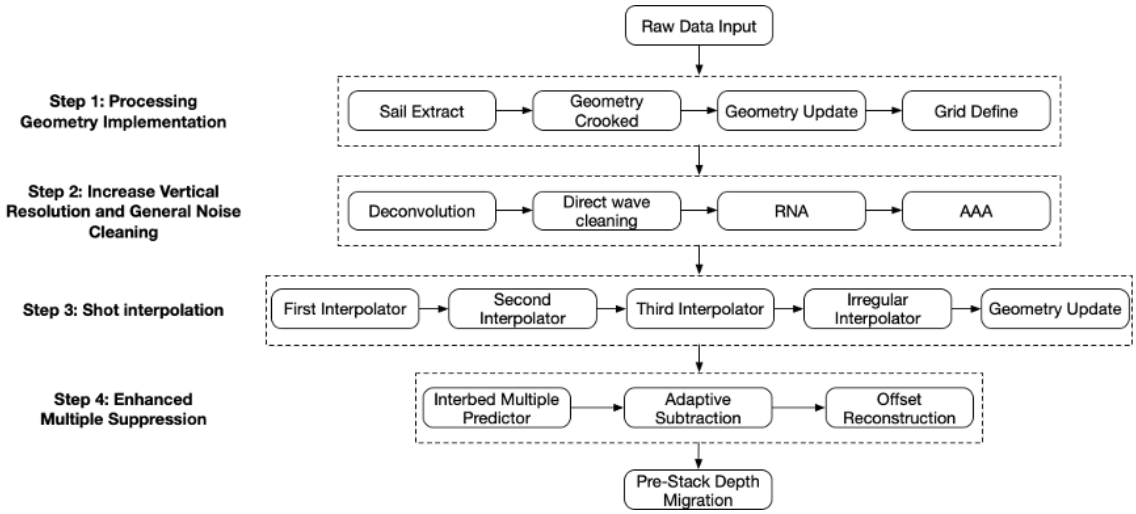


**Figure 3.5:** Overview of the processing sequence.

### C. Step3: Shot Interpolation

To avoid prominent spatial aliasing between neighboring shots resulting from the large shot interval, shot-ordered seismic data were interpolated three times from 125 m to 15.625 m by f-k trace interpolation. As the result is not a multiple of the receiver interval, an irregular interpolator module was used to interpolate it to 12.5 m, where aliased components have been eliminated (Fig. 3.6b).

### D. Step 4: Multiple attenuation

Prior to multiple attenuation, the plate boundary reflection is severely obscured by multiples (Fig. 3.7a). The multiples were predicted by surface related multiple elimination (SRME) using wavefield inversion based on the Kirchhoff integral and subtracted from the raw data after shot interpolations. After the multiple attenuation, we applied the f-k filtering to remove the high frequencies to enhance the image (Fig. 3.7b). The plate boundary reflection is clearly observed in the travel time range where the first multiple occurs and we can now trace the plate boundary interface further landward on the time section of seismic line MC04 (Fig. 3.8). The extensive data volume generated by the shot interpolations led to long calculation times in the pre-stack time domain and the pre-stack depth domain, so we reconstructed the offsets of CMP gathers with an increment of 100 m. After the reconstruction of offset distances, a preliminary *vp* model based on an unpublished 3D *vp* model from ocean bottom seismometers (OBS) during cruise MGL1610 of the *R/V Marcus G. Langseth* in 2016 was applied for the pre-stack depth migration. Referring to the OBS velocity field, we calculated the velocity gradient starting from the seafloor to yield an initial velocity model (Fig. 3.9) for application to the multichannel seismic profiles. Although this initial velocity model is not sufficiently confining the shallow depth ($<$ 8 km below seafloor) and may produce an inaccuracy of 1 - 2 km in the

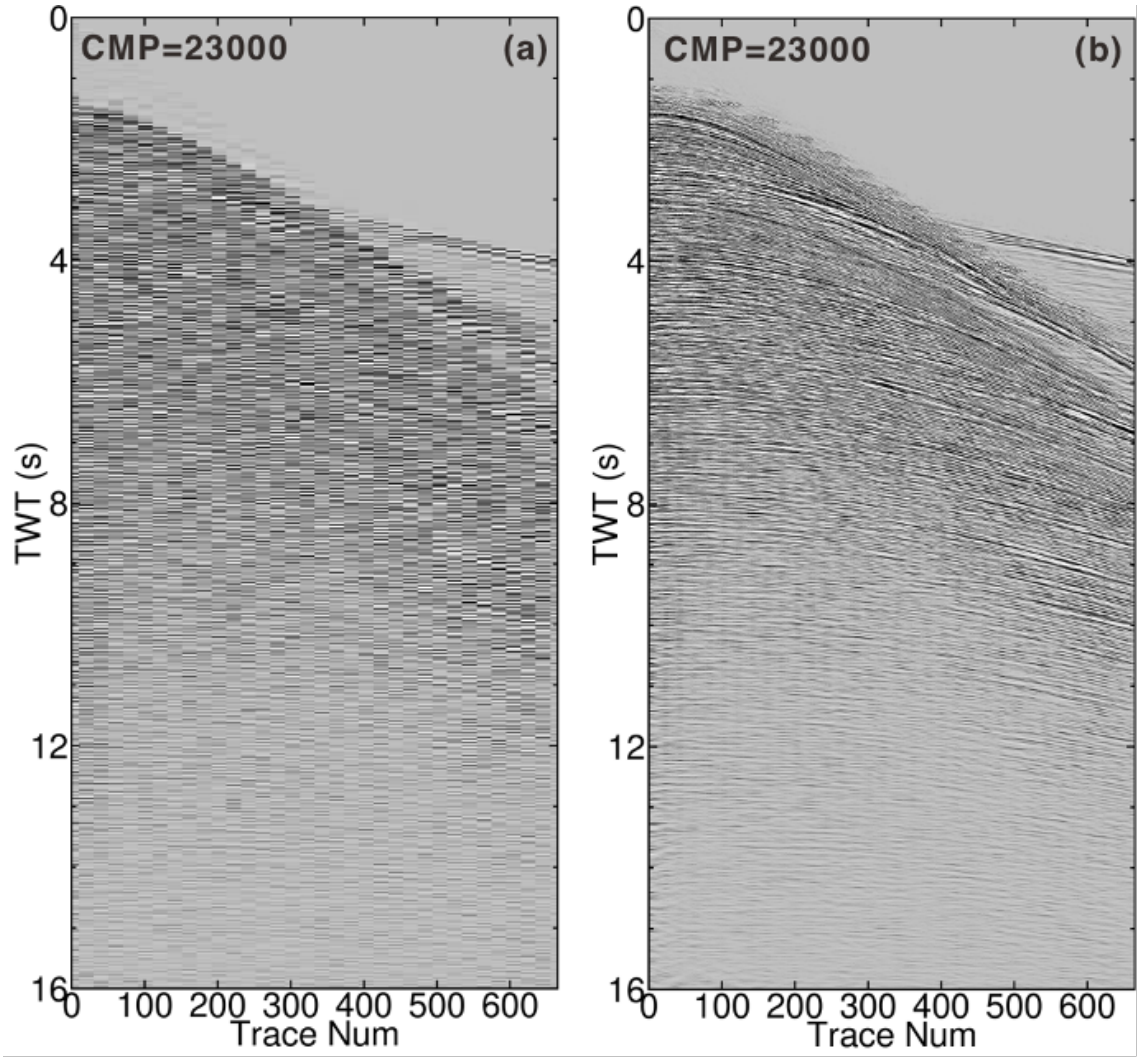


**Figure 3.6:** The CMP gathers before and after interpolation of seismic line MC04. Before the interpolation processing, the trace spacing is 250 m, which is shown in (a). After the interpolation processing the trace spacing is 25 m in (b).

depth of the plate boundary compared to an accurate velocity model, it does not affect the spatial distribution of the reflectivity. In the meanwhile, this initial velocity does not enable to carry out amplitude analysis at shallow depth. However, our main focus is on the reflectivity pattern and the lateral coherence and continuity of the plate boundary reflectivity. The pre-stack depth migrated seismic images are not significantly affected by seafloor multiples anymore and resolve sub-seafloor structures in the upper plate and subducting lower plate at high resolution (Fig. 3.10).

### E. Step 5: Amplitude calibration

To quantify the amplitudes of the seismic sections, the reflection coefficient was estimated based on the ratio of the seafloor reflection to the seafloor multiple reflection. Due to

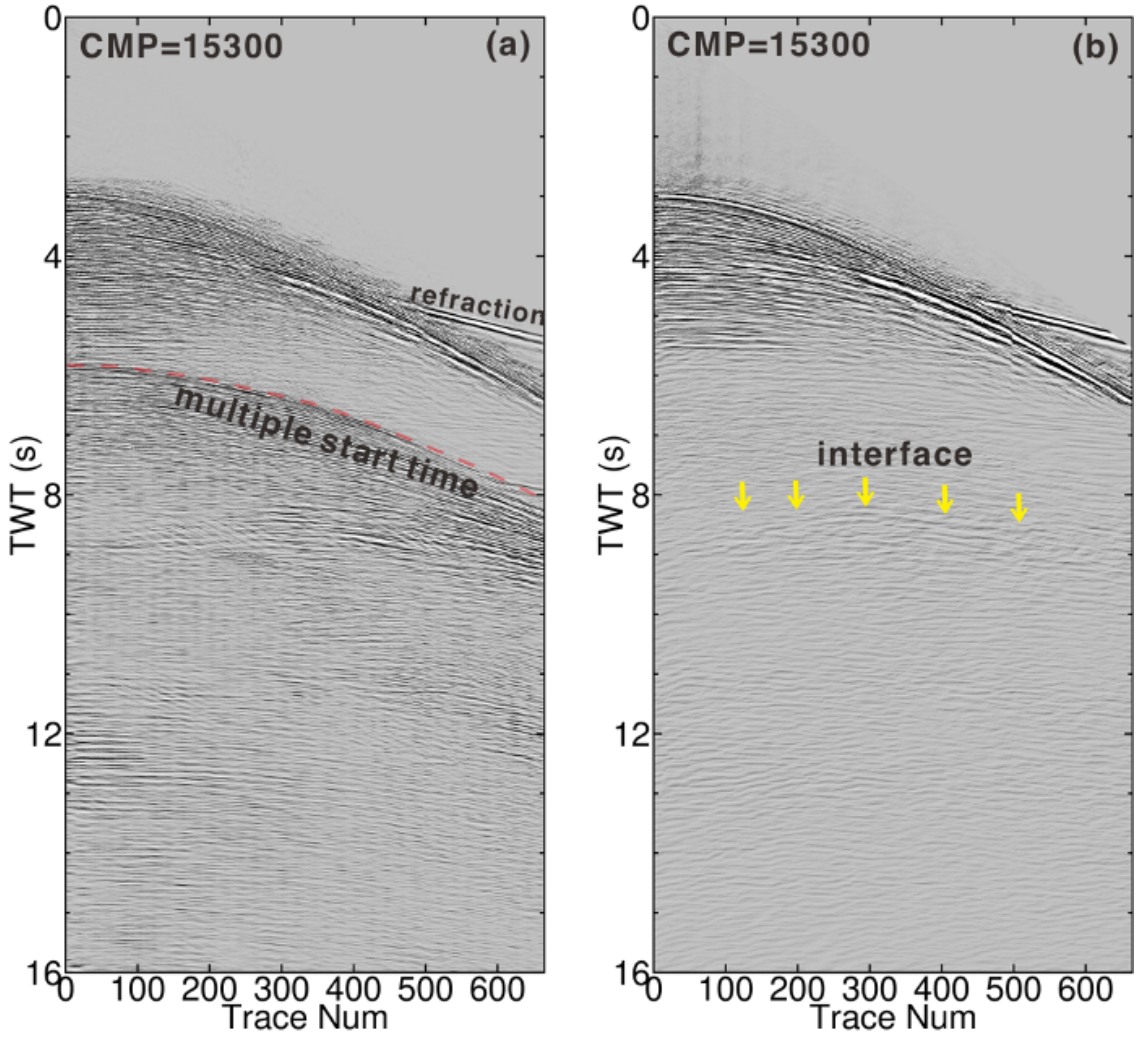


**Figure 3.7:** The CMP gathers before and after the de-multiple step of MC04. Before the de-multiple processing, seismic signals are obscured by several multiple orders below the seafloor multiple start time indicated by the transparent red dashed line in (a). After the de-multiple processing and high frequencies elimination, the multiples are mostly eliminated and we can see the interface traced by yellow arrows around 8-9 s TWT in (b).

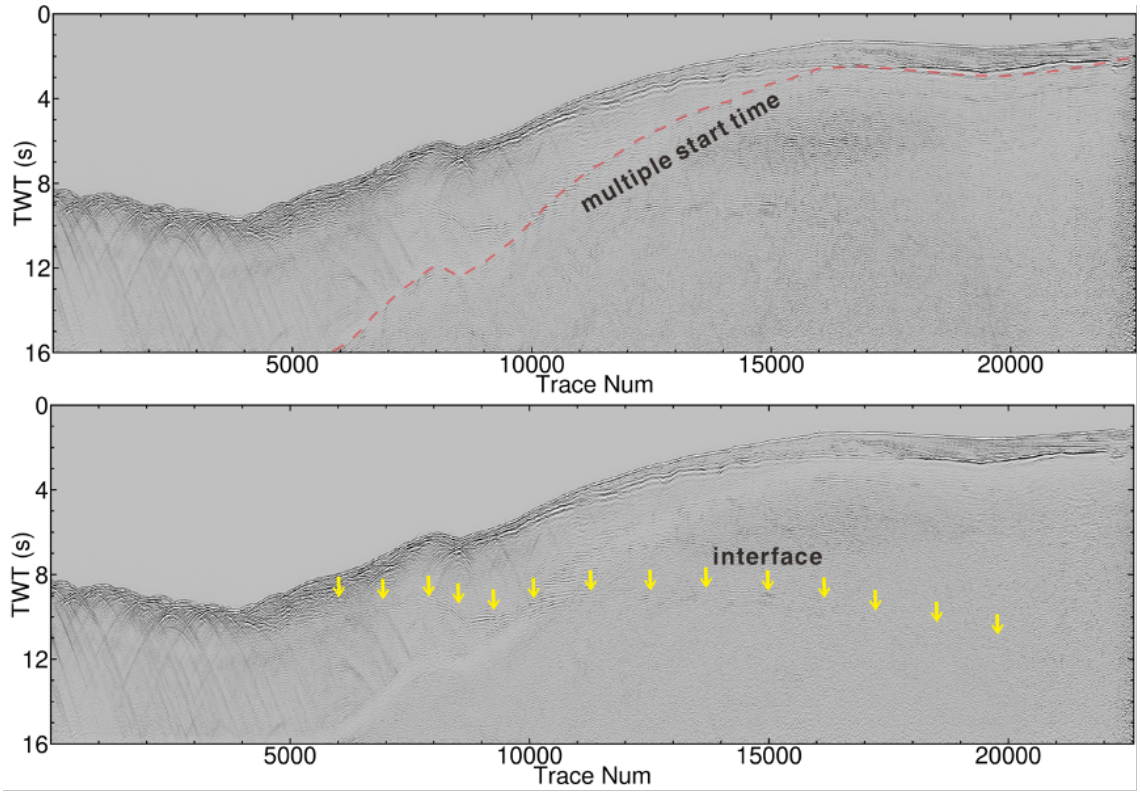


**Figure 3.8:** Stack section in the time domain of seismic line MC04 before and after the de-multiple processing. Before the de-multiple processing, the interface reflection is obscured by the multiples below the seafloor multiple start time indicated by the transparent red dashed line in (a). After the de-multiple processing, the interface reflection can be traced around trace number 20000, as indicated by the yellow arrows in (b). Sections are shown after application of a depth customized gain of amplitudes.

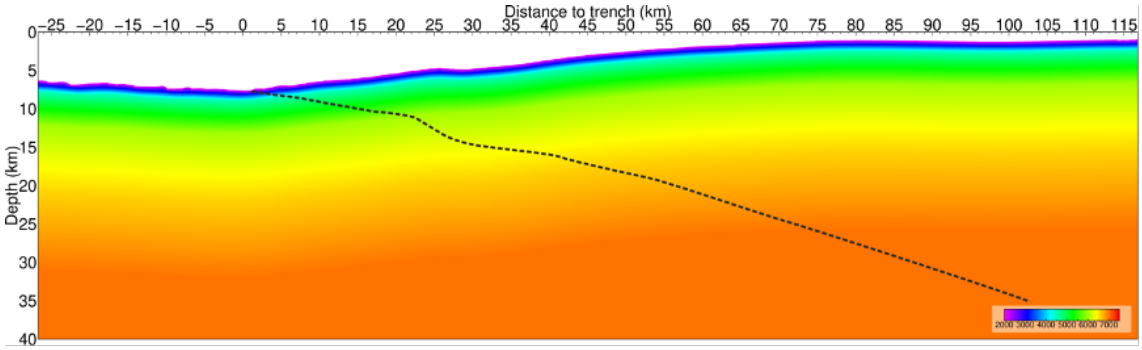


**Figure 3.9:** An initial velocity model based on an unpublished 3D OBS velocity model (K. Davenport, personal communication) was applied for the pre-stack depth migration. The black dashed line indicates the plate boundary of profile MC04.

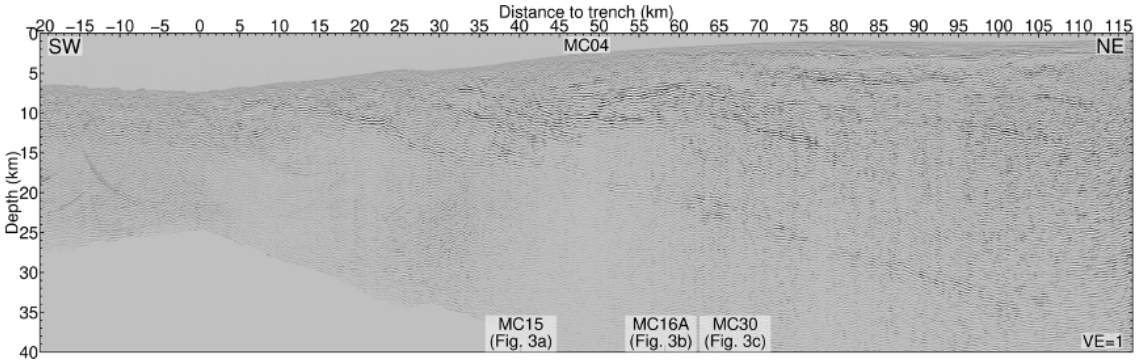


**Figure 3.10:** The pre-stack depth migrated seismic image of seismic line MC04.

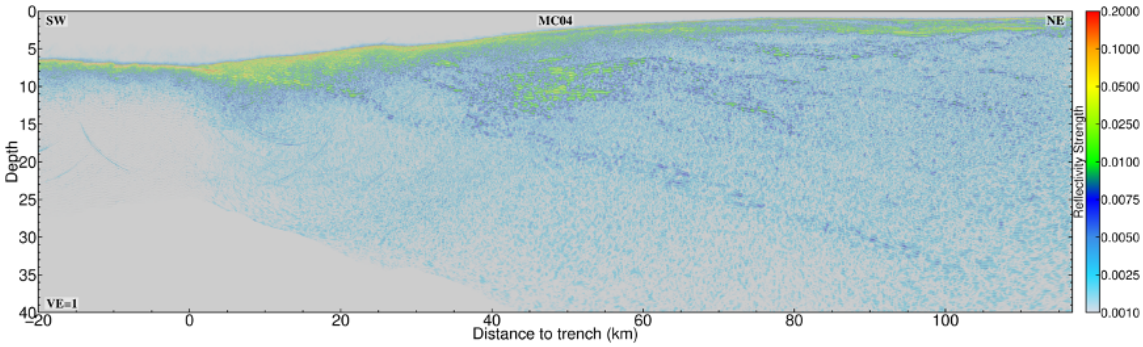


**Figure 3.11:** Estimated reflection strength of pre-stack depth migrated seismic image of seismic line MC04. The plate boundary shows a unique reflection strength than the internal crustal reflector elements. Vertical exaggeration is 1.

interference of several reflector elements resulting in inverse and mix phased signals especially in the crustal overburden the envelope was calculated representing the absolute reflection strength (Fig. 3.11). The plate boundary shows a unique reflection strength of 0.005 to 0.0075 in a depth range between 15 to 35 km, whereas the internal crustal reflector elements show a higher variability ranging from 0.0075 to 0.025 at a depth range of 5 to 15 km.

## 2. Thermal Model Setup

It has long been recognized that the rupture zone of subduction zone megathrust earthquakes is at least partially controlled by the thermal state of the fault zone (Tichelaar and Ruff, 1993; Hyndman et al., 1993). Analytical models reveal that the geometry of the subduction zone, the thermal state of the incoming subducting plate and the shear or frictional heating along the megathrust are critical parameters controlling megathrust temperatures (Molnar and England, 1990; England, 2018), which in turn, define the sea-

ward and landward limit of large subduction earthquakes rupture zones. The seaward or updip limit is generally associated with temperatures of 100 °- 150 °C, marking the smectite to chlorite transition (Hyndman and Wang, 1993) or a suite of diagenetic reactions and release of water from underthrusted sediments (Spinelli and Saffer, 2004) and/or basement (Kameda et al., 2011). The landward or downdip limit is assumed to be associated with a critical temperature of 350 °- 400 °C, which marks the transition from stick-slip to stable sliding at the onset of quartz and feldspar plasticity of continental crustal rocks (Scholz, 1988).

The geometry of the subduction zone is readily known from geophysical data or the hypocentral depth of large megathrust earthquakes and the basal heat flow is defined by the age of the incoming oceanic plate. Most thermal parameters of subduction zones show little variation along the Pacific Ring of Fire and are well established, especially for Chile (Völker et al., 2011; Rotman and Spinelli, 2014). Based on these data, most subduction zones have been studied using two-dimensional thermal models. Here, we use two different approaches. First, we calculate the thermal state along the plate interface or megathrust fault using analytical solutions based on the formalism (England, 2018) and second, we consider a 2-dimensional thermal model (Kellner, 2007) for northern Chile, incorporating corner flow in the mantle wedge.

Analytical expressions, which relate surface heat flux to temperature, geometrical constraints, and shear stress, provide an efficient approach to study the thermal state of the megathrust fault and are discussed in detail (Molnar and England, 1995, 1990; England, 2018). We follow the approach (England, 2018) and first calculate the temperature $T_f$ as a function of the depth z on the interplate fault zone as:

$$(1)\ T(z) = K_m T_0 z / S K_s \left[\pi\kappa\left(t_0 + t_s\right)\right]^{1/2} \tag{3.1}$$

where $S(z) = 1 + bK_m \left[\left(V_n z \sin\delta\right)/k\right]^{1/2} / K_s$. $K_m$ $\left(3.3\mathrm{Wm}^{-1}\ \mathrm{K}^{-1}\right)$ and $K_s$ $\left(2.55\mathrm{Wm}^{-1}\ \mathrm{K}^{-1}\right)$ are the mantle and forearc thermal conductivity, respectively. $T_0$ is the asthenospheric mantle temperature (1300 °C) and $k$ is the thermal diffusivity ($10^{-6}$ $\mathrm{m}^2\ \mathrm{s}^{-1}$). $t_0$ is the average age of the subducting plate (50 Myr, Müller et al., 2008), whereas $t_s$ is the time it takes the lithosphere to subduct to a depth $z$. $V_n$ is the convergence rate normal to the subduction (~70 km/Myr), $\delta$ is the dip angle of subduction, and $b$ $\left(\pi^{-1/2}\right)$ is a factor that depends on the specific geometry (Molnar and England, 1995).

The dip angle of subduction was taken directly from the seismic reflection images (Fig. 3.2), and the time $t_s$ is computed by dividing the integrated downdip length of the fault surface by $V_n$ (McCaffrey et al., 2008). We neglect the effect of the horizontal heat flow. To

calculate the radiogenic heat production $T_r$ in the forearc crust we used the following expression (McCaffrey et al., 2008):

$$(2)\ T_r(z) = A_r z^2 / (2K_s S(z)) \tag{3.2}$$

where $A_r$ is the radiogenic heat production rate ($10^{-6}\mathrm{Wm}^{-3}$) (Grevemeyer et al., 2003). Radiogenic heat production adds 0-45 °C to the fault temperature from the trench axis up to the downdip limit.

Further, we include in our model frictional shear heating $T_{sh}(z)$ on the thermal field by using:

$$(3)\ T_{sh}(z) = \tau(z) V_t z / (K_s S(z)) \tag{3.3}$$

where $\tau(z)$ is the shear stress on the fault and $V_t$ is the total slip rate (Molnar and England, 1995; England, 2018). $\tau(z)$ on a gently dipping fault at shallow depth is approximately

$$(4)\ \tau(z) = \mu\,(\sigma_n(z) - p(z)) \tag{3.4}$$

where $\mu$ is the friction coefficient, $\sigma_n$ is the normal stress applied on the fault plane (approximately the overburden pressure), and $p$ is the pore fluid pressure. Following McCaffrey et al. (2008), we use $\mu = 0.85$, $\sigma_n(z) = \rho g z$ and $p(z) = 0.95\sigma_n(z)$with acceleration of gravity $g = 9.8ms^{-2}$ and the average crustal density $\rho = 2500kgm^{-3}$.

The final predicted temperature on the fault plate boundary $T_f(z)$ is the sum of Eqs. 3.1 - 3.3 (i.e., $T_f(z) = T(z) + T_r(z) + T_{sh}(z)$.) Fig. 3.2 shows the estimated temperature values for $T_f(z)$ along our seismic reflection lines.

We compare our model to the numerical model (Kellner, 2007). The geometry of this model is based on a suite of geophysical data (Oncken et al., 2003) and thermal parameters were rated against a number of observed features, including the maximum depth of subduction thrust earthquakes and observed heat flow. Interestingly, the maximum depth of seismic faulting of megathrust earthquakes in northern Chile occurs at 40 - 50 km (Tichelaar and Ruff, 1991; Peyrat et al., 2010), suggesting that temperatures of 350 ° - 400 °C are reached at ~40 - 50 km, too. To mimic this feature, Kellner (2007) had to introduce a considerable amount of shear heating, in the order of $\tau = 33MPa$ to $\tau = 67MPa$, with the upper limit providing a better fit to the data. The predictions from the $\tau = 67MPa$ model mimic the prediction of our preferred analytic solution down to a depth of approx. 30 km. At greater depth, the models differ with (Kellner, 2007) model showing somewhat lower temperatures. The observed differences may stem from the effects of the asthenospheric corner flow incorporated into the numerical model and a change in dip angle, which is not considered in the analytic model. We also compare our model with other thermal models from the Northern Chilean margin. A comparison of all the models for the temperature

along the plate interface is shown in Fig. 3.13, including the thermal model with shear stress $\tau = 67MPa$ (Kellner, 2007) as the black dashed line, the thermal model with frictional heating we used in the main text as the red dashed line, the thermal model with shear stress $\tau = 33MPa$ (Kellner, 2007) as the orange dashed line, the thermal model (Cabrera et al., 2021) as the magenta dashed line, and a thermal model we built without the frictional heating as the green dashed line. Please note that for the study of the up-limit limit at shallow depth (~15 km) and its correlation to the reflectivity pattern of the seismic data, the model we established with frictional heating and the model with shear stress $\tau = 67MPa$ (Kellner, 2007) show consistent features.

As previously mentioned in the main text, the established new thermal model uses a friction coefficient $\mu = 0.85$ and pore fluid pressure $\lambda = 0.95$ (McCaffrey et al., 2008). Since these values vary in each tectonic setting, we applied different $\mu_b$ in the new analytical thermal model in Fig. 3.14. The effective coefficient of basal friction $\mu_b$ depends on both the friction coefficient $\mu$ and pore fluid pressure $\lambda$ along the fault zone: $\mu_b = \mu(1 - \lambda)$ (Hubbert and Rubey, 1959). Based on this formula, the $\mu_b$ of the model in our main text is 0.0425, which is shown as the red dashed line. We applied a range of $\mu_b$ from 0.03-0.13, consistent with the global thermal measurement (Gao and Wang, 2014). In this range, the predictions depth of the analytical model ($< 20$ km) is close to the downdip limit of the megathrust reflectivity (~15 km) observed from MCS images at the upper threshold of the clay dehydration temperature of 150 °C (Fig. 3.14). Moreover, the thermal model and reflectivity show a better spatial matching with a higher effective coefficient of basal friction $\mu_b$ value.

An interesting feature is that the models for northern Chile show larger frictional heating compared to those observed in south-central Chile (Grevemeyer et al., 2003; Völker et al., 2011; Rotman and Spinelli, 2014). However, already Rotman and Spinelli (2014) suggested that frictional heating at the plate boundary increases northward, perhaps mimicking the increasing age of the subducting plate. Furthermore, patterns are consistent with heat flow anomalies over the marine forearc. Heat flow anomalies over the marine forearc are in the order of 50 - 60, 40 - 50, and 24 - 31 $mW/m^2$ at 39 °S, 36 °S and 33 °S, respectively(Grevemeyer et al., 2003), decreasing northward and hence reflecting increasing crustal age of the subducting plate and supporting a decrease of basal heat flow. At 21 °S, however, the age of the subducting plate has increased by roughly 20 Myr with respect to 33 °S, but the forearc heat flow is in the order of 30 - 40 mW/m (Springer and Forster, 1998) and thus higher than near 33 °S, supporting higher values frictional heating than found further south. It might be reasonable to hypothesize that sediment starved subduction erosion supports a higher degree of friction than the accretionary margin of south-central Chile, but this interpretation is beyond the scope of our work.

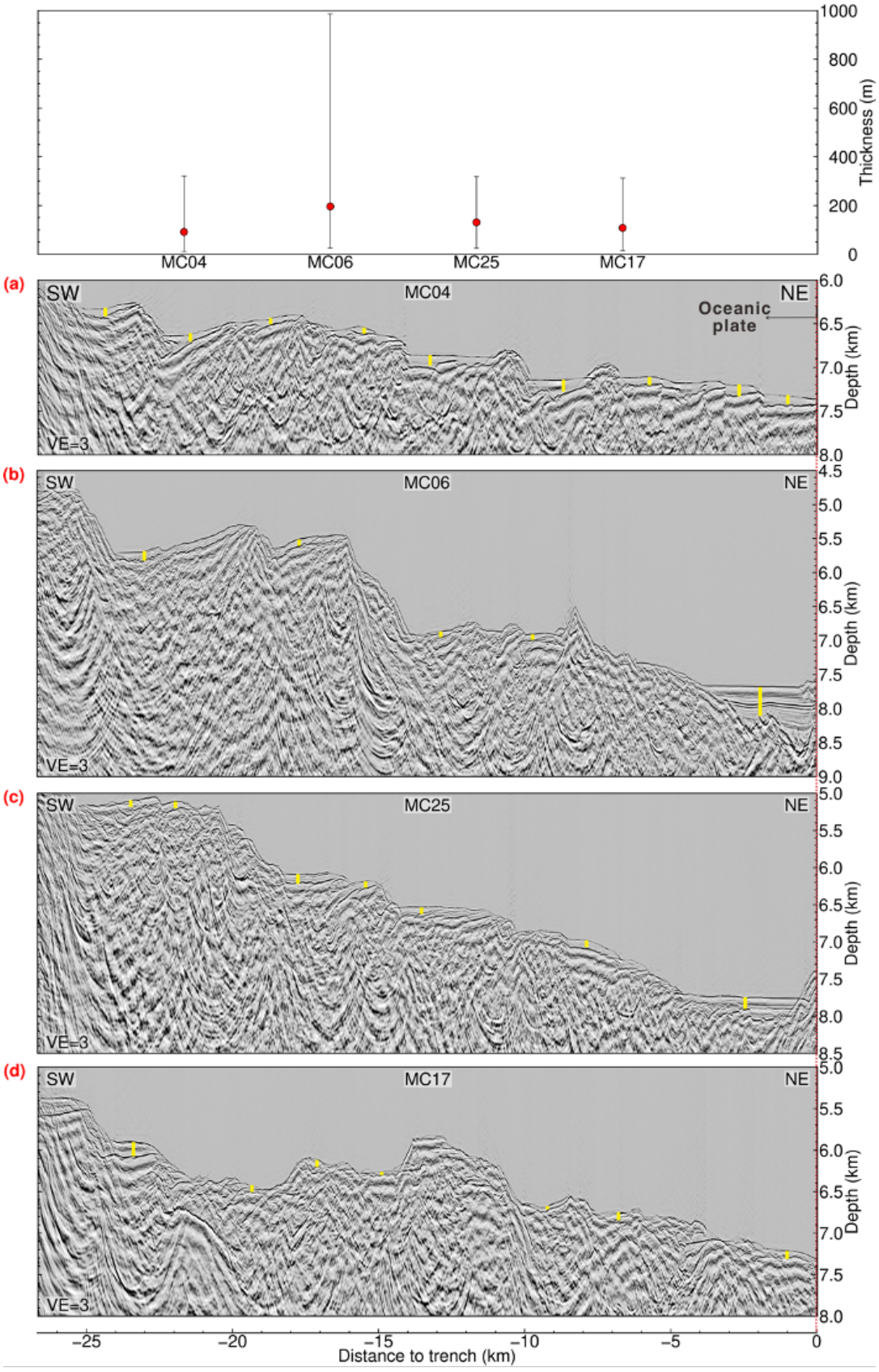


**Figure 3.12:** Oceanic crust of pre-stack depth migrated section along seismic dip-lines (Caption next page).

Both our analytical model and the numeric 2D model (Kellner, 2007) show higher temperatures along the subduction megathrust fault with respect to other models for northern Chile. For example, Cabrera et al. (2021) (Fig. 3.13, magenta dashed line) did not consider any frictional heating with the argument that in south-central Chile shear heating was low and therefore they obtained lower temperatures.

## 3. Supplementary Discussion

Reflection energy absorption, seismic processing parameters, differences of gun energy during seismic acquisition and shooting direction may all potentially cause a variation of reflectivity along the plate boundary. To allow a spatial comparison of the reflectivity and avoid issues caused by seismic processing, the same processing strategy is used for all profiles. In addition, we discuss the following issues:

**A. Is the plate interface on seismic line MC04 visible to greater depth because of stronger gun energy during data acquisition?**

The plate interface is traced to a depth of approximately 35 km on the northern dip line MC04 but disappears at shallower depth on the dip lines that run through the rupture area of the 2014 Iquique earthquake. The acquisition geometry and gun array remained unchanged during the survey, which covered seismic lines parallel to the trench as well as profiles in the dip direction. Strike line MC30, which crosses the middle continental slope and is located furthest from the trench axis, documents that the plate interface along the northern part of the line can be traced to greater depth than along the southern part. This observation is augmented by all seismic dip lines and seismic strike lines of our survey.

**B. Is the difference in the plate interface reflection strength caused by shooting direction?**

The shooting direction did not cause the observed differences of the plate interface reflection as seismic dip lines MC04, MC06, and MC25 were shot from west to east, while

**Figure 3.12:** Oceanic crust of pre-stack depth migrated section along seismic dip-lines. The error bar on top indicates the sediment upon the oceanic crust, in which the red dots show the average thickness of sediment on oceanic crust. The upper limit of the error bar represents the maximum thickness of sediments, while the lower limit indicates the minimum thickness of sediment. The maximum thickness anomaly along MC06 is due to more sediment in the trench than along the other seismic lines. In (a)-(d), yellow solid lines indicate the thickness of sediment on oceanic crust. Due to the bending of the oceanic crust, the sediments are accumulated in half-graben structures. (a): seismic line MC04; (b): seismic line 06; (c): seismic line 25; (d): seismic line 17. Vertical exaggeration is 3.

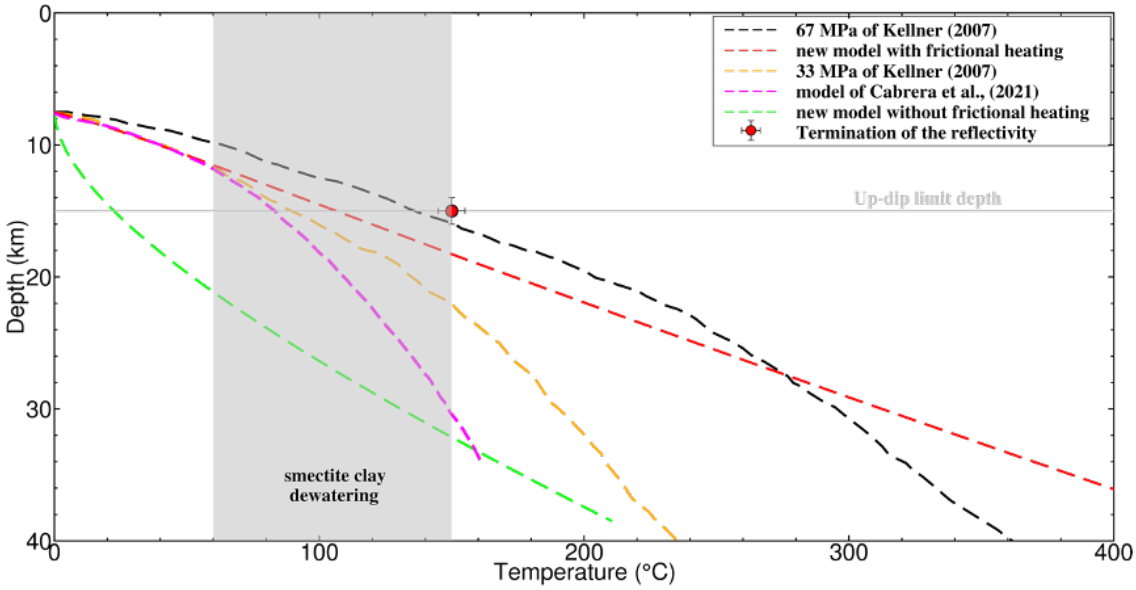


**Figure 3.13:** Comparison of different thermal models. Black dashed line: thermal model with shear stress $\tau = 67MPa$ (Kellner, 2007); red dashed line: thermal model with frictional heating discussed in main text; orange dashed line: thermal model with shear stress $\tau = 33MPa$ (Kellner, 2007); magenta dashed line: thermal model of (Cabrera et al., 2021); green dashed line: alternative thermal model computed without frictional heating. The approximate depth range of smectite clay dehydration is based on (Saffer and Tobin, 2011; Kastner et al., 1991; Bekins et al., 1994; Spinelli and Saffer, 2004; Underwood, 2007).

seismic dip lines MC17 and MC23 (Petersen et al., 2021) were shot from east to west. There are at least two seismic lines in the same direction, documenting that the shooting direction does not exert a major influence.

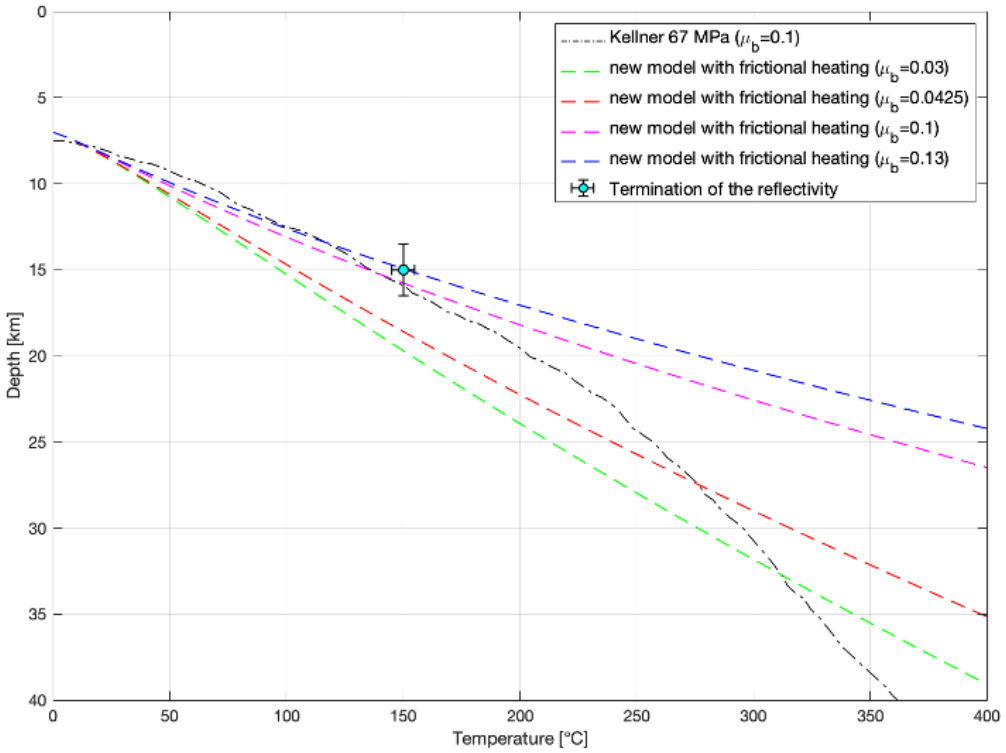


**Figure 3.14:** New thermal model with varying effective coefficient of basal friction $\mu_b$ values. The range of $\mu_b$ is from 0.03 - 0.13, consistent with the global thermal measurement (Gao and Wang, 2014). The estimated average basal friction $\mu_b = 0.1$ of (Kellner, 2007) $67MPa$ is shown as a black dashed line. Using the same basal friction value, our new analytical model is shown as a magenta dashed line. In the main text, we used a friction coefficient of $\mu = 0.85$ and pore fluid pressure $\lambda = 0.95$ (McCaffrey et al., 2008). The effective coefficient of basal friction $\mu_b$ depends on both the friction coefficient $\mu$ and pore fluid pressure $\lambda$ along the fault zone: $\mu_b = \mu(1-\lambda)$ (Hubbert and Rubey, 1959). Based on this formula, the $\mu_b$ of the model in our main text is 0.0425, which is shown as red dashed line. $\mu_b = 0.03$ and $\mu_b = 0.13$ are shown as green and blue dashed lines, respectively.

# 4 Impact of the Iquique Ridge on structure and deformation of the North Chilean subduction zone

**Bo Ma**[1], Jacob Geersen[2], Dirk Klaeschen[1], Eduardo Contreras-Reyes[3], Michael Riedel[1], Yueyang Xia[1], Anne M. Tréhu[4], Dietrich Lange[1] and Heidrun Kopp[1,2]

1) GEOMAR Helmholtz Centre for Ocean Research Kiel, Kiel, Germany.

2) Institute of Geosciences, Kiel University, Kiel, Germany.

3) Departamento de Geofísica, Facultad de Ciencias Físicas y Matemáticas, Universidad de Chile, Santiago, Chile.

4) Oregon State University, College of Earth, Ocean, and Atmospheric Sciences, Corvallis, USA

Submitted to **Journal of South American Earth Sciences** special issue "Geophysical Studies along the Chilean Subduction Zone", Dec. 2022.

## Abstract

The subduction of seamounts and basement ridges affects the structure, morphology, and physical state of a convergent margin. To evaluate their impact on the seismo-tectonic setting of the subduction zone and the tectonic development of the lower subducting and upper overriding plate, it is essential to know the precise location of subducted topographic features under the marine forearc. Offshore Northern Chile, the Iquique Ridge represents a broad zone of complex and heterogeneous structure of variable width on the oceanic Nazca Plate, which complicates attempts to project it beneath the forearc of the Chilean subduction zone. Here we use a state-of-the-art seismic reflection data processing approach to map structures related to ridge subduction under the marine forearc with unprecedented accuracy and resolution and evaluate their impact on the deformation of both the plate boundary and the upper plate. We show that significant ridge-related topography is currently subducting south of 20.5 °S and that the combined effect of horst and graben subduction with subduction of Iquique ridge-related thickened and elevated crust causes an upward bulging of the entire upper plate from the plate interface up to the seafloor as well as the presence of kilometer-scale anticlinal structures observed in multibeam bathymetric data that are approximately aligned with horsts seaward of the trench. In the area affected by the subducting ridge, a frontal prism is absent, which may relate to frontal subduction erosion caused by the excess lower plate topography. In contrast farther towards the north, where only isolated seamounts subduct, a small frontal prism and a slope/apron sediment cover down to 3000 m water depth are found.

## Keywords

Iquique Ridge,
Northern Chile,
Trench,
2014 Iquique Earthquake,
Seismic Reflection

## 4.1 Introduction

The subduction of seamount chains, aseismic ridges, and other bathymetric highs on the oceanic crust is a common process along convergent margins, which has a significant impact on the geometry and dynamics of both the subducting and overriding plates (Contreras-Reyes et al., 2019; Dominguez et al., 1998; Hampel et al., 2004; Kopp et al.,

2004; Lallemand et al., 1992; Morell, 2016; Myers et al., 2022; Xia et al., 2021; Yamazaki and Okamura, 1989). As the oceanic basement relief forces its way into the subduction zone, it often causes a variety of distinctive features, including the reduction of the slab dip (Martinod et al., 2013; Pilger Jr, 1981), the indentation of the overriding plate (Dominguez et al., 1998; Zeumann and Hampel, 2016), or uplift and over steepening of the overriding plate (Lallemand et al., 1992; McCann and Habermann, 1989), following by the gravitational collapse of the frontal margin due to basal subduction erosion (e.g., Contreras-Reyes et al., 2015).

Offshore Northern Chile, the Iquique Ridge represents a notable morphologic feature on the incoming oceanic plate, that has partly been mapped with multibeam bathymetric data (Fig. 4.1; Geersen et al., 2018). Previous investigations recognize the critical role played by the Iquique Ridge with respect to altering seafloor morphology (Contreras-Reyes and Carrizo, 2011; Geersen et al., 2015, 2018), density structure (Contreras-Reyes and Carrizo, 2011), and forearc gravity gradient (Maksymowicz et al., 2018). Studies included the analysis of marine seismic data (Geersen et al., 2015; Storch et al., 2021, 2022), finite-element modeling (Zeumann and Hampel, 2016), and kinematic plate reconstructions (Bello-González et al., 2018). These studies have partly revealed the geometry of the Iquique Ridge on the outer rise of the subduction zone. However, the position of the Iquique Ridge underneath the marine forearc remains enigmatic. Geersen et al. (2015) identified several subducted seamounts on the already subducted segment of the Iquique Ridge from three multichannel seismic lines and suggested that these seamounts exert a first-order control on the 2014 Iquique seismic rupture propagation. In contrast, Storch et al. (2021) did not observe subducted seamounts along one of these lines at the same place. These contradictory observations result from a lack of deep-penetrating, high-resolution seismic reflection data that unambiguously document the geometry of the ridge and any seamounts underneath the forearc. Clarifying the morphology of the Iquique Ridge underneath the upper plate would contribute to the understanding of the heterogeneity of the plate interface and possibly related seismic segmentation in Northern Chile.

In this study, we analyze deep-penetrating, high-resolution multichannel seismic reflection data to image the oceanic crust, plate interface configuration, and overriding plate associated with the subduction of the Iquique Ridge. The data used in this study were acquired in 2016 during the MGL1610 cruise of R/V Marcus G. Langseth offshore Northern Chile (Myers et al., 2022; Tréhu et al., 2017). We use two downdip seismic profiles covering the Iquique Ridge and surrounding areas (Fig. 4.1), with one line documenting the effects of the subducting Iquique Ridge (MC27) in comparison to another line that does not image subducting ridge related topography (MC06). The main objective of this study is to image the shallow plate interface underneath the lower to middle slope of the upper plate, revealing changes incurred by the subduction of the Iquique Ridge.

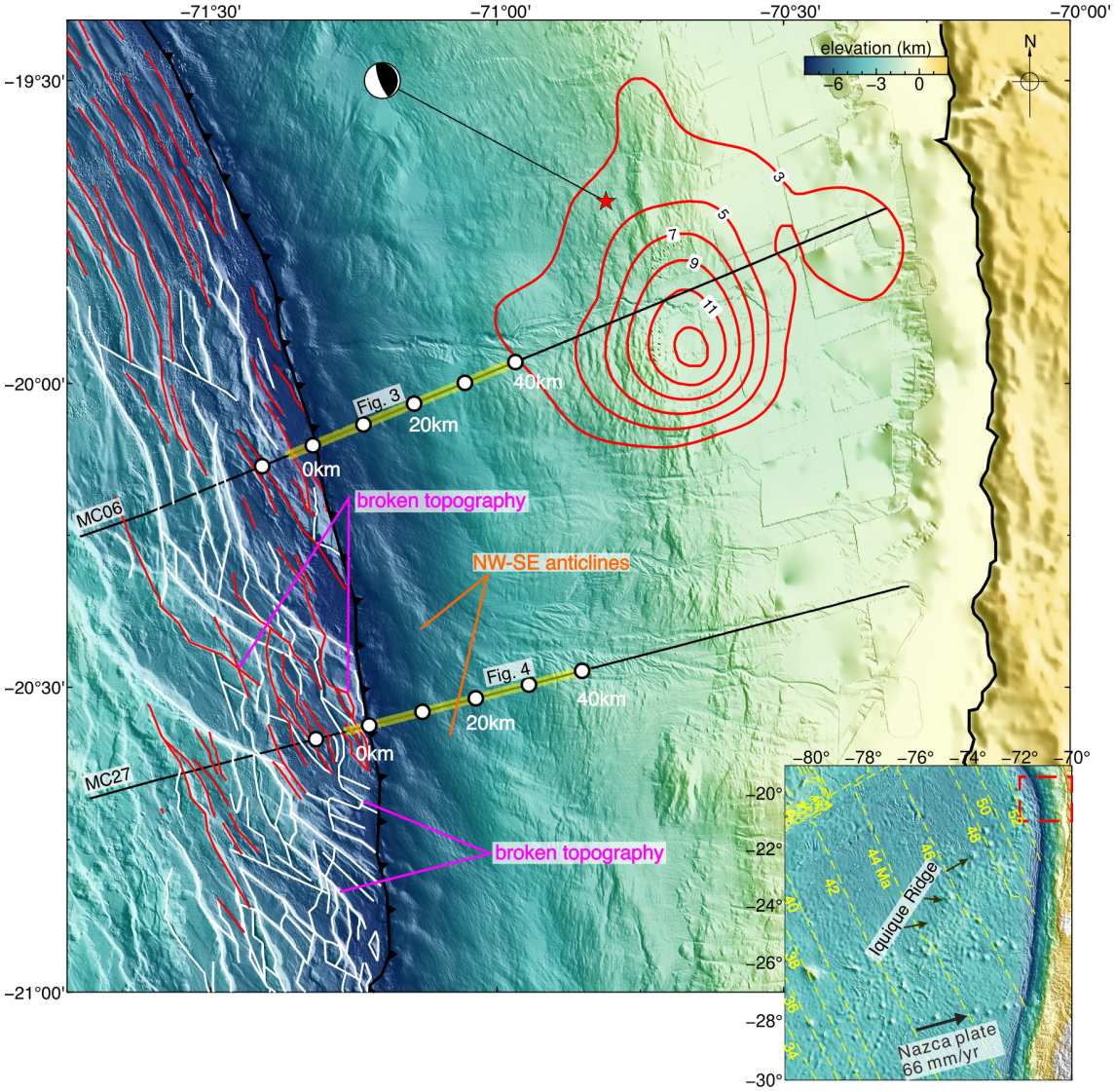


**Figure 4.1:** High-resolution multibeam bathymetry data offshore Northern Chile (Geersen et al., 2018) combined with GEBCO_2019 (www.gebco.net) bathymetry. Black solid lines indicate the seismic profiles, with yellow regions presented in Figs. 4.3 - 4.4. The hypocenter (star) and slip contours (in meters) of the 2014 Iquique $M_w$ 8.1 mainshock are from Duputel et al. (2015). Red and white lines indicate the reactivated spreading fabric and bending-related normal faults, respectively (Geersen et al., 2018). Inset shows seafloor bathymetry from GEBCO_2019 with SW-NE trending Iquique Ridge. Yellow dashed lines indicate age of the subducting Nazca plate. (www.ngdc.noaa.gov/mgg/ocean_age/ocean_age_2008.html; Müller et al., 2008)

## 4.2 Tectonic Setting

The Nazca plate and South America have a 66 - 67 mm/yr convergence rate offshore Northern Chile (Angermann et al., 1999). Along-trench sediment supply from southern Chile is blocked by the Juan Fernández Ridge, and little sediment is supplied from the super-arid

Atacama Desert onshore in north Chile. Sediment cover on the oceanic crust and in the trench offshore northern Chile is therefore restricted to small, local basin, and much of the seafloor is bare (Ma et al., 2022; Sallares and Ranero, 2005; von Huene and Ranero, 2003). The region of northern Chile between 18 ° and 23 °S is one of the most recognized seismic gaps in the world, with no rupture having occurred from 1877 to 2014 (Chlieh et al., 2004). The 2014 Iquique interplate thrust earthquake (Fig. 4.1, red star) ruptured the region between 19.5 ° and 21 °S, closing about one-third of the 1877 seismic gap (Hayes et al., 2014; Lay et al., 2014; Petersen, 2021; Ruiz et al., 2014; Schurr et al., 2014).

As a result of plate bending, normal faults are prevalent on the oceanic crust offshore Northern Chile (Geersen et al., 2018; Leon-Rios et al., 2016). The bending of the incoming plate induces stress on the outer rise, which may reactivate pre-existing features in the oceanic crust (Geersen et al., 2018; Shillington et al., 2015), affect the distribution of outer rise earthquakes (Christensen and Ruff, 1988; Jiao et al., 2000; Lefeldt et al., 2009; Leon-Rios et al., 2016; Ranero et al., 2005), generate faults cutting deep into the upper oceanic lithosphere (Grevemeyer et al., 2005; Ranero et al., 2003) and thus hydrate the oceanic crust and upper lithospheric mantle (Myers et al., 2022; Ranero et al., 2003, 2005). Multichannel seismic and bathymetric data have revealed prevalent bending-related faults in many subduction zones, including the Tonga Trench (Lonsdale, 1986), the Chile Trench (Ranero et al., 2005), and the Middle America Trench (Grevemeyer et al., 2005). On the Chile outer rise, reactivated spreading-related faults (i.e. the abyssal hill fabric formed at the mid-ocean ridge) dominates north of ~20 °S (Fig. 4.1, red lines; Geersen et al., 2018, 2022), whereas new bend-faults cut through the oceanic plate south of ~20 °S (Fig. 4.1, white lines). The reactivated spreading fabric predominantly strikes in the N25 °W direction, while the new bend-faults are roughly trending in a N-S direction. The interplay of the two extensional fault systems partly modifies the morphology of the Iquique Ridge, adding complexity to the incoming crust (Geersen et al., 2018).

The SW-NE trending Iquique Ridge is a hotspot track that is manifested in a ~200 km wide swell with an average height of 500 - 1000 m (Fig. 4.1; Bello-González et al., 2018; Contreras-Reyes and Carrizo, 2011; Contreras-Reyes et al., 2021). It has a thickness of 15 km beneath the ridge axis as estimated from 3-D gravity modelling (Uieda and Barbosa, 2017) or 10-13 km as calculated from wide-angle seismic data (Myers et al., 2022). This ridge is dotted with variable morphologic features, including conical seamounts and elongated ridges (Contreras-Reyes and Carrizo, 2011; Contreras-Reyes et al., 2021; Geersen et al., 2018).

The subduction history of the Iquique Ridge is still debated. Starting off northern Peru >40 Ma, the collision of the Iquique Ridge and South America gradually migrated southward until its present position beneath the northern Chilean margin (Contreras-Reyes et al., 2021). Paleo-kinematic modelling (Bello-González et al., 2018) suggests

that the Iquique Ridge was formed by the Foundation Hotspot on or near the Pacific-Farallon/Nazca spreading center and that the easternmost component of the ridge is about 45 - 52 Ma (Fig. 4.1). Assuming a constant convergence rate of 66 - 67 mm/yr (Angermann et al., 1999), the Iquique Ridge should extend about 130 km east of the trench in the subsurface where the age of the Iquique seamounts immediately prior to subduction is 40 - 50 Mry old (Bello-González et al., 2018). Espurt et al. (2008) estimate the subduction length of the ridge at ~150 km. Rosenbaum et al. (2005), however, suggested that the Iquique Ridge represents the counterpart of the Austral Plateau located west of the East Pacific Rise, which would imply that it only subducts since around 2 Ma ago.

## 4.3 Data

Seismic signals were generated with a source of 6600 cubic inches (108.15 liters), provided by four strings of 10 air-guns each. Data were recorded with an 8 km long streamer towed by R/V Marcus G. Langseth. The source was towed at 9 m depth below the water surface, and the record length was 16 s. To avoid prominent spatial aliasing between neighboring shots resulting from the large shot interval, we interpolate the shot intervals four times from 125 m to 12.5 m. The data processing is described in detail in Ma et al. (2022).

An accurate subsurface *vp* model is essential for geological interpretation from seismic depth images. In this study, we updated the *vp* model to get the accurate depth based on residual move-out analysis of reflectors in common image point (CIP) gathers. Four times interpolation of the data volume led to long calculation times in the pre-stack time domain and the pre-stack depth domain, so we reconstructed the offsets of Common Midpoint (CMP) gathers with an increment of 100 m to optimize calculation time.

The estimation of the velocity model is achieved by an iterative seismic reflection tomography. This method is based on residual move-out analysis of reflectors in CIP gathers, and the update of the *vp* model is estimated by a ray-based tomography as described in detail by Xia et al. (2022). The most critical part is the depth error estimation to calculate the residual move-out for the reflector in the CIP gathers. After several iterations, an accurate subsurface *vp* field is produced and the depth of the reflectors is more precise.

The conventional method comprising manual picking based on coherence or semblance analysis is widely used for updating the *vp* model, under which the accurate subsurface model can be inferred corresponding to a high degree of matching (semblance). However, this method is highly time-consuming, human-biased, and not reproducible. Meanwhile, little valid information could be used for manual picking in sediment-starved subduction zones, where diffractions may mislead the manual picking. To overcome this, we applied

the warping method named plane-wave destruction filter (PWD) to iterate the *vp* field. The PWD is widely used to estimate the move-out dip slopes on seismic sections or gathers (Fomel, 2002; Sripanich et al., 2020; Xia et al., 2022). This method splits the data into spatial and temporal windows and assumes that the slopes are stationary within each window (Fomel, 2002; Xue et al., 2019). The normal-moveout (NMO) analysis is critical in updating the *vp* model. Using the PWD filter, automatic NMO correction of CMP gathers can directly and automatically be estimated from the gathers based on local slope (Fomel, 2002).

In Figure 4.2 we illustrate the *vp* model iteration for seismic line MC27. Firstly, CIP gathers are created to show the seismic reflections, and a dip filter is applied to the gathers to eliminate the extreme dipping events and migration noise. Then the dip field/coherency field of the migrated section is calculated, which determines the ray coverage propagation direction. Subsequently, we apply the PWD filter to estimate a depth error displacement field. Residual moveout (RMO) is calculated from the displacement to determine if the results are appropriate. If the RMO picks are flattened, we stop the *vp* iteration. Otherwise, we continue with the next iteration, in which step we apply tomography to update the velocity.

To document the change in the CIP-gather domain in detail, we compare selected subareas of initial and final CIP gathers of line MC27. A series of CIP gathers ranging from CIP 10592 to 11136 (Fig. 4.2b and d) are displayed with an increment of 32 (200 m). The reflectors in the CIP gathers of the initial iteration are significantly upward dipping, which means that the velocity is under-estimated. In contrast, compared to the initial data (Fig. 4.2b), the updated events in the CIP gather become optimally flattened (Fig. 4.2d). Comparing the initial PSDM and final PSDM profiles (Fig. 4.2a and c), we can find that the reflections around 5 km landward of the deformation front (Fig. 4.2a and c, yellow regions) are better resolved and sharper. After three times iterations, the reflections in the CIP gathers are mostly flattened.

## 4.4 Results

### 4.4.1 Structures along seismic line MC06

Seismic line MC06 crosses the deformation front around ~20.2 °S, trending in a SW-NE direction (Figs. 4.1 and 4.3). It images the marine forearc and the oceanic plate in the region of the 2014 Iquique earthquake, between the epicenter and the maximum slip area (Fig. 4.1). Along the lower continental slope (below 3000 m water depth), the seafloor dips at a uniform angle of ~7 ° (Fig. 4.3). It is largely devoid of any prominent morphological

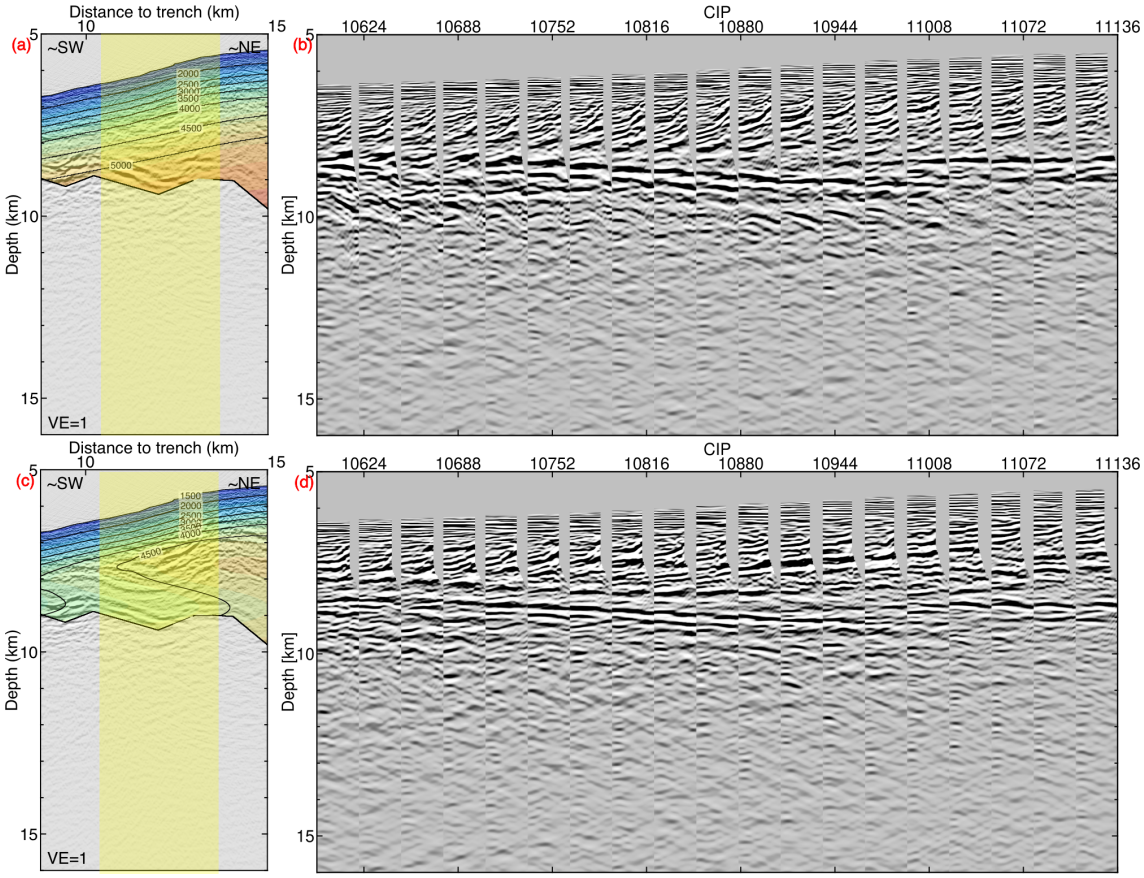


**Figure 4.2:** Example of the residual move-out analysis of common image point gathers (CIP). **(a)** PSDM of the initial iteration (without applying any gain functions); **(b)** CIP gathers from (a); **(c)** the PSDM after third iteration (without applying any gain functions); **(d)** CIP gathers from (c), with the same area as (b). Notice that after three iterations, the updated events in the CIP gathers become optimally flattened.

structures. Within the first ~6 km of the margin toe, a sequence of landward dipping reflections between the seafloor and the top of the subducting slab indicates the presence of a small frontal prism (Fig. 4.3b). The prism is likely constructed of slope debris and the marginal oceanic plate sediments that are available in the study area. Seaward of the deformation front, a 5 km wide trench basin is filled by up to 700 m of uniformly layered trench sediment, likely derived from the upper plate as the oceanic plate is devoid of any sedimentary cover. The oceanic plate around MC06 and farther towards the north is dominated by small offset bending related faults that reactivate the paleo-spreading fabric formed at the mid-oceanic ridge (Fig. 4.1, red lines; Geersen et al., 2022). The generated vertical offsets and the resulting lower plate topography is smaller compared to the region farther towards the south.

Upper plate strata at the lower continental slope, landward of the frontal prism, is rather discontinuous without prominent internal reflections below the basement. Landward of

distance-to-trench kilometer 13, an up to 1 km thick sequence of slope sediment is seismically imaged, covering the framework rock of the upper plate.

The homogenous dipping angle of the seafloor is mimicked by the top of the subducting oceanic plate, which dips at an angle of 9.5 ° and is continuously imaged down to a depth of about 14 km below sea level. Up to distance-to-trench km 40 the plate interface reflection is repeatedly disturbed by small perturbations, resulting in a segmented seismic signal underneath the lower slope and margin front. Some topographic variation of the top of the subducting crust is recognized most distinctly underneath the trench and frontal prism. However, the overall geometry of the plate interface shows little undulation.

### 4.4.2 Structures along seismic line MC27

Seismic line MC27 trends roughly parallel to line MC06 in a SW-NE direction. It crosses the deformation front around 20.55 °S (Figs. 4.1 and 4.4). While it is located only 50 km south of line MC06, the structure of both the upper (overriding) and lower (subducting) plate. The dip angle of the seafloor of the lower continental slope is similar to line MC06 (7 °).

A distinct frontal prism characterized by landward dipping reflections as recognized on line MC06 is not present at the margin toe. Here, the trench and lowermost slope are not overprinted by the typical horizontally layered trench sediment fill. Around 20.5 °S, the oceanic plate seaward of the deformation front shows an elevated (shallow) morphology (Fig. 4.1). Prominent fault scarps at the seafloor result from the generation of new bending faults trending in a north-south direction (Fig. 4.1, white lines). A series of NW-SE trending topographic heights within the trench depression may link to the presence of the Iquique Ridge. The pronounced basement topography of the oceanic crust can be traced underneath the margin toe, modulating the seafloor above.

Also, in contrast to the northern line MC06, no continuous section of slope sediment is found along MC27. Landward dipping reflections are recognized in the upper plate, but do not offset the seafloor. The seafloor along MC27 hosts a series of upward bulges, with the most prominent located between distance-to-trench kilometers 11 - 17. The upward bulge corresponds to the NW-SE striking anticlines described by Geersen et al. (2018). The seismic image now shows that not only the seafloor, but also the underlying strata of the upper plate bulges upward. Interestingly, the anticlinal structure that involves the entire upper plate, develops above a topographic high on the lower subducting plate (distance-to-trench kilometers 12 - 16). The ~4 km wide topographic high is elevated up to 900 m from the surrounding top of the subducting plate. Further topographic highs on the subducting plate, however less pronounced, are found between distance-to-trench

kilometers 3 - 9, 9 - 12, 20 - 23, and less clearly imaged between 24 - 29. The average dip of 10.5 ° of the plate interface is steeper than on line MC06. The plate interface reflection underneath the lower slope is much more coherent on the southern line compared to MC06. On both profiles, the reflection strength diminishes approximately 30 km landward of the deformation front but may still be traced to 15 km depth on line MC27.

## 4.5 Discussion

Off Northern Chile, the subducting Iquique Ridge has been suggested to shape the structure of the subduction zone as well as the physical state and seismic behavior of the plate boundary (Bello-González et al., 2018; Contreras-Reyes and Carrizo, 2011; Geersen et al.,

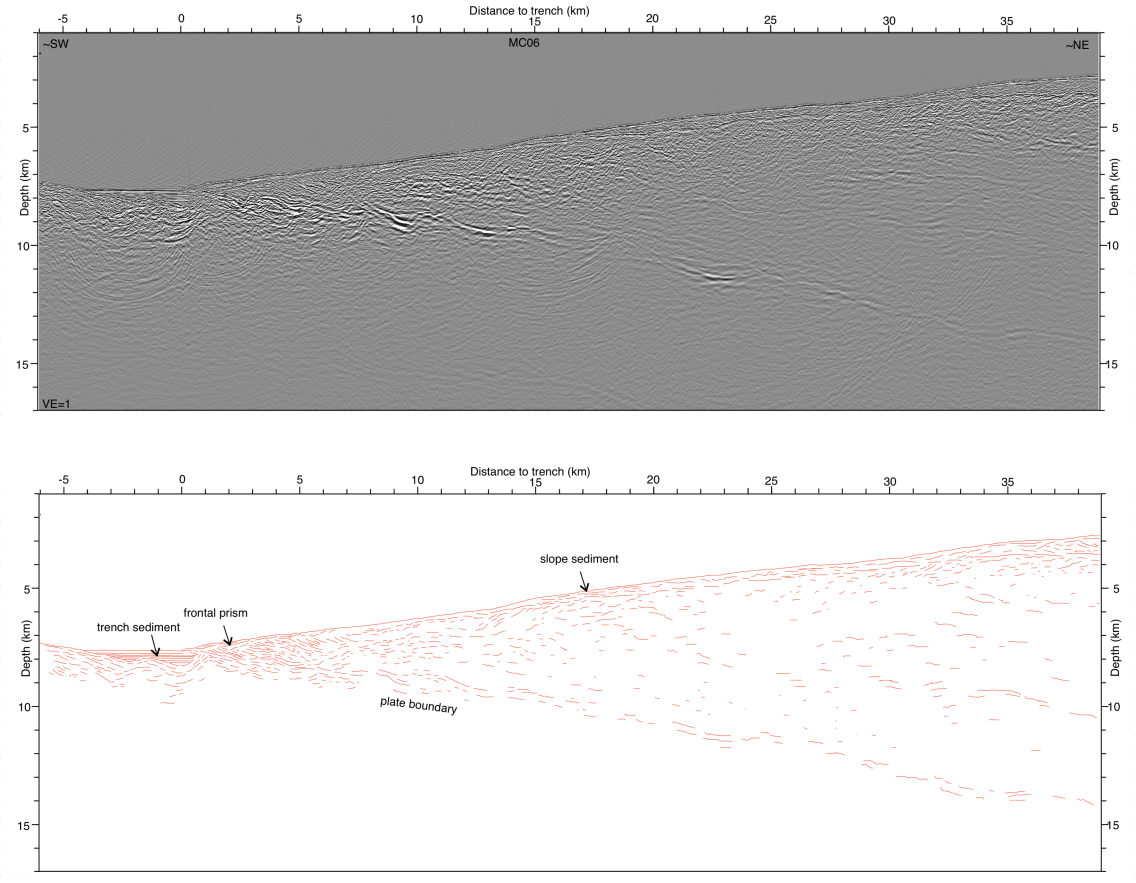


**Figure 4.3:** (a) Pre-stack depth migrated seismic data along northern profile MC06 without vertical exaggeration. Location shown in Fig. 4.1. A small frontal prism is observed landward of the deformation front (distance to trench km 0 - 6) and the slope sediment apron thickens landwards. The overall smooth geometry of the plate interface is breached by small-scale undulations underneath the trench and frontal prism. (b) line drawing of seismic line MC06.

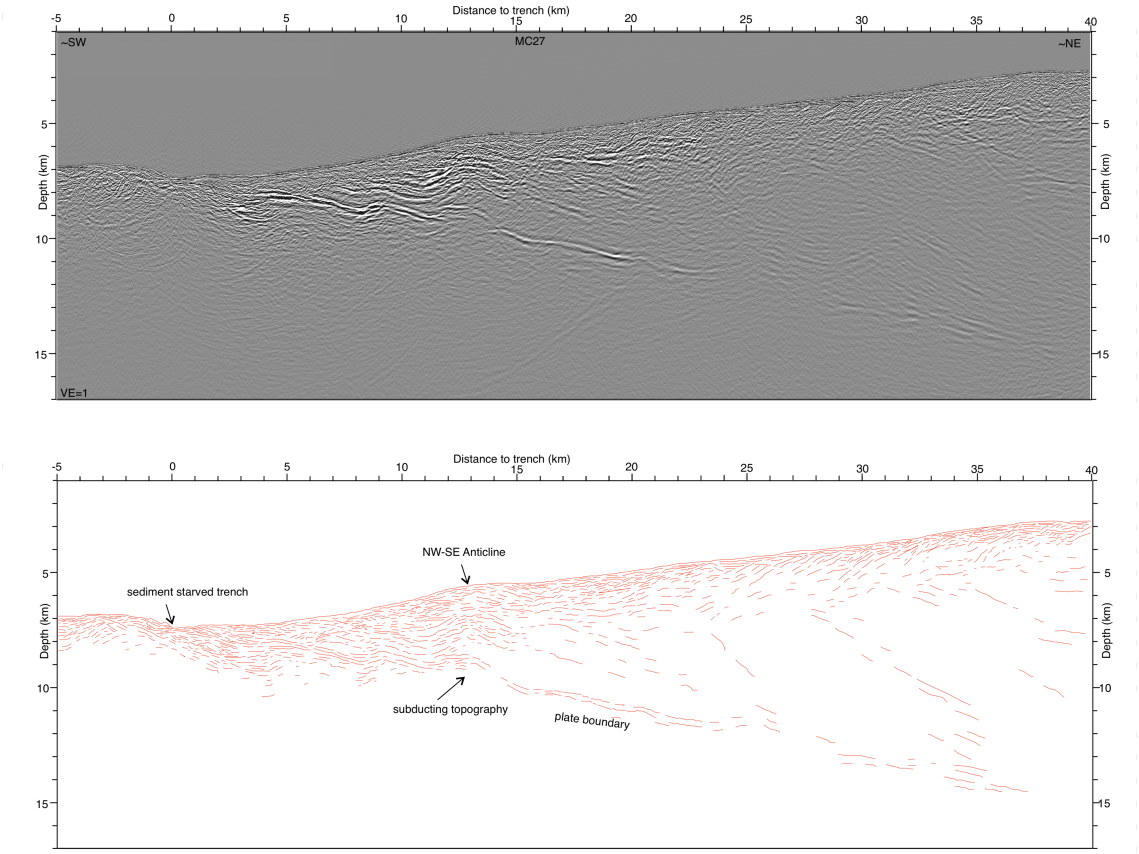


**Figure 4.4:** (a) Pre-stack depth migrated seismic data along southern profile MC27 without vertical exaggeration. Location shown in Fig. 4.1. In contrast to the northern profile, a trench sediment fill is not observed along this line and a distinct frontal prism is poorly developed. The plate interface is characterized by pronounced oceanic basement topography (e.g. around distance to trench km 12 - 16), modulating the upper plate and seafloor. (b) line drawing of seismic line MC27.

2018; Myers et al., 2022). The non-subducted part of the ridge is a broad swell of complex and heterogeneous structure and variable width and crustal thickness, including apparent discontinuities and changes in trend as it approaches the Arica Bend. Moreover, this part of the Nazca plate comprises many seamounts in a variety of clusters and alignments whose relationship to the Iquique ridge swell is unclear. The regional consequences of Iquique Ridge subduction are therefore still debated with large uncertainties regarding the extent of the affected area.

Along the outer trench wall, the bending of the oceanic plate into the subduction zone is accommodated across bending-related normal faults. These faults break the pre-existing relief of the oceanic plate and lead to the formation of hundreds of meter-high fault scarps at the seafloor (Fig. 4.1). Off Northern Chile around 20 °S, the trench starts to rotate towards the NW, forming the Arica Bend. In our study area, this leads to the co-existence

of N-S striking new bend faults and reactivated, spreading-related faults which strike in NW-SE direction, parallel to the magnetic fabric of the ocean floor (Fig. 4.1, red and white lines). As all fault types induce comparable vertical displacements (Geersen et al., 2022), the different strike directions around 20.55 °S, where seismic line MC27 is located, result in the breaking of the oceanic plate seafloor into relatively small pieces of less than 10 km horizontally and a few hundred meters in height (Fig. 4.1). This obliquely trending, broken, and faulted topography makes it difficult to separate the trace of the Iquique Ridge as a continuous morphologic feature in the trench axis from the swell induced by plate bending.

On a regional scale, the seafloor of the oceanic plate seaward of the trench in the region of line MC27 is shallower compared to the seafloor farther towards the north. Along line MC27, the elevated topography continues into the subduction zone, forming a series of topographic highs along the top of the subducting plate (distance-to-trench kilometers 3 - 9, 9 - 12, 20 - 23, 24 - 29). In contrast, the oceanic plate seafloor around line MC06 is smoother both seaward of the trench and beneath the outer wedge. It neither seems to carry significantly elevated topography, nor do we observe any topographic highs along the top of the subducting slab (Fig. 4.3). Combining the multibeam bathymetric map with the two seismic images, we conclude that ridge related topography, which may include the up to 13 km thick crust described by Contreras-Reyes et al. (2021) and Myers et al. (2022), is currently subducting south of 20.5 °S. Projecting the results of (Myers et al., 2022) to the latitude of MC27 requires that the axis of thickest crust locally has an approximately north-south trend or that it is broken into multiple segments in this region. Topographic and gravity data suggest the latter (Myers et al., 2022; Tassara et al., 2007).

Upper plate deformation induced by the subducting Iquique Ridge is manifold. While a small frontal prism has developed in the northern study area (around line MC06), no similar prism is imaged between 20.5 °S - 21 °S (line MC27). One explanation for the lack of a prism in the south is enhanced frontal subduction erosion induced by the collision of the subducting Iquique Ridge, similar to other margins where seamounts collide with the marine forearc and are subducted (Ballance et al., 1989; Lallemand et al., 1989; Lallemand and Lepichon, 1987; Laursen et al., 2002; Marcaillou et al., 2016). A second, related, explanation is that seismic lines MC06 and MC27 reflect different stages in a cycle of subduction of excess topography that trends oblique to the trench.

Seismic line MC27 further shows that the NW-SE trending anticlines at the lower slope described by Geersen et al. (2018) genetically link to the topographic highs along the plate boundary. Landward of the deformation front between kilometers 11 - 17, a prominent upward bulge seen on MC27 (Fig. 4.4) correlates with an anticline on the seafloor (Fig. 4.1). The upward bulge locates above a subducted topographic high which is ~4 km wide and ~900 m high. The apparent continuity of NW-SE trending anticlines at the lower slope

described by Geersen et al. (2018) with structures seaward of the trench, and the direct correlation of plate boundary topography with one of these anticlines on MC27, suggest that subducting topography alters the spatial and temporal pattern of accretion and deformation of the outermost wedge. These two mechanisms are not mutually exclusive, and additional seismic imaging should help to separate the relative importance of these two processes along this portion of the margin as well as clarify the roll that subduction of individual seamounts plays on modifying upper plate deformation in this complex region (Geersen et al., 2015; Storch et al., 2021, 2022).

The subducting Iquique Ridge in our study area between 20.5 °S-21 °S correlates to a region of low interseismic coupling along the lowermost continental slope (Fig. 4.5; Geersen et al., 2018, 2022). Coupling in such far offshore regions is generally not well resolved (Métois et al., 2016). However, if robust, the low coupling across the shallow most (most up-dip) plate-boundary may result from fracturing and faulting induced by the subducting Iquique Ridge (Wang and Bilek, 2011). For comparison, the seismic line MC06 images a smoother plate interface (Fig. 4.3), indicating less deformation of the outer wedge in the north of ~20.5 °S. In this region, the model indicates higher coupling than in the south.

## 4.6 Conclusion

To investigate the current location of the subducting Iquique Ridge under the marine forearc and to evaluate its impact on plate boundary structure and upper plate deformation, we analyzed two seismic reflection lines from the North Chilean marine forearc. Along the northern line MC06, which crosses the deformation front around 20.2 °S, we document a relatively straight dipping lower plate, sediments along the offshore forearc slope, and a small frontal prism. In contrast, seismic line MC27 located about 50 km towards the south, does not host significant slope sediments or a frontal prism. Instead, this line shows elevated topographic features on the subducting lower plate, that we interpret to represent the combined effect of the subducting Iquique Ridge and the complex horst and graben structure of the incoming plate. The subducting ridge causes an upward bulging of the entire upper plate up to the seafloor. Variations in interseismic coupling across the subducting ridge suggest that the excess topography may impact on the structure and physical state of the plate boundary, although this interrelation needs further investigation.

## Acknowledgments

B.M. acknowledges funding from the China Scholarship Council (grant 201706400073) and from GEOMAR Helmholtz Centre for Ocean Research Kiel. This work would not have

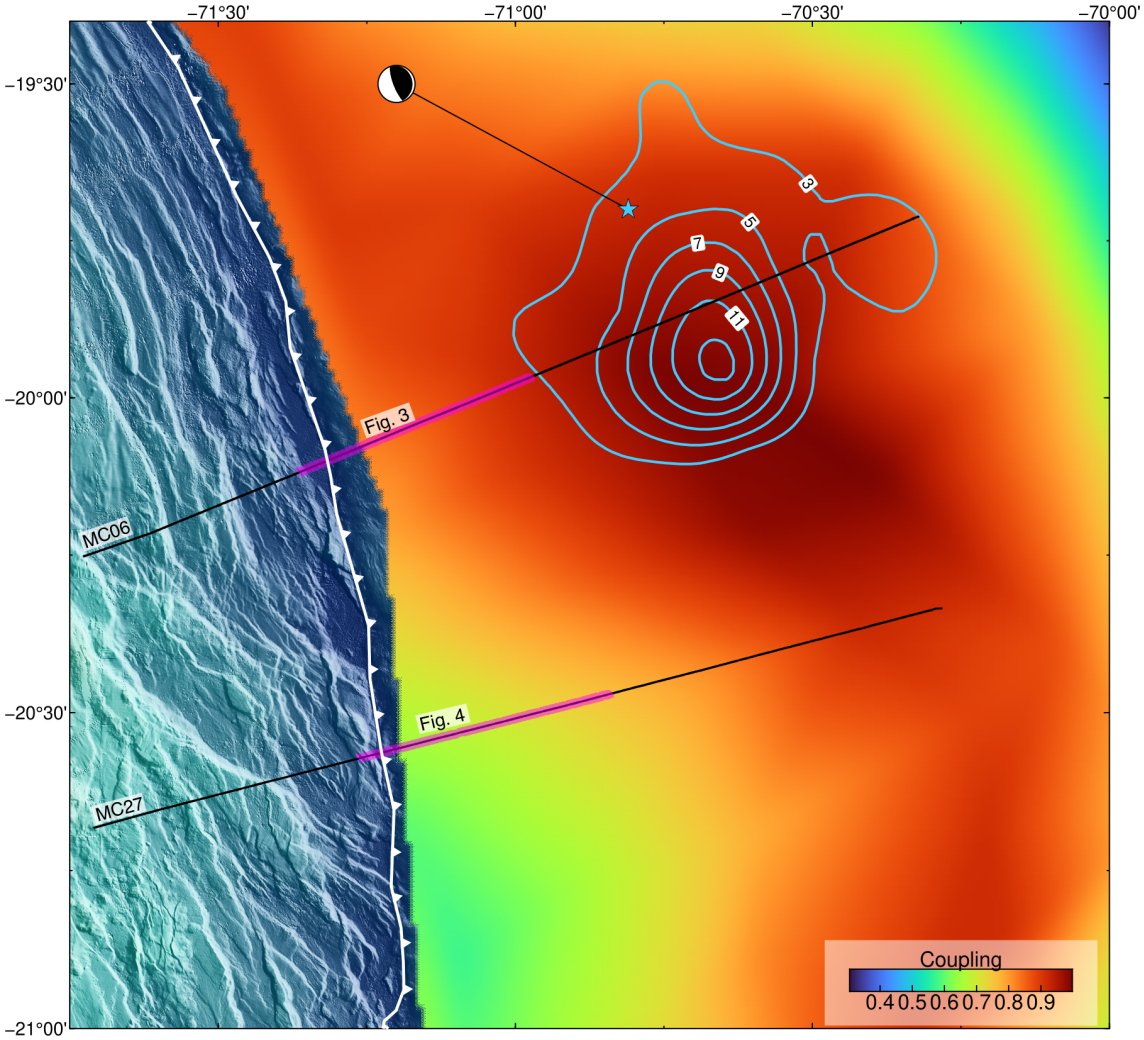


**Figure 4.5:** Interseismic coupling model from Schurr et al. (2020) around the 2014 Iquique rupture zone. Low coupling along the shallow megathrust south of ~20.5 °S occurs where seismic line MC27 images significant basement topography on the plate interface, compared to the high coupling north of ~20.5 °S where seismic line MC06 images a smooth plate interface. The hypocenter (star) and slip contours (in meters) of the 2014 Iquique $M_w$ 8.1 mainshock are from Duputel et al. (2015).

been possible without the acquisition of the MCS data and bathymetric data during cruise MGL1610 of the *R/V Marcus G. Langseth* in 2016 (NSF grant OCE-1459368 to Oregon State University). Additional bathymetry data were acquired during *R/V SONNE* cruise SO244 in 2015 (BMBF grant 03G0244A to GEOMAR). E.C.R. acknowledges the support of the ANID/FONDECYT grant 1210101.

## Author contributions

B.M. processed the seismic data with the support of D.K. B.M., J.G. and H.K. wrote the initial draft of the paper, which was critically revised by all co-authors. M.R., A.T., E.C.R. participated in cruise MGL1610 of *R/V Marcus G. Langseth*. M.R., Y.X. and D.L. contributed to the discussion of the seismic data.

## Competing interests

The authors declare no competing interests.

## References

Angermann, D., Klotz, J., & Reigber, C. (1999). Space-geodetic estimation of the nazca-south america euler vector. *Earth and Planetary Science Letters*, *171*(3), 329–334, https://doi.org/10.1016/S0012-821x(99)00173-9.

Ballance, P. F., Scholl, D. W., Vallier, T. L., Stevenson, A. J., Ryan, H., & Herzer, R. H. (1989). Subduction of a late cretaceous seamount of the louisville ridge at the tonga trench: A model of normal and accelerated tectonic erosion. *Tectonics*, *8*(5), 953–962, https://doi.org/10.1029/TC008i005p00953.

Bello-González, J. P., Contreras-Reyes, E., & Arriagada, C. (2018). Predicted path for hotspot tracks off south america since paleocene times: Tectonic implications of ridge-trench collision along the andean margin. *Gondwana Research*, *64*(september), 216–234, https://doi.org/10.1016/j.gr.2018.07.008.

Chlieh, M., de Chabalier, J. B., Ruegg, J. C., Armijo, R., Dmowska, R., Campos, J., & Feigl, K. L. (2004). Crustal deformation and fault slip during the seismic cycle in the north chile subduction zone, from gps and insar observations. *Geophysical Journal International*, *158*(2), 695–711, https://doi.org/10.1111/j.1365-246X.2004.02326.x.

Christensen, D. H. & Ruff, L. J. (1988). Seismic coupling and outer rise earthquakes. *Journal of Geophysical Research: Solid Earth*, *93*(B11), 13421–13444, https://doi.org/10.1029/JB093iB11p13421.

Contreras-Reyes, E. & Carrizo, D. (2011). Control of high oceanic features and subduction channel on earthquake ruptures along the chile-peru subduction zone. *Physics of the Earth and Planetary Interiors*, *186*(1-2), 49–58, https://doi.org/10.1016/j.pepi.2011.03.002.

Contreras-Reyes, E., Munoz-Linford, P., Cortes-Rivas, V., Bello-Gonzalez, J. P., Ruiz, J. A., & Krabbenhoeft, A. (2019). Structure of the collision zone between the nazca ridge and the peruvian convergent margin: Geodynamic and seismotectonic implications. *Tectonics*, *38*(9), 3416–3435, https://doi.org/10.1029/2019tc005637.

Contreras-Reyes, E., Obando-Orrego, S., Geersen, J., & Bello-Gonzalez, J. P. (2021). Density structure, flexure, and tectonics of the iquique ridge, northern chile. *Journal of South American Earth Sciences*, *111*, https://doi.org/ARTN 103423 10.1016/j.jsames.2021.103423.

Contreras-Reyes, E., Ruiz, J. A., Becerra, J., Kopp, H., Reichert, C., Maksymowicz, A., & Arriagada, C. (2015). Structure and tectonics of the central chilean margin (31 degrees-33 degrees s): implications for subduction erosion and shallow crustal seismicity. *Geophysical Journal International*, *203*(2), 776–791, https://doi.org/10.1093/gji/ggv309.

Dominguez, S., Lallemand, S. E., Malavieille, J., & von Huene, R. (1998). Upper plate deformation associated with seamount subduction. *Tectonophysics*, *293*(3-4), 207–224, https://doi.org/10.1016/S0040-1951(98)00086-9.

Duputel, Z., Jiang, J., Jolivet, R., Simons, M., Rivera, L., Ampuero, J. P., Riel, B., Owen, S. E., Moore, A. W., Samsonov, S. V., Culaciati, F. O., & Minson, S. E. (2015). The iquique earthquake sequence of april 2014: Bayesian modeling accounting for prediction uncertainty. *Geophysical Research Letters*, *42*(19), 7949–7957, https://doi.org/10.1002/2015gl065402.

Espurt, N., Funiciello, F., Martinod, J., Guillaume, B., Regard, V., Faccenna, C., & Brusset, S. (2008). Flat subduction dynamics and deformation of the south american plate: Insights from analog modeling. *Tectonics*, *27*(3), https://doi.org/Artn Tc3011 10.1029/2007tc002175.

Fomel, S. (2002). Applications of plane-wave destruction filters. *Geophysics*, *67*(6), 1946–1960, https://doi.org/10.1190/1.1527095.

Geersen, J., Ranero, C. R., Barckhausen, U., & Reichert, C. (2015). Subducting seamounts control interplate coupling and seismic rupture in the 2014 iquique earthquake area. *Nat Commun*, *6*, 8267, https://doi.org/10.1038/ncomms9267.

Geersen, J., Ranero, C. R., Klaucke, I., Behrmann, J. H., Kopp, H., Trehu, A. M., Contreras-Reyes, E., Barckhausen, U., & Reichert, C. (2018). Active tectonics of the north chilean marine forearc and adjacent oceanic nazca plate. *Tectonics*, *37*(11), 4194–4211, https://doi.org/10.1029/2018tc005087.

Geersen, J., Sippl, C., & Harmon, N. (2022). Impact of bending-related faulting and oceanic-plate topography on slab hydration and intermediate-depth seismicity. *Geosphere*, *18*(2), 562–584, https://doi.org/10.1130/ges02367.1.

Grevemeyer, I., Kaul, N., Diaz-Naveas, J. L., Villinger, H. W., Ranero, C. R., & Reichert, C. (2005). Heat flow and bending-related faulting at subduction trenches: Case studies offshore of nicaragua and central chile. *Earth and Planetary Science Letters*, *236*(1-2), 238–248, https://doi.org/10.1016/j.epsl.2005.04.048.

Hampel, A., Kukowski, N., Bialas, J., Huebscher, C., & Heinbockel, R. (2004). Ridge subduction at an erosive margin: The collision zone of the nazca ridge in southern peru. *Journal of Geophysical Research-Solid Earth*, *109*(B2), https://doi.org/10.1029/2003jb002593.

Hayes, G. P., Herman, M. W., Barnhart, W. D., Furlong, K. P., Riquelme, S., Benz, H. M., Bergman, E., Barrientos, S., Earle, P. S., & Samsonov, S. (2014). Continuing megathrust earthquake potential in chile after the 2014 iquique earthquake. *Nature*, *512*(7514), 295–8, https://doi.org/10.1038/nature13677.

Jiao, W. J., Silver, P. G., Fei, Y. W., & Prewitt, C. T. (2000). Do intermediate- and deep-focus earthquakes occur on preexisting weak zones? an examination of the tonga subduction zone. *Journal of Geophysical Research-Solid Earth*, *105*(B12), 28125–28138, https://doi.org/10.1029/2000jb900314.

Kopp, H., Flueh, E. R., Papenberg, C., & Klaeschen, D. (2004). Seismic investigations of the o'higgins seamount group and juan fernandez ridge: Aseismic ridge emplacement and lithosphere hydration. *Tectonics*, *23*(2), 1–21, https://doi.org/10.1029/2003tc001590.

Lallemand, S., Culotta, R., & Von Huene, R. (1989). Subduction of the daiichi kashima seamount in the japan trench. *Tectonophysics*, *160*(1-4), 231–247.

Lallemand, S. & Lepichon, X. (1987). Coulomb wedge model applied to the subduction of seamounts in the japan trench. *Geology*, *15*(11), 1065–1069, https://doi.org/10.1130/0091-7613(1987)15<1065:Cwmatt>2.0.Co;2.

Lallemand, S. E., Malavieille, J., & Calassou, S. (1992). Effects of oceanic ridge subduction on accretionary wedges - experimental modeling and marine observations. *Tectonics*, *11*(6), 1301–1313, https://doi.org/10.1029/92tc00637.

Laursen, J., Scholl, D. W., & von Huene, R. (2002). Neotectonic deformation of the central chile margin: Deepwater forearc basin formation in response to hot spot ridge and seamount subduction. *Tectonics*, *21*(5), 2–1, https://doi.org/10.1029/2001tc901023.

Lay, T., Yue, H., Brodsky, E. E., & An, C. (2014). The 1 april 2014 iquique, chile, mw 8.1 earthquake rupture sequence. *Geophysical Research Letters*, *7*(April), 1–8, https://doi.org/10.1002/2014GL060238.Received.

Lefeldt, M., Grevemeyer, I., Goßler, J., & Bialas, J. (2009). Intraplate seismicity and related mantle hydration at the nicaraguan trench outer rise. *Geophysical Journal International*, *178*(2), 742–752, https://doi.org/10.1111/j.1365-246X.2009.04167.x.

Leon-Rios, S., Ruiz, S., Maksymowicz, A., Leyton, F., Fuenzalida, A., & Madariaga, R. (2016). Diversity of the 2014 iquique's foreshocks and aftershocks: clues about the complex rupture process of a mw 8.1 earthquake. *Journal of Seismology*, *20*(4), 1059–1073, https://doi.org/10.1007/s10950-016-9568-6.

Lonsdale, P. (1986). A multibeam reconnaissance of the tonga trench axis and its intersection with the louisville guyot chain. *Marine Geophysical Researches*, *8*(4), 295–327, https://doi.org/Doi 10.1007/Bf02084016.

Ma, B., Geersen, J., Lange, D., Klaeschen, D., Grevemeyer, I., Contreras-Reyes, E., Petersen, F., Riedel, M., Xia, Y., Trehu, A. M., & Kopp, H. (2022). Megathrust reflectivity reveals the updip limit of the 2014 iquique earthquake rupture. *Nat Commun*, *13*(1), 3969, https://doi.org/10.1038/s41467-022-31448-4.

Maksymowicz, A., Ruiz, J., Vera, E., Contreras-Reyes, E., Ruiz, S., Arraigada, C., Bonvalot, S., & Bascunan, S. (2018). Heterogeneous structure of the northern chile marine forearc and its implications for megathrust earthquakes. *Geophysical Journal International*, *215*(2), 1080–1097, https://doi.org/10.1093/gji/ggy325.

Marcaillou, B., Collot, J. Y., Ribodetti, A., d'Acremont, E., Mahamat, A. A., & Alvarado, A. (2016). Seamount subduction at the north-ecuadorian convergent margin: Effects on structures, inter-seismic coupling and seismogenesis. *Earth and Planetary Science Letters*, *433*, 146–158, https://doi.org/10.1016/j.epsl.2015.10.043.

Martinod, J., Guillaume, B., Espurt, N., Faccenna, C., Funiciello, F., & Regard, V. (2013). Effect of aseismic ridge subduction on slab geometry and overriding plate deformation: Insights from analogue modeling. *Tectonophysics*, *588*, 39–55, https://doi.org/10.1016/j.tecto.2012.12.010.

McCann, W. R. & Habermann, R. E. (1989). *Morphologic and geologic effects of the subduction of bathymetric highs*, (pp. 41–69). Springer.

Morell, K. D. (2016). Seamount, ridge, and transform subduction in southern central america. *Tectonics*, *35*(2), 357–385, https://doi.org/10.1002/2015tc003950.

Myers, E. K., Roland, E. C., Trehu, A. M., Davenport, K., & Grp, P. (2022). Crustal structure of the incoming iquique ridge offshore northern chile. *Journal of Geophysical Research-Solid Earth*, *127*(2), https://doi.org/10.1029/2021JB023169.

Métois, M., Vigny, C., & Socquet, A. (2016). Interseismic coupling, megathrust earthquakes and seismic swarms along the chilean subduction zone (38°–18°s). *Pure and Applied Geophysics*, *173*(5), 1431–1449, https://doi.org/10.1007/s00024-016-1280-5.

Müller, R. D., Sdrolias, M., Gaina, C., & Roest, W. R. (2008). Age, spreading rates, and spreading asymmetry of the world's ocean crust. *Geochemistry, Geophysics, Geosystems*, *9*(4), https://doi.org/10.1029/2007gc001743.

Petersen, F. (2021). *Analysis of seismic and aseismic deformation using shoreline-crossing observations*. Thesis.

Pilger Jr, R. H. (1981). Plate reconstructions, aseismic ridges, and low-angle subduction beneath the andes. *Geological Society of America Bulletin*, *92*(7), 448–456.

Ranero, C. R., Morgan, J. P., McIntosh, K., & Reichert, C. (2003). Bending-related faulting and mantle serpentinization at the middle america trench. *Nature*, *425*(6956), 367–73, https://doi.org/10.1038/nature01961.

Ranero, C. R., Villasenor, A., Morgan, J. P., & Weinrebe, W. (2005). Relationship between bend-faulting at trenches and intermediate-depth seismicity. *Geochemistry Geophysics Geosystems*, *6*(12), https://doi.org/10.1029/2005gc000997.

Rosenbaum, G., Giles, D., Saxon, M., Betts, P. G., Weinberg, R. F., & Duboz, C. (2005). Subduction of the nazca ridge and the inca plateau: Insights into the formation of ore deposits in peru. *Earth and Planetary Science Letters*, *239*(1-2), 18–32, https://doi.org/10.1016/j.epsl.2005.08.003.

Ruiz, S., Metois, M., Fuenzalida, A., Ruiz, J., Leyton, F., Grandin, R., Vigny, C., Madariaga, R., & Campos, J. (2014). Intense foreshocks and a slow slip event preceded the 2014 iquique mw 8.1 earthquake. *Science*, *345*(6201), 1165–9, https://doi.org/10.1126/science.1256074.

Sallares, V. & Ranero, C. R. (2005). Structure and tectonics of the erosional convergent margin off antofagasta, north chile (23 degrees 30 ' s). *Journal of Geophysical Research-Solid Earth*, *110*(B6), https://doi.org/10.1029/2004jb003418.

Schurr, B., Asch, G., Hainzl, S., Bedford, J., Hoechner, A., Palo, M., Wang, R., Moreno, M., Bartsch, M., Zhang, Y., Oncken, O., Tilmann, F., Dahm, T., Victor, P., Barrientos, S., & Vilotte, J. P. (2014). Gradual unlocking of plate boundary controlled initiation of the 2014 iquique earthquake. *Nature*, *512*(7514), 299–302, https://doi.org/10.1038/nature13681.

Schurr, B., Moreno, M., Tréhu, A. M., Bedford, J., Kummerow, J., Li, S., & Oncken, O. (2020). Forming a mogi doughnut in the years prior to and immediately before the 2014 m8.1 iquique, northern chile, earthquake. *Geophysical Research Letters*, *47*(16), e2020GL088351, https://doi.org/10.1029/2020gl088351.

Shillington, D. J., Becel, A., Nedimovic, M. R., Kuehn, H., Webb, S. C., Abers, G. A., Keranen, K. M., Li, J. Y., Delescluse, M., & Mattei-Salicrup, G. A. (2015). Link between plate fabric, hydration and subduction zone seismicity in alaska. *Nature Geoscience*, *8*(12), 961–U98, https://doi.org/10.1038/Ngeo2586.

Sripanich, Y., Fomel, S., Trampert, J., Burnett, W., & Hess, T. (2020). Probabilistic moveout analysis by time warping. *Geophysics*, *85*(1), U1–U20, https://doi.org/10.1190/geo2018-0797.1.

Storch, I., Buske, S., Victor, P., & Oncken, O. (2021). Seismic images of the northern chilean subduction zone at 19 degrees 40 ' s, prior to the 2014 iquique earthquake. *Geophysical Journal International*, *225*(2), 1048–1061, https://doi.org/10.1093/gji/ggab035.

Storch, I., Buske, S., Victor, P., & Oncken, O. (2022). A topographic depression on the subducting nazca plate controls the april 1st 2014 m8. 1 iquique earthquake rupture in northern chile. *Tectonophysics*, (pp. 229684).

Tassara, A., Swain, C., Hackney, R., & Kirby, J. (2007). Elastic thickness structure of south america estimated using wavelets and satellite-derived gravity data. *Earth and Planetary Science Letters*, *253*(1-2), 17–36.

Tréhu, A., Vera, E., & Riedel, M. (2017). Pictures: Pisagua/iquique crustal tomography to understand the region of the earthquake source. *MGL1610 Cruise Report*.

Uieda, L. & Barbosa, V. C. (2017). Fast nonlinear gravity inversion in spherical coordinates with application to the south american moho. *Geophysical Journal International*, *208*(1), 162–176.

von Huene, R. & Ranero, C. R. (2003). Subduction erosion and basal friction along the sediment-starved convergent margin off antofagasta, chile. *Journal of Geophysical Research-Solid Earth*, *108*(B2), https://doi.org/10.1029/2001jb001569.

Wang, K. L. & Bilek, S. L. (2011). Do subducting seamounts generate or stop large earthquakes? *Geology*, *39*(9), 819–822, https://doi.org/10.1130/G31856.1.

Xia, Y. Y., Geersen, J., Klaeschen, D., Ma, B., Lange, D., Riedel, M., Schnabel, M., & Kopp, H. (2021). Marine forearc structure of eastern java and its role in the 1994 java tsunami earthquake. *Solid Earth*, *12*(11), 2467–2477, https://doi.org/10.5194/se-12-2467-2021.

Xia, Y. Y., Klaeschen, D., Kopp, H., & Schnabel, M. (2022). Reflection tomography by depth warping: a case study across the java trench. *Solid Earth*, *13*(2), 367–392, https://doi.org/10.5194/se-13-367-2022.

Xue, Z., Zhang, H., Zhao, Y., & Fomel, S. (2019). Pattern-guided dip estimation with plane-wave destruction filters. *Geophysical Prospecting*, *67*(7), 1798–1810.

Yamazaki, T. & Okamura, Y. (1989). Subducting seamounts and deformation of overriding forearc wedges around japan. *Tectonophysics*, *160*(1-4), 207–229, https://doi.org/10.1016/0040-1951(89)90392-2.

Zeumann, S. & Hampel, A. (2016). Three-dimensional finite-element models on the deformation of forearcs caused by aseismic ridge subduction: The role of ridge shape, friction coefficient of the plate interface and mechanical properties of the forearc. *Tectonophysics*, *684*(SI), 76–91, https://doi.org/10.1016/j.tecto.2015.12.022.

# 5 Relationship between subduction erosion and the up-dip limit of the 2014 Mw 8.1 Iquique earthquake

Florian Petersen[1], Dietrich Lange[1], **Bo Ma**[1], Ingo Grevemeyer[1], Jacob Geersen[2], Dirk Klaeschen[2], Eduardo Contreras-Reyes[3], Sergio Barrientos[4], Anne M. Tréhu[5], Emilio Vera[3] and Heidrun Kopp[1,2]

1) GEOMAR Helmholtz Centre for Ocean Research Kiel, Kiel, Germany.

2) Institute of Geosciences, Kiel University, Kiel, Germany.

3) Departamento de Geofísica, Facultad de Ciencias Físicas y Matemáticas, Universidad de Chile, Santiago, Chile.

4) Centro Sismológico Nacional, Facultad de Ciencias Físicas y Matemáticas, Universidad de Chile, Santiago, Chile.

5) Oregon State University, College of Earth, Ocean, and Atmospheric Sciences, Corvallis, USA

Published in **Geophysical Research Letters**, May 2021.

DOI: 10.1029/2020GL092207

**Key Points**

- We investigate structure and seismicity at the up-dip end of the 2014 Iquique earthquake rupture using amphibious seismic data.
- Seismicity up-dip of the 2014 Iquique earthquake occurs over a broad range likely interpreted to be related to the basal erosion processes.
- Coseismic stress changes and aftershocks activate extensional faulting of the upper plate and subduction erosion.

## Abstract

The aftershock distribution of the 2014 $M_w$ 8.1 Iquique earthquake offshore northern Chile, identified from a long-term deployment of ocean bottom seismometers installed eight months after the mainshock, in conjunction with seismic reflection imaging, provides insights into the processes regulating the up-dip limit of coseismic rupture propagation. Aftershocks up-dip of the mainshock hypocenter frequently occur in the upper plate and are associated with normal faults identified from seismic reflection data. We propose that aftershock seismicity near the plate boundary documents subduction erosion that removes mass from the base of the wedge and results in normal faulting in the upper plate. The combination of very little or no sediment accretion and subduction erosion over millions of years has resulted in a very weak and aseismic frontal wedge. Our observations thus link the shallow subduction zone seismicity to subduction erosion processes that control the evolution of the overriding plate.

## Plain Language Summary

To better understand the controls on shallow seismicity and subduction erosion following large subduction earthquakes, we use marine recordings of the $M_w$ 8.1 2014 Iquique earthquake aftershocks and long-offset multi-channel seismic data. By comparing the aftershock locations and seismic imaging, we observe that most aftershocks occurred in the upper continental plate and abruptly stopped in the frontal forearc. The amplitude characteristics of upper-crust reflections indicate a fractured and fluid-filled outer forearc, which is associated with the absence of aftershocks. Large-scale faulting, as evidenced by disrupted reflections in the seismic image, can be correlated to upper plate seismicity. We propose that the aftershocks up-dip of the main earthquake area reflect active subduction erosion processes.

## 5.1 Introduction

The largest earthquakes on the globe occur along convergent plate margins, rupturing the boundary between upper overriding and lower subducting plates. For most subduction zones, the precise location of the far offshore located up-dip limit of coseismic slip and its controlling parameters remain poorly resolved, despite being of fundamental importance for earthquake hazard assessment. Controls on the up-dip limit were suggested to be related to forearc structure and morphology (Wang and Hu, 2006; Tilmann et al., 2010), metamorphic processes (Moore and Saffer, 2001), or thermal properties (Oleskevich et al., 1999; Moore and Saffer, 2001). Earthquake ruptures that extend into the shallow frontal subduction domain cause larger seafloor displacement and hence trigger potentially large tsunamis as evidenced by a historical slip-to-trench megathrust event offshore Costa Rica (Vannucchi et al., 2017) or exemplified by the 2011 $M_w$ 9.0 Tohoku-Oki earthquake and associated tsunami (Simons et al., 2011; Kodaira et al., 2012). Knowledge of the seismogenic up-dip limit and its controlling factors are thus essential for assessing subduction zone hazards. Material transfer at subduction zones is primarily governed by either frontal or basal accretion of oceanic sediments or by tectonic erosion at the front and base of the upper plate (hereafter referred to as subduction erosion).

A slight majority of subduction zones worldwide are of erosive nature (Scholl and von Huene, 2007; Straub et al., 2020). It has been suggested that subduction erosion and the occurrence of seismicity along subduction zone megathrusts and in the upper overriding plates are inherently related (Wang et al., 2010). Long-term permanent subsidence of the forearc (von Huene and Lallemand, 1990) and the landward migration of the trench and the volcanic arc (Rutland, 1971) have been linked to subduction erosion (Clift and Vannucchi, 2004). Two modes of subduction erosion have been identified: (1) frontal erosion as commonly caused by the underthrusting of rough seafloor topography, like bending related horst-and-grabens or seamounts colliding with the lower slope (Ranero and von Huene, 2000; Sallarès and Ranero, 2005) and (2) basal erosion by the continuous removal of material from the base of the overriding plate (von Huene et al., 2004). The latter directly impacts the structural development of the plate boundary and might be essential to understand the up-dip limit of seismic rupture during megathrust earthquakes and the onset of seismicity at the seismogenic up-dip end (Byrne et al., 1988; Wang et al., 2010). The offshore location of the shallow subduction interface complicates the recording of earthquake-related processes by geophysical data, causing a gap in our understanding of the structural configuration of the plate boundary, overriding plate and subducting plate. Hence, the slip-rate deficit (kinematic coupling ratio) and the detailed seismicity are not accurately resolved during the seismic cycle. However, the extent and termination of coseismic slip are frequently revealed through the spatial distribution of seismicity after

the mainshock, (Mendoza and Hartzell, 1988), therefore, the postseismic period offers the opportunity to study postseismic processes (Husen et al., 1999; Tilmann et al., 2010).

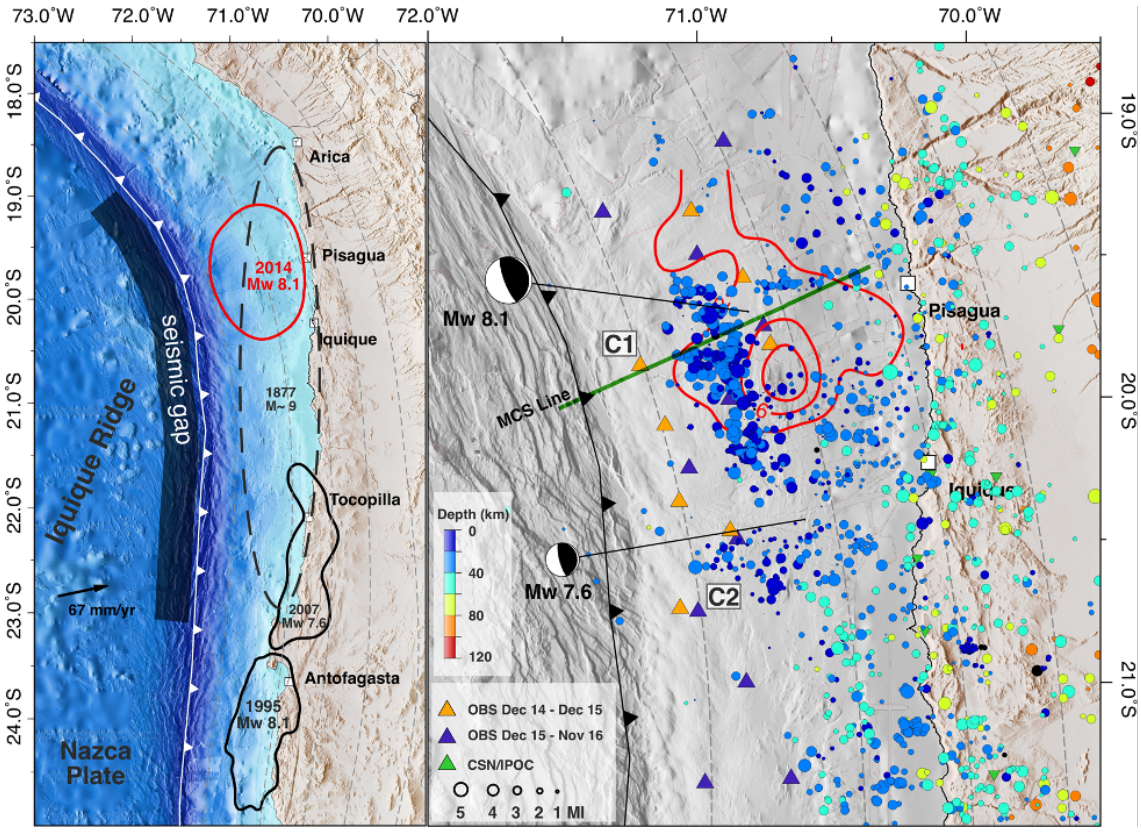


**Figure 5.1:** (a) Map of historical earthquakes along northern Chile. The 2014 Iquique earthquake is sketched in red by the 2 m slip contour line Duputel et al. (2015). The 1877 $M$ ~9 North Chilean earthquake is displayed as an dashed ellipse (Comte and Pardo, 1991), the rupture area of the M8.1 1995 Antofagasta (Chlieh et al., 2004) and the 2007 M7.7 Tocopilla earthquake (Schurr et al., 2012) are outlined by 0.5 m slip contours. Depths of the plate interface (Slab2; Hayes et al., 2018) are shown with dashed gray lines and 20 km depth intervals. Plate convergence rate is shown as a black arrow (Angermann et al., 1999). Bathymetry from Geersen et al. (2018a) combined with GEBCO, SRTM Topography from Farr et al. (2007). (b) Map of the aftershock hypocenter distribution (1,471 events) of the $M_w$ 8.1 2014 Iquique earthquake from 9th December, 2014, until 31$^{st}$ October 2016, recorded by Ocean Bottom Seismometers (OBS) and land stations from the CSN and IPOC networks. C1 marks the up-dip cluster of the aftershock seismicity and C2 the up-dip cluster of seismicity following the greatest aftershock with $M_w$ 7.6. The green line indicates the MC23 profile (Tréhu et al., 2017) shown in Figure 5.2a. gCMT solutions indicate the $M_w$ 8.1 2014 Iquique mainshock and the largest M7.6 aftershock. (c) Seismicity cross section of depth versus latitude.

The South American subduction zone off the coast of northern Chile is a convergent margin dominated by subduction erosion since Mesozoic times (Rutland, 1971; von Huene and Scholl, 1991). This is manifested in the landward migration of the volcanic arc and

pervasive extensional faulting of the terrestrial (Armijo and Thiele, 1990; Allmendinger and González, 2010) and marine forearc (von Huene et al., 1999; von Huene and Ranero, 2003; Geersen et al., 2018b). Further, erosional systems are characterized by the sediment-starved trenches, lacking accretionary prisms and vast amount of trench sediments (Clift and Vannucchi, 2004; Geersen et al., 2018a). The 2014 Iquique earthquake on 1st April broke a central segment between 19 °S and 21 °S of the north Chilean seismic gap, which previously ruptured in 1877 during a M~9 earthquake (Figure 5.1; Comte and Pardo, 1991). A long precursory phase preceded the 2014 mainshock (e.g., Bedford et al., 2015) and devolved into an intense foreshock series before the 2014 Iquique mainshock (Brodsky and Lay, 2014; Schurr et al., 2014; Yagi et al., 2014; Cesca et al., 2016; Herman et al., 2016; León-Ríos et al., 2016). The 2014 Iquique earthquake did not result in enough shallow rupture to trigger a significant tsunami in the Pacific Ocean (An et al., 2014; Lay et al., 2014).

To study the processes that govern the up-dip limit of seismic rupture in the northern Chilean subduction zone, we combine data from amphibious seismic observations from the postseismic phase of the 2014 Iquique earthquake with multi-channel seismic reflection data of the marine forearc acquired in 2016. We suggest that the up-dip limit of the 2014 Iquique earthquake activates subduction erosion at the up-dip limit of the seismogenic zone during the postseismic and possibly the coseismic phase, which leads to extensive faulting of the upper plate, thereby manifesting the location of the up-dip limit over many earthquake cycles.

## 5.2 Data and Methods

We installed two temporary passive seismic networks on the marine forearc. The first deployment was an array of 15 short period ocean bottom seismometers (OBS) eight months after the 1st April 2014 Iquique mainshock, using the Chilean Navy vessel *OVP Toro*. After one year, the seismic network was recovered and 14 OBS were redeployed during *R/V SONNE* cruise SO244/2 in December 2015 and subsequently with a denser station distribution to focus on the up-dip aftershock distribution (Figure 5.1)Furthermore, we used waveform data of the permanent seismic network of the Centro Seismológico Nacional (CSN, `www.sismologia.cl`) and the Integrated Plate Boundary Observatory Chile (IPOC, `www.ipoc-network.org`).

Earthquakes were detected with the scanloc module of SeisComP3 (GFZ and gempa GmbH, 2008) using a cluster search algorithm to associate phase detections to one or many potential earthquake sources. Source scanning was done with the local 1-D velocity model from Husen et al. (1999). Next, P-phases (Aldersons, 2004; Lange et al., 2012) and S-phases

were picked automatically (Diehl et al., 2009), however, automated phase picking on OBS data proved to be unsatisfactory on small magnitude events due to the elevated noise level on some waveform data. Therefore, we manually revised the P- and S-phase onsets of all offshore events.

We calculated a minimum 1D velocity model (Kissling et al., 1995; Husen et al., 1999) and a local 2D earthquake tomography for vp and vs across the South American margin at 20 °S from 71.5 °W to 69.4 °W using SIMUL2000 (Thurber, 1983, 1992). Subsequently, we estimated absolute locations based on the 2D velocity model with NonLinLoc (Lomax et al., 2000). The velocity model used was constructed from the 2D model transposing it across the whole study region by following the geometry of the trench. Relative hypocenter locations were estimated using a double-difference location scheme (Waldhuser and Ellsworth, 2000). After the final relocation, seismicity in the up-dip area forms distinct clusters compared to previous processing steps.

Finally, we calculated moment magnitudes (Ottemoller and Havskov, 2003) and local magnitudes (Hutton and Boore, 1987), followed by the calculation of focal mechanisms for 98 stronger events (Reasenberg et al., 1985). We used focal mechanisms from the Global Centroid Moment Tensor catalog (Dziewonski et al., 1981; Ekström et al., 2012) for the largest events as those overloaded our data loggers, in turn, causing problems in identifying first motion polarities. Additional details on the seismological data processing are given in the supporting information and Figures 5.4 - 5.15.

To provide additional structural context for the seismicity analysis, we use a multi-channel reflection seismic (MCS) line MC23 acquired during the *R/V Marcus Langseth* cruise MGL1610 in November 2016 (Tréhu et al., 2017). The along-dip MCS profile is processed up to pre-stack depth migration (Ma et al., 2020) and images the structure around the Iquique mainshock down to 35 km depth (Figure 5.2a). The MCS data were collected with an 8-km long, 640 channel streamer and 6600 cubic inch airgun array and resolve the plate boundary and the internal structure of the marine forearc in greater detail and to a greater depth than available from previous seismic reflection studies of the northern Chilean margin (Coulbourn and Moberly, 1977; Moberly et al., 1982; von Huene et al., 1999; von Huene and Ranero, 2003; Geersen et al., 2015).

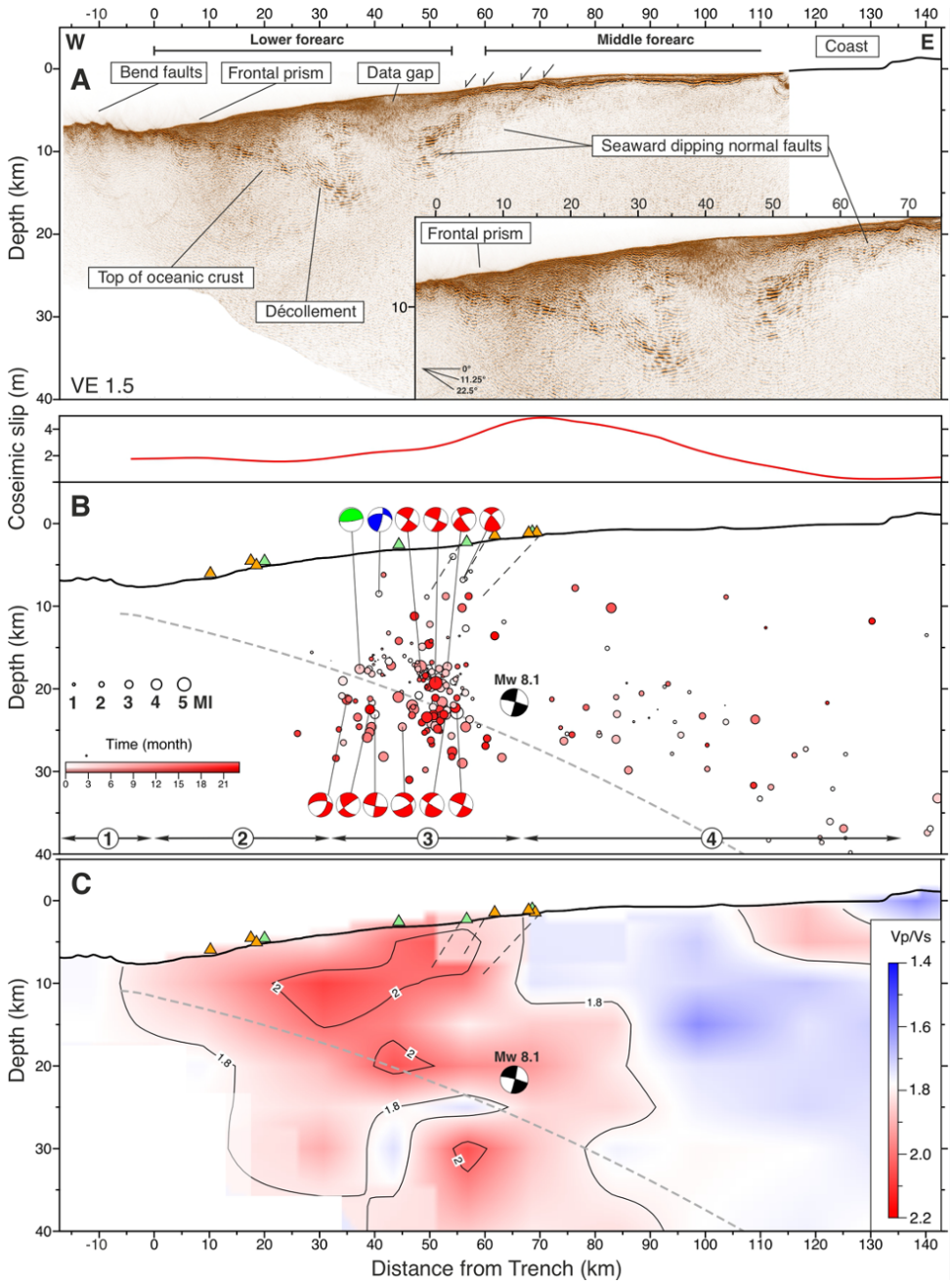


**Figure 5.2:** Seismogenic up-dip limit crossing profile illustrated by different datasets. Subplots A - C showing the same seismicity MCS profile of Figure 5.1. (a) Pre-stack depth migrated multi-channel seismic reflection line MC23. (b) coseismic slip from Duputel et al. (2015) above the aftershock distribution (287 events) using a 15 km swath on each side of the seismic profile. The aftershocks are colored according to the time scale from 9th December until the end of the operation in October 2016. Focal mechanisms from FPFIT and gCMT are classified by faulting type in thrust (red), normal (green), strike-slip (yellow), or oblique (blue) fault mechanism. OBS station locations are marked as green and orange triangles. The $M_w$ 8.1 Iquique mainshock hypocenter is indicated by the black focal mechanism. (c) Projection of *vp/vs* ratio from 2D local earthquake tomography to the MCS profile of panel a using the hypocenters from panel b. Black solid line indicates the region of good resolution.

## 5.3 Results

### 5.3.1 Aftershock distribution in the marine forearc

Our final seismicity catalog spans 23 months and starts eight months after the mainshock occurred (Figure 5.1). Since we focus on the marine forearc, our local seismic catalog covers the region between 72 ° W and 69.5 °W in longitude and between 22 °S and 19 °S in latitude, comprising 1,778 local earthquakes (Figure 5.4). Aftershocks outside this region and deeper than 40 km will be excluded from the following discussion. Generally, the majority of hypocenters are widely distributed, occurring along the plate interface, in the subducting slab, and the overriding plate (Figure 5.2). However, a significant number of events with higher magnitudes occurred up-dip of the mainshock and the largest aftershock. These occurred in two major clusters, marked as C1 and C2 in Figure 5.1, which are separated by a zone of low aftershock activity. C1 forms an NNW-SSE trending band, whereas C2 trends west to east, forming a less focused cluster of smaller magnitude earthquakes. Similar elevated aftershock seismicity up-dip of the mainshock area has been reported for other subduction zones (e.g., Tilmann et al., 2010) and has elsewhere been correlated to changes in the slope or subducting plate topography interacting with the upper plate (Wang and Bilek, 2014). The elevated Iquique aftershock activity in the shallow marine forearc was previously described in studies using land stations only (León-Ríos et al., 2016; Soto et al., 2019; Schurr et al., 2020; Sippl et al., 2018). However, the seismicity of the marine forearc occurs far outside the land network, resulting in increased uncertainties and a systematic bias in hypocenters for offshore earthquakes. We compare our seismicity with the catalog from Soto et al. (2019). Both catalogs have 23 days and 425 events in common. Soto et al. (2019) observe several west-east striking seismicity streaks interpreted as markers of surrounding aseismic creep along the plate interface. We do not observe the east-west striking seismicity clusters, and offshore our events tend to be located in the continental crust. In general, the horizontal location discrepancies increase with increasing distance from the coast and are largest at the seismogenic up-dip limit, where the OBS are located (see Figure 5.11; Soto et al., 2019, Figure 5.5). We explain the difference between the catalogs by the much better coverage of the forearc seismicity with the OBS stations. Furthermore, we use a more accurate 2D velocity model derived from the offshore seismicity

The depth uncertainties, estimated by absolute locations, of events in C1, on which the following discussion focusses, shows a range between 0.5 km and 2 km (Figure 5.6) and thus indicates to be a smaller depth error compared to previous seismicity studies offshore Iquique (Sippl et al., 2018; Soto et al., 2019). The observed seismicity in the forearc cross-section of Figure 5.2 will be described from west to east following the subduction direction. Beneath the outer rise, westward of the trench, no significant seismic activity was detected

during the 23 months of OBS recording. Elsewhere outer rise aftershock seismicity has been correlated to slip during large earthquakes that extend to the trench (Sladen and Trevisan, 2018). East of the trench, a ~35 km wide zone with very sparse seismicity is observed. Further East of the observed aseismic zone (> 35 km), a large number of events are located within 5 km distance of the plate boundary, that is derived from the multi-channel seismic data. Below the plate interface, seismicity occurred between 20 and 30 km depth, indicating earthquakes are located in the lower plate. Above the plate interface, several earthquakes occurred in the upper plate during the entire observations period. The local earthquake tomography (LET) reveals an elevated *vp/vs* ratio in the upper crust that decreases towards the inner forearc (Figure 5.2 and Figure 5.8). East of the mainshock, the aftershocks are diffusely distributed in the upper crust with local magnitudes mostly lower than 3. The vast majority of focal mechanisms at the seismogenic up-dip end indicate thrust faulting with one focal plane oriented subparallel to slab dip (Figure 5.13).

### 5.3.2 Marine forearc structure and active tectonics in the 2014 Iquique earthquake region

The multi-channel seismic profile MC23 crosses the epicentral region of the 2014 Iquique earthquake (Figure 5.1) and images the structure of the incoming and subducting oceanic plate and the marine forearc (Figure 5.2). On the incoming plate, the crust of the oceanic Nazca Plate is repeatedly offset by up to 500 m along bending related landward and seaward dipping normal faults (Geersen et al., 2018a). The trench is characterized by less than 500 m of sediment cover. Landward of the trench, a series of shallow, landward-dipping reflections indicates a ca. 7 km wide frontal prism (Figure 5.2). Below the frontal prism, the top of the subducting oceanic basement has a landward dip of ~12°. The high reflectivity of the oceanic basement under the marine forearc can be observed down to depths of ~17 km at 35 km from the trench, where aftershock seismicity commences. Between 50 and 70 km from the trench, a series of pronounced seaward dipping normal faults cut from the seafloor into the framework rock of the upper plate (dashed lines; Figure 5.2b). Their locations correlate to some of the aftershock hypocenters in the upper plate (also compare Reginato et al., 2020).

## 5.4 Discussion

The combined analysis of the 2014 Iquique aftershocks and the seismic reflection image of the marine forearc within the rupture area offers the possibility to link short term deformation associated with a single seismic cycle to the permanent deformation history of an erosive convergent margin. Previous studies of the marine forearc structure of the

2014 Iquique earthquake related the up-dip aftershock seismicity to postseismic processes, including postseismic relaxation or afterslip (Cesca et al., 2016; León-Ríos et al., 2016; Soto et al., 2019). In contrast to Soto et al. (2019), our aftershock catalog, which is based on 23 months of amphibious and deep crustal MCS data, does not resolve any E-W elongated streaks of seismicity. Instead, we find a broad band of seismicity with individual earthquake clusters up-dip of the coseismic rupture in the upper and lower plate, besides the plate interface related seismicity. Similar lower plate aftershocks related to the up-dip limit were observed in Costa Rica (Bilek and Lithgow-Bertelloni, 2005) and Japan (Obana et al., 2013). Obana et al. (2013) related oceanic upper crustal events to bending of the incoming plate since they observed normal faulting events in the oceanic plate. Since we observe few thrust mechanisms at the Iquique up-dip limit and below the plate interface (in the oceanic plate) this might be similar to thrust faulting in the downgoing plate as observed by Nippress and Rietbrock (2007) after the 1995 Antofagasta earthquake (Figure 5.1). The thrust faulting in the oceanic crust and mantle was suggested to be associated with the re-activation of horst and graben structures from the plate bending at the outer rise bend (Nippress and Rietbrock, 2007). Above the lower plate seismicity, we document an up-dip limit of aftershock seismicity that is correlated with crustal reflectivity (Figure 5.1 and Figure 5.2), indicative of long-term along-dip seismo-tectonic segmentation of the subduction zone.

If the up-dip limit of plate-boundary seismicity is stable in space over many earthquake cycles, it can induce permanent forearc deformation expressed in first-order topographic changes (Rosenau and Oncken, 2009). Indeed, at other subduction zones, similar intense up-dip clusters of seismicity often correlate with structural or topographic changes of the forearc (Lange et al., 2007; Tilmann et al., 2010; Lieser et al., 2014; Tréhu et al., 2019). Furthermore, such up-dip seismicity occurs predominantly along the plate boundary. The aftershocks associated with the 2014 Iquique earthquake in northern Chile show a very different pattern. Most aftershocks occur in a narrow band roughly up-dip of the main coseismic rupture (upper panel in Figure 5.2b), implying postseismic deformation at the seismic-to-aseismic transition. These aftershocks are, however, not associated with a structural or topographic change of the forearc (Figure 5.2). They are further not limited to the megathrust fault but also occur in the upper overriding and lower subducting plates (Figure 5.2b).

We interpret the striking aftershock sequence at the up-dip limit of seismic rupture following the 2014 Iquique earthquake as an indication of active subduction erosion during the coseismic and early postseismic phase. From fossil subduction zones, we have learned that a wide shear zone, as exemplified by the different depths of the 2014 Iquique aftershocks, is characteristic for margins dominated by subduction erosion (Vannucchi et al., 2008). In the concept of subduction erosion, fracturing at the base of the upper plate

starts at the up-dip limit of the seismogenic zone and increases towards the shallow plate interface up to the frontal prism (von Huene et al., 2004). This basal erosion induced by the 2014 Iquique earthquake is indicated by the high number of aftershocks that occur at or slightly above the plate boundary (Figure 5.2b). Such abrasion of material from the underside of the upper plate is expected to be in a dynamic equilibrium between the removal of material and steepening of forearc slope (von Huene et al., 2004). The associated deformation of the entire upper plate is illustrated by the overall fewer but still significant number of aftershocks above the up-dip limit of seismic rupture (Figure 5.2b). These aftershocks seem to occur along seaward dipping planes that match the location of seismically imaged normal faults within the upper plate (Figure 5.2a). This implies that the faults have moved in the postseismic phase of the 2014 Iquique earthquake. Although the absolute depths of the normal faults are not fully resolved by the seismic data, data from other erosive convergent margins suggest that they may cut to the plate boundary (Ranero et al., 2008; Kodaira et al., 2012; Contreras-Reyes et al., 2015).

While the aftershocks of the 2014 Iquique earthquake represent forearc deformation during the early postseismic phase of one earthquake, the seismically imaged structure of the marine forearc is a result of forearc deformation from hundreds to thousands of seismic cycles (Scholz, 1998). Repeated coseismic and postseismic deformation and associated subduction erosion force extensive faulting and pervasive fracturing at the up-dip limit of seismic rupture. Deformation is not limited to the plate boundary but active throughout the entire upper plate from the plate boundary to the seafloor (compare Geersen et al., 2018a). This is consistent with earlier studies based on numerical and analog modeling and conceptional considerations on the relationship between long-term forearc deformation of the overriding plate and earthquake behavior of subduction zone forearcs (Wang and Hu, 2006; Rosenau and Oncken, 2009). Northern Chile is an end-member margin in terms of trench sediment thickness, and subduction erosion is likely the dominant tectonic mode since at least Mesozoic times (Rutland, 1971). This is manifested in about 250 km loss of overriding continental plate since 150 Ma (Scheuber and Reutter, 1992) and associated eastward migration of the trench and volcanic arc. Over time, tectonic erosion of the upper plate (von Huene and Ranero, 2003) causes the up-dip limit to migrate landwards, mimicking the migration of the volcanic arc and the trench.

In the Iquique region of the 2014 Iquique earthquake, long-term upper plate faulting and fracturing at the up-dip limit of the seismogenic zone are manifested in the permanent deformation pattern of the marine forearc seaward of the 2014 Iquique aftershocks. This part of the marine forearc between the trench and the current up-dip limit (40 km distance) has migrated through the up-dip limit over the last millions of years. It is heavily faulted as indicated by discontinuous seismic reflections. The overall high reflection amplitudes

in this region further support a high degree of fracturing and possibly fluids within the fractures.

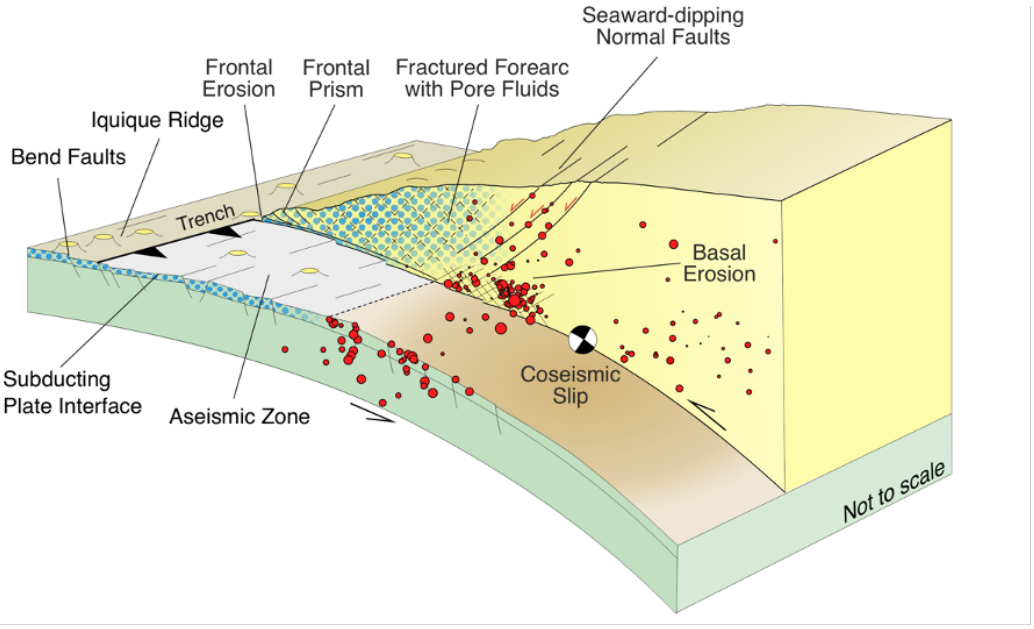


**Figure 5.3:** Conceptional model of seismotectonic segmentation and basal erosion of the North Chilean margin offshore Iquique. Pore-fluid extent marks the region of increased *vp/vs* ratio.

The elevated *vp/vs* ratio in the upper plate recognized from local earthquake tomography (Figure 5.2c) further supports the presence of fluids in the highly fractured outermost marine forearc (Popp and Kern, 1994; Wang et al., 2012). The fractured and fluid-rich outermost marine forearc, seaward of the 2014 Iquique earthquake rupture is likely too weak (and heavily deformed) to store sufficient elastic energy to nucleate a great earthquake. Further down-dip, the decrease in faulting and fluid content in the marine forearc, together with the onset of aftershock seismicity, indicates an increase in strength of the overriding plate that allows the storing of elastic energy (Figure 5.3). A similar down-dip segmentation of the North Chilean forearc that can build up elastic energy and rupture during great earthquakes has been previously suggested based on gravity data and seismic velocity structure (Sallarès and Ranero, 2005; Contreras-Reyes et al., 2012; Maksymowicz et al., 2018). The segmentation is in-line with our amphibious aftershock observation of the 2014 Iquique earthquake rupture. It is further supported by the decrease of coseismic rupture at the transition from the heavily deformed outermost marine forearc to the less deformed section of the forearc between the coast and the up-dip limit of the seismic rupture (Schurr et al., 2014; Duputel et al., 2015; Jara et al., 2018).

## 5.5 Conclusion

Combining two years of local seismicity observations following the 2014 Iquique earthquake and structural constraints on forearc architecture derived from MCS data, we provide evidence for the interplay of plate boundary rupture and upper plate deformation in the context of long-term subduction erosion. The majority of aftershocks of the 2014 Iquique earthquake occurred up-dip of the coseismic slip and ~32 - 60 km landward of the trench. Although most of the seismicity was within ~5 km of the plate boundary, earthquakes extended through the upper plate, defining a seaward dipping zone that coincides with seaward dipping normal faults imaged in the MCS data. The up-dip band of aftershock seismicity separates a pervasively fractured and likely fluid-filled marine forearc farther seaward from a less deformed section of the upper plate forearc. At the transition, active subduction erosion during the postseismic and possibly coseismic phases leads to basal abrasion of the upper plate and associated extensional faulting of the upper plate at the up-dip end of the seismogenic zone. Landward migration of the up-dip end of the seismogenic zone, at similar rates compared to the trench and the volcanic arc, preconditions the structural setting of the heavily fractured, fluid-filled and therefore weak and aseismic outermost marine forearc.

## Acknowledgments

This publication is funded by the German Research Foundation (DFG) under grant LA2970/4-1. We greatly appreciate the support from the Armada de Chile and SHOA, providing ship time on the *OPV Toro* to deploy the OBS in December 2014. GEOMAR's OCEANS program funded the OBS deployment. The SO244 cruise in 2015 was financed in the scope of the project GeoSEA by the German Federal Ministry for Education and Research (Bundesministerium für Bildung und Forschung/BMBF) under grant No. 03G0244A. The authors gratefully acknowledge the de-installation of the OBS with RV Langseth in 2016 (Oregon State University, grant OCE-1459368). We acknowledge the excellent sea-going support provided by all captains and their crews. ECR acknowledges the support of the Chilean National Research Agency (ANID, grant FONDECYT 1170009). We thank Soto et al. (2019) for providing their event catalog and Z. Duputel for providing the coseismic slip maps. Figures were created using Generic Mapping Tools (Wessel et al., 2013). We gratefully acknowledge the comments by P. Vannucchi and one anonymous reviewer in improving the manuscript.

## Data Availability Statement

The seismic waveform data from network CX are available from GFZ and CNRS-INSU (2006). OBS seismic catalog and waveform data are available from PANGAEA https://doi.pangaea.de/10.1594/PANGAEA.929899. Arrival times from the permanent land network were provided by the CSN (Barrientos, 2018). Earthquake focal mechanisms were obtained from Global Centroid-Moment-Tensor catalog (https://www.globalcmt.org/). Multibeam data from Geersen et al. (2018a) can be accessed via https://doi.pangaea.de/10.1594/PANGAEA.893034.

## References

Aldersons, F. (2004). *Toward a Three-Dimensional Crustal Structure of the Dead Sea region from Local Earthquake Tomography*. Ph.d. thesis.

Allmendinger, R. W. & González, G. (2010). Invited review paper: Neogene to quaternary tectonics of the coastal cordillera, northern chile. *Tectonophysics*, *495*(1-2), 93–110, https://doi.org/10.1016/j.tecto.2009.04.019.

An, C., Sepúlveda, I., & Liu, P. L. F. (2014). Tsunami source and its validation of the 2014 iquique, chile, earthquake. *Geophysical Research Letters*, *41*(11), 3988–3994, https://doi.org/10.1002/2014gl060567.

Angermann, D., Klotz, J., & Reigber, C. (1999). Space-geodetic estimation of the nazca-south america euler vector. *Earth and Planetary Science Letters*, *171*(3), 329–334, https://doi.org/10.1016/s0012-821x(99)00173-9.

Armijo, R. & Thiele, R. (1990). Active faulting in northern chile: ramp stacking and lateral decoupling along a subduction plate boundary? *Earth and Planetary Science Letters*, *98*(1), 40–61, https://doi.org/10.1016/0012-821x(90)90087-e.

Barrientos, S. (2018). The seismic network of chile. *Seismological Research Letters*, *89*(2A), 467–474, https://doi.org/10.1785/0220160195.

Bedford, J., Moreno, M., Schurr, B., Bartsch, M., & Oncken, O. (2015). Investigating the final seismic swarm before the iquique-pisagua 2014 mw 8.1 by comparison of continuous gps and seismic foreshock data. *Geophysical Research Letters*, *42*(10), 3820–3828, https://doi.org/10.1002/2015gl063953.

Bilek, S. L. & Lithgow-Bertelloni, C. (2005). Stress changes in the costa rica subduction zone due to the 1999 mw=6.9 quepos earthquake. *Earth and Planetary Science Letters*, *230*(1-2), 97–112, https://doi.org/10.1016/j.epsl.2004.11.020.

Brodsky, E. E. & Lay, T. (2014). Recognizing foreshocks from the 1 april 2014 chile earthquake. *Science*, *344*(6185), 700–2, https://doi.org/10.1126/science.1255202.

Byrne, D. E., Davis, D. M., & Sykes, L. R. (1988). Loci and maximum size of thrust earthquakes and the mechanics of the shallow region of subduction zones. *Tectonics*, *7*(4), 833–857, https://doi.org/10.1029/TC007i004p00833.

Cesca, S., Grigoli, F., Heimann, S., Dahm, T., Kriegerowski, M., Sobiesiak, M., Tassara, C., & Olcay, M. (2016). The mw8.1 2014 iquique, chile, seismic sequence: a tale of foreshocks and aftershocks. *Geophysical Journal International*, *204*(3), 1766–1780, https://doi.org/10.1093/gji/ggv544.

Chlieh, M., de Chabalier, J. B., Ruegg, J. C., Armijo, R., Dmowska, R., Campos, J., & Feigl, K. L. (2004). Crustal deformation and fault slip during the seismic cycle in the north chile subduction zone, from gps and insar observations. *Geophysical Journal International*, *158*(2), 695–711, https://doi.org/10.1111/j.1365-246X.2004.02326.x.

Clift, P. & Vannucchi, P. (2004). Controls on tectonic accretion versus erosion in subduction zones: Implications for the origin and recycling of the continental crust. *Reviews of Geophysics*, *42*(2), https://doi.org/10.1029/2003rg000127.

Collings, R., Lange, D., Rietbrock, A., Tilmann, F., Natawidjaja, D., Suwargadi, B., Miller, M., & Saul, J. (2012). Structure and seismogenic properties of the mentawai segment of the sumatra subduction zone revealed by local earthquake traveltime tomography. *Journal of Geophysical Research: Solid Earth*, *117*(B1), https://doi.org/10.1029/2011jb008469.

Comte, D. & Pardo, M. (1991). Reappraisal of great historical earthquakes in the northern chile and southern peru seismic gaps. *Natural Hazards*, *4*(1), 23–44, https://doi.org/10.1007/bf00126557.

Contreras-Reyes, E., Jara, J., Grevemeyer, I., Ruiz, S., & Carrizo, D. (2012). Abrupt change in the dip of the subducting plate beneath north chile. *Nature Geoscience*, *5*(5), 342–345, https://doi.org/10.1038/ngeo1447.

Contreras-Reyes, E., Ruiz, J. A., Becerra, J., Kopp, H., Reichert, C., Maksymowicz, A., & Arriagada, C. (2015). Structure and tectonics of the central chilean margin (31°–33°s): implications for subduction erosion and shallow crustal seismicity. *Geophysical Journal International*, *203*(2), 776–791, https://doi.org/10.1093/gji/ggv309.

Coulbourn, W. T. & Moberly, R. (1977). Structural evidence of the evolution of fore-arc basins off south america. *Canadian Journal of Earth Sciences*, *14*(1), 102–116, https://doi.org/10.1139/e77-011.

Diehl, T., Deichmann, N., Kissling, E., & Husen, S. (2009). Automatic s-wave picker for local earthquake tomography. *Bulletin of the Seismological Society of America*, *99*(3), 1906–1920, https://doi.org/10.1785/0120080019.

Duputel, Z., Jiang, J., Jolivet, R., Simons, M., Rivera, L., Ampuero, J. P., Riel, B., Owen, S. E., Moore, A. W., Samsonov, S. V., Ortega Culaciati, F., & Minson, S. E. (2015). The iquique earthquake sequence of april 2014: Bayesian modeling accounting for prediction uncertainty. *Geophysical Research Letters*, *42*(19), 7949–7957, https://doi.org/10.1002/2015gl065402.

Dziewonski, A. M., Chou, T. A., & Woodhouse, J. H. (1981). Determination of earthquake source parameters from waveform data for studies of global and regional seismicity. *Journal of Geophysical Research: Solid Earth*, *86*(B4), 2825–2852, https://doi.org/10.1029/JB086iB04p02825.

Ekström, G., Nettles, M., & Dziewoński, A. M. (2012). The global cmt project 2004–2010: Centroid-moment tensors for 13,017 earthquakes. *Physics of the Earth and Planetary Interiors*, *200-201*, 1–9, https://doi.org/10.1016/j.pepi.2012.04.002.

Farr, T. G., Rosen, P. A., Caro, E., Crippen, R., Duren, R., Hensley, S., Kobrick, M., Paller, M., Rodriguez, E., Roth, L., Seal, D., Shaffer, S., Shimada, J., Umland, J., Werner, M., Oskin, M., Burbank, D., & Alsdorf, D. (2007). The shuttle radar topography mission. *Reviews of Geophysics*, *45*(2), https://doi.org/10.1029/2005rg000183.

Frohlich, C. (1992). Triangle diagrams: ternary graphs to display similarity and diversity of earthquake focal mechanisms. *Physics of the Earth and Planetary Interiors*, *75*(1-3), 193–198, https://doi.org/10.1016/0031-9201(92)90130-n.

Geersen, J., Ranero, C. R., Barckhausen, U., & Reichert, C. (2015). Subducting seamounts control interplate coupling and seismic rupture in the 2014 iquique earthquake area. *Nat Commun*, *6*, 8267, https://doi.org/10.1038/ncomms9267.

Geersen, J., Ranero, C. R., Klaucke, I., Behrmann, J. H., Kopp, H., Tréhu, A. M., Contreras-Reyes, E., Barckhausen, U., & Reichert, C. (2018a). Active tectonics of the north chilean marine forearc and adjacent oceanic nazca plate. *Tectonics*, *37*(11), 4194–4211, https://doi.org/10.1029/2018tc005087.

Geersen, J., Ranero, C. R., Kopp, H., Behrmann, J. H., Lange, D., Klaucke, I., Barrientos, S., Diaz-Naveas, J., Barckhausen, U., & Reichert, C. (2018b). Does permanent extensional deformation in lower forearc slopes indicate shallow plate-boundary rupture? *Earth and Planetary Science Letters*, *489*, 17–27, https://doi.org/10.1016/j.epsl.2018.02.030.

GFZ & CNRS-INSU (2006). Ipoc seismic network. integrated plate boundary observatory chile - ipoc. *Other/Seismic Network*, https://doi.org/10.14470/ PK615318.

GFZ & gempa GmbH (2008). The seiscomp seismological software package. *GFZ Data Services*, https://doi.org/10.5880/GFZ.2.4.2020.003.

Haberland, C., Rietbrock, A., Lange, D., Bataille, K., & Dahm, T. (2009). Structure of the seismogenic zone of the southcentral chilean margin revealed by local earthquake traveltime tomography. *Journal of Geophysical Research: Solid Earth*, *114*(B1), https://doi.org/10.1029/2008jb005802.

Havskov, J., Voss, P. H., & Ottemoller, L. (2020). Seismological observatory software: 30 yr of seisan. *Seismological Research Letters*, *91*(3), 1846–1852, https://doi.org/10.1785/0220190313.

Hayes, G. P., Moore, G. L., Portner, D. E., Hearne, M., Flamme, H., Furtney, M., & Smoczyk, G. M. (2018). Slab2, a comprehensive subduction zone geometry model. *Science*, *362*(6410), 58–61, https://doi.org/10.1126/science.aat4723.

Herman, M. W., Furlong, K. P., Hayes, G. P., & Benz, H. M. (2016). Foreshock triggering of the 1 april 2014 mw 8.2 iquique, chile, earthquake. *Earth and Planetary Science Letters*, *447*, 119–129, https://doi.org/10.1016/j.epsl.2016.04.020.

Husen, S., Kissling, E., Flueh, E. R., & Asch, G. (1999). Accurate hypocentre determination in the seismogenic zone of the subducting nazca plate in northern chile using a combined on-/offshore network. *Geophysical Journal International*, *138*(3), 687–701, https://doi.org/10.1046/j.1365-246x.1999.00893.x.

Husen, S. & Smith, R. B. (2004). Probabilistic earthquake relocation in three-dimensional velocity models for the yellowstone national park region, wyoming. *Bulletin of the Seismological Society of America*, *94*(3), 880–896, https://doi.org/10.1785/0120030170.

Hutton, L. K. & Boore, D. M. (1987). The ml scale in southern california. *Bulletin of the Seismological Society of America*, *77*(6), 2074–2094.

Jara, J., Sánchez-Reyes, H., Socquet, A., Cotton, F., Virieux, J., Maksymowicz, A., Díaz-Mojica, J., Walpersdorf, A., Ruiz, J., Cotte, N., & Norabuena, E. (2018). Kinematic study of iquique 2014 m 8.1 earthquake: Understanding the segmentation of the seismogenic zone. *Earth and Planetary Science Letters*, *503*, 131–143, https://doi.org/10.1016/j.epsl.2018.09.025.

Kissling, E., Kradolfer, U., & Maurer, H. (1995). *Program VELEST user's Guide-Short Introduction*. Report.

Kodaira, S., No, T., Nakamura, Y., Fujiwara, T., Kaiho, Y., Miura, S., Takahashi, N., Kaneda, Y., & Taira, A. (2012). Coseismic fault rupture at the trench axis during the 2011 tohoku-oki earthquake. *Nature Geoscience*, *5*(9), 646–650, https://doi.org/10.1038/ngeo1547.

Lange, D., Rietbrock, A., Haberland, C., Bataille, K., Dahm, T., Tilmann, F., & Flüh, E. R. (2007). Seismicity and geometry of the south chilean subduction zone (41.5°s–43.5°s): Implications for controlling parameters. *Geophysical Research Letters*, *34*(6), https://doi.org/10.1029/2006gl029190.

Lange, D., Tilmann, F., Barrientos, S. E., Contreras-Reyes, E., Methe, P., Moreno, M., Heit, B., Agurto, H., Bernard, P., Vilotte, J.-P., & Beck, S. (2012). Aftershock seismicity of the 27 february 2010 mw 8.8 maule earthquake rupture zone. *Earth and Planetary Science Letters*, *317-318*, 413–425, https://doi.org/10.1016/j.epsl.2011.11.034.

Lay, T., Yue, H., Brodsky, E. E., & An, C. (2014). The 1 april 2014 iquique, chile, mw 8.1 earthquake rupture sequence. *Geophysical Research Letters*, *41*(11), 3818–3825, https://doi.org/10.1002/2014gl060238.

León-Ríos, S., Ruiz, S., Maksymowicz, A., Leyton, F., Fuenzalida, A., & Madariaga, R. (2016). Diversity of the 2014 iquique's foreshocks and aftershocks: clues about the complex rupture process of a mw 8.1 earthquake. *Journal of Seismology*, *20*(4), 1059–1073, https://doi.org/10.1007/s10950-016-9568-6.

Lieser, K., Grevemeyer, I., Lange, D., Flueh, E., Tilmann, F., & Contreras-Reyes, E. (2014). Splay fault activity revealed by aftershocks of the 2010 mw 8.8 maule earthquake, central chile. *Geology*, *42*(9), 823–826, https://doi.org/10.1130/g35848.1.

Lomax, A., Virieux, J., Volant, P., & Berge-Thierry, C. (2000). *Probabilistic Earthquake Location in 3D and Layered Models*, volume 18 of *Modern Approaches in Geophysics*, book section Chapter 5, (pp. 101–134).

Ma, B., Klaeschen, D., Kopp, H., Geersen, J., & Tréhu, A. M. (2020). Variations in plate interface reflectivity within the rupture zone of the 2014 iquique earthquake sequence: evidence from seismic and bathymetric data. *AGU Fall Meeting 2020*.

Maksymowicz, A., Ruiz, J., Vera, E., Contreras-Reyes, E., Ruiz, S., Arraigada, C., Bonvalot, S., & Bascuñan, S. (2018). Heterogeneous structure of the northern chile marine forearc and its implications for megathrust earthquakes. *Geophysical Journal International*, *215*(2), 1080–1097, https://doi.org/10.1093/gji/ggy325.

Mendoza, C. & Hartzell, S. (1988). Aftershock patterns and main shock faulting. *Bull. Seismol. Soc. Am.*, *78*(4), 1438–1449.

Moberly, R., Shepherd, G. L., & Coulbourn, W. T. (1982). Forearc and other basins, continental margin of northern and southern peru and adjacent ecuador and chile. *Geological Society, London, Special Publications*, *10*(1), 171–189, https://doi.org/10.1144/gsl.Sp.1982.010.01.11.

Moore, J. C. & Saffer, D. (2001). Updip limit of the seismogenic zone beneath the accretionary prism of southwest japan: An effect of diagenetic to low-grade metamorphic processes and increasing effective stress. *Geology*, *29*(2), https://doi.org/10.1130/0091-7613(2001)029<0183:Ulotsz>2.0.Co;2.

Nippress, S. E. J. & Rietbrock, A. (2007). Seismogenic zone high permeability in the central andes inferred from relocations of micro-earthquakes. *Earth and Planetary Science Letters*, *263*(3-4), 235–245, https://doi.org/10.1016/j.epsl.2007.08.032.

Obana, K., Kodaira, S., Shinohara, M., Hino, R., Uehira, K., Shiobara, H., Nakahigashi, K., Yamada, T., Sugioka, H., Ito, A., Nakamura, Y., Miura, S., No, T., & Takahashi, N. (2013). Aftershocks near the updip end of the 2011 tohoku-oki earthquake. *Earth and Planetary Science Letters*, *382*, 111–116, https://doi.org/10.1016/j.epsl.2013.09.007.

Oleskevich, D. A., Hyndman, R. D., & Wang, K. (1999). The updip and downdip limits to great subduction earthquakes: Thermal and structural models of cascadia, south alaska, sw japan, and chile. *Journal of Geophysical Research: Solid Earth*, *104*(B7), 14965–14991, https://doi.org/10.1029/1999jb900060.

Ottemoller, L. & Havskov, J. (2003). Moment magnitude determination for local and regional earthquakes based on source spectra. *Bulletin of the Seismological Society of America*, *93*(1), 203–214, https://doi.org/10.1785/0120010220.

Popp, T. & Kern, H. (1994). The influence of dry and water saturated cracks on seismic velocities of crustal rocks - a comparison of experimental data with theoretical model. *Surveys in Geophysics*, *15*(5), 443–465, https://doi.org/10.1007/bf00690169.

Ranero, C. R., Grevemeyer, I., Sahling, H., Barckhausen, U., Hensen, C., Wallmann, K., Weinrebe, W., Vannucchi, P., von Huene, R., & McIntosh, K. (2008). Hydrogeological system of erosional convergent margins and its influence on tectonics and interplate seismogenesis. *Geochemistry, Geophysics, Geosystems*, *9*(3), https://doi.org/10.1029/2007gc001679.

Ranero, C. R. & von Huene, R. (2000). Subduction erosion along the middle america convergent margin. *Nature*, *404*(6779), 748–52, https://doi.org/10.1038/35008046.

Reasenberg, P., Oppenheimer, D., & USGS (1985). *FPFIT, FPPLOT and FPPAGE Fortran computer programs for calculating and displaying earthquake fault-plane solutions*. Report.

Reginato, G., Vera, E., Contreras-Reyes, E., Tréhu, A. M., Maksymowicz, A., Bello-González, J. P., & González, F. (2020). Seismic structure and tectonics of the continental wedge overlying the source region of the iquique mw8.1 2014 earthquake. *Tectonophysics*, *796*, https://doi.org/10.1016/j.tecto.2020.228629.

Rosenau, M. & Oncken, O. (2009). Fore-arc deformation controls frequency-size distribution of megathrust earthquakes in subduction zones. *Journal of Geophysical Research*, *114*(B10), https://doi.org/10.1029/2009jb006359.

Rutland, R. W. (1971). Andean orogeny and ocean floor spreading. *Nature*, *233*(5317), 252–5, https://doi.org/10.1038/233252a0.

Sallarès, V. & Ranero, C. (2005). Structure and tectonics of the erosional convergent margin off antofagasta, north chile (23°30ś). *Journal of Geophysical Research*, *110*(B6), https://doi.org/10.1029/2004jb003418.

Scheuber, E. & Reutter, K.-J. (1992). Magmatic arc tectonics in the central andes between 21° and 25°s. *Tectonophysics*, *205*(1-3), 127–140, https://doi.org/10.1016/0040-1951(92)90422-3.

Scholl, D. & von Huene, R. (2007). *Crustal recycling at modern subduction zones applied to the past—Issues of growth and preservation of continental basement crust, mantle geochemistry, and supercontinent reconstruction*. 4-D Framework of Continental Crust. Geological Society of America.

Scholz, C. H. (1998). Earthquakes and friction laws. *Nature*, *391*, 37–42, https://doi.org/10.1038/34097.

Schurr, B., Asch, G., Hainzl, S., Bedford, J., Hoechner, A., Palo, M., Wang, R., Moreno, M., Bartsch, M., Zhang, Y., Oncken, O., Tilmann, F., Dahm, T., Victor, P., Barrientos, S., & Vilotte, J. P. (2014). Gradual unlocking of plate boundary controlled initiation of the 2014 iquique earthquake. *Nature*, *512*(7514), 299–302, https://doi.org/10.1038/nature13681.

Schurr, B., Asch, G., Rosenau, M., Wang, R., Oncken, O., Barrientos, S., Salazar, P., & Vilotte, J. P. (2012). The 2007 m7.7 tocopilla northern chile earthquake sequence: Implications for along-strike and downdip rupture segmentation and megathrust frictional behavior. *Journal of Geophysical Research: Solid Earth*, *117*(B5), https://doi.org/10.1029/2011jb009030.

Schurr, B., Moreno, M., Tréhu, A. M., Bedford, J., Kummerow, J., Li, S., & Oncken, O. (2020). Forming a mogi doughnut in the years prior to and immediately before the 2014 mw8.1 iquique, northern chile, earthquake. *Geophysical Research Letters*, *47*(16), https://doi.org/10.1029/2020gl088351.

Sielfeld, G., Lange, D., & Cembrano, J. (2019). Intra-arc crustal seismicity: Seismotectonic implications for the southern andes volcanic zone, chile. *Tectonics*, *38*(2), 552–578, https://doi.org/10.1029/2018tc004985.

Simons, M., Minson, S. E., Sladen, A., Ortega, F., Jiang, J., Owen, S. E., Meng, L., Ampuero, J. P., Wei, S., Chu, R., Helmberger, D. V., Kanamori, H., Hetland, E., Moore, A. W., & Webb, F. H. (2011). The 2011 magnitude 9.0 tohoku-oki earthquake: mosaicking the megathrust from seconds to centuries. *Science*, *332*(6036), 1421–5, https://doi.org/10.1126/science.1206731.

Sippl, C., Schurr, B., Asch, G., & Kummerow, J. (2018). Seismicity structure of the northern chile forearc from >100,000 double-difference relocated hypocenters. *Journal of Geophysical Research: Solid Earth*, *123*(5), 4063–4087, https://doi.org/10.1002/2017jb015384.

Sladen, A. & Trevisan, J. (2018). Shallow megathrust earthquake ruptures betrayed by their outer-trench aftershocks signature. *Earth and Planetary Science Letters*, *483*, 105–113, https://doi.org/10.1016/j.epsl.2017.12.006.

Soto, H., Sippl, C., Schurr, B., Kummerow, J., Asch, G., Tilmann, F., Comte, D., Ruiz, S., & Oncken, O. (2019). Probing the northern chile megathrust with seismicity: The 2014 m8.1 iquique earthquake sequence. *Journal of Geophysical Research: Solid Earth*, *124*(12), 12935–12954, https://doi.org/10.1029/2019jb017794.

Straub, S. M., Gómez-Tuena, A., & Vannucchi, P. (2020). Subduction erosion and arc volcanism. *Nature Reviews Earth and Environment*, *1*(11), 574–589, https://doi.org/10.1038/s43017-020-0095-1.

Thurber, C. H. (1983). Earthquake locations and three-dimensional crustal structure in the coyote lake area, central california. *Journal of Geophysical Research*, *88*(B10), https://doi.org/10.1029/JB088iB10p08226.

Thurber, C. H. (1992). Hypocenter-velocity structure coupling in local earthquake tomography. *Physics of the Earth and Planetary Interiors*, *75*(1-3), 55–62, https://doi.org/10.1016/0031-9201(92)90117-e.

Tilmann, F. J., Craig, T. J., Grevemeyer, I., Suwargadi, B., Kopp, H., & Flueh, E. (2010). The updip seismic/aseismic transition of the sumatra megathrust illuminated by aftershocks of the 2004 aceh-andaman and 2005 nias events. *Geophysical Journal International*, https://doi.org/10.1111/j.1365-246X.2010.04597.x.

Tréhu, A. M., Hass, B., de Moor, A., Maksymowicz, A., Contreras-Reyes, E., Vera, E., & Tryon, M. D. (2019). Geologic controls on up-dip and along-strike propagation of slip during subduction zone earthquakes from a high-resolution seismic reflection survey across the northern limit of slip during the 2010 mw 8.8 maule earthquake, offshore chile. *Geosphere*, *15*(6), 1751–1773, https://doi.org/10.1130/ges02099.1.

Tréhu, A. M., Vera, E., & Riedel, M. (2017). *PICTURES: Pisagua/Iquique crustal tomography to understand the region of the earthquake source*. Report.

Vannucchi, P., Remitti, F., & Bettelli, G. (2008). Geological record of fluid flow and seismogenesis along an erosive subducting plate boundary. *Nature*, *451*(7179), 699–703, https://doi.org/10.1038/nature06486.

Vannucchi, P., Spagnuolo, E., Aretusini, S., Di Toro, G., Ujiie, K., Tsutsumi, A., & Nielsen, S. (2017). Past seismic slip-to-the-trench recorded in central america megathrust. *Nature Geoscience*, *10*(12), 935–940, https://doi.org/10.1038/s41561-017-0013-4.

von Huene, R. & Lallemand, S. (1990). Tectonic erosion along the japan and peru convergent margins. *Geological Society of America Bulletin*, *102*(6), 704–720, https://doi.org/10.1130/0016-7606(1990)102<0704:TEATJA>2.3.CO;2.

von Huene, R. & Ranero, C. R. (2003). Subduction erosion and basal friction along the sediment-starved convergent margin off antofagasta, chile. *Journal of Geophysical Research: Solid Earth*, *108*(B2), https://doi.org/10.1029/2001jb001569.

von Huene, R., Ranero, C. R., & Vannucchi, P. (2004). Generic model of subduction erosion. *Geology*, *32*(10), https://doi.org/10.1130/g20563.1.

von Huene, R. & Scholl, D. W. (1991). Observations at convergent margins concerning sediment subduction, subduction erosion, and the growth of continental crust. *Reviews of Geophysics*, *29*(3), https://doi.org/10.1029/91rg00969.

von Huene, R., Weinrebe, W., & Heeren, F. (1999). Subduction erosion along the north chile margin. *Journal of Geodynamics*, *27*(3), 345–358, https://doi.org/10.1016/s0264-3707(98)00002-7.

Waldhuser, F. & Ellsworth, W. L. (2000). A double-difference earthquake location algorithm method and application to the northern hayward fault, california. *Bulletin of the Seismological Society of America*, *90*(6), 1253–1368, https://doi.org/10.1785/0120000006.

Wang, K. & Bilek, S. L. (2014). Invited review paper: Fault creep caused by subduction of rough seafloor relief. *Tectonophysics*, *610*, 1–24, https://doi.org/10.1016/j.tecto.2013.11.024.

Wang, K. & Hu, Y. (2006). Accretionary prisms in subduction earthquake cycles: The theory of dynamic coulomb wedge. *Journal of Geophysical Research: Solid Earth*, *111*(B6), https://doi.org/10.1029/2005jb004094.

Wang, K., Hu, Y., von Huene, R., & Kukowski, N. (2010). Interplate earthquakes as a driver of shallow subduction erosion. *Geology*, *38*(5), 431–434, https://doi.org/10.1130/g30597.1.

Wang, X. Q., Schubnel, A., Fortin, J., David, E. C., Guéguen, Y., & Ge, H. K. (2012). High vp/vs ratio: Saturated cracks or anisotropy effects? *Geophysical Research Letters*, *39*(L11307), https://doi.org/10.1029/2012GL051742.

Wessel, P., Smith, W. H. F., Scharroo, R., Luis, J., & Wobbe, F. (2013). Generic mapping tools: Improved version released. *Eos, Transactions American Geophysical Union*, *94*(45), 409–410, https://doi.org/10.1002/2013eo450001.

Yagi, Y., Okuwaki, R., Enescu, B., Hirano, S., Yamagami, Y., Endo, S., & Komoro, T. (2014). Rupture process of the 2014 iquique chile earthquake in relation with the foreshock activity. *Geophysical Research Letters*, *41*(12), 4201–4206, https://doi.org/10.1002/2014GL060274.

# Supporting Information

## Introduction

This appendix provides supporting information on the methods we used to investigate the local seismicity following the 2014 $M_w$ 8.1 Iquique earthquake. We used the continuous waveform data from two subsequent Ocean Bottom Seismometer installations and the permanent land stations from CSN (Barrientos, 2018) and IPOC (GFZ and CNRS-INSU, 2006) between December 9, 2014, and October 31, 2016.

Our local seismic catalog covers the region between 72 °W and 69.5 °W and between 22 °S and 19 °S. In total, the amphibious catalog comprises 1,990 earthquakes observed on at least eight stations (Figure S1), including 27,877 P-phase picks and 7,229 S-phases. The entire seismic catalog and waveform data are available from the PANGAEA archive (`https://www.pangaea.de`). The local magnitude of completeness is $M_l$ 1.75 in the first year and $M_l$ 2.5 in the second year. The decrease in the magnitude of completeness results from less operating OBS in the second year.

## Earthquake detection and picking of P-phases

Earthquakes were detected with the scanloc module of SeisComP3 (GFZ and gempa GmbH, 2008) using a cluster search algorithm to associate phase detections to one or many potential earthquake sources. Source scanning was done with the local 1-D velocity model from Husen et al. (1999) (Figure 5.4). In the next step, the SeisComP3 estimated P-phase picks were used to re-pick P-phases onsets using the automatic Manneken Pix (MPX) algorithm (Aldersons, 2004) following the procedure of (Lange et al., 2012). All phase picks manually revised and associated with uncertainty from 0 to 4 according to their quality and re-picked using the SEISAN software (Havskov et al., 2020).

## Picking of S-phases

In the next step, S-phases were picked for all events with more than 8 P picks using the S-phase pick algorithm of Diehl et al. (2009). All phase picks are associated with uncertainty from 0 to 4 according to their quality, and we removed all phases with a ratio of station residual to epicentral distance higher than 0.05 s/km. However, automated phase picking on OBS data turned out to be unsatisfactory due to increased noise on the waveform data. Hence, we manually revised the phase picks on the OBS data.

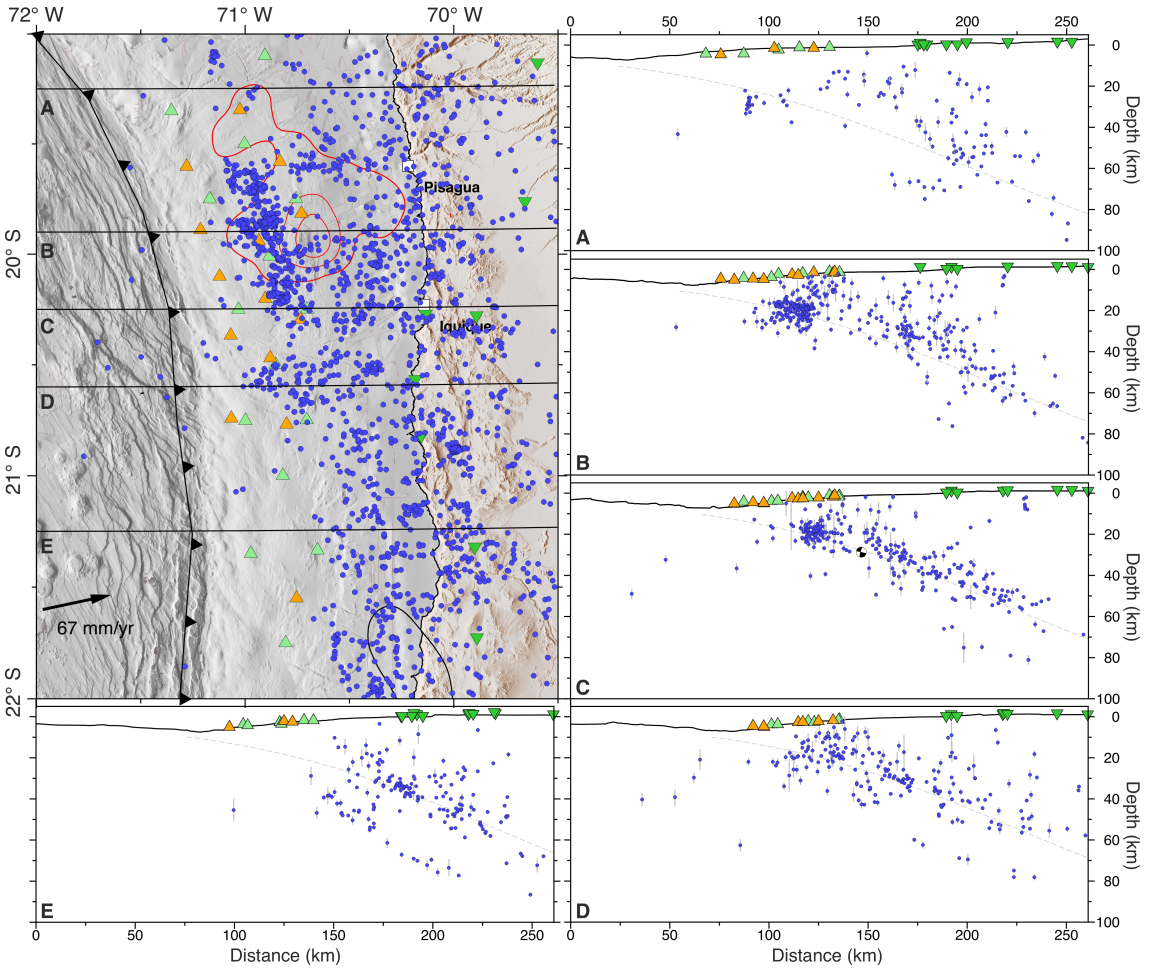


**Figure 5.4:** (Left) Map view of the total seismic catalog from December 9, 2014, until October 31, 2016. Coseismic slip model from Duputel et al. (2015) (Right) Profiles A-C crossing the rupture area of the 2014 Iquique earthquake. Blue dots indicate earthquakes located within the two-dimensional local earthquake tomography velocity model. Triangles mark the locations of the OBS deployments and land stations of CSN/IPOC, respectively.

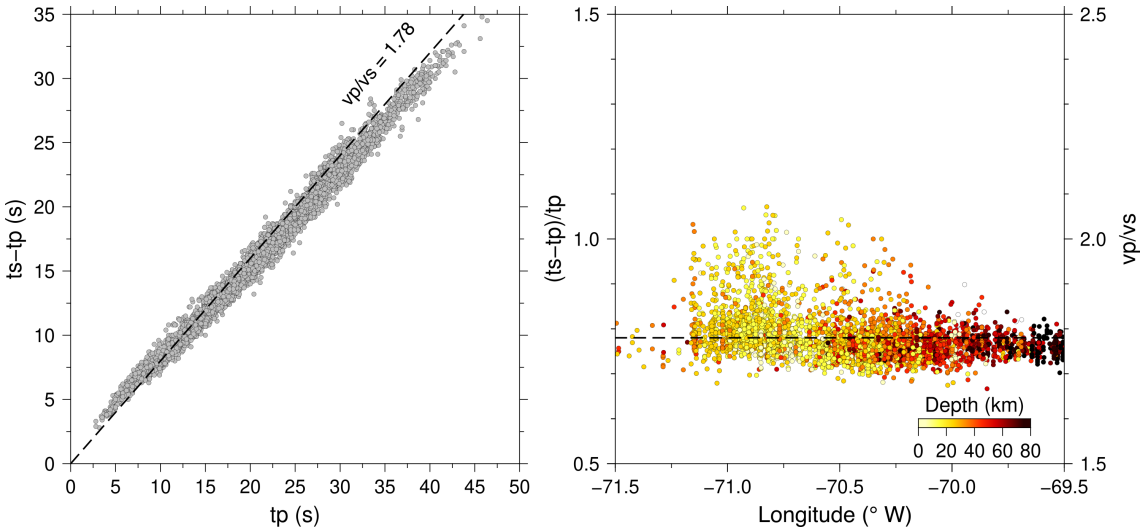


**Figure 5.5:** (Left) Wadati diagram of all events detected OBS06, located in the center of the OBS network. The dashed line marks the *vp/vs* ratio of 1.78. (Right) Plot of *vp/vs* ratios versus hypocenter longitudes (e.g., Haberland et al., 2009). Events east of 70.5 °W show an increase in the *vp/vs* ratio.

## 1D minimum Velocity Model

We selected 520 events from our local earthquake catalog with a gap of less than 180° and more than 12 P-wave arrivals and 8 S-wave arrivals to calculate local one-dimensional (1D) *vp* models and 1D *vp/vs* velocity models. The inversion is performed with VELEST (Kissling et al., 1995) using the staggered approach for inverting *vp* and *vp/vs* 1D velocity models (Husen et al., 1999) using a wide range of input velocity models (e.g., Sielfeld et al., 2019). The 1D velocity models are shown in Figure 5.6).

## 2D-tomography

The 1D models are then used as input for the 2D local earthquake tomography (LET) using SIMUL2000 (e.g., Thurber, 1983, 1992) following the procedure of Collings et al. (2012). The earthquake locations from the minimum 1D velocity model and the one-dimensional input velocity model were used for the 2D tomography (Figure 5.8). The resolution matrix contains at each row an averaging vector for a single model parameter and reflects how individual model parameters are dependent on all other model parameters (Collings et al., 2012). High resolution and large diagonal elements result in a low spread value (Figure 5.9). The two-dimensional tomography resolution indicates good resolution for the updip region and the coastal area for both *vp* and *vp/vs*. The marine forearc basin

is poorly resolved because of a small amount of shallow seismic activity and no station coverage. The 2D velocity model was used to relocate the entire catalog using NonLinLoc (Lomax et al., 2000).

## Magnitudes

We calculated moment magnitudes after Ottemoller and Havskov (2003) using standard values for geometric spreading and local magnitudes after Hutton and Boore (1987) using the maximum amplitudes of horizontal components of OBS and land stations. The instrument responses of OBS sensors are calibrated to match event magnitudes from land stations of the CSN (Figure 5.12) and result in similar magnitudes.

## Earthquake locations and uncertainties

Hypocenter locations were determined using the non-linear oct-tree search algorithm NonLinLoc (Lomax et al., 2000). The maximum likelihood location is chosen as the preferred location from the probability density functions of event scatter samples. Furthermore, the oct-tree algorithm estimates hypocenter uncertainties based on a 3D error ellipsoid (68 % confidence). The distribution of the obtained location errors was averaged in the latitude, longitude and depth for all the events within each of the spatial 0.1° x 0.1° grid cells in which we subdivided the study region. To classify hypocenter locations in best (A), good (B), and fair (C) events, we use the procedure from Husen and Smith, 2004. We only consider the highest two classes, A and B with the most reliable earthquake locations (Husen and Smith, 2004).

## Double-difference locations

To obtain precise relative relocations and to investigate the internal seismicity structure of the marine forearc, we applied the double-difference algorithm (HypoDD, Waldhuser and Ellsworth, 2000) on our local earthquake catalog with events relocated using the 2D local earthquake tomography (section 5.5). The algorithm minimizes the residual between observed and theoretical travel time differences based on waveform cross-correlations between two nearby earthquakes at the same station that recorded both events. Cross-correlations for events pairs with calculated time differences are considered with a maximum distance of 10 km and a cross-correlation coefficient greater than 0.8. The local catalog now encompasses 916 earthquakes relocated using the double-difference algorithm HypoDD

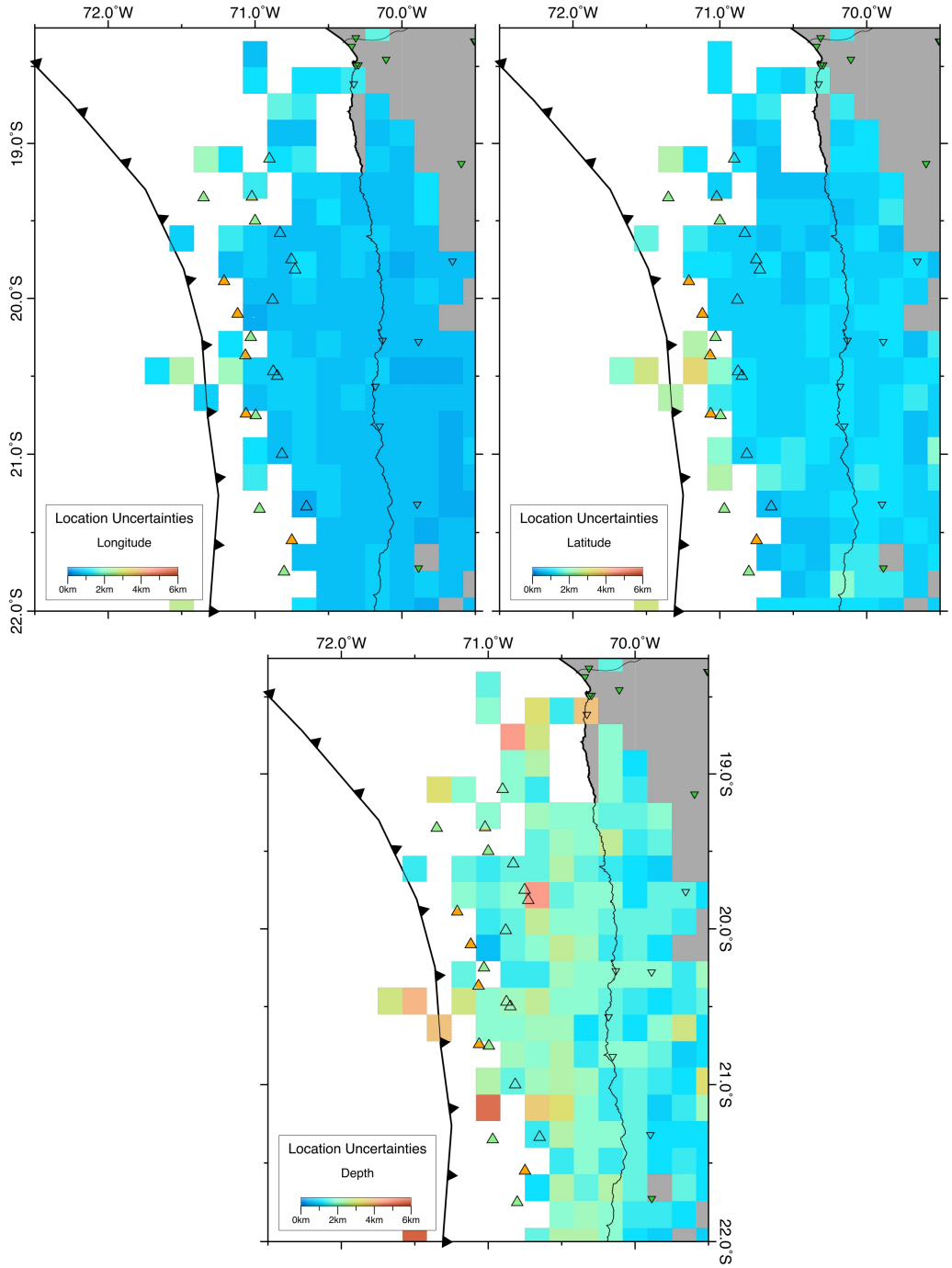


**Figure 5.6:** Location uncertainties from average event locations for hypocenters at 0 – 60 km depth for 0.25° × 0.25° squares. Uncertainties estimated using the oct-tree algorithm of the probabilistic location scheme of NonLinLoc. Error ellipsoids (68 % confidence) in three components x (longitude), y (latitude) and z (depth). Depth errors for shallow events outside the station network are not comparable to the large horizontal errors as the oct-tree search algorithm only explores the PDF within the pre-defined grid (e.g., no air-quakes).

(Waldhuser and Ellsworth, 2000) and 862 earthquakes located using the non-linear oct-tree search algorithm NonLinLoc (Lomax et al., 2000) with the quality classes A and B (Husen and Smith, 2004).

## Catalog comparison

The aftershock seismic catalog presented here overlaps in 23 days with the local seismicity catalog from Soto et al. (2019), starting on December 9, 2014, with the deployment of the first Ocean Bottom Seismometer (OB01) (Figure 5.11). We compared both catalogs and searched the OBS data for missing events by comparing the origin times. Both catalogs have 425 events in common, but we could not locate 25 events from Soto et al. (2019) in our OBS data (Figure 5.11) due to a low signal-to-noise ratio on OBS waveforms. Our OBS network detected additional 58 events missing in the catalog from Soto et al. (2019). These 58 events are mainly located offshore at the seismogenic up-dip limit. In contrast, the 25 events observed only by Soto et al. (2019) are primarily located in the down-dip region of the Iquique earthquake. The earthquake locations from the Soto et al. (2019) catalog are biased $1.6 \pm 0.04$ km southwards, $3.27 \pm 0.02$ km westwards and $0.9 \pm 0.06$ km in depth relative to the locally determined hypocenters (Figure 5.11).

## Focal mechanisms

Focal mechanisms of 98 events are calculated based on revised first motion P phase polarities of events with more than 20 P polarities (FPFIT, Reasenberg et al., 1985). Unique solutions are considered, which are based on event azimuths and take-off angles from hypocenters. Besides, we used focal mechanisms from the Global Centroid Moment Tensor (gCMT) catalog (`www.globalcmt.org`) (Dziewonski et al., 1981; Ekström et al., 2012), which comprises 20 earthquakes ($M_w > 4.7$) that occurred during the two years of the OBS deployment. CMT and focal mechanisms of the marine forearc are shown in Figure 5.13). In addition, we compared the focal mechanisms from FPFIT with three larger events of the global CMT catalog. We identified the largest discrepancy in the strike angle of the focal mechanisms (Figure 5.15). We calculated the bias in location as a weighted average for the events that the gCMT catalog and the local aftershock catalog have in common to compare the focal mechanism locations. The global gCMT catalog is displaced by $25 \pm 0.5$ km in the North direction and $2.9 \pm 0.5$ km in the East direction and 8 km deeper relative to our local catalog based on amphibious data.

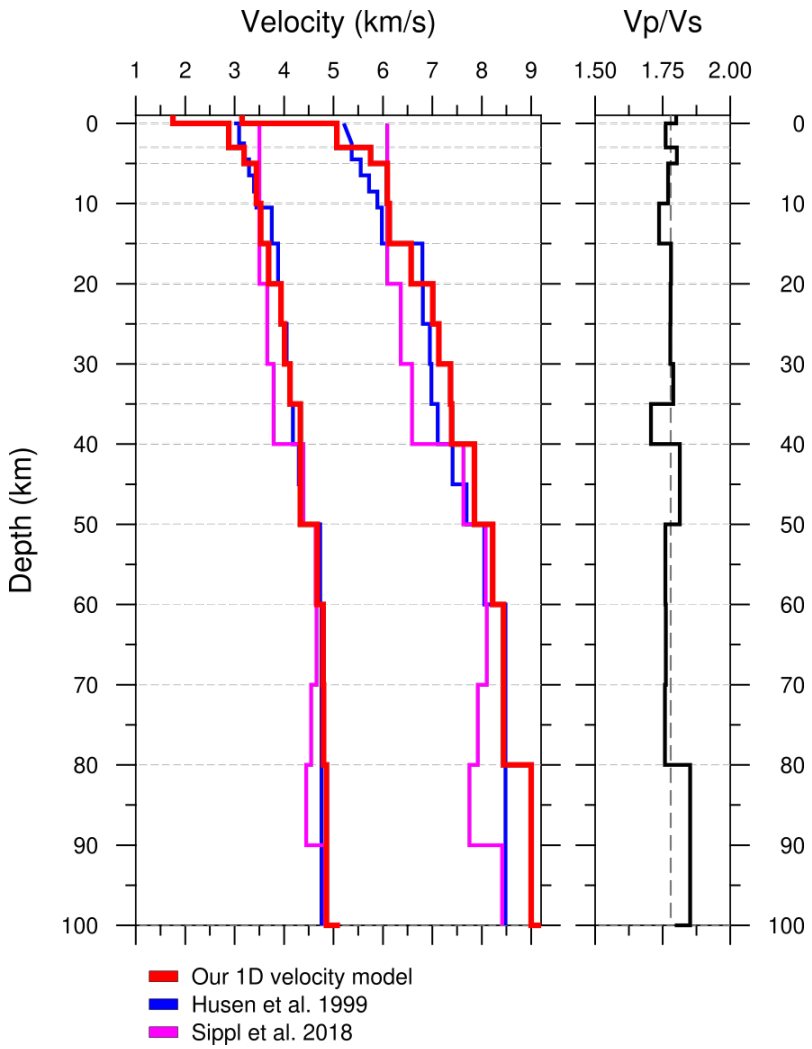


**Figure 5.7:** Minimum 1D velocity model for the marine forearc. The red line indicates the velocity model calculated with the offshore recorded Iquique aftershock sequence determined using VELEST (Kissling et al., 1995). The upper layers up to 15 km are not well constrained due to the near-vertical ray paths below the seismic network (Sippl et al., 2018; Husen et al., 1999).

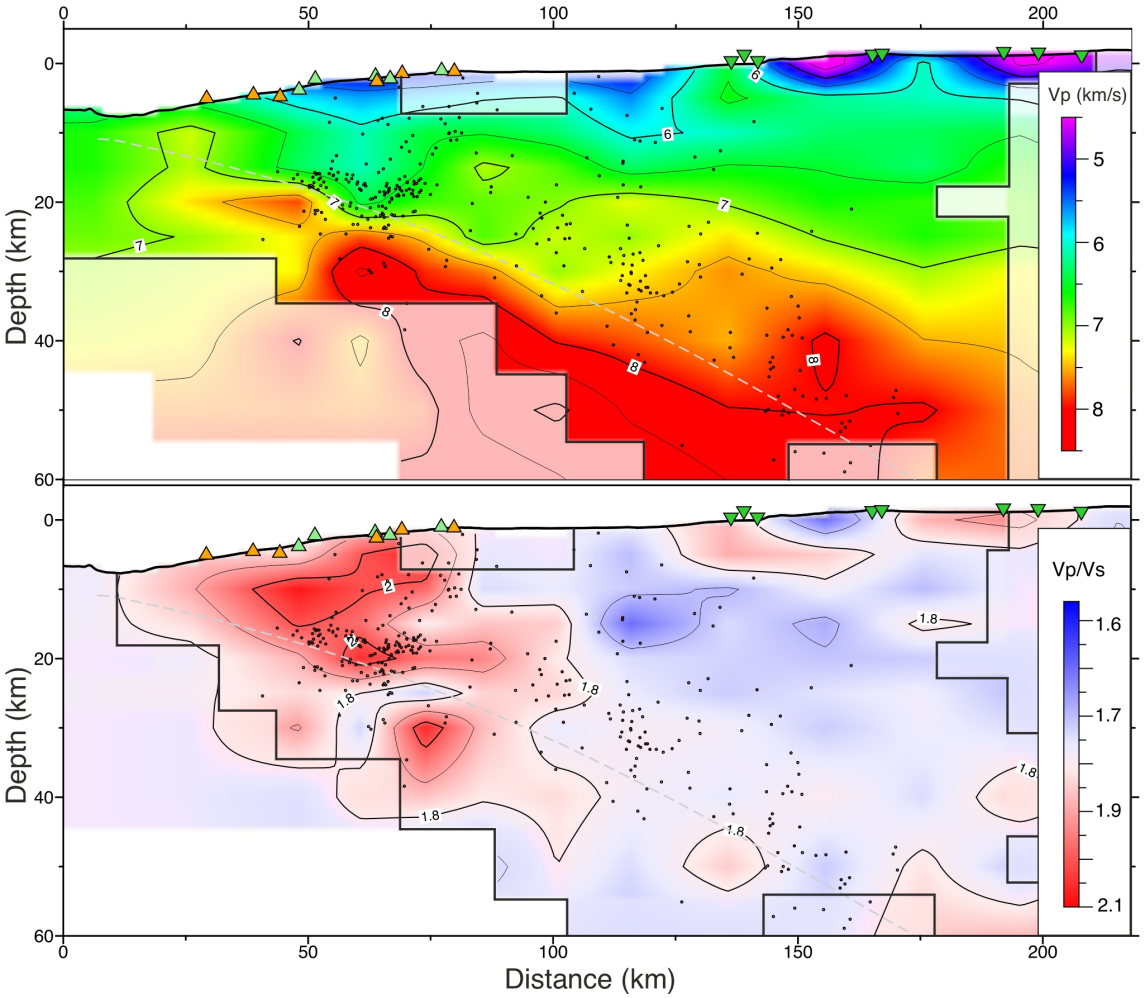


**Figure 5.8:** Local earthquake tomography at 20 °S west to east starting at 71.49 °W using SIMUL2000 (e.g., Thurber, 1983) and aftershock seismicity. The grey dashed line indicated the Slab2 model by (Hayes et al., 2018). OBS locations on the marine forearc are marked as triangles with defined color codes as in Figure 5.1 of the main manuscript. (Top) the *vp* model, (Bottom) *vp/vs* ratio. Black solid line encircles the region of good resolution.

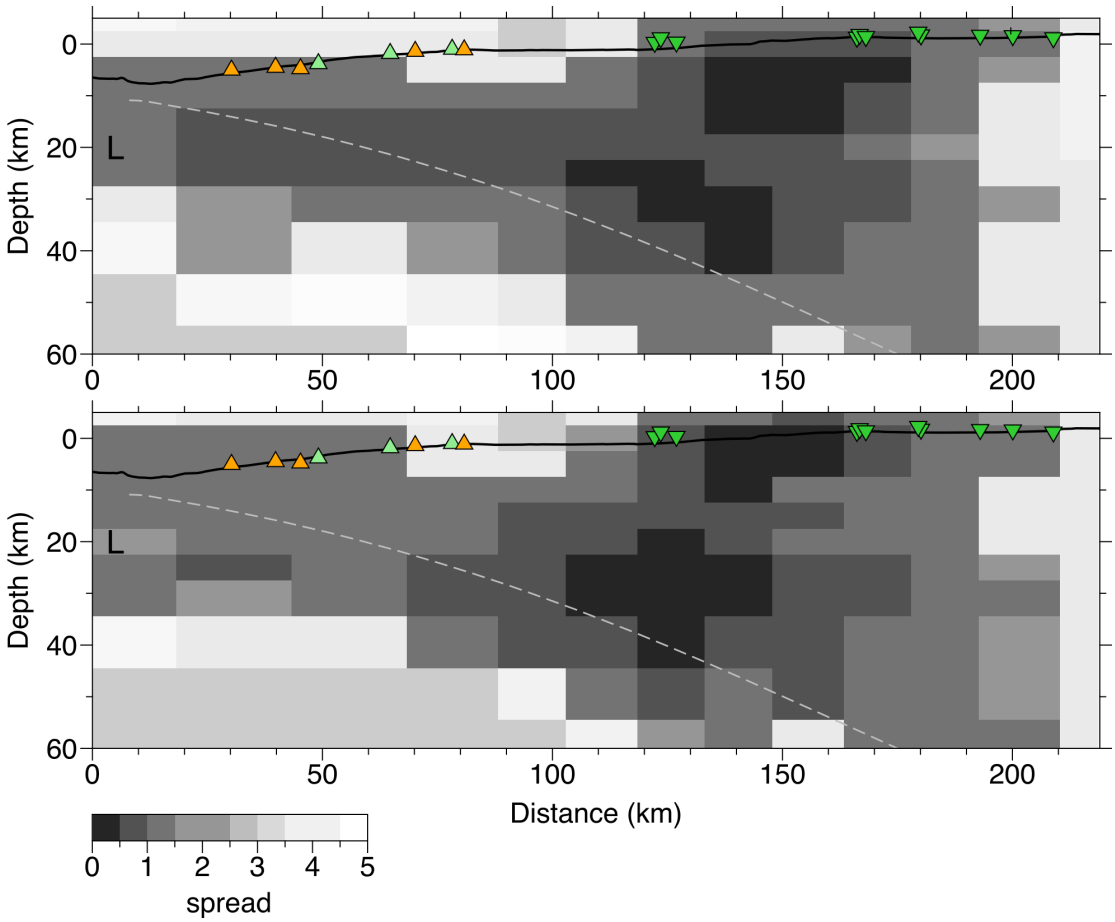


**Figure 5.9:** Spread of the two-dimensional local earthquake tomography model for *vp* (top) and *vp/vs* (bottom). Estimates are based on the analysis of the resolution matrix with gray shading following the spread function values.

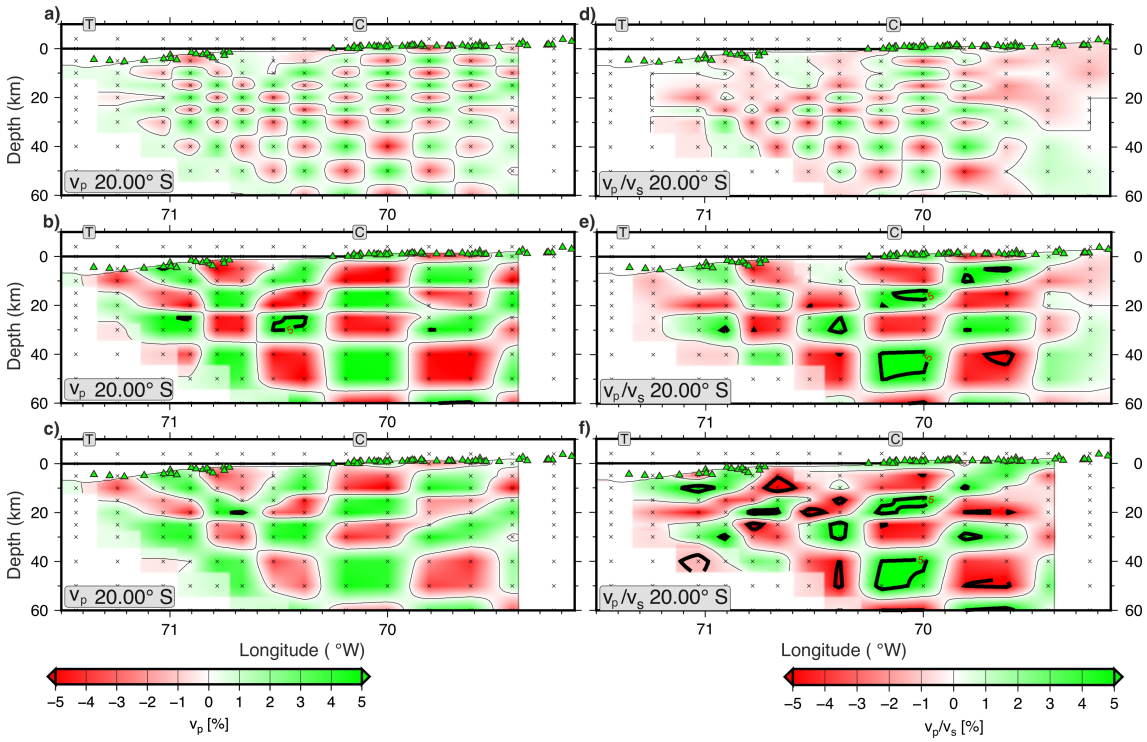


**Figure 5.10:** Checkerboards from the 2D local earthquake tomography. The profiles are oriented east west at 20 °S. Stations are shown with green triangles at their real depths (projected onto the profile at 20 °S. Contours lines exceeding the 5 % of the input checkerboard are indicated with black thick lines and are labelled. Nodes are indicated with crosses. The location of the coast (trench) is marked with C and T, respectively. (Left) (a) 1x1 checkerboard test vp, without noise; (b) 2x2 checkerboard test vp, without noise; (c) 2x2 checkerboard test vp, with noise dependent on the uncertainties of the different qualities of the picked phases. (Right) (d) 1x1 checkerboard test *vp/vs*, without noise; (e) 2x2 checkerboard test vp/vs, without noise; (f) 2x2 checkerboard test *vp/vs*, with noise dependent on the uncertainties of the different qualities of the picked phases.

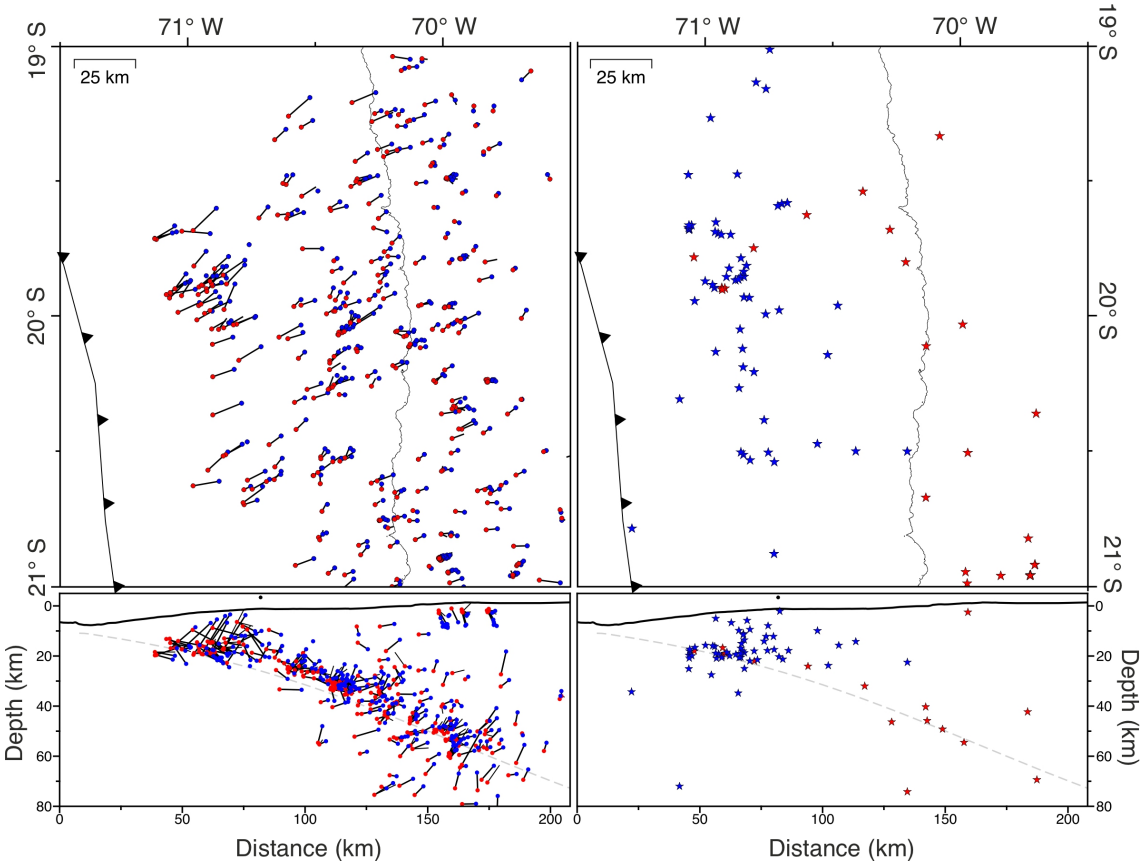


**Figure 5.11:** Difference between the OBS catalog of this study (blue dots/stars) and the catalog based on land stations from Soto et al. (2019) (red dots/stars). Both Catalogs overlapping 23 days in December 2014 and have 425 in common. (Right) Common events in both catalogs with the epicentral difference displayed as a black line. (Left) Blue stars indicate event locations that appear only in the amphibious catalog and red stars indicate event locations in the catalog of Soto et al. (2019).

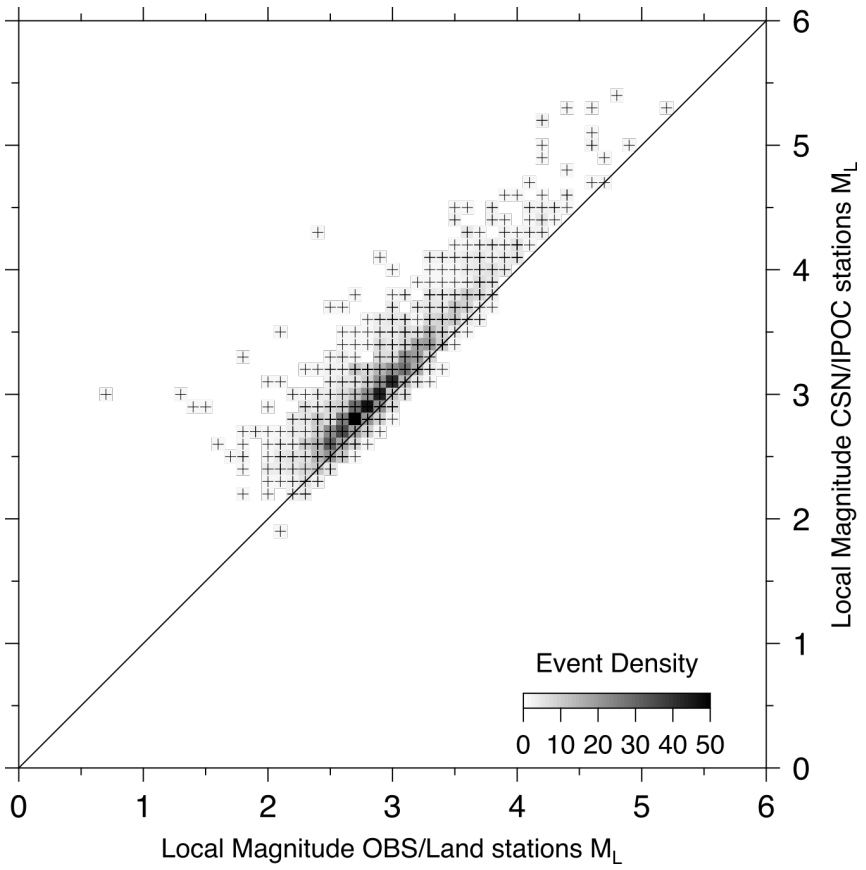


**Figure 5.12:** Local magnitudes of our catalog versus the local magnitudes of the CSN catalog (Barrientos, 2018).

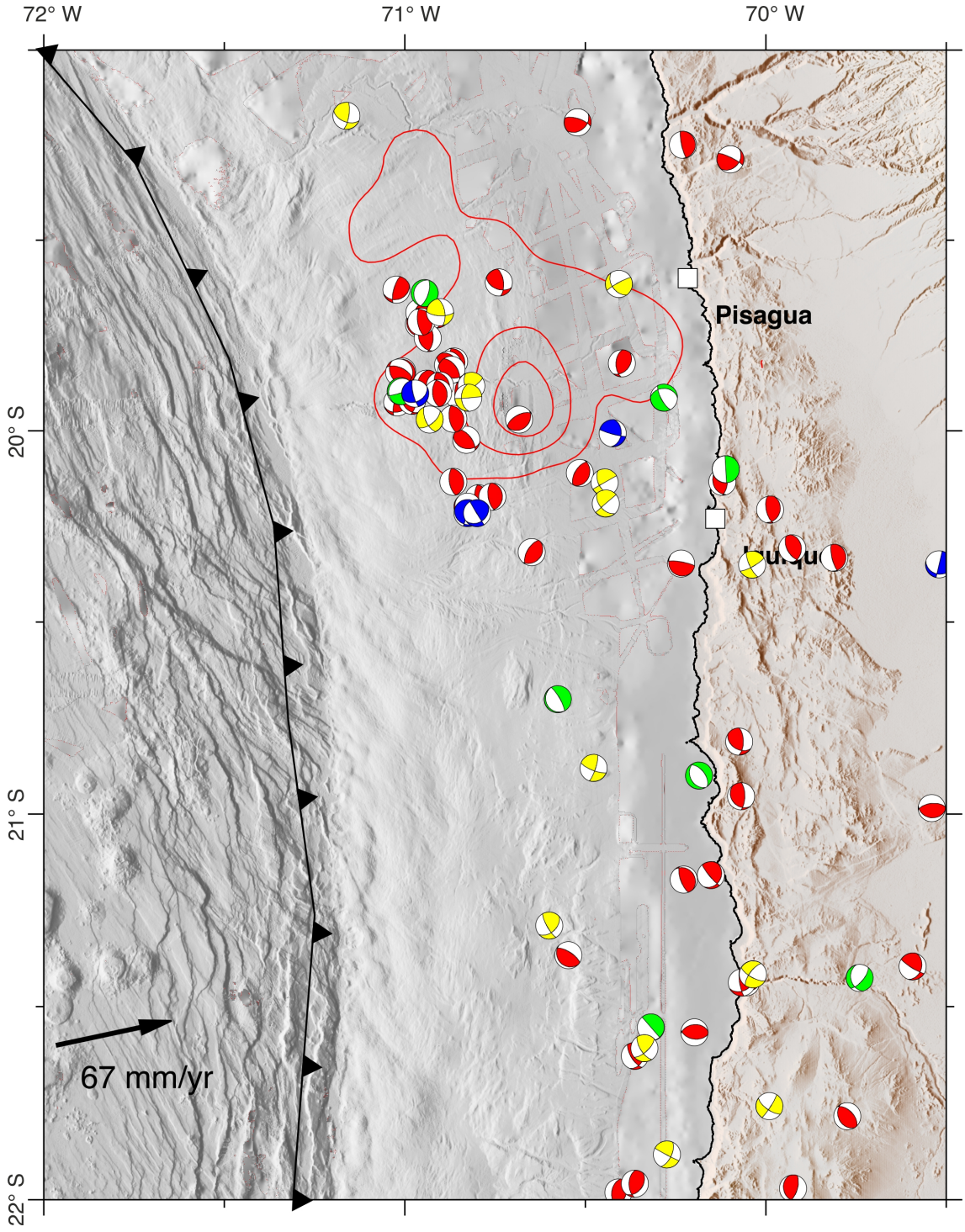


**Figure 5.13:** Focal mechanisms from FPFIT shown together with moment tensors from the gCMT catalogs (www.globalcmt.org). Beachballs are color-coded by faulting type in thrust (red), normal (green), strike-slip (yellow), or oblique (blue) fault mechanisms.

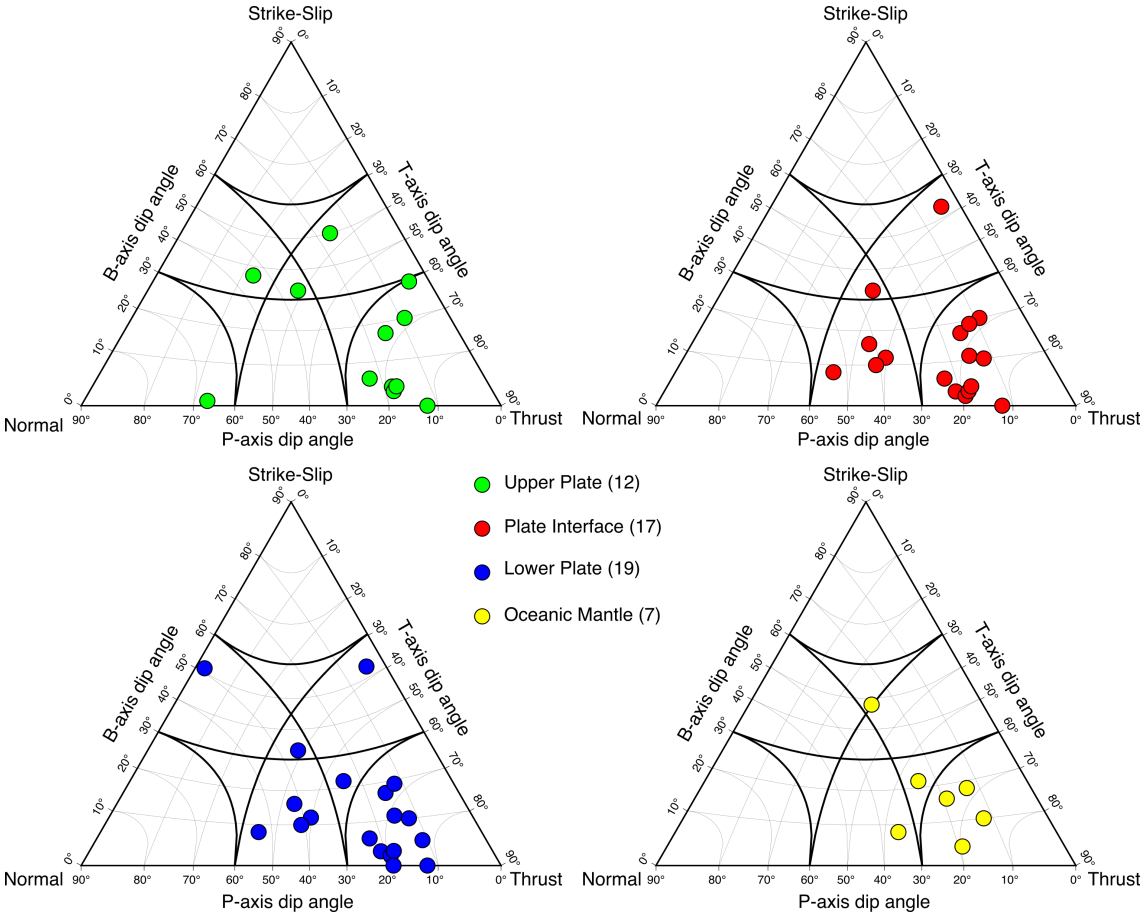


**Figure 5.14:** Ternary azimuthal gnomonic projection for the classification of focal mechanisms (Frohlich, 1992). Red circles indicate earthquakes with vertical distances to the plate interface of 5 km on either side of the plate interface of the global Slab2 model (Hayes et al., 2018). Blue circles are focal mechanisms of earthquakes in the subducting lower plate and orange circles are focal mechanisms deeper 10 km below the global Slab2 model.

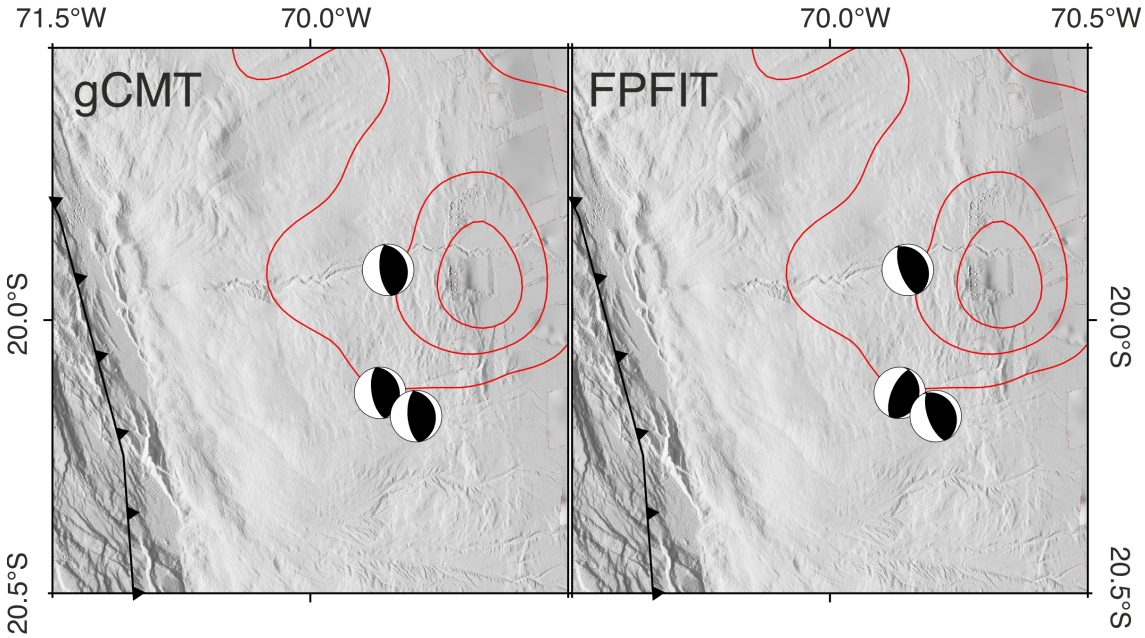


**Figure 5.15:** Comparison of focal mechanisms between the (left) global gCMT catalog solutions and (right) our FPFIT solutions (Reasenberg et al., 1985).

# 6 Marine forearc structure of eastern Java and its role in the 1994 Java tsunami earthquake

Yueyang Xia[1], Jacob Geersen[2], Dirk Klaeschen[1], **Bo Ma**[1], Dietrich Lange[1], Michael Riedel[1], Michael Schnabel[3], and Heidrun Kopp[1,2]

1) GEOMAR Helmholtz Centre for Ocean Research Kiel, Wischhofstr. 1-3, 24148 Kiel, Germany
2) Christian-Albrechts-Universität zu Kiel, Christian-Albrechts-Platz 4, 24118 Kiel, Germany
3) Bundesanstalt für Geowissenschaften und Rohstoffe (BGR), Stilleweg 2, 30655 Hannover, Germany

Published in **Solid Earth**, Nov 2021.

DOI: 10.5194/se-12-2467-2021

## Abstract

We resolve a previously unrecognized shallow subducting seamount from a re-processed multichannel seismic profile crossing the 1994 M7.8 Java tsunami earthquake rupture area. Seamount subduction occurs where the overriding plate experiences uplift by lateral shortening and vertical thickening. Pronounced back-thrusting at the landward slope of the forearc high and the formation of splay faults branching off the landward flank of the subducting seamount are observed. The location of the seamount in relation to the 1994 earthquake hypocentre and its co-seismic slip model suggests that the seamount acted as a seismic barrier to the up-dip co-seismic rupture propagation of this moderate size earthquake.

## 6.1 Introduction

Tsunami earthquakes represent a special class of seismic events that rupture the very shallow portion of a subduction plate boundary (Kanamori, 1972; Satake and Tanioka, 1999). They are characterized by a longer source duration compared to conventional earthquakes with a similar magnitude that nucleate at greater depth (Bilek and Lay, 2002). Despite being of only moderate surface wave magnitude, tsunami earthquakes commonly trigger an anomalously large tsunami. Due to the lack of severe ground shaking, coastal communities are often caught by surprise by the associated tsunami, resulting in potentially high numbers of fatalities (Satake et al., 2003). In spite of their often severe consequences, our current knowledge on tsunami earthquakes is insufficient to comprehensively understand their seismo-tectonic genesis and to identify regions that are particularly endangered.

The reduced rupture speed, large shallow slip, and moderate shaking of earthquakes that break the shallow plate boundary might be preconditioned by low rigidity in the outermost forearc (Bilek and Lay, 2002; Sallares and Ranero, 2019; Şen et al., 2015). Structural features invoked to explain the unusual slow rupture of tsunami earthquakes include the presence of excess topography on the subducting plate, which may act as a localized asperity (Abercrombie et al., 2001; Tanioka et al., 1997). Further explanations include rupture within unconsolidated subducted sediments (Kanamori, 1972; Satake and Tanioka, 1999), re-activated splay-faulting in the upper plate (Fan et al., 2017; von Huene et al., 2016; Wendt et al., 2009), vertical pop-up expulsion (Hananto et al., 2020), or inelastic shoving of unconsolidated sediments under the action of shallow slip (Seno, 2002; Tanioka and Seno, 2001).

With only 13 known events since 1896, tsunami earthquakes occur sporadically but are observed globally (Geersen, 2019). The Java margin, which constitutes the eastern portion

of the Sunda Arc (Kopp et al., 2006) was, however, affected twice by tsunami earthquakes in recent times (1994 and 2006). The 1994 Mw 7.8 earthquake (2 June, 1994 18:17:34 UTC) ruptured the shallow part of the plate boundary offshore easternmost Java (Fig. 6.1; Abercrombie et al., 2001). The co-seismic slip model is characterized by a non-uniform pattern, with the maximum slip under the forearc high (Abercrombie et al., 2001; Bilek, 2007). The induced ground motion and seafloor perturbation resulted in a severe tsunami with run-up heights of up to ~14 meters (Tsuji et al., 1995), causing significant damage to the local coastal area and approximately 250 casualties (Polet and Kanamori, 2000). The tsunami modelling for the 1994 Java earthquake reveals that the source of the larger-than-expected tsunami run-up could be linked to the horizontal displacement of the steep seafloor slope on the overriding plate (Tanioka and Satake, 1996).

The 1994 Java tsunami earthquake has been interpreted as having ruptured over a subducting seamount that induces a localized asperity within an overall low-coupled shallow plate boundary environment (Abercrombie et al., 2001; Bilek, 2007). This interpretation is based on the presence of multiple seamounts within the Java trench as recognized in early side-scan data (Masson et al., 1990), the presence of a well-developed shallow forearc-high (Fig. 6.1b), a positive gravity anomaly under the forearc high (Fig. 6.1c) and the dominance of normal faulting aftershocks in the outer rise (Abercrombie et al., 2001). To date, the presence of the seamount in the peak slip region of the 1994 earthquake has not been confirmed by marine seismic data (Lüschen et al., 2011; Shulgin et al., 2011). The previous interpretation (Abercrombie et al., 2001; Bilek, 2007) is in contrast to the notion that subducting seamounts affect the plate interface as a geometrical irregularity, induce permanent brittle deformation of the overriding plate and develop a heterogeneous stress field which does not support the generation of large earthquakes ($M > 8$) but rather favours moderate and small events ($4 < M < 8$) or aseismic creep (Kodaira et al., 2000; Ruh et al., 2016; Wang and Bilek, 2011; Martinez-Loriente et al., 2019).

In this study, we image the structure of the Java margin using multichannel reflection seismic data (MCS) in the region of the 1994 tsunami earthquake in order to resolve the relation of subducting lower plate topography and upper plate structure to the co-seismic slip distribution. Our study is based on enhanced processing of a multichannel seismic reflection line crossing the epicentral area. Re-processing of the profile aimed to improve the subsurface velocity model and to enhance the multiple suppression to augment the imaging quality. Pre-stack depth migration refines a combined P-wave velocity model from a MCS reflection tomography (Xia et al., 2022) and ocean bottom seismometer (OBS) refraction tomography (Shulgin et al., 2011).

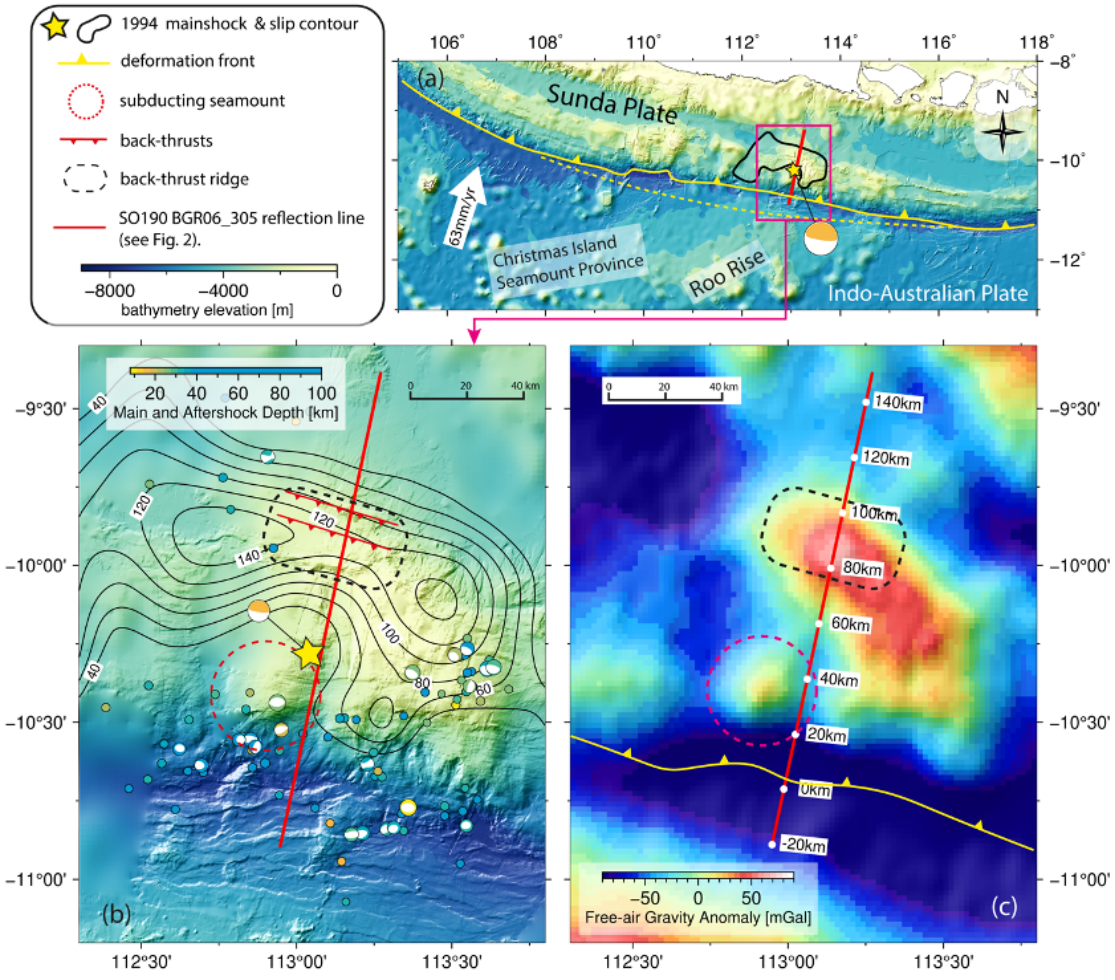


**Figure 6.1:** (a) Bathymetric overview, from the General Bathymetric Chart of the Oceans (GEBCO, 2020), of the Eastern Java Margin. Yellow line: deformation front. Dashed yellow line: assumed trend of the deformation front prior to frontal erosion related to the Roo Rise (Kopp et al., 2006). Yellow star: 1994 Java Tsunami earthquake epicentre. The moment tensor of the 1994 mainshock (gCMT, Dziewonski and Anderson, 1981; Ekström et al., 2012) is plotted at the position of the 1994 epicentre from the ISC-EHB Bulletin catalogue (Engdahl et al., 2020). Black line: rupture area of the 1994 Java Tsunami earthquake (Bilek, 2007). Red line: Seismic line SO190 BGR06_305 shown in Fig. 6.2. (b) Local bathymetry acquired during SO190 cruise overlain on the GEBCO_2020 grid. Black lines are slip contours (in cm) of the 1994 Java tsunami earthquake from (Bilek, 2007). The locations of the mainshock and largest aftershocks (03 June - 14 October 1994) are from the ISC-EHB Bulletin catalogue (Engdahl et al., 2020) and focal mechanisms from the gCMT catalogue (Dziewonski and Anderson, 1981; Ekström et al., 2012). The black dashed rectangle and the red triangle markers indicate the back-thrust ridge. The red dashed circle marks the bathymetric elevation associated with the shallow subducting seamount. Note the decrease of co-seismic slip and bending of contour lines around the subducting seamount. (c) Free-air gravity anomaly (Sandwell et al., 2014).

## 6.2 Data and Methods

The multichannel seismic reflection profile SO190 BGR06_305 was acquired in 2006 under the scope of the Sindbad Project during RV SONNE cruise SO190 conducted by the Federal Institute for Geosciences and Natural Resources (BGR) (Müller and Neben, 2006). The profile is part of a 2D survey covering the marine forearc offshore eastern Java and the Lesser Sunda Islands (Lüschen et al., 2011; Planert et al., 2010; Shulgin et al., 2011). BGR's G-Gun airgun array was used as a seismic source with a maximum total volume of 3,100 $in^3$ (50.8 l) and a towing depth of 6 m. Seismic signals were recorded by the 3,000 m long digital cable of BGR's SEAL System, which consists of 20 seismic sections with 240 channels in total.

Seismic pre-processing is summarized in Table 6.1 and is based on a routine that includes geometry set-up, common midpoint (CMP) binning, zero offset traces padding, bandpass filtering, shot interpolation, and random noise attenuation. We employed a free surface-related multiple prediction method to predict the multiple waves from the primary events based on the Kirchhoff integral (Fig. 6.6; Verschuur et al., 1992). An adaptive subtraction was used to eliminate the multiple (Guitton and Verschuur, 2004) and was applied using cascaded frequency bands (Table 6.1, Figs. 6.6 and 6.7). Three bands of frequency (0 - 12 Hz, 12 - 50 Hz, and 50 - 90 Hz) are defined in the adaptive subtraction to fit the spectrum discrepancies of the two inputs of the original data and modelled multiple (Fig. 6.7). This novel multiple suppression strategy greatly improved the resolution at depth by unveiling and preserving the deeper reflections previously blurred and covered by the seafloor multiple (Figs. 6.8 and 6.9). Fig. 6.9 illustrates the efficiency of this application. The multiple overprinted on the primaries in Fig. 6.9(a) are step-by-step eliminated by the adaptive subtraction, Radon dip filter, and the amplitude clipping. Remarkably, the adaptive subtraction of modelled multiple (Fig. 6.9, panel c) removed most of the multiple with similar dipping angle as the primaries, which are difficult to discriminate using a conventional dip filter (e.g., Radon filter in Fig. 6.9, panel d) at the near-offset. The initial velocity analysis is performed in the time domain with a CMP increment of 250 m and converted to the depth domain. This MCS *vp* model is subsequently merged with the OBS refraction model (Shulgin et al., 2011) to correct the *vp* field at greater depth (2 – 4 km below seafloor), from where little effective MCS reflection signal and moveout sensitivity is recorded (marked as the white band in Fig. 6.10). The merging of the velocity models is conducted with a smooth taper zone with a width of ~2 km to eliminate any abrupt *vp* changes. We used the final merged *vp* model as the initial model for the pre-stack depth migration. Subsequently, we conducted an iterative ray-based reflection depth tomography with a warping method to minimize the residual depth error to retrieve an optimized *vp* model (Xia et al., 2022). Most significant are the image improvements compared to Fig.3 of Lüschen et al. (2011) in the shallow subsurface structure of splay

fault - a, b, and c (Fig. 6.2) and in the deeper parts where the seafloor multiple overprinted the primary reflections.

Multibeam bathymetric data were collected during the SO190 cruise, using a SIMRAD EM120 multibeam echo sounder. The bathymetry survey was edited and merged with the GEBCO_2020 bathymetry (GEBCO, 2020) in the areas not covered by the multibeam soundings. Gravity data in this study are from Sandwell et al. (2014) based on satellite radar measurements.

## 6.3 Results

The oceanic Indo-Australian Plate off Java features a large number of seamounts and oceanic plateau (e.g. the Roo Rise) that form the northern extension of the Christmas Island Seamount Province (Fig. 6.1a). In the region of the 1994 earthquake, oceanic basement relief breaching the sediment infill is observed in the trench and currently colliding with the marine forearc (Fig. 6.1b, Masson et al., 1990; Kopp et al., 2011). The oceanic plate, which locally carries up to 1000 m of sediment, is shaped by bending related normal faults. The normal faults repeatedly offset the oceanic basement and shallow trench sediments, including the seamounts, leading to prominent seafloor escarpments (Fig. 6.1b). From around kilometre 5 landward of the trench, the décollement forms a ~40 km wide bulge or topographic elevation (Fig. 6.2c). The dip angle of the subducting oceanic basement increases from 2.6 ° on the seaward side of the bulge to ~10.2 ° on its landward side (Fig. 6.2a). With a height of ~2 km (Fig. 6.2) and a possible width of 40 km (interpreted from the bathymetry and free-air gravity (Fig. 6.1b-c)), this large subducting ridge or seamount (hereafter referred to as seamount) corresponds to some of the broad and wide topographic highs observed in the seafloor bathymetry that are associated with the Christmas Island Seamount Province (Fig. 6.1a). The seismic reflection pattern of the plate boundary differs substantially up-dip and down-dip of the seamount (Fig. 6.2a). High amplitude and negative polarity patches are imaged on the seaward side of the seamount crest (Figs. 6.2a and 6.3a, kilometres: 15 – 30), and associated a low *vp* (2500 – 3500 m/s) in the outermost forearc (Fig. 6.2c, depth 6 – 8 km, kilometres: 15 – 30). On the landward side, an increased *vp* (4000 – 5000 m/s) is inferred from the wide-angle seismic data (Shulgin et al., 2011) at the leading edge of the seamount (Fig. 6.2c, kilometres: 35 – 60, depth: 8 – 12 km) followed by a slight decrease farther landward (kilometres: 60 – 70, depth: 12 – 14 km).

Below the lowermost continental slope (Fig. 6.2a, kilometres: 0 – 12), a distinct set of landward dipping imbricate faults with high amplitudes defines the actively deforming frontal prism. The internal structure of the middle slope regime (Fig. 6.2a, kilometres: 12 – 32) is

characterized by lower amplitudes and an overall fine-scale fragmented reflection pattern (Fig. 6.2a). Comparable imbricate faults are much less distinct underneath the middle

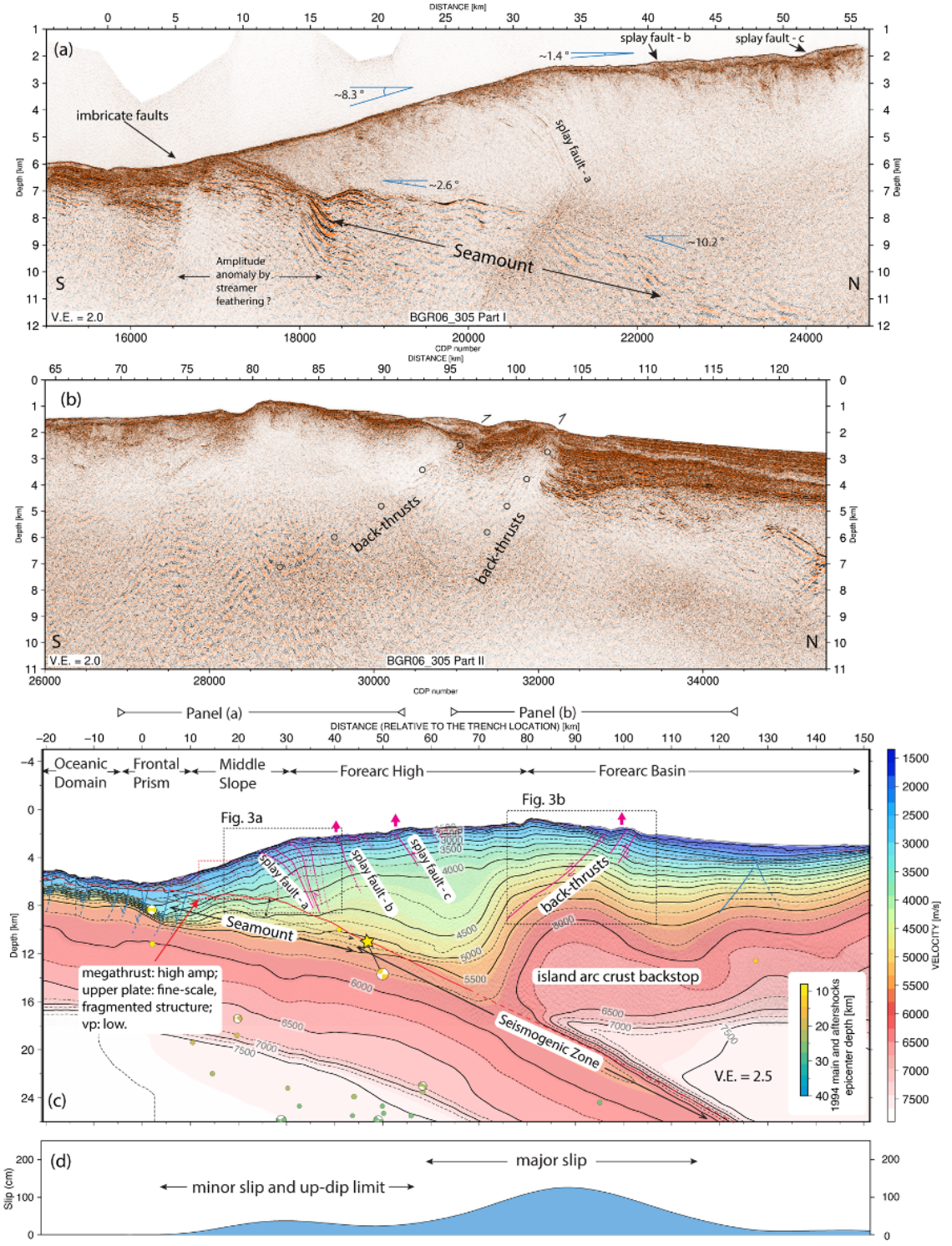


**Figure 6.2:** Pre-stack depth migrated section of seismic profile SO190 BGR06_305(Caption next page).

slope (Fig. 6.2a) than underneath the frontal prism. Both the frontal prism and middle slope domain host a steep seafloor with an inclination of about 8.3 ° (Fig. 6.2a, c). A distinct change in the slope of the seafloor at kilometre 32 defines the transition from the steeply inclined middle slope to the almost flat forearc high that extends between kilometres 32 - 102 (Fig. 6.2). The transition correlates with a prominent splay fault system that connects from the landward flank of the subducting seamount to the seafloor (Figs. 6.2a, c: splay fault - a, and 6.3a). At shallow depths (<5 km), the main splay fault divides into several branches that crop out at the seafloor between kilometres 24 - 30 (Figs. 6.2a and c, 6.3a). Reversed polarity reflections, relative to the seafloor are observed along the splay fault branches (Fig. 6.3a, insets (iii) and (iv)). At kilometres 40 and 52 in the forearc high, splay faults are also imaged from the seafloor to a depth of 3.5 km below the seafloor (Fig. 2a, c: splay fault - b, - c). The transition from the forearc high into the forearc basin (Fig. 6.2, kilometres: 95 - 105) is defined by a pronounced back-thrust (Figs. 6.2b, c, and 6.3b). The back-thrust dips seaward and is traced to 9 – 12 km depth, where seismic resolution diminishes and blurs a possible connection to the plate boundary below (Figs. 6.2b and 6.3b). It offsets the shallow sediments (vertical throw of 600 m) and links to a compressional ridge at the seafloor (Figs. 6.1b, 6.2b, 6.3b, and 6.4b).

A distinct positive gravity anomaly outlines the forearc high (dashed rectangle in Fig. 6.1c). This anomaly, however, does not correlate with a subducting topographic feature, as suggested in previous studies (Abercrombie et al., 2001; Bilek, 2007). Projected onto the seismic line (Fig. 6.2b), it correlates with a prominent block of high *vp* (6 – 7 km/s) in the island arc crust that has been interpreted as a forearc backstop (Shulgin et al., 2011). The above-mentioned back-thrust evolves along the edge of this high-velocity feature (Figs. 6.2c, and 6.5). A smaller, circular positive gravity anomaly is visible farther up-dip close to the deformation front (red dashed circle in Fig. 6.1c). This anomaly corre-

**Figure 6.2:** (a) Pre-stack depth migrated section of seismic profile SO190 BGR06_305 from the trench to the forearc high domain. (b) Pre-stack depth migrated section of seismic profile SO190 BGR06_305 covering the transition from the forearc high to the forearc basin. (c) Seismic section overlain by the vp model (based on MCS reflection tomography above 3 km depth, velocities below from (Shulgin et al., 2011), see Fig. 6.10), our structural interpretation, and the aftershock seismicity (from catalogue ISC-EHB Bulletin; Engdahl et al., 2020) of the 1994 Java tsunami earthquake. The hypocentre is marked as a yellow star. Coloured circles and beach-balls are aftershocks (Timespan: 03 June, 1994 to 14 Oct, 1994) from the ISC-EHB Bulletin catalogue (Engdahl et al., 2020) and focal mechanisms from the gCMT catalogue (Dziewonski and Anderson, 1981; Ekström et al., 2012). The well-developed forearc high (75 – 100 km) results from back-thrusting above the island arc crust backstop. A subducting seamount between kilometres 5 – 45 is overlain by upper plate splay faults. (d) Co-seismic slip model of the 1994 earthquake along the profile (Bilek, 2007). Peak slip occurred underneath the backstop (55 – 105 km) and decreased towards the subducting seamount (5 – 45 km).

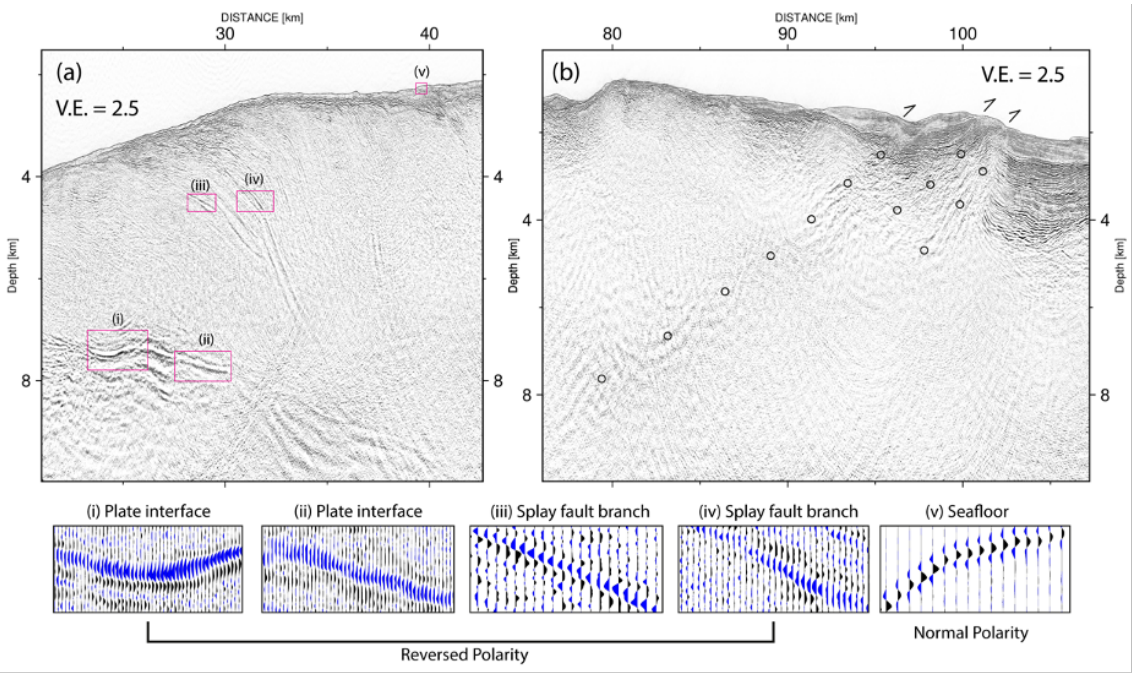


**Figure 6.3:** (a) Seismic section with a close-up view of the splay fault - a (compare Fig. 6.2c for location) branching from the landward side of the subducting seamount. Red boxes indicate close-up views shown in the lower panels. Reversed polarity reflections (relative to the seafloor) are observed at the plate interface seaward of the seamount and along the splay fault. The black and blue colors present positive and negative wavelet polarity, respectively. (b) Seismic section with a close-up view of the back-thrust (compare Fig. 6.2c for location). Black circles mark the back-thrust fault planes.

lates to the shallow subducting seamount under the middle slope identified in the seismic line.

## 6.4 Discussion

The depth section of seismic line SO190 BGR06_305 (Fig. 6.2a-b), which is based on advanced seismic processing techniques, resolves the tectonic structure in the region of the 1994 Java tsunami earthquake at a level of detail that largely exceeds earlier studies (Lüschen et al., 2011; Shulgin et al., 2011). In contrast to (Lüschen et al., 2011), who interpreted multiple small subducting seamounts in the shallow subduction zone, the improved imaging quality of the seismic profile reveals a single broad subducting seamount at the shallow plate boundary seaward of the forearc high. The distinct change in the dip of the décollement from ~2.6 ° under the outermost forearc to >10 ° seaward of kilometre 40 outlines the flanks of the seamount. The seamount modulates the seafloor bathymetry, causing a small circular bathymetric elevation (red circle in Fig. 6.1b) and is further manifested in

the circular free-air gravity anomaly close to the trench (red circle in Fig. 6.1c). Consistent with other well-imaged subducting seamounts (e.g., Kodaira et al., 2000; Bell et al., 2010) and results from analogue and numerical modelling (Ruh et al., 2016; Sun et al., 2020), we observe intensified compressional features at the leading edge of the seamount (Fig. 6.2a, c, kilometres: 32 – 65). In contrast, gravitational relaxation (e.g., decreased *vp*, fine-scale fragmented internal reflection, and high plate-boundary amplitudes with reversed polarity) is observed at the trailing edge of and above the seamount (Fig. 6.2a, c, kilometres: 15 – 32). Based on the extent of the seamount (2 km high, possibly 40 km wide) and the moderate crest angle (~10 degrees), we speculate that the true dimension of the seamount is even larger (~40 – 60 km) as the seismic line might only cross the seamount's eastern flank (compare the location of the bathymetry and gravity anomaly in Fig. 6.1c).

In the seismic profile, we observe splay faults, which feature seismic reflections with a strong amplitude, merging at the landward side of the seamount (Fig. 6.2a, c: splay fault - a, - b and - c, 6.3a, 6.4b). The reversed reflection polarity on the splay fault branches and shallow décollement (Fig. 6.3a) suggest that these faults act as fluid conduits and are weak, likely due to high porosity and high fluid content. Splay fault -b (Fig. 6.2a) causes a minor seafloor offset in the seismic section, while splay fault -c offsets the seafloor by ~500 m as seen both in the seismic section (Fig. 6.2a) and bathymetry map (Fig. 6.4b), indicating recent activity. Generically, splay faults form when the primary fault, in this case, the plate interface, becomes critically misaligned with the original principal stresses on the optimum plane (Scholz, 2010). Though a variety of scenarios could result in such a change of principal stress, we note that the structural modification of the plate boundary dipping angle induced by the subducting seamount at its leading edge will cause such a misalignment of the primary stress with the basal fault and further enhances the vertical thickening and lateral shortening of the upper plate (Lallemand and Lepichon, 1987).

The forearc high in the region of the 1994 Java tsunami earthquake is more evolved (i.e. shallower seafloor) compared to the adjacent regions along the margin (Fig. 6.1). This, in combination with the collocated gravity anomaly (dashed rectangle in Fig. 6.1b-c; kilometres: 75 – 105 in Fig. 6.2b), has fostered speculations about the presence of a subducting seamount in the peak slip region of the 1994 earthquake (Abercrombie et al., 2001). The re-processed seismic reflection image, however, suggests that the shallow forearc high is associated with lateral shortening and vertical thickening of the upper plate ahead of a seamount currently underthrust at shallow depth. Regional uplift of the forearc slope might be enhanced by the presence of an island arc backstop (Byrne et al., 1993). The backstop underneath the forearc high is expressed as a high *vp* block interpreted as crystalline island arc crust due to its *vp* of 6 – 7 km/s (Shulgin et al., 2011). The strong lateral velocity gradient underneath the crest of the forearc high is associated with an abrupt change in material properties, manifested in back-thrusting along the well-imaged

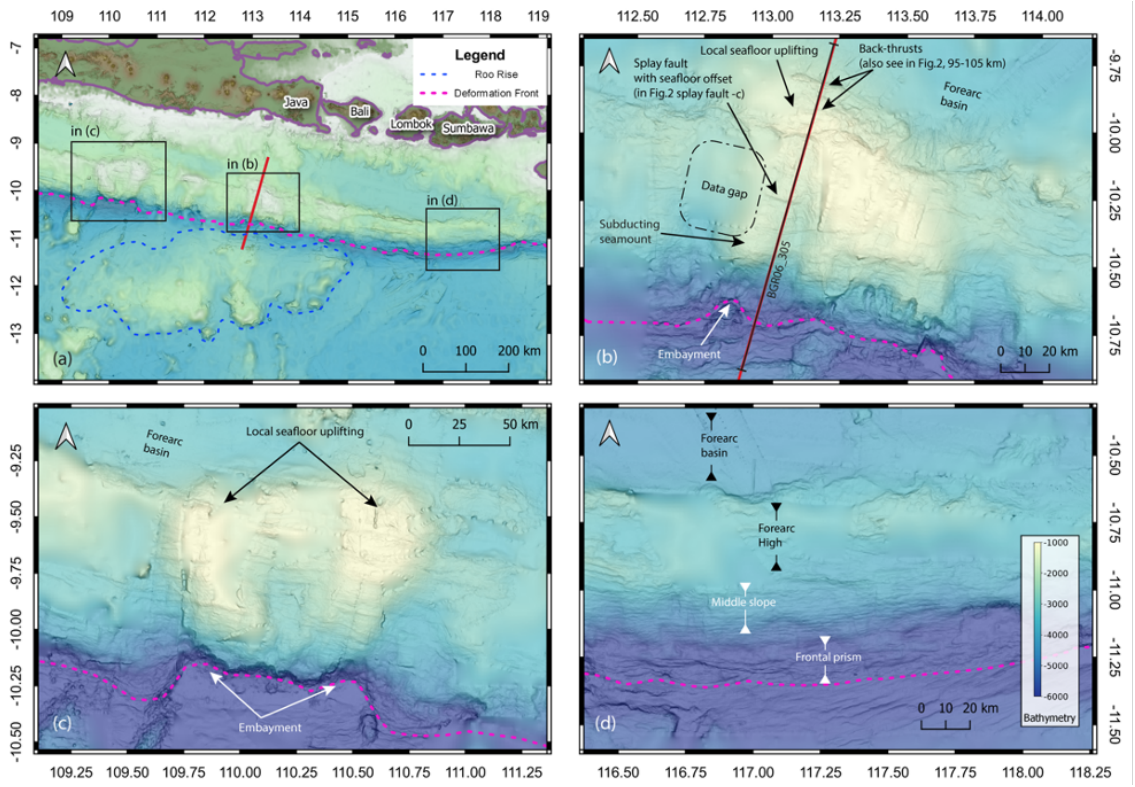


**Figure 6.4:** Global satellite bathymetry merged with ship-based multibeam data along the Java margin and Lesser Sunda islands (Bali, Lombok, and Sumbawa). Black squares indicate locations of close-up views in b) - d); red line indicates location of MCS profile BGR06_305 discussed in this study. (a) Bathymetry from 108.5 °E to 119.5 °E. The accretionary wedge from 109 °E to 115 °E is deformed and disturbed by the subducting seamounts and ridges associated with the Roo Rise. In comparison, the accretionary wedge from 115 °E to 119 °E forms a more homogeneous structure compared to the western area. (b) A close-up view of the bathymetry in the vicinity of MCS profile BGR06_305. An embayment of the deformation front is observed at the trailing edge of the subducting seamount. A thrust fault offsets the seafloor landward of the seamount. The forearc high and the southern margin of the forearc basin experience uplift to a water depth less than 1000 m. (c) A close view of the seafloor bathymetry off central Java. The accretionary wedge and forearc high are uplifted to shallow water depth of ~750 m, and the deformation front is characterized by a large embayment at the trench. (d) The seafloor bathymetry map offshore Lombok-Sumbawa reveals a much more homogenous accretionary wedge compared to its western counterparts.

fault plane (Fig. 6.3b - c) and the development of thrust ridges in the bathymetry at the seafloor outcrop of the back-thrust fault (Figs. 6.1b, and 6.4b). Along this line of argumentation, the mature forearc high reaching shallower water depths compared to its vicinity (Figs. 6.1b, and 6.4b), in the peak slip region of the 1994 Java tsunami earthquake, likely results from the combined effect of increased horizontal stress (pushing) ahead of the seamount and the presence of island arc crust serving as a rigid backstop. The resulting

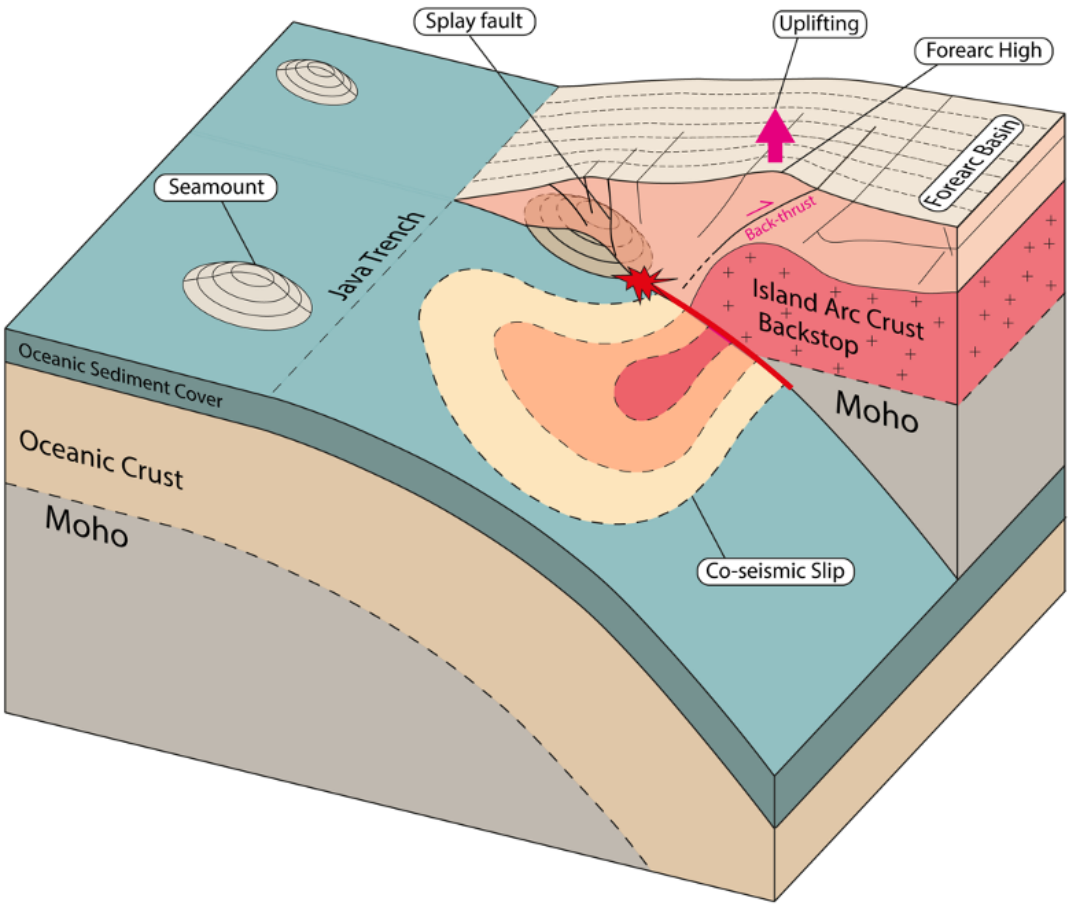


**Figure 6.5:** Conceptual seismo-tectonic model of the eastern Java margin in the region of the 1994 tsunami earthquake. Back-thrusting above the island arc crust backstop causes locally enhanced uplift of the forearc high. The 1994 hypocentre (red star) originated at the leading edge of a subducting seamount. The seamount stalled the co-seismic slip propagation locally along the plate boundary.

shortening and thickening of the upper plate are elucidated through a series of seaward vergent upper plate splay faults above the seamount and at least two well-imaged landward vergent backthrusts along the edge of the island arc backstop.

The rugged topography of the marine forearc in the central-eastern Java segment of the Sunda margin between 110 - 115 °E stands in contrast to adjacent regions offshore western Java or offshore the Lesser Sunda islands (Kopp et al., 2011). Figure 6.4 shows high-resolution bathymetric data acquired during cruises SO176, SO179 and SO190 with RV SONNE, merged with global satellite bathymetry (GEBCO, 2020). The subduction of the pronounced seafloor relief of the Christmas Island Seamount province literally breaks up the formerly coherent slopes of the forearc (Fig. 6.4a), as observed to the west and east.

This is evident from the crooked trend of the deformation front in this segment (Fig. 6.4b - c) compared to the uniformly developed lower and middle slope to the east (Fig. 6.4d). Between 110 - 114 °E the pronounced forearc basin found offshore western Java and offshore the Lesser Sunda islands is virtually squeezed together, as the forearc high and middle and lower slopes are offset to the north (Figs. 6.1a, 6.4a). These regional-scale processes are associated with local seafloor uplift, as observed in our study area (Fig. 6.4b) or around 110 °E (Fig. 6.4c), where water depth above the forearc high is even shallower (750 m). It should be noted in this context, though, that the 2006 Java tsunami earthquake (Ammon et al., 2006; Bilek, 2007), for which the reactivation of splay faults has been discussed (Fan et al., 2017), occurred west of the subduction of the Christmas Island Seamount province at 107.4 °E and that splay faults have also been imaged offshore the Sunda Strait and western Java (Kopp and Kukowski, 2003).

Abercrombie et al. (2001); Bilek (2007) relocated the 1994 hypocentre and modelled the co-seismic slip. Both studies share a similar event location and a grossly similar characteristic of the co-seismic slip models. The relocated hypocentre of the 1994 earthquake and the main co-seismic slip patch are located at the leading edge of the shallow subducting seamount (Fig. 6.1). The co-seismic slip further seems to taper around the subducting seamount, whereas in the seamount region (red dashed circle in Fig. 6.1b), the slip value decreases significantly (Figs. 6.1b, 6.2c - d,, kilometres: 5 – 45). These observations lead us to reconsider if the 1994 Java tsunami earthquake ruptured across a subducting seamount or if the seamount might have played a different role in the event. From numerical models, there is evidence that subducting seamounts induce overpressures and increase shear stress at their leading edge in a region that is equivalent to their own size (Ruh et al., 2016). This would be approximately 1250 $km^2$ for a seamount of over 40 km in diameter as the one observed, which could be enough to generate an earthquake of M 7 - 8 (Blaser et al., 2010). From this, we conclude that increased shear stress in front of the subducting seamount may have preconditioned the 1994 Java tsunami earthquake.

The warping of the slip model isolines around the subducting seamount (Fig. 6.1b) indicates that the seamount acted as a geometrical barrier at shallow depth during the co-seismic phase. Along the seismic section BGR06_305, the co-seismic slip value tracked from the model (Bilek, 2007) illustrates a low slip value in the seamount region, compared to a much higher value further downdip (Fig. 6.2d). Yang et al. (2012, 2013) modelled a dynamic rupture scenario with a seamount as a seismic barrier. The seamount imaged on our seismic profile may have halted seismic rupture at its leading edge, while rupture might have progressed closer to the trench to the west and east of the seamount (Figs. 6.1b and 6.5). Due to the lack of 3D seismic coverage of the rupture area, the exact structural control on the three-dimensional evolution of the rupture cannot be constrained. A similar mechanism of plate boundary rupture terminating against subducting lower plate relief is,

however, discussed for the 2006 Java tsunami earthquake (Bilek, 2007) as well as numerous other plate boundary events (Wang and Bilek, 2011).

## 6.5 Conclusion

A re-processed multichannel seismic reflection image with effective seafloor multiple suppression and a combined subsurface velocity from reflection and refraction tomography reveals a large subducting seamount at shallow depth (2 km – 8 km below seafloor) trenchward of the rupture area of the 1994 Java tsunami earthquake. Lateral shortening and vertical thickening of the upper plate control the uplift of the forearc high, manifested in active back-thrusting along distinct fault planes above the island arc crust backstop (Fig. 6.5). The 1994 earthquake main shock hypocentre and main co-seismic slip patch locate in front of the shallow subducting seamount. The wrapping of the co-seismic slip contours around this seamount suggests that it may have acted as a seismic barrier during the 1994 Java tsunami earthquake (Fig. 6.1). These observations suggest that the seamount diverted the co-seismic rupture propagation in the up-dip direction and document the control of the shallow marine forearc structure on co-seismic rupture distribution (Fig. 6.5).

## Acknowledgments

The seismic data were processed with Schlumberger's Omega2 seismic processing suite OMEGA and Seismic Unix - an open-source software package for seismic research and processing, Centre for Wave Phenomena, Colorado School of Mines. Bathymetry and seismic images are plotted by the Generic Mapping Tools (GMT). We thank S. Bilek, and R. Abercrombie for sharing the co-seismic slip models of the 1994 Java tsunami earthquake. We thank Nathan L. Bangs and Sara Martínez-Loriente for insightful comments and suggestions that helped us improve the paper. Figure 6.1 and 6.4 were prepared using GMT (Wessel et al., 2019).

## Data availability

The pre-stack depth migration section of the profile BGR06_305 is available upon reasonable request. Bathymetric data from *R/V SONNE* cruise SO190 can be requested through the German Bundesamt für Seeschifffahrt und Hydrographie (BSH; `http://www.bsh.de`).

Aftershock data displayed in Figures 6.1b and 6.2c are available through the ISC-EHB Bulletin catalogue (www.isc.ac.uk/isc-ehb; (Engdahl et al., 2020)). Focal mechanisms are available through the gCMT catalogue (https://www.globalcmt.org/; (Dziewonski and Anderson, 1981; Ekström et al., 2012)). The free-air gravity data shown in Figure 1c is available through https://topex.ucsd.edu/WWW_html/mar_grav.html (Sandwell et al., 2014).

## Competing interest

The authors declare that they have no competing interests.

## Financial support

*R/V SONNE* cruise SO190 and the SINDBAD project were funded by the German Federal Ministry of Education and Research (BMBF) under grants 03G0190A and 03G0190B. Y. Xia acknowledges funding from the China Scholarship Council (grant 201506400067).

## References

Abercrombie, R. E., Antolik, M., Felzer, K., & Ekstrom, G. (2001). The 1994 java tsunami earthquake: Slip over a subducting seamount. *Journal of Geophysical Research-Solid Earth*, *106*(B4), 6595–6607, https://doi.org/10.1029/2000jb900403.

Ammon, C. J., Kanamori, H., Lay, T., & Velasco, A. A. (2006). The 17 july 2006 java tsunami earthquake. *Geophysical Research Letters*, *33*(24), https://doi.org/10.1029/2006gl028005.

Bell, R., Sutherland, R., Barker, D. H. N., Henrys, S., Bannister, S., Wallace, L., & Beavan, J. (2010). Seismic reflection character of the hikurangi subduction interface, new zealand, in the region of repeated gisborne slow slip events. *Geophysical Journal International*, *180*(1), 34–48, https://doi.org/10.1111/j.1365-246X.2009.04401.x.

Bilek, S. L. (2007). Influence of subducting topography on earthquake rupture. *The Seismogenic Zone of Subduction Thrust Faults*, (pp. 123–146).

Bilek, S. L. & Lay, T. (2002). Tsunami earthquakes possibly widespread manifestations of frictional conditional stability. *Geophysical Research Letters*, *29*(14), 18–1, https://doi.org/10.1029/2002gl015215.

Blaser, L., Krüger, F., Ohrnberger, M., & Scherbaum, F. (2010). Scaling relations of earthquake source parameter estimates with special focus on subduction environment. *Bulletin of the Seismological Society of America*, *100*(6), 2914–2926, https://doi.org/10.1785/0120100111.

Byrne, D. E., Wang, W. H., & Davis, D. M. (1993). Mechanical role of backstops in the growth of fore-arcs. *Tectonics*, *12*(1), 123–144, https://doi.org/10.1029/92tc00618.

Dziewonski, A. M. & Anderson, D. L. (1981). Preliminary reference earth model. *Physics of the earth and planetary interiors*, *25*(4), 297–356, https://doi.org/10.1016/0031-9201(81)90046-7.

Ekström, G., Nettles, M., & Dziewoński, A. (2012). The global cmt project 2004–2010: Centroid-moment tensors for 13,017 earthquakes. *Physics of the Earth and Planetary Interiors*, *200*, 1–9, https://doi.org/10.1016/j.pepi.2012.04.002.

Engdahl, E. R., Di Giacomo, D., Sakarya, B., Gkarlaouni, C. G., Harris, J., & Storchak, D. A. (2020). Isc-ehb 1964–2016, an improved data set for studies of earth structure and global seismicity. *Earth and Space Science*, *7*(1), e2019EA000897, https://doi.org/10.1029/2019EA000897.

Fan, W., Bassett, D., Jiang, J., Shearer, P. M., & Ji, C. (2017). Rupture evolution of the 2006 Java tsunami earthquake and the possible role of splay faults. *Tectonophysics*, *721*(September), 143–150, https://doi.org/10.1016/j.tecto.2017.10.003 http://dx.doi.org/10.1016/j.tecto.2017.10.003.

Geersen, J. (2019). Sediment-starved trenches and rough subducting plates are conducive to tsunami earthquakes. *Tectonophysics*, *762*, 28–44, https://doi.org/10.1016/j.tecto.2019.04.024.

Guitton, A. & Verschuur, D. (2004). Adaptive subtraction of multiples using the l1-norm. *Geophysical prospecting*, *52*(1), 27–38, https://doi.org/10.1046/j.1365-2478.2004.00401.x.

Hananto, N., Leclerc, F., Li, L., Etchebes, M., Carton, H., Tapponnier, P., Qin, Y., Avianto, P., Singh, S., & Wei, S. (2020). Tsunami earthquakes: Vertical pop-up expulsion at the forefront of subduction megathrust. *Earth and Planetary Science Letters*, *538*, 116197, https://doi.org/10.1016/j.epsl.2020.116197.

Kanamori, H. (1972). Mechanism of tsunami earthquakes. *Physics of the earth and planetary interiors*, *6*(5), 346–359, https://doi.org/10.1016/0031-9201(72)90058-1.

Kodaira, S., Takahashi, N., Nakanishi, A., Miura, S., & Kaneda, Y. (2000). Subducted seamount imaged in the rupture zone of the 1946 nankaido earthquake. *Science*, *289*(5476), 104–6, https://doi.org/10.1126/science.289.5476.104.

Kopp, H., Flueh, E. R., Petersen, C. J., Weinrebe, W., Wittwer, A., & Scientists, M. (2006). The java margin revisited: Evidence for subduction erosion off java. *Earth and Planetary Science Letters*, *242*(1-2), 130–142, https://doi.org/10.1016/j.epsl.2005.11.036.

Kopp, H. & Kukowski, N. (2003). Backstop geometry and accretionary mechanics of the sunda margin. *Tectonics*, *22*(6), https://doi.org/10.1029/2002tc001420.

Kopp, H., Weinzierl, W., Becel, A., Charvis, P., Evain, M., Flueh, E. R., Gailler, A., Galve, A., Hirn, A., Kandilarov, A., Klaeschen, D., Laigle, M., Papenberg, C., Planert, L., Roux, E., Team, T., & Team, T. (2011). Deep structure of the central lesser antilles island arc: Relevance for the formation of continental crust. *Earth and Planetary Science Letters*, *304*(1-2), 121–134, https://doi.org/10.1016/j.epsl.2011.01.024.

Lallemand, S. & Lepichon, X. (1987). Coulomb wedge model applied to the subduction of seamounts in the japan trench. *Geology*, *15*(11), 1065–1069, https://doi.org/10.1130/0091-7613(1987)15<1065:Cwmatt>2.0.Co;2.

Lüschen, E., Müller, C., Kopp, H., Engels, M., Lutz, R., Planert, L., Shulgin, A., & Djajadihardja, Y. S. (2011). Structure, evolution and tectonic activity of the eastern sunda forearc, indonesia, from marine seismic investigations. *Tectonophysics*, *508*(1-4), 6–21, https://doi.org/10.1016/j.tecto.2010.06.008.

Martinez-Loriente, S., Sallares, V., Ranero, C. R., Ruh, J. B., Barckhausen, U., Grevemeyer, I., & Bangs, N. (2019). Influence of incoming plate relief on overriding plate deformation and earthquake nucleation: Cocos ridge subduction (costa rica). *Tectonics*, *38*(12), 4360–4377, https://doi.org/10.1029/2019tc005586.

Masson, D. G., Parson, L. M., Milsom, J., Nichols, G., Sikumbang, N., Dwiyanto, B., & Kallagher, H. (1990). Subduction of seamounts at the java trench - a view with long-range sidescan sonar. *Tectonophysics*, *185*(1-2), 51–65, https://doi.org/10.1016/0040-1951(90)90404-V.

Müller, C. & Neben, S. (2006). Research cruise so190 leg 1, sindbad, seismic and geoacoustic investigations along the sunda-banda arc transition (seismische und geoakustische untersuchungen entlang des Übergangs vom sunda- zum banda-bogen) with rv sonne, jakarta, indonesia 09th october 2006 - darwin, australia 09th november 2006 https://www.tib.eu/de/suchen/id/awi%3A4f0d205a97610f05343bdca9a2a3ab03fcce996e.

Planert, L., Kopp, H., Lueschen, E., Mueller, C., Flueh, E., Shulgin, A., Djajadihardja, Y., & Krabbenhöft, A. (2010). Lower plate structure and upper plate deformational segmentation at the sunda-banda arc transition, indonesia. *Journal of Geophysical Research: Solid Earth*, *115*(B8), https://doi.org/10.1029/2009JB006713.

Polet, J. & Kanamori, H. (2000). Shallow subduction zone earthquakes and their tsunamigenic potential. *Geophysical Journal International*, *142*(3), 684–702, https://doi.org/10.1046/j.1365-246x.2000.00205.x.

Ruh, J. B., Sallares, V., Ranero, C. R., & Gerya, T. (2016). Crustal deformation dynamics and stress evolution during seamount subduction: High-resolution 3-d numerical modeling. *Journal of Geophysical Research-Solid Earth*, *121*(9), 6880–6902, https://doi.org/10.1002/2016jb013250.

Sallares, V. & Ranero, C. R. (2019). Upper-plate rigidity determines depth-varying rupture behaviour of megathrust earthquakes. *Nature*, *576*(7785), 96–+, https://doi.org/10.1038/s41586-019-1784-0.

Sandwell, D. T., Müller, R. D., Smith, W. H., Garcia, E., & Francis, R. (2014). New global marine gravity model from cryosat-2 and jason-1 reveals buried tectonic structure. *science*, *346*(6205), 65–67, https://doi.org/10.1126/science.1258213.

Satake, K. & Tanioka, Y. (1999). Sources of tsunami and tsunamigenic earthquakes in subduction zones. *Pure and Applied Geophysics*, *154*(3), 467–483, https://doi.org/10.1029/2003jb002521.

Satake, K., Wang, K. L., & Atwater, B. F. (2003). Fault slip and seismic moment of the 1700 cascadia earthquake inferred from japanese tsunami descriptions. *Journal of Geophysical Research-Solid Earth*, *108*(B11), https://doi.org/10.1007/s000240050240.

Scholz, C. H. (2010). Predicting the unpredictable the tumultuous science of earthquake prediction. *Science*, *327*(5969), 1082–1082, https://doi.org/10.1126/science.1187372.

Seno, T. (2002). Tsunami earthquakes as transient phenomena. *Geophysical research letters*, *29*(10), 58–1, https://doi.org/10.1029/2002GL014868.

Shulgin, A., Kopp, H., Mueller, C., Planert, L., Lueschen, E., Flueh, E. R., & Djajadihardja, Y. (2011). Structural architecture of oceanic plateau subduction offshore eastern java and the potential implications for geohazards. *Geophysical Journal International*, *184*(1), 12–28, https://doi.org/10.1111/j.1365-246X.2010.04834.x.

Sun, T. H., Saffer, D., & Ellis, S. (2020). Mechanical and hydrological effects of seamount subduction on megathrust stress and slip. *Nature Geoscience*, *13*(3), 249–+, https://doi.org/10.1038/s41561-020-0542-0.

Tanioka, Y., Ruff, L., & Satake, K. (1997). What controls the lateral variation of large earthquake occurrence along the japan trench? *Island Arc*, *6*(3), 261–266, https://doi.org/10.1111/j.1440-1738.1997.tb00176.x.

Tanioka, Y. & Satake, K. (1996). Fault parameters of the 1896 sanriku tsunami earthquake estimated from tsunami numerical modeling. *Geophysical Research Letters*, *23*(13), 1549–1552, https://doi.org/10.1029/96gl01479.

Tanioka, Y. & Seno, T. (2001). Sediment effect on tsunami generation of the 1896 sanriku tsunami earthquake. *Geophysical Research Letters*, *28*(17), 3389–3392, https://doi.org/10.1029/2001GL013149.

Tsuji, Y., Imamura, F., Matsutomi, H., Synolakis, C. E., Nanang, P. T., Harada, S., Han, S. S., Arai, K., Cook, B., et al. (1995). Field survey of the east java earthquake and tsunami of june 3, 1994. In *Tsunamis: 1992–1994* (pp. 839–854). Springer.

Verschuur, D. J., Berkhout, A. J., & Wapenaar, C. P. A. (1992). Adaptive surface-related multiple elimination. *Geophysics*, *57*(9), 1166–1177, https://doi.org/10.1190/1.1443330.

von Huene, R., Miller, J. J., Klaeschen, D., & Dartnell, P. (2016). A possible source mechanism of the 1946 unimak alaska far-field tsunami: Uplift of the mid-slope terrace above a splay fault zone. *Pure and Applied Geophysics*, *173*(12), 4189–4201, https://doi.org/10.1007/s00024-016-1393-x.

Wang, K. L. & Bilek, S. L. (2011). Do subducting seamounts generate or stop large earthquakes? *Geology*, *39*(9), 819–822, https://doi.org/10.1130/G31856.1.

Wendt, J., Oglesby, D. D., & Geist, E. L. (2009). Tsunamis and splay fault dynamics. *Geophysical Research Letters*, *36*(15), https://doi.org/10.1029/2009GL038295.

Wessel, P., Luis, J. F., Uieda, L., Scharroo, R., Wobbe, F., Smith, W. H. F., & Tian, D. (2019). The generic mapping tools version 6. *Geochemistry, Geophysics, Geosystems*, *20*(11), 5556–5564, https://doi.org/10.1029/2019gc008515.

Xia, Y. Y., Klaeschen, D., Kopp, H., & Schnabel, M. (2022). Reflection tomography by depth warping: a case study across the java trench. *Solid Earth*, *13*(2), 367–392, https://doi.org/10.5194/se-13-367-2022.

Yang, H., Liu, Y., & Lin, J. (2012). Effects of subducted seamounts on megathrust earthquake nucleation and rupture propagation. *Geophysical Research Letters*, *39*(24), https://doi.org/10.1029/2012GL053892.

Yang, H., Liu, Y., & Lin, J. (2013). Geometrical effects of a subducted seamount on stopping megathrust ruptures. *Geophysical Research Letters*, *40*(10), 2011–2016, https://doi.org/10.1002/grl.50509.

Şen, A. T., Cesca, S., Lange, D., Dahm, T., Tilmann, F., & Heimann, S. (2015). Systematic changes of earthquake rupture with depth: A case study from the 2010 mw 8.8 maule, chile, earthquake aftershock sequence. *Bulletin of the Seismological Society of America*, *105*(5), 2468–2479, https://doi.org/10.1785/0120140123.

## Supporting Information

**Table 6.1:** Seismic processing sequences.

| **Sequence Step Names** |
|---|
| Normal and Nominal Geometry Establishment with Common Midpoint (CMP) spacing of 6.25 m |
| Anomalous and Random Noise Attenuation |
| Offset regularization and Interpolation to Zero Offset |
| Interactive Velocity Analysis in Time Domain |
| Initial Time-domain Velocity building |
| Shot Interpolation for Aliasing Elimination (from 50 m to 12.5 m shot distance) |
| Free Surface-Related Multiple Prediction |
| Multiple Attenuation 1: Frequency-Split 2D Cascaded Adaptive Filter |
| Multiple Attenuation 2: Radon Dip Filter |
| Multiple Attenuation 3: Inside Mute and Amplitude Clipping |
| Kirchhoff Pre-stack Time Migration |
| Initial Depth Domain Velocity Building (Merge with Wide-angle model) |
| Kirchhoff Pre-stack Depth Migration with Common Image Point (CIP) gather output (Initial) |
| **Iteration Loop** |
| CIP Gather Pre-filtering for Non-Rigid-Matching (NRM) Calculation |
| NRM Displacement Field Calculation |
| CIP Gather Residual Move-Out (RMO) Calculation from NRM Field |
| Dip and Coherency Field Estimation from Depth Migrated Stack |
| Ray-based RMO Depth-Tomography with preconditioning of Dip and Coherency Field |
| Update the Tomography Model Properties to Reduce the CIP-gather RMO |
| Kirchhoff Pre-stack Depth Migration with CIP-gather Output |
| Iteration Stopped if RMO is Minimized |
| Stacking of the Pre-stack Depth Migrated Gathers |

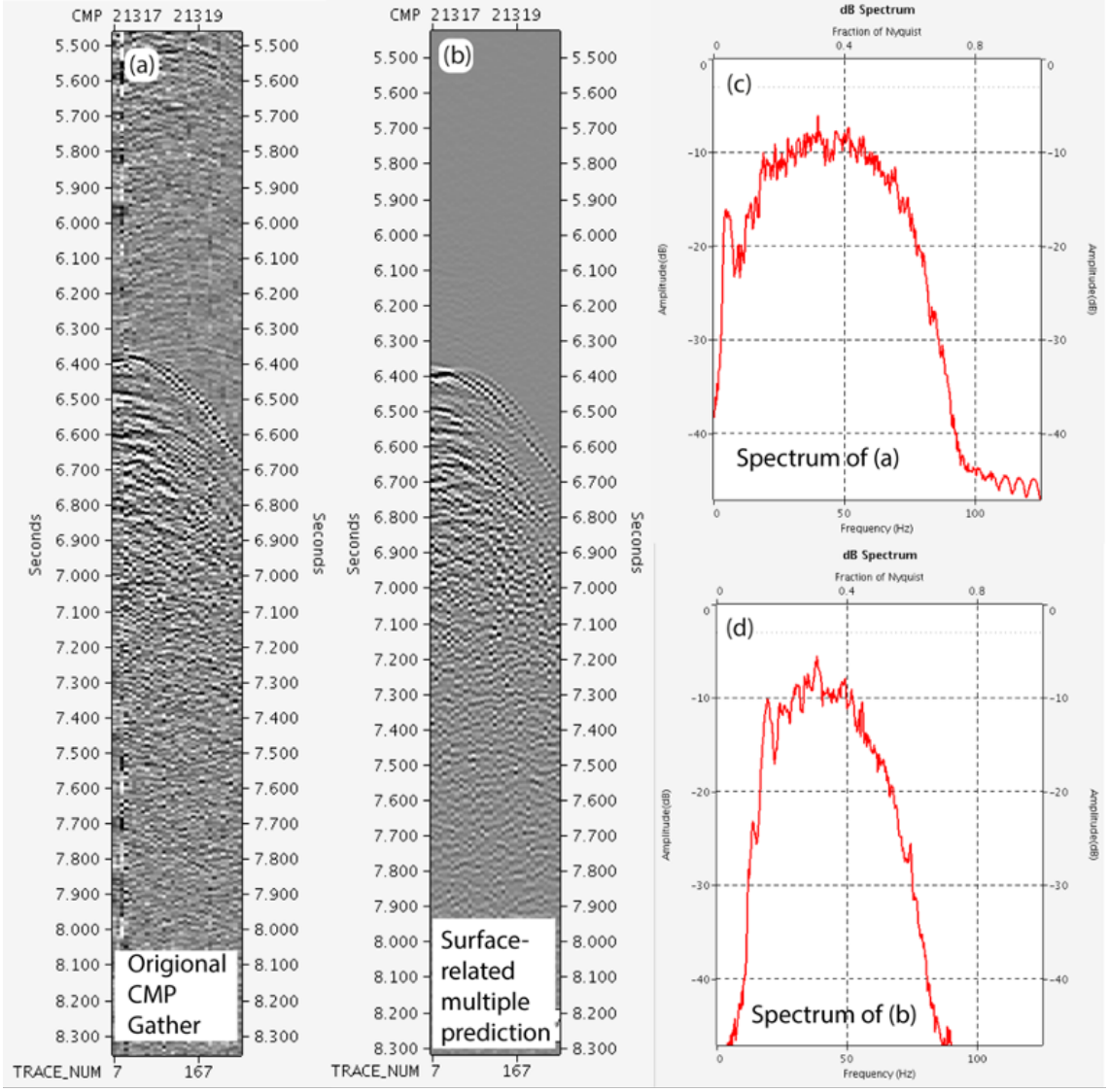


**Figure 6.6:** (a) Original CMP gather with multiple contamination. (b) Free Surface-related predicted multiple model. (c) The frequency spectrum of the original data. (d) The frequency spectrum of the modelled multiple.

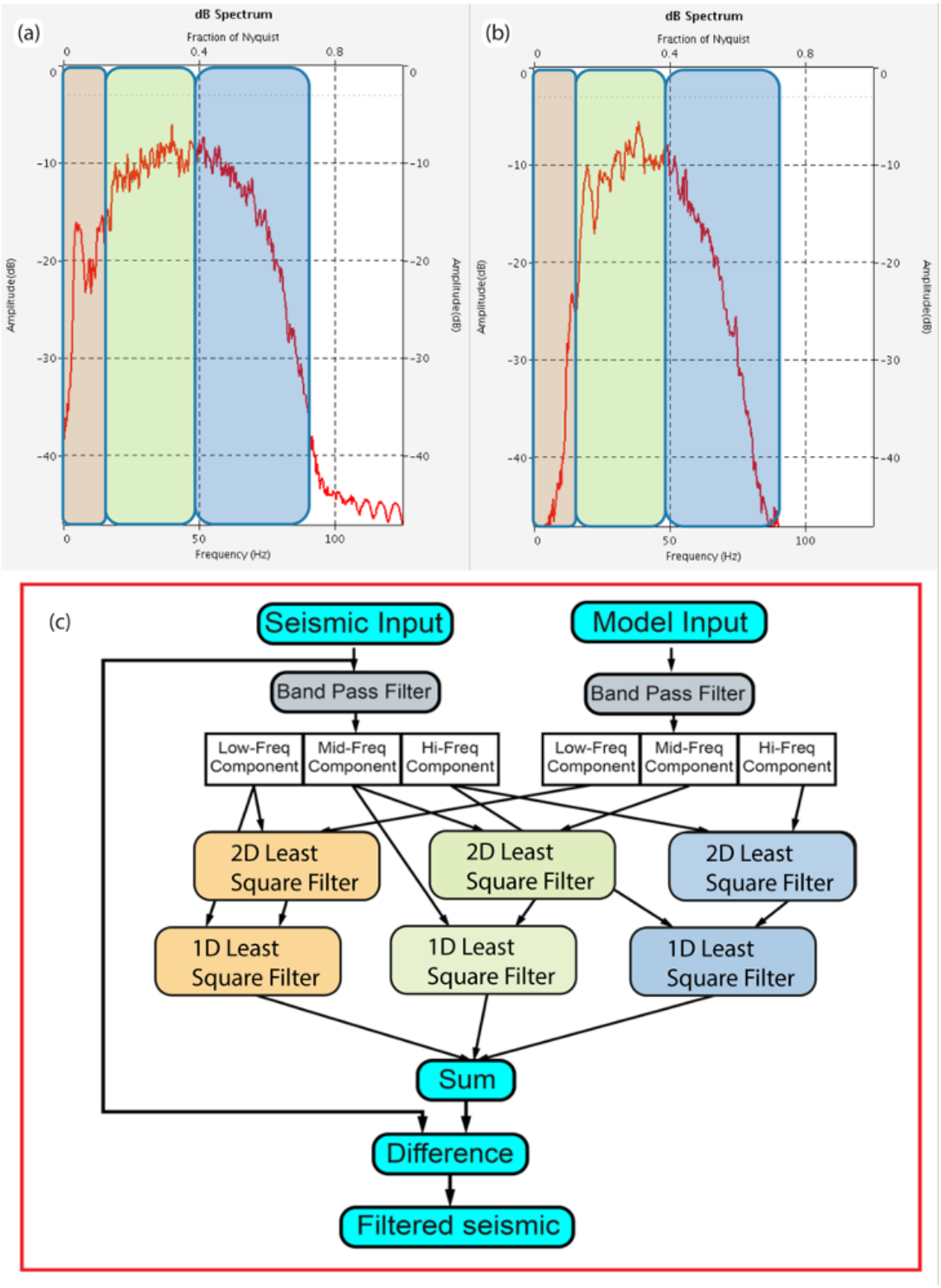


**Figure 6.7:** (a) Frequency bands segmentation of the original data used in the adaptive subtraction. (b) Frequency bands segmentation of the modelled multiple used in the adaptive subtraction. (c) Adaptive subtraction strategy.

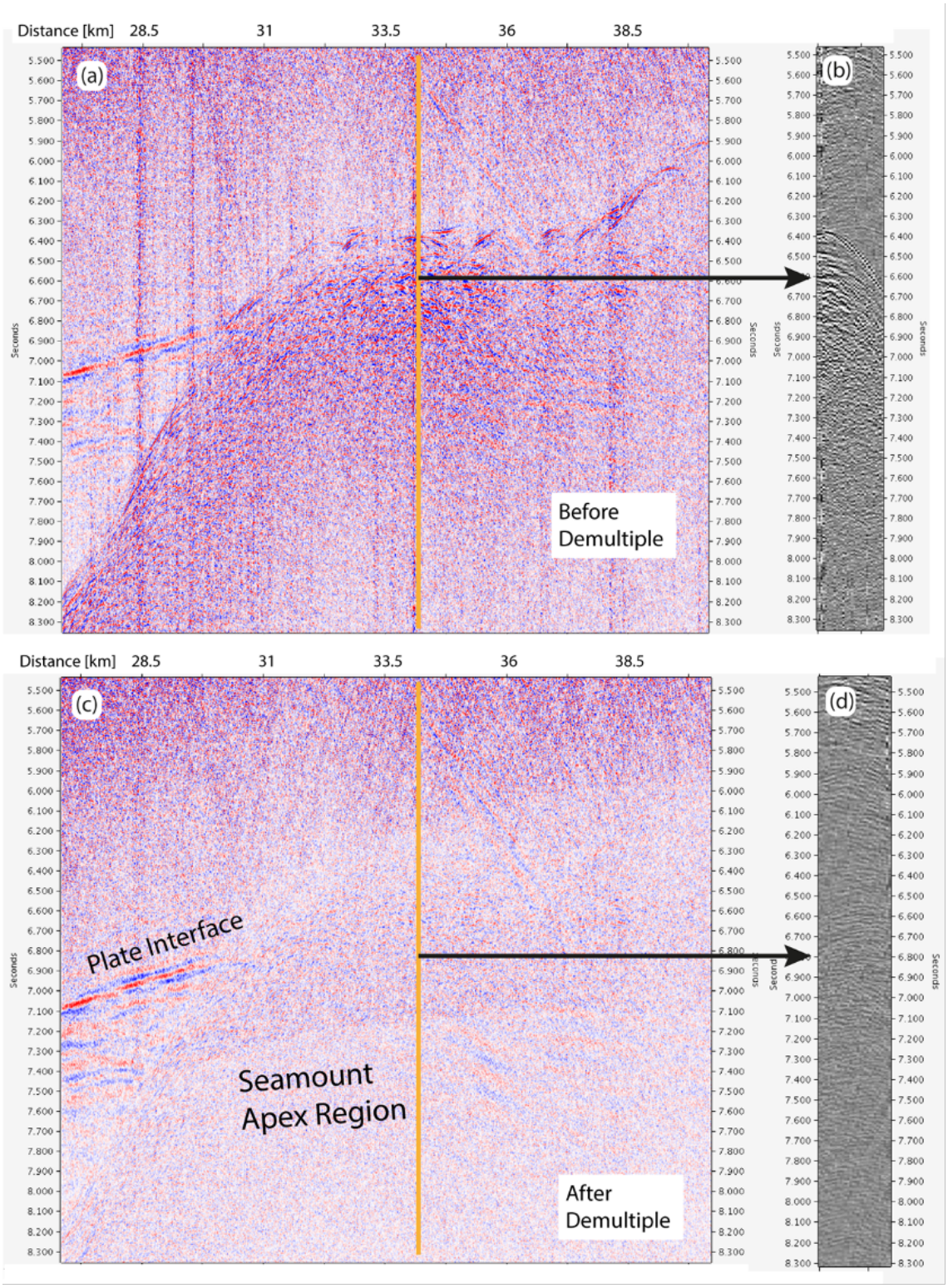


**Figure 6.8:** (a) Original MCS stacked image with multiple contamination. (b) Original CMP gather. (c) MCS stacked section after multiple attenuation. (d) CMP gather after multiple attenuation.

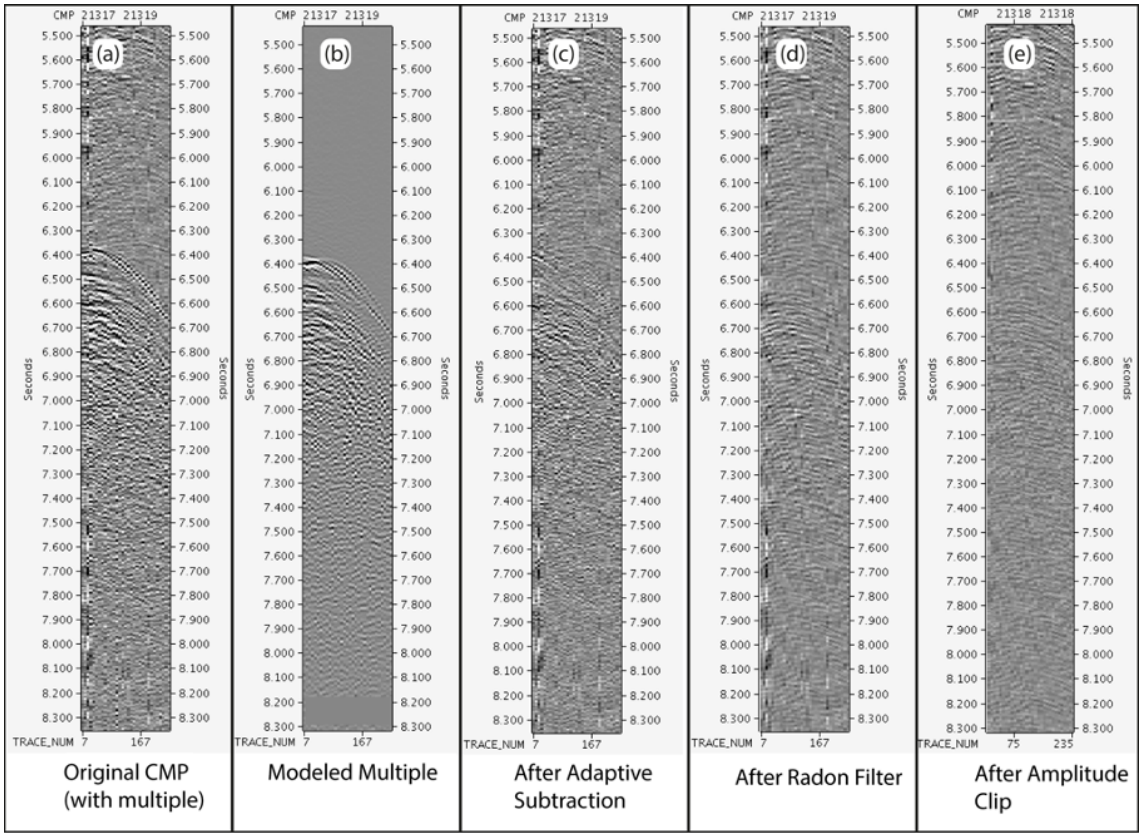


**Figure 6.9:** Multiple attenuation working flow in CMP domain (panels a to e). (a) Original CMP gather with multiple contamination. (b) Surface related modelled multiple. (c) CMP gather after frequency split adaptive subtraction. (d) CMP gather after additional Radon filter. (e) CMP gather after additional amplitude clip.

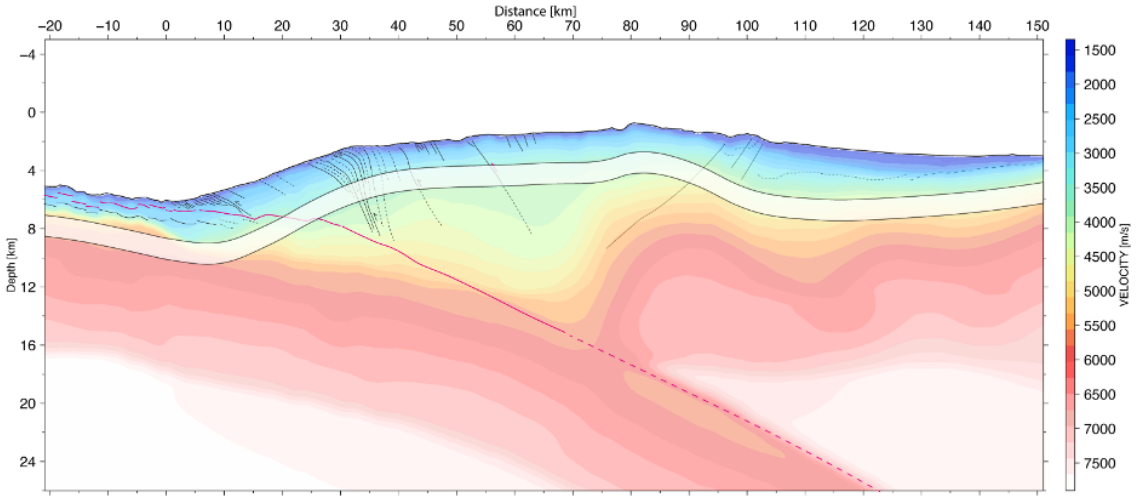


**Figure 6.10:** The final velocity model merged from the multi-channel seismic velocity analysis (above the white transparent band) and the wide-angle velocity model (Shulgin et al., 2011) (below the white transparent band). The line drawing is based on the final pre-stack depth migrated image.

# 7 Scale-dependent upper plate deformation caused by the subduction of seafloor relief

Yueyang Xia[1], Heidrun Kopp[1,2], Dirk Klaeschen[1], Jacob Geersen[2], **Bo Ma**[1], and Michael Schnabel[3]

1) GEOMAR Helmholtz Centre for Ocean Research Kiel, Wischhofstr. 1-3, 24148 Kiel, Germany
2) Christian-Albrechts-Universität zu Kiel, Christian-Albrechts-Platz 4, 24118 Kiel, Germany
3) Bundesanstalt für Geowissenschaften und Rohstoffe (BGR), Stilleweg 2, 30655 Hannover, Germany

submit to **Journal of Geophysical Research: Solid Earth**.

**Key Points**

- Upper plate deformation scales with variable lower plate subducting relief, identified in seismic depth sections and high-resolution bathymetry across the Java trench.
- Subducting basement highs provoke vertical migration of the décollement and cause permanent brittle deformation of the upper plate.
- Subduction of seafloor topography induces progression from an accretion-dominated domain towards a phase of subduction erosion.

## Abstract

The Java - Lesser Sunda margin, which features multi-scale subducting oceanic basement relief and a landward shift of the deformation front, is classified as a neutral (Lombok and Sumbawa) to erosional (Central Java to Bali) margin in comparison to its accretionary counterpart offshore Sumatra. However, a comprehensive analysis of the upper plate structure modulated by the subduction of oceanic basement relief and the associated erosional processes is lacking to date. Here we process and present multi-channel reflection seismic profiles offshore eastern Java, Bali, Lombok, and Sumbawa. The new seismic processing routine, which is underpinned by a grid-based tomographic P-wave velocity inversion, provides a more reliable velocity model than previous studies and results in improved resolution of the seismic images with revised reflector dips. The data document the upper plate deformation pattern and the erosional effects of the subducting relief at different scales. The seismic profiles and bathymetric map highlight the diversity and varying scales (diameters from <1 km to ~40 km) of the subducting relief (seamounts, ridges, and normal fault scarps) observed along strike on both the oceanic seafloor and on the submerged subducting interface. Basement relief subduction exerts a first-order control on the forearc seafloor topography, structure of the upper plate, and evolution of the décollement. The impact of different scales of subducting relief on the sedimentary units of the accretionary wedge results in shared characteristics (e.g., a shallower seafloor surface slope and enhanced compressional structure in front of subducting relief). Concurrently, the variation of scales leads to different levels of upper plate deformation. Large and medium scale subducting relief cause a noticeable landward (arc-ward) shift of the deformation front, shortening, and uplift of the accretionary wedge material, steepening of the frontal slope, and strike-slip faulting at the rear of the subducting topography. Small-scale subducting ridges primarily impact the frontal prism resulting in a more localized undulation of the surface slope and over-steepening of the slope at the trench, causing local mass transport (e.g., landslides or slumping). Décollement migration is observed in the vicinity of subducting relief when the height of the oceanic relief is larger than the thickness of oceanic sediment, implying a weak upper plate material compared to Byerlee's law.

## 7.1 Introduction

Subduction of rough seafloor relief is widely observed at subduction zones around the globe. Different scales of subducting oceanic basement structures (e.g., seamounts, basement ridges, fault scarps, horst-and-grabens) have been shown to modulate the structure and morphology of the plate interface (Bangs et al., 2006; Barker et al., 2018; Bell et al.,

2010; Bonnet et al., 2019; Davidson et al., 2020; Geersen et al., 2015; Kodaira et al., 2000; Martinez-Loriente et al., 2019; Morton et al., 2018; Ranero and von Huene, 2000; Todd et al., 2018), modify regional mass transport (Dominguez et al., 1998; Ruh et al., 2016; Sun et al., 2020a), and result in pervasive and potentially permanent deformation of the upper plate (Wang and Bilek, 2011). Subducting basement relief can further modify the stress distribution (Lallemand and Lepichon, 1987; Ruh et al., 2016) or enhance fluid expulsion into the wedge material (Chesley et al., 2021; Sun et al., 2020b; von Huene et al., 2004).

Oceanic basement features vary in height and volume and exhibit a wide variety of forms, comprising conical shapes (peaked or flat-top), multiple branches, or parallel ridges (Fig. 7.1b, c). Seamounts, which represent one of the most common and most widespread topographic features on oceanic plates, have been documented within numerous subduction zone systems, including the Tonga-Kermadec trench (Timm et al., 2013), Nankai trench (Bangs et al., 2006), Japan and Kuril trenches (Lallemand et al., 1989), Cascadia (Trehu et al., 2012), Hikurangi (Bell et al., 2014), and the Central America trench system (Ranero and von Huene, 2000). Upper plate deformation associated with the subduction of oceanic basement relief is manifested by re-entrants or scarps at the lower slope (Ranero and von Huene, 2000), gravitational submarine landslides (Brune et al., 2010), strike-slip faulting (Davidson et al., 2020), regional uplift (Laursen et al., 2002) or the landward shift of the deformation front (Kopp et al., 2006). Underthrusting of oceanic plate topography is a driving factor of subduction erosion, removing material from the toe of the overriding plate as well as from its base. Structural erosive packages removed from the upper plate related to seamount or oceanic relief subduction are documented in seismic studies (Kirkpatrick et al., 2020; Marcaillou et al., 2016).

Subduction of seafloor topography has been associated with marine geohazards including submarine landslides, earthquake seismicity, and tsunamis. A long-standing, controversial discussion has focused on the relationship between seamount subduction and the generation of large earthquakes. This is based on the intuitive hypothesis that the positive relief would increase normal stress, resulting in enhanced coupling patches along the plate interface, which would favor large earthquakes (Cloos, 1992; Cloos and Shreve, 1996; Scholz and Small, 1997). The Java 1994 tsunami earthquake ($M_w = 7.8$) has been discussed as slip over a subducted seamount (Abercrombie et al., 2001; Bilek, 2007), though the seamount's exact location remains ambiguous due to sparse data coverage (Xia et al., 2022). Recent discussions (Wang and Bilek, 2014) and modeling results (Dominguez et al., 1998; Ruh et al., 2016; Van Rijsingen et al., 2019; Yang et al., 2013), however, imply that seamounts or bathymetric basement highs favor aseismic creeping, promote smaller magnitude earthquakes ($M_w < 7$), and potentially act as seismic barriers during the co-seismic phase, due to the complex fault network and heterogeneous stress distribution in the vicinity of the seamount. Underthrusting of basement topography can induce localized uplift of the fore-

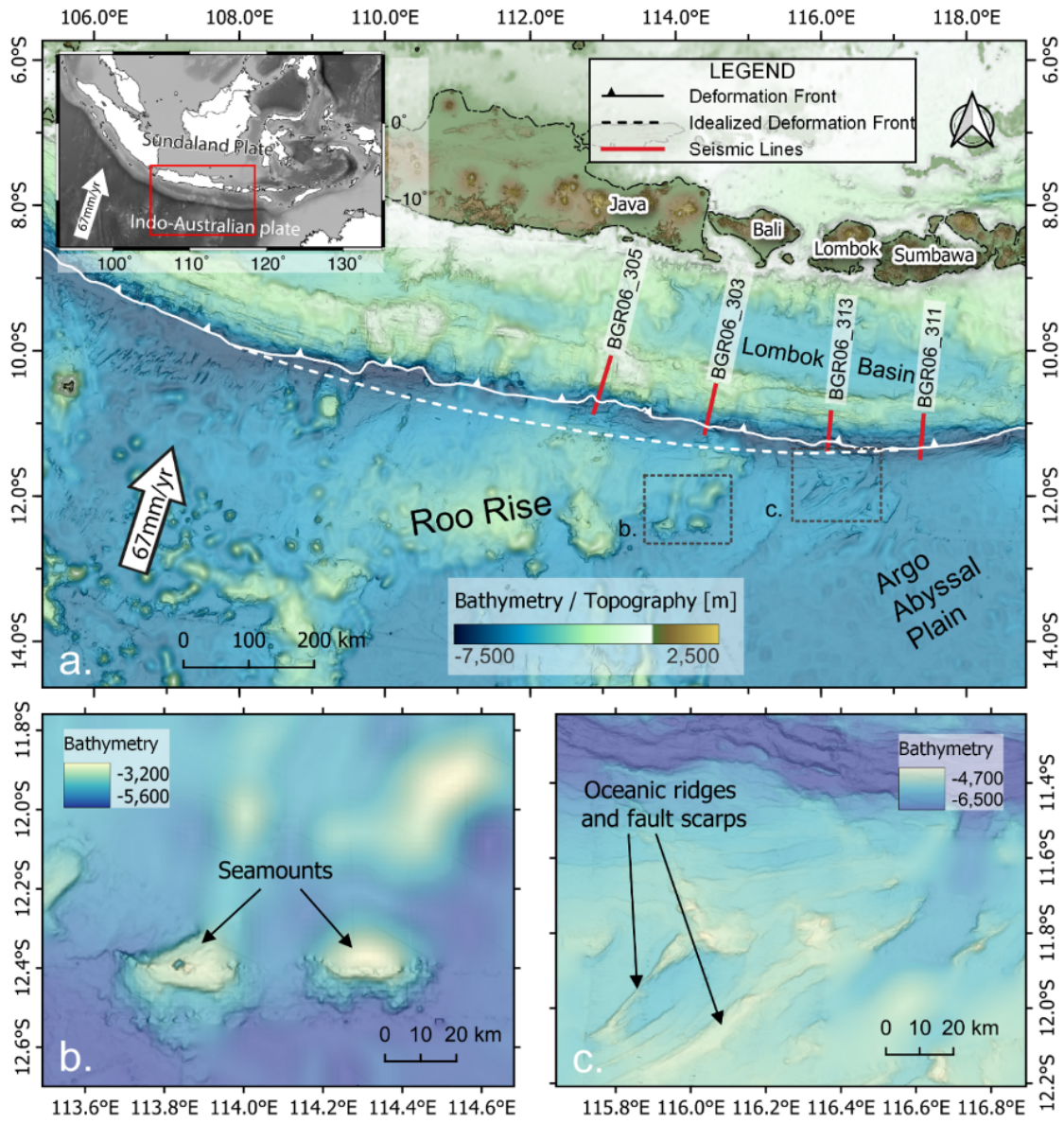


**Figure 7.1:** a. Regional tectonic setting and bathymetry of the study area. Red lines indicate the location of the four MCS profiles. The deformation front is shown in a solid white line, and the undisturbed hypothetical trend of the deformation front is shown by the white dashed line. b. A close-up view of the conical seamounts observed on the oceanic crust of the Roo Rise. c. A close-up view of the linear-shaped ridges on the oceanic crust offshore Lombok.

arc slope resulting in rapid or long-term gravitational collapse and submarine landslides (Hühnerbach et al., 2005; Kopp et al., 2006; Ruh et al., 2016).

Here we discuss the impact of oceanic basement features identified on four re-processed and depth-migrated multi-channel seismic (MCS) profiles from the Java-Lesser Sunda forearc. The grid-based tomography and pre-stack depth migration provide seismic images with corrected reflector dipping angles. The seismic images reveal the response of the upper plate and the plate interface to the subduction of basement relief at various scales, ranging from seamounts to ridges to smaller-scale relief such as subducting fault scarps.

We analyze the scale-dependent effect of the subducting topography on the geometry and deformation of the marine forearc and the accretionary wedge as well as on the evolution of the décollement. Our study documents the progression from an accretion-dominated domain towards a phase of subduction erosion.

## 7.2 Tectonic setting of the Java-Lesser Sunda margin

The ~5000 km long Sunda arc extends westward from Flores to Java and then trends northwest towards Sumatra and Myanmar (Fig. 7.1; Hamilton, 1988).The tectonic evolution of the Sunda arc is controlled by the active subduction of the Indo-Australian plate underneath Eurasia since the Eocene - Oligocene (Moore et al., 1982; Hamilton, 1988; Hall, 2002; Hall et al., 2008), following the Eocene collision of India with Eurasia. Given the great lateral extent of the Sunda arc, segmentation and variations in several geological parameters are observed along the margin (Moore et al., 1980). The age of the subducting lithosphere decreases towards the west from 150 Ma offshore Sumba to 125 Ma off Bali, reaching 90 Ma off Sumatra (Heine et al., 2004). The plate age variation correlates to an eastward increase in trench depth to >7000 m off Bali and Lombok. Offshore Java and the Lesser Sunda Islands, the subduction orientation is almost orthogonal with a current convergence rate of 67 mm/yr in a direction N 11 °E ± 4 ° (Tregoning et al., 1994; Bock et al., 2003) (Fig. 7.1).

Information on the crustal structure of the Java-Lesser Sunda marine forearc is mostly based on the analysis of a suite of wide-angle and MCS seismic lines (Karig et al., 1980; Moore et al., 1980; Kopp et al., 2006, 2009; Müller et al., 2008; Planert et al., 2010; Lüschen et al., 2011; Shulgin et al., 2011). An overview of the main geological parameters for each seismic profile presented here is provided in Table 7.1.

Offshore central Java around 109 °E, a change in the tectonic regime from subduction accretion to subduction erosion is related to the underthrusting of the Roo Rise oceanic plateau, which forms the eastern extension of the Christmas Island seamount province, off central and eastern Java (109 °E to 115 °E) (Fig. 7.1; Kopp et al., 2006). In the projection of the Roo Rise from central Java to Bali, subduction erosion causes a deflection of the

**Table 7.1:** An overview of the main geological parameters for each seismic profile

| MCS Line Number | The surface slope of the mature accretionary wedge/ middle slope [°] | water depth [km] at the trench | water depth [km] of slope break | water depth [km] of forearc high | Distance between the deformation front and the slope break [km] | Distance of the trench retreat [km] | Length of the accretionary wedge [km] |
|---|---|---|---|---|---|---|---|
| **06_311 (Sumbawa)** | 5.0 | 6.65 | 3.62 | 2.80 | 43 | 0 | 68 |
| **06_313 (Lombok)** | - | 6.62 | no slope break? | 2.38 | - | 16 | 77 |
| **06_303 (Bali)** | 7.6 | 5.92 | 2.27 | 1.52 | 37 | 30 | 82 |
| **06_305 (Eastern Java)** | 8.3 | 6.30 | 2.34 | 0.75 | 32 | 50 | 99 |

Java trench and deformation front towards the arc by 40 km on average from the normal curvature trend of the deep-sea trench (Kopp et al., 2006; Krabbenhöft et al., 2010). The Roo Rise is manifested in a ~500 km broad bathymetric plateau dotted with isolated seamounts with an average elevation of >2000 m above the surrounding ocean floor (Fig. 7.1b) that covers approximately 100000 $km^2$ offshore central-eastern Java (Shulgin et al., 2011). The Christmas Island seamount province is formed through the shallow recycling of the delaminated continental lithosphere entrained in the mantle, based on the isotope analyses of volcanic rocks (Hoernle et al., 2011). Refraction tomography studies have shown that the crustal thickness of the Roo Rise close to the trench is between 12 km to 18 km, with a lower P-wave velocity than for conventional oceanic crust (Shulgin et al., 2011) ($vp$ = 6.6 km/s compared to $vp$ = 7.2 km/s at the oceanic Moho). The marine forearc morphology offshore eastern Java is significantly modulated by the distinct lower plate topography of the Roo Rise entering the trench. Local landslide scarps, frontal embayments (concave-shaped 'cookie bites' or re-entrants), and over-steepened surface slopes, which are interpreted as evidence for mass failure, are observed at the lower slope in the bathymetry (Figure 7.1a, e.g., at 110 °E, 112 °E, 113 °E; Kopp et al., 2011).

The easternmost portion of the Sunda subduction system is characterized by the underthrusting of the Argo abyssal plain, located seaward of the deep-sea trench offshore Lombok and Sumbawa islands (115 °E to 119 °E) (Fig. 7.1). With a mean water depth of 5500 m, the Argo abyssal plain is largely devoid of terrigenous sediment (Moore et al., 1982; Planert et al., 2010). The crust of the Argo abyssal plain has an average thickness of 8.6 km, indicating a very mature oceanic crust of ~128 Ma to 150 Ma (Seton et al., 2020). The roughness of the seafloor turns from rugged offshore Bali to generally smooth offshore Sumbawa (Lüschen et al., 2011) (Figs. 7.1 and 7.2). Offshore Lombok (at ~116 °E), linear-shaped oceanic basement structures characterize the seafloor and trend at angles between 45 ° and 60 ° (Fig. 7.2), roughly parallel to the magnetic anomalies (Fig. 7.10; Lüschen et al., 2011). These are inherited structures mirroring the original spreading fabric (Planert et al., 2010). On the outer rise seaward of the trench, a pervasive pattern of plate-bending induced normal faults with throws up to 150 m and individual fault segment lengths of up to 60 km is observed starting at about 30 km seaward of the trench axis (Fig. 7.2; Lüschen et al., 2011). The bathymetry and MCS data show a strong horst-and-graben relief in the trench, which is the surface expression of faults that have been imaged to cut deep into the oceanic basement (Lüschen et al., 2011).

To the north, a mature forearc basin, the Lombok basin, has an average water depth of 4400 m and is limited by the Roo Rise subduction to the west and the Scott plateau to the east (Fig. 7.1; Planert et al., 2010). The basin and the adjacent forearc high are uniformly developed along the entire Lombok segment and remain largely undisturbed by the subduction of the pronounced basement relief as observed, e.g., further to the west in the Roo Rise segment off eastern Java and Bali, where the forearc high rises to a water depth of less than ~1500 m compared to ~2300 - 3000 m offshore Lombok-Sumbawa (Krabbenhöft et al., 2010).

## 7.3 Results

We present the four MCS profiles covering the trench and lower slope of the Eastern Java-Lesser Sunda margin starting with the easternmost profile offshore Sumbawa and progressively moving westwards toward Java (Fig. 7.1, Table 7.1). The easternmost profile BGR06_311 offshore Sumbawa serves as a reference line for the upper plate accretionary wedge structure, which along this profile is not significantly affected by large-scale (>150 m) subducting relief (Figs. 7.2, 7.3). Profiles BGR06_313 (offshore Lombok), BGR06_303 (offshore Bali), and BGR06_305 (offshore eastern Java), in contrast, are characterized by the subduction of oceanic basement relief of various dimensions, including basement ridges and seamounts. An overview of the different features is provided in Table 7.2. In the following presentation of the seismic profiles, we distinguish between the oceanic domain

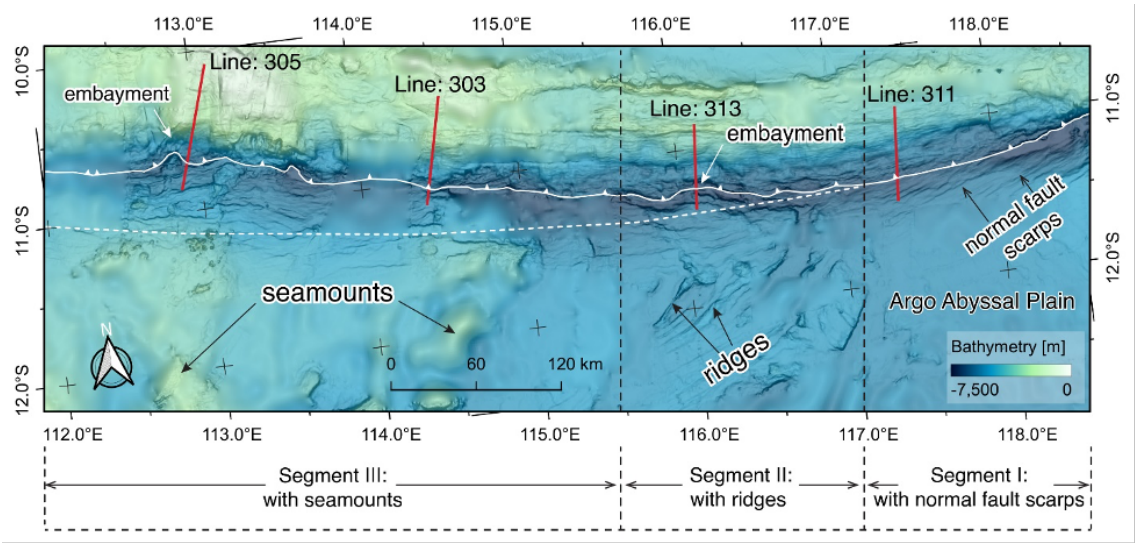


**Figure 7.2:** Bathymetry map around profiles BGR06_313 (off Lombok), BGR06_311 (off Sumbawa), BGR06_303 (off Bali), and BGR06_305 (off eastern Java). The solid white line indicates the deformation front, and the white dashed line illustrates the idealized trend of the deformation front. Please note that the study area could be divided into three different geological units (segments) along the strike. In Segment I from ~117 ° E to ~118.5 ° E, the oceanic plate is devoid of a large seamount or basement ridge, but is featured by minor bending-related normal faults with a small offset (< 150 m) close to the trench. The oceanic plate in Segment II from ~115.5 ° E to ~117 ° E features linear-shaped ridges on the oceanic crust. Segment III from ~112 ° E to ~115.5 ° E is featured by numerous conical or semi-conical shape seamounts on the oceanic plate.

and outer rise, the trench, the active frontal prism, the mature accretionary wedge, the forearc high and the forearc basin as the main tectonic units.

### 7.3.1 Profile BGR06_311 - offshore Sumbawa

MCS profile BGR06_311 (Fig. 7.1) is located offshore Sumbawa where the Argo Abyssal plain is subducting below the island arc (Fig. 7.1). The incoming oceanic crust carries about 420 m of sediment (Fig. 7.3a, 7.11, km -10 to 0). In the trench, approximately 500 - 600 m of sediment has accumulated. This portion of the Java-Lesser Sunda margin (termed Segment I in Fig. 7.2) is not significantly affected by seamount subduction and frontal subduction erosion, which causes a northward deflection of the deformation front further west (Fig. 7.1a). The incoming seafloor is much smoother than in the Roo Rise domain (Segment III in Fig. 7.2) to the west and no large-scale (>500 m height) topographic features are observed seaward of the trench (Fig. 7.2). The high-resolution bathymetry data reveal bending-related normal fault scarps (vertical throw < 150 m) on the outer rise (Figs. 7.2 and 7.4a), aligned parallel to the magnetic isochrons (Fig. 7.10) and trending

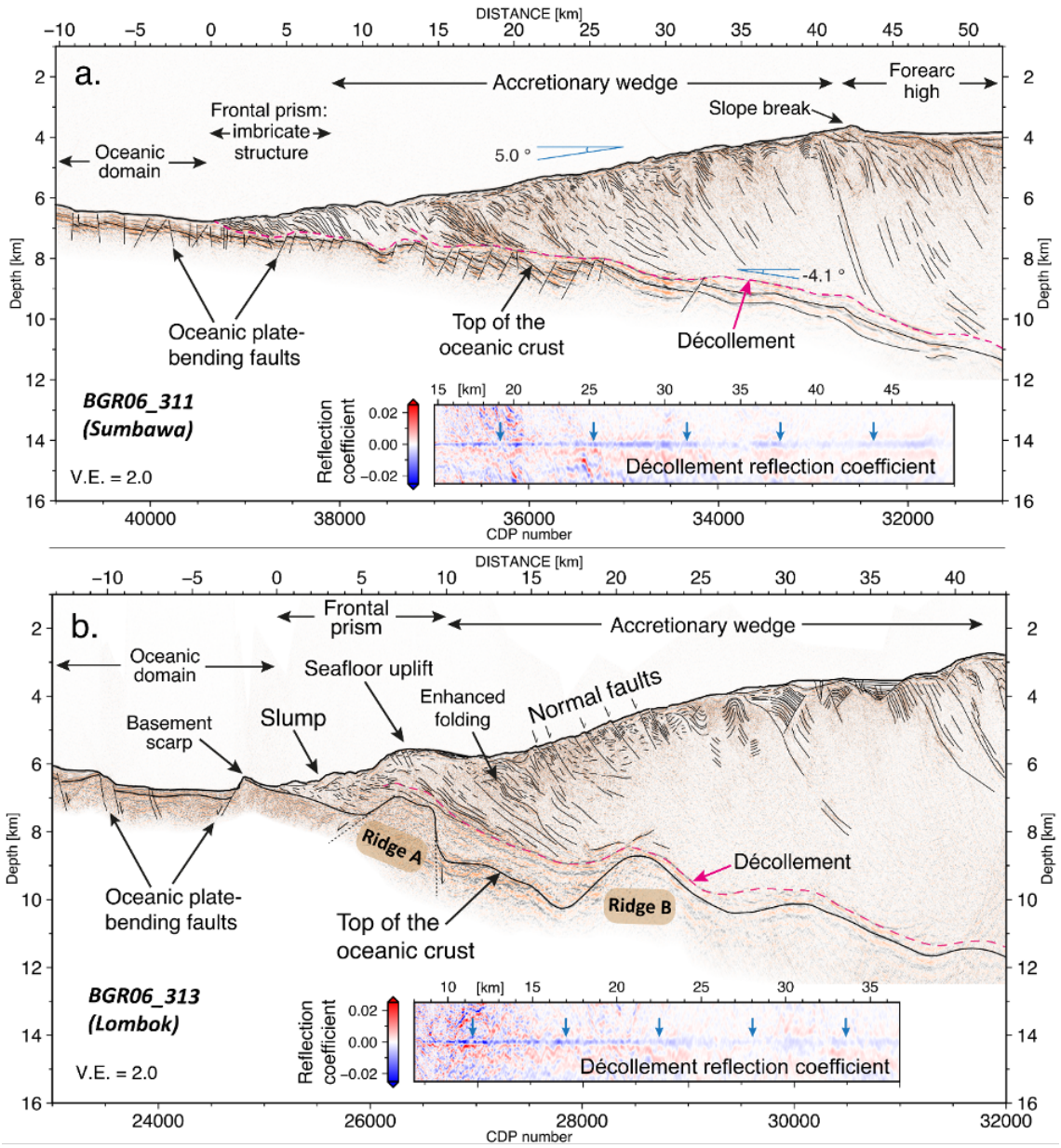


**Figure 7.3:** a. MCS depth migration image and the line-drawing of the seismic line BGR06_311 offshore Sumbawa. b. MCS depth migration image and the line-drawing of the seismic line BGR06_313 offshore Lombok. The reflection coefficient subgraph of horizontally aligned décollement is plotted within each subfigure.

obliquely to the strike of the deformation front. The faults dissect the oceanic basement and the overlying sediment cover (Fig. 7.3a, km -10 to 0). As the plate subducts, the fault throw is enhanced due to the increased bending of the oceanic crust, resulting in a horst-and-graben structure of the oceanic basement with moderate offsets (100 – 500 m) underneath the frontal prism (Fig. 7.4c) and the accretionary wedge (Fig. 7.4b) . A

**Table 7.2:** An overview of the different features of subduction seamount.

| Relief ID | Height [km] | Width [km] | Aspect ratio | Distance to trench [km] | Depth (abs) [km] | Depth (below seafloor) [km] | Relief type | Elapsed time of the relief subduction (ka) |
|---|---|---|---|---|---|---|---|---|
| **Ridge A in 06_313** | 1.3 | 4.5 | 0.28 | 7 | 7 | 1.5 | Basement Ridge | 150 |
| **Ridge B in 06_313** | 1.6 | 6.3 | 0.25 | 22 | 8.5 | 3.5 | Basement Ridge | 400 |
| **Ridge in 06_303** | 1.3 | 4.1 | 0.31 | 7 | 5.5 | 0.5 | Basement Ridge | 130 |
| **Seamount in 06_303** | 2.1 | 26.2 | 0.08 | 36 | 8 | 5 | Seamount | 700 |
| **Seamount in 06_305** | 2.7 | 39.3 | 0.07 | 33 | 7.5 | 5.5 | Seamount | 850 |

previously interpreted thrust fault, dissecting the entire oceanic crust down to Moho depth (Fig. 8 in Lüschen et al., 2011) is not observed in the new depth migrated seismic section presented here.

Landward of the deformation front (profile km 0), approximately 60% of the incoming sediment sequence is frontally accreted, while the remaining sediment constitutes a band of underthrust material with a thickness of ~170 m (Fig. 7.4c). The frontal prism on this profile (km 0 to 8) is a textbook example of frontal sediment accretion and documents the formation of imbricate thrusts that progressively steepen and rotate landwards to accommodate the incoming material (Fig. 7.4c). Approximately 8 km landward of the deformation front, the upper plate reflectivity decreases and marks the transition from the actively accreting frontal prism to the mature accretionary wedge (Fig. 7.3a, km 8 to 41). Landward dipping fore-thrusts and imbricate sediment layers are observed in the accretionary wedge, connecting from the seafloor to the plate boundary at depth (e.g. at around profile km 13 and 20, Fig. 7.3a). The thrust faults cause minor seafloor offsets and undulations at the lower and middle slope (e.g., around profile km 21 to 23) (Fig. 7.3a). The surface slope of the accretionary wedge (Fig. 7.3a, km 10 - 41) is relatively uniform ~5 °.

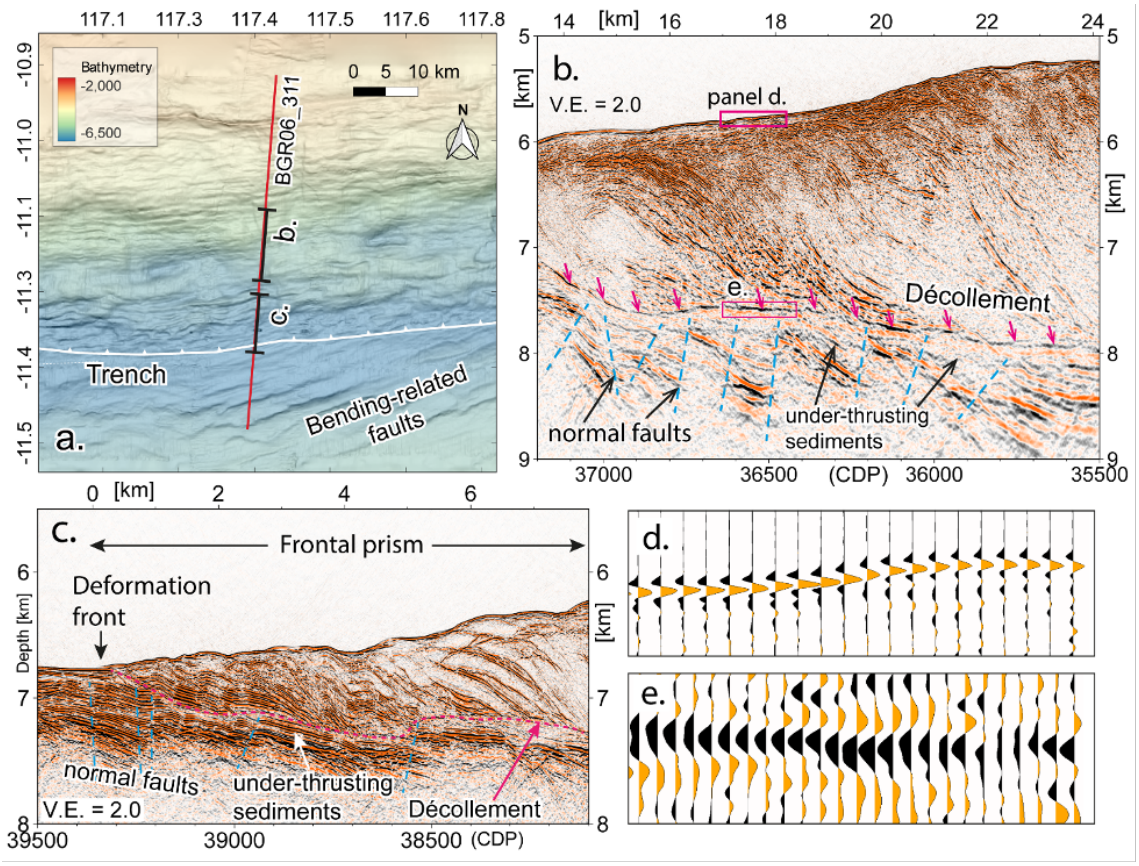


**Figure 7.4:** a. Bathymetry map around profile BGR06_311. b. Close-up view of the upper plate lower slope. Plate-bending induced normal faulting affects the oceanic basement. The plate interface reflection features a reversed polarity wavelet compared to the seafloor reflection (compare panels d and e). c. Close-up view of the trench and frontal prism. d. Zoom-in wiggle display of the seafloor reflection. e. Zoom-in wiggle display of the décollement reflection. Orange in-fill indicates positive polarity, and black color in-fill indicates reversed polarity.

A prominent slope break at profile km 42 coincides with a steeply dipping reflector that offsets the seafloor and cuts through the accretionary wedge to connect to the megathrust at 9.5 km depth (Fig. 7.3a). The décollement is imaged as a coherent reflector from profile km 14 to 50 (Fig. 7.3a) and is characterized by a reversed polarity relative to the seafloor reflection (Fig. 7.4d, e). The plate interface dipping angle is around -4.1 ° underneath the frontal prism and accretionary wedge (Fig. 7.3a, km 5 - 40).

### 7.3.2 Profile BGR06_313 - offshore Lombok 518

Profile BGR06_313 trends offshore Lombok, approximately 140 km west of the Sumbawa profile BGR06_311 (Figs. 7.1 and 7.2). The outer rise offshore Lombok carries a number of linear-shaped ridges (Fig. 7.1c, Segment II in Fig. 7.2). Here, the trench is partially

devoid of any sediment and isolated sediment patches reach a thickness of less than 150 m (Fig. 7.1b, km -10 to 0), though a sediment cover of 400 - 500 m is observed on the incoming crust (Lüschen et al., 2011; Planert et al., 2010). The deformation front in this region along the margin (116.1 °E) starts to deviate from the normal trend of the trench (Fig. 7.1, white stippled line), which has previously been attributed to frontal erosion caused by the subduction of pronounced oceanic basement relief (Kopp et al., 2006). At the location where line BGR06_313 crosses the trench, a ~30 km wide embayment at the lower slope is visible in the seafloor bathymetry (Fig. 7.2). The frontal prism, as observed on the neighboring line BGR06_311 to the east, is disrupted and features little imbricate structure (Figs. 7.3b and 7.5a, profile km 0 to 10). The exact location of the deformation front on the profile is obscured by a steep oceanic basement scarp (around profile km -2) with a vertical throw of ~600 m which is currently entering the subduction system (Fig. 7.3b).

On the subducting crust, a ~1.3 km height oceanic basement high (Ridge A in Figs. 7.3b, 7.3a, and 7.2) is found at a depth of 7 km and ~1.5 km below the seafloor (Figs. 7.3b 7.5a, profile km 5 to 10) underneath the frontal prism. It coincides with a shallowing of the seafloor by about 1000 m (Fig. 7.5a), where a local seafloor bulge (profile km 6 to 11) extends laterally in a trench-parallel direction for ~30 km (Fig. 7.5b, Ridge A). Landslide scars on the trench-ward flank of the seafloor bulge (Fig. 7.5b) are recognized in the bathymetry map and coincide with the chaotic and discontinuous nature of the shallow sedimentary strata in the frontal prism as described above (Fig. 7.5a km 0 to 6).

Further downdip, a second subducting basement high (Ridge B) with a height of approximately 1.6 km (Table 7.2, Figs. 7.3b and 7.5c, profile km 17 - 23) coincides with a seafloor surface slope of 9 ° (Fig. 7.5c). Shallow landward dipping normal faults offsetting the seafloor (Fig. 7.5d) are observed here. The internal reflection pattern of the accretionary wedge is characterized by complex and small-scale reflectors (Fig. 7.5d).

The décollement, which parallels the oceanic basement reflection further downdip (Fig. 7.3b, profile km 21 and beyond), deviates from the basement between the two basement highs (Ridges A and B) and trends ~1000 m above the top of the oceanic crust (Fig. 7.3b, profile km 10 - 21), migrating upward on the leading flank of Ridge A (Fig. 7.5a, km 6 to 10). It is characterized by a band of reflectors showing a negative reflection coefficient (Figs. 7.3b, 7.5e).

### 7.3.3 Profile BGR06_303 - offshore Bali 510

Profile BGR06_303 is located offshore Bali where the easternmost portion of the Roo Rise with its significant basement relief is currently entering the trench (Segment III

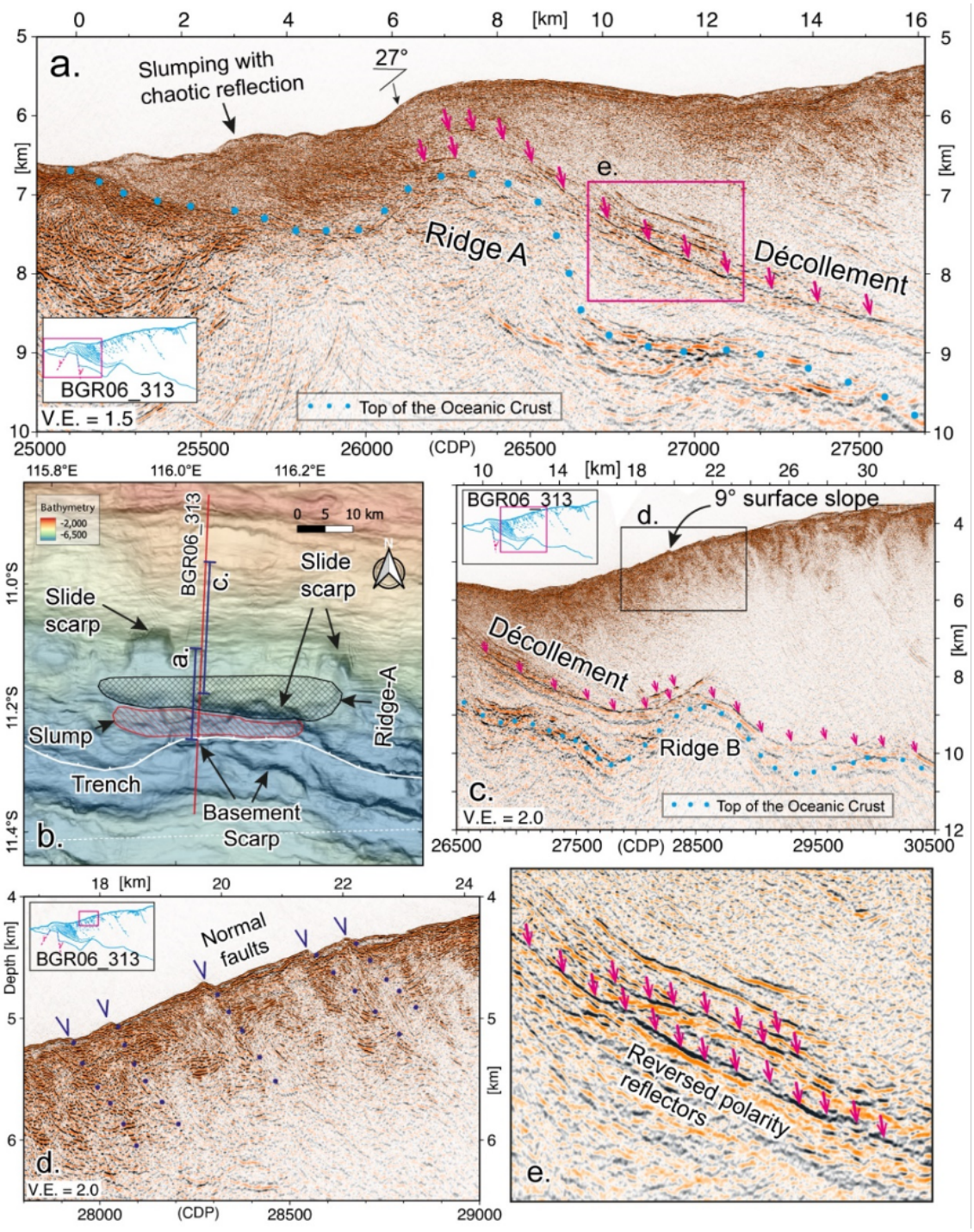


**Figure 7.5:** a. Close-up view of subducting Ridge A. Uplift of the upper plate causes a seafloor bulge above the subducting ridge. Mass wasting deposits seaward of Ridge A are characterized by a chaotic internal reflection pattern. b. Upper plate seafloor morphology modulated by subducting ridges offshore Lombok around profile BGR06_313. c. Close-up view of subducting Ridge B. Trend of the décollement indicated by red arrows. Blue dots indicate the oceanic basement. d. Close-up view of the upper plate above Ridge B. Please note that the normal faults (marked by dark blue dots) crop out at the seafloor, indicating recent fault activity. e. Close-up view of the décollement between Ridge A and Ridge B. The reversed polarity reflectors are marked by red arrows.

in Fig. 7.2). In the trench, the incoming oceanic basement is blanketed by a sediment cover ranging from 300 m to more than 500 m thickness (Figs. 7.6a and 7.7c, km -2 to 0). Landward of the deformation front (Fig. 7.7c, km 0), the horizontally layered trench sediments form imbricate structures (profile km 0-6), and the original stratigraphy is still recognized in the frontal prism (Fig. 7.7c). At profile km 6 to 10, the seafloor is uplifted by a subducting basement ridge (Figs. 7.6a and 7.7c), also traced in the bathymetry as an 18 km long escarpment (Fig. 7.7a, in the black polygon). This situation is similar to profile BGR06_313 (Fig. 7.5a). The ridge disrupts the stratigraphy of the frontal prism as it is underthrust underneath the lowermost slope. Landward of the subducting ridge, underthrusted sediment is observed with an average thickness of 600 m (Fig. 7.6a).

Above the accretionary wedge, the seafloor features an average slope of 7.6 ° (Fig. 7.6a, km 12 to 35) (Table 7.1). A seafloor slope break at profile km 36 - 40 corresponds to the surface outcrop of a high-amplitude landward dipping reflector. This reflector reaches the plate interface at ~10 km depth (Fig. 7.6a). Landward of the slope break, the seafloor slope becomes shallow to horizontal between profile km 38 and 52 (Fig. 7.6a). The shallow water depth (1500 m) and active thrusting of the accretionary wedge forearc high (most pronounced around profile km 53 and 64), which offsets the seafloor, documents the compressional state of this domain (Fig. 7.6a, km 50 – 77). The active thrust fault at profile km 51 to 55 is characterized by a reversed polarity (Fig. 7.7d) compared to the seafloor reflection. The sedimentary strata from km 41 to further landward has been rotated to an angle of ~45 ° (Fig. 7.7b).

Underneath the slope break between profile kilometers 30 to 45, a subducting seamount is identified at a depth of 8 km (Fig. 7.6a). It coincides with a semi-conical bulge in the seafloor bathymetry (Fig. 7.7a). Landward of the leading flank of the seamount, the décollement lies ~1500 m above the top of the oceanic crust (Figs. 7.6a and 7.13, profile km 46 to 62, red dashed line) at a depth of 8 to 12 km. Between the subducted seamount and the ridge (Fig. 7.6a), the décollement parallels the subducting oceanic basement between km 18 to 30 (Fig. 7.6a) and is shifted upwards between km 12 and 18 (Fig. 7.6a). At around profile km 14, the inclination of the décollement is deflected in front of the subducting ridge and steeply trends towards the seafloor, where it crops out at km 8.5. This complex adaptation in the structural level of the décollement is also reflected in the variation of the reflection coefficient (Fig. 7.6a).

### 7.3.4 Profile BGR06_305 - offshore Eastern Java

The westernmost profile of our study locates offshore eastern Java, where the oceanic domain features a large number of seamounts on the Roo Rise plateau (Fig. 7.1b, Segment III in Fig. 7.2). The forearc high in this segment reaches a water depth of 750 m and is

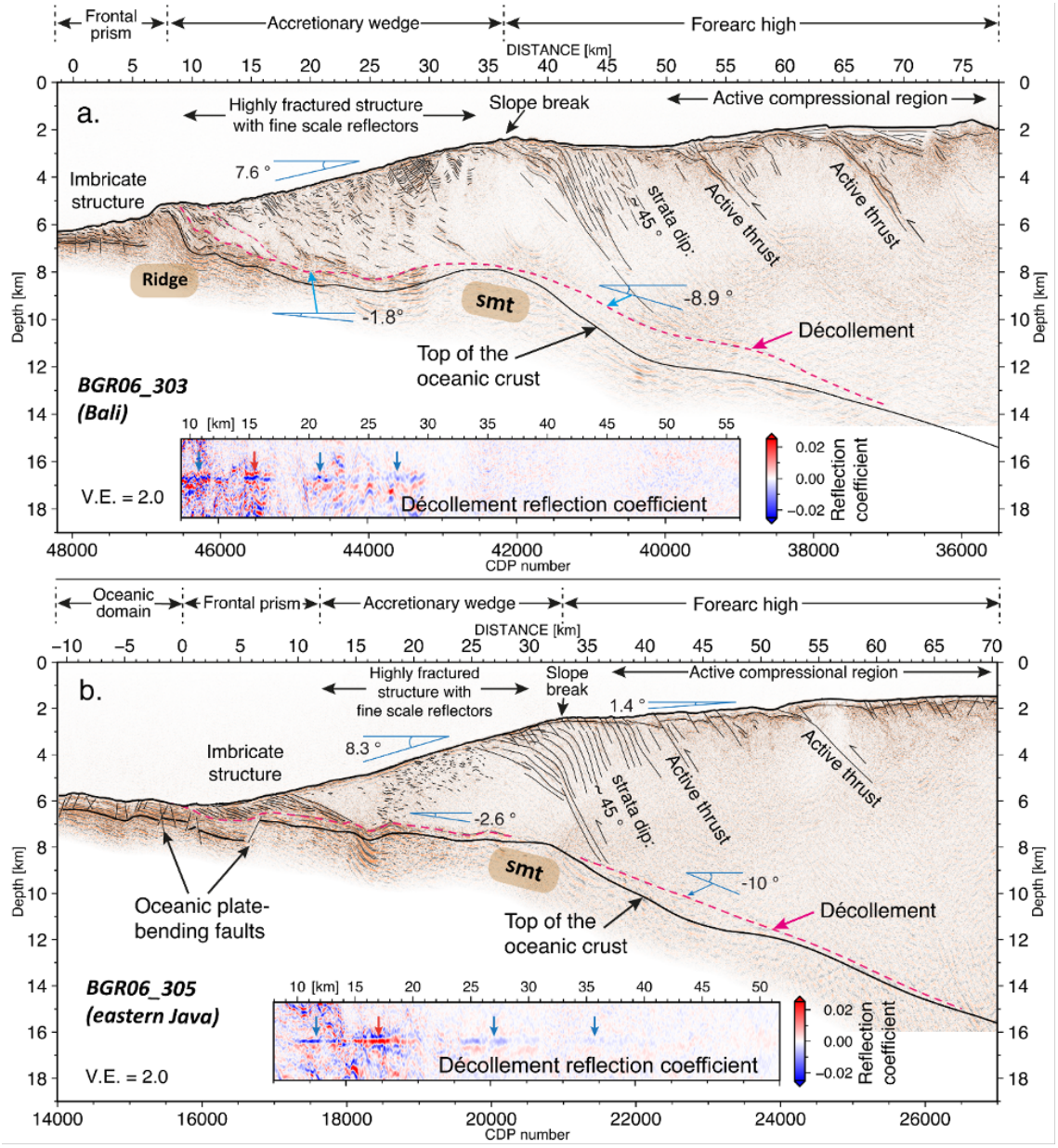


**Figure 7.6:** a. MCS depth migration image and the line-drawing of the seismic line BGR06_303 offshore Bali. b. MCS depth migration image and the line-drawing of the seismic line BGR06_305 offshore eastern Java. The reflection coefficient subgraph of horizontally aligned décollement is plotted within each subfigure.

thus approximately 2000 m shallower than offshore Sumbawa (Table 7.1). The northward deflection of the deformation front by about 50 km (Table 7.1, Fig. 7.1) has been attributed to frontal subduction erosion due to the impact of oceanic basement relief on the lower slope of the upper plate (Kopp et al., 2006). The incoming plate in the oceanic domain carries ~850 m of well-stratified sediment (Figs. 7.6b and 7.14). Oceanic basement and

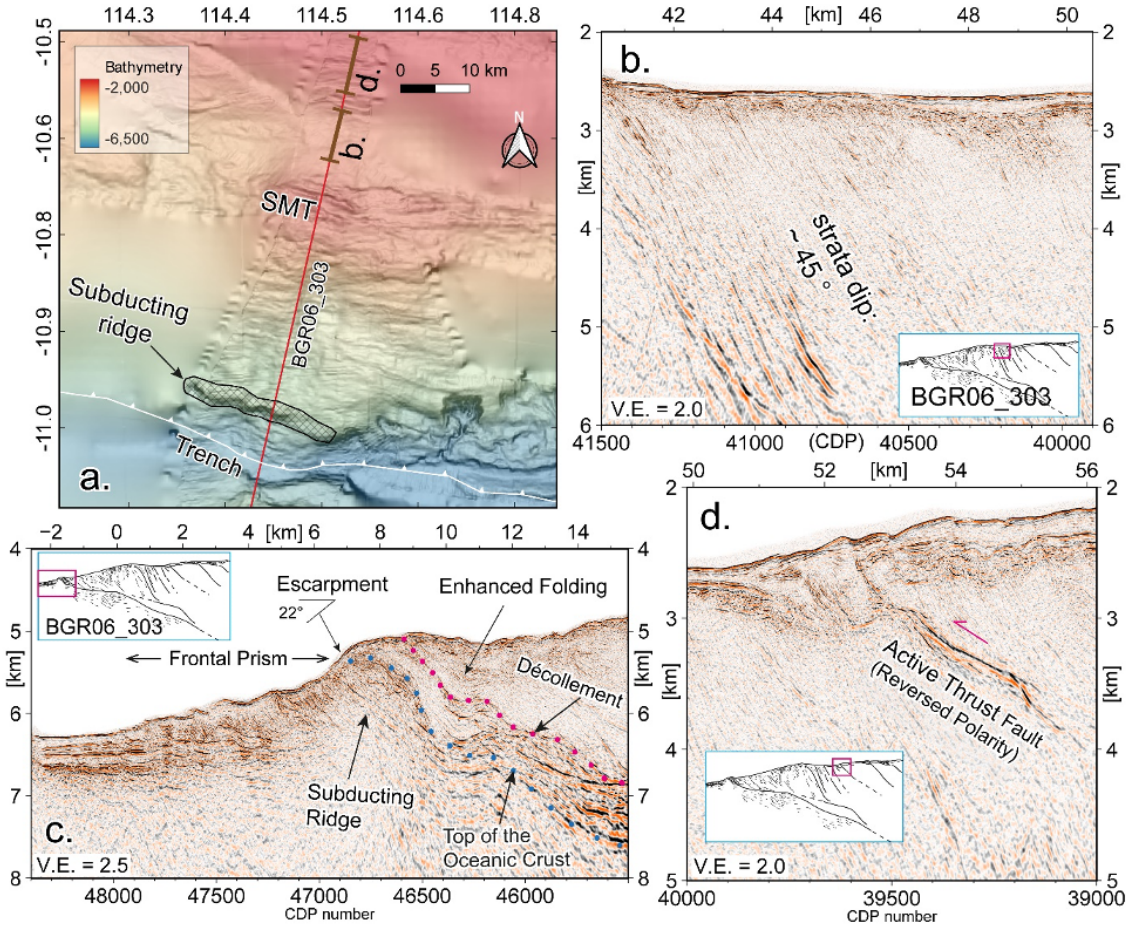


**Figure 7.7:** a. Upper plate deformation induced by a subducting oceanic basement topography offshore Bali close to profile BGR06_303. b. Upper plate close-up view of the ~45 ° dipping reflectors in front of the subducting seamount. c. Close-up view of frontal prism and lower accretionary prism where a subducting basement ridge causes seafloor uplift resulting in a local steep slope angle of 22 °. Upper plate deformation in response to the under-thrusting ridge is expressed in enhanced folding in front of the ridge. The décollement is marked by red dots in this panel. d. Close-up view of active thrust fault landward of the seamount. The thrust fault features a reversed polarity wavelet compared to that of the seafloor reflection.

overlying sediments are disrupted by bending induced normal faulting of the oceanic crust as it enters the trench (Fig. 7.6b, km -10 to 0).

At the deformation front, 40-50% of the sediment is frontally accreted, resulting in imbricate thrusting within the frontal prism (Figs. 7.6b and 7.8e, km 0 to 12). Approximately 10 - 12 km landward of the deformation front, reflectivity decreases, marking the transition from the frontal prism (profile km 0 - 12) to the mature accretionary wedge (Fig. 7.6b). The accretionary wedge is dominated by a chaotic reflection pattern of small-scale reflections (Figs. 7.6b and 7.8e, profile km 12 – 19) and fine-scale folding (Fig. 7.8e, profile km

20 – 30). The seafloor surface slope reaches 8.3 ° (Fig. 7.6b, km 10 – 30). A distinct slope break at profile km 33 (Figs. 7.6b and 7.8d) is associated with a large semi-conical seafloor bulge observed in the bathymetry (smt in Fig. 7.8c). Small-scale, superficial normal faults offset the seafloor (Fig. 7.8d: black dashed lines) to compensate the extension above the bulge. The bulge coincides with a subducting seamount (Abercrombie et al., 2001; Xia et al., 2021) on the oceanic crust at a depth of about 7.5 km. Profile BGR06_305 cuts the eastern flank of this ~1250 $km^2$ large seamount (Fig. 7.8c). The seamount and overlying slope break also mark a change in the dipping angle of the plate interface, which steepens from approximately -2.6 ° seaward of the slope break to around -10 ° landward of the seamount (Fig. 7.6b). The décollement runs parallel to the top of the oceanic crust at depths beyond 12 km (profile km 50 and beyond) but starts to deviate from the oceanic basement at the leading flank of the seamount (Fig. 7.6b, profile km 35 – 50).

Above the seamount and on its landward side (km 33 – 40), the internal reflectors of the accretionary wedge and forearc high feature a coherent structure with steep dipping angles of about 45 ° (Fig. 7.6b). A prominent reflector offsets the seafloor at the slope break and cuts through the accretionary wedge down to the plate interface at 9 km depth (Fig. 7.6b). Further landward, we observe seafloor perturbations in both the seismic data (Fig. 7.8b) and the bathymetry (Fig. 7.8a, c). Two thrust faults are actively deforming the uppermost sedimentary unit (Fig. 7.8a, b), flanked by numerous minor fault planes for which the stress mechanism is not unambiguously discernible from the seismic image (Fig. 7.8b). On the bathymetry map, these faults feature an oblique orientation of 45 ° with respect to the strike of the fore-thrusts (Fig. 7.8a).

## 7.4 Discussion

Although oceanic relief subduction is observed in many subduction zones (Bangs et al., 2006; Bell et al., 2010; Trehu et al., 2012), the comparatively thin oceanic sediment layer (< 1000 m) along the Java margin in combination with the significant accretionary wedge (ranging from 700 - 1000 $km^2$ per arc length) make this area unique, as oceanic basement relief is observed to breach the oceanic sediment cover to come into direct contact with the upper plate. This setting provides the opportunity to study the impact of basement relief of different scales on the deformation of the upper plate, the forearc mass balance, and the development of the décollement.

The four multi-channel seismic profiles presented in this study illustrate distinctly different subducting oceanic basement features, ranging from large-scale offshore eastern Java (~40 km wide seamounts, > 2.5 km high) to moderate-scale offshore Bali (20 - 25 km wide seamounts, > 2 km high) to subducting ridges off Lombok (4 - 7 km wide, > 1 km high)

(Table 7.2). The easternmost profile offshore Sumbawa shows no significant subducting relief but only minor bending fault scarps (< 150 m) and therefore serves as a reference line for the purpose of this discussion. Accordingly, the upper plate structure as well as the trend of the décollement at depth vary between these profiles, documenting the impact of seafloor relief subduction at different scales and different stages of subduction.

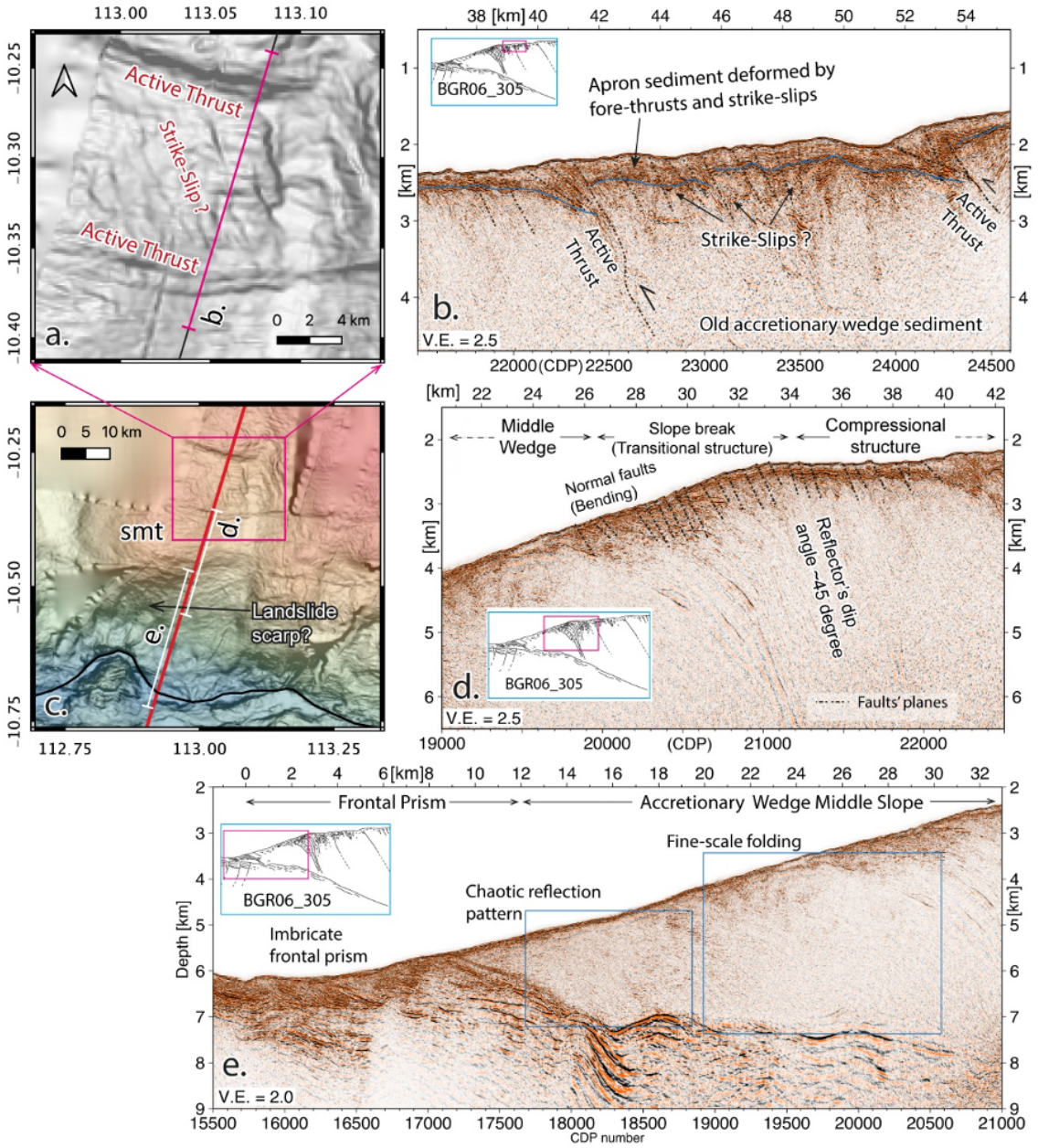


**Figure 7.8:** Upper plate seafloor morphology landward of subducting seamount offshore eastern Java (Caption next page).

### 7.4.1 Response of the marine forearc to oceanic basement relief subduction

The subducting oceanic basement relief exerts a first-order control on the seafloor surface slope. Across the accretionary wedge, the seafloor slope increases from 5 ° offshore Sumbawa to 7.6 ° offshore Bali and then 8.3 ° offshore Java (Table 7.1). This coincides with the increasing size of the subducted basement features and is particularly evident for the Java and Bali profiles (BGR06_305 and BGR06_303), where large to moderate scale seamounts (scale length along the dip: 20 – 40 km, height > 2 km) of the Roo Rise push into the wedge (Fig. 7.1) and the water depth of the forearc high is much shallower (~1000 m) compared to the eastern profiles.

#### Arc-ward retreat of the trench offshore central Java to Lombok

While the volume and the elevation of the forearc high diminish along the arc from west to east (Table 7.1) in relation to the decreasing amount of incoming sediment in the trench, the seaward portion of the forearc encompassing the frontal prism and accretionary wedge shows an opposite trend and increases in size (Fig. 7.1; Table 7.1). The seafloor slope break marks the transition from the actively accreting frontal prism and accretionary wedge to the older and fossil forearc (Fig. 7.2c). On the easternmost profile offshore Sumbawa (BGR06_311), the slope break is located ~43 km from the deformation front (Fig. 7.3a) and marks a decrease in seafloor slope in the landward direction. Along the Lombok profile (BGR06_313), where relief with smaller scale is currently entering the subduction zone, the slope break is found at a similar distance (42 - 43 km) (Fig. 7.3b; see also Fig. 7 in Lüschen et al., 2011). Towards the west, the slope break develops at a distance of ~37 km on the Bali profile (BGR06_303) and at ~32 km on the Java line (BGR06_305) (Fig. 7.6). This trend coincides with the northward deflection of the deformation front

**Figure 7.8:** a) Upper plate seafloor morphology landward of subducting seamount offshore eastern Java. Surface traces of thrusts and strike-slip faults are identified in the bathymetry. b) Close-up view of upper plate structures dominated by active thrusting in front of the seamount with a complex pattern of thrust faults and strike-slip faulting. The blue line indicates the basement of the newly deposited apron sediment unit. c) Upper plate seafloor morphology modulated by a subducting seamount adjacent to profile BGR06_305. Seamount subduction induces landslide and mass wasting on its seaward flank. d) Close-up view of the seafloor slope break. Small-scale near-surface normal faults are observed induced by the seafloor curvature, resulting in shallow extension. e. Close-up view of upper plate seismic signatures in the wake of seamount subduction. The chaotic and fine-scale folding reflections dominate the accretionary wedge middle slope. Frontal sediment accretion results in imbricate thrusting of the frontal prism (km 0 - 12).

west of 115 °E (Fig. 7.1) and documents the erosive impact of the subducting seamounts on the frontal prism and accretionary wedge of the forearc, decreasing the distance between the deformation front and the slope break (Table 7.1).

Profile BGR06_305 locates at the central part of the 25,000 $km^2$ broad region of trench retreat (Fig. 7.1) and the subsurface structure of this line sheds light on its relation to the along-strike variation of subduction erosion. The northward deflection of the deformation front is mirrored in a similar curved trend of the forearc high's northern boundary, as indicated in the bathymetry data (Fig. 7.15). Conventionally, a plate margin experiencing significant subduction erosion should not only feature a large trench retreat in the arc-ward direction, as recognized for central Java but also a substantial narrowing and thinning in the middle wedge (Scholl and von Huene, 2007). This is not observed for the Java case, where the marine forearc high is thicker and shallower compared to the surrounding areas (Fig. 7.1; Shulgin et al., 2011). This observation raises the question to what extent is the arc-ward retreat of the trench induced by 1) frontal subduction erosion related to seamount or ridge subduction as discussed above and by 2) trench-normal displacement and translation of the accretionary wedge and forearc high due to the collision and 'pushing' of the numerous large seamounts spanning over the Roo Rise. Distinctively, compared to the profiles BGR06_313 and BGR06_311 off Bali and Lombok, which are located at the eastern portion of the retreating segment, the structural image of line BGR06_305 does not present a larger volume of eroded or underthrusting material in the frontal part of the accretionary wedge (Fig. 7.6b), indicating that frontal erosion is not the sole contribution to the trench retreat and that the northward pushing of the Roo Rise into the forearc must be considered as an additional effect to explain the arcward deflection of the deformation front as well as of the wedge's northern boundary (Fig. 7.15).

The structural variations between the four seismic lines further support this concept. A distinct back-thrusting fault, which offsets the northern edge of the forearc high and overlying sediment unit (Xia et al., 2021) at the transition into the forearc basin, is coincidently observed where the maximum arc-ward deflection (50 km) occurs off central Java (profile BGR06_305). Similar back-thrusting is absent in the other profiles off Bali, Lombok, and Sumbawa. This indicates a much stronger regional compressional stress across the forearc high off central Java, likely induced by the pushing of the Roo Rise and its seamounts spanning a distance of over 600 km along the strike of the trench.

### Effects of seamount subduction on the surface slope and deformation of accretionary wedge

The two western seismic profiles image the consequences of seamount subduction on the stratigraphy of the accretionary wedge. Above and landward of the seamounts' leading

flanks, the sedimentary strata are rotated to steep angles of ~45 ° (Fig. 7.6a, b) as they are integrated into the mature portion of the forearc. In front of the largest subducting seamount observed on profiles BGR06_305 and BGR06_303, active fore-thrusts are observed in both the seismic section and the bathymetry map (Fig. 7.6a, b). They cause offsets between 100 - 300 m in the recent sediment apron, increasing to ~500 m in the older accreted sediment (Figs. 7.6b, 7.8b). During seamount subduction, its frontal flank pushed the accretionary wedge material landward, and led to the shortening and thickening of the wedge (Fig. 7.9d - f). This is documented by the much shallower water depth (< 1600 m) of the forearc high on the eastern Java and Bali profiles compared to the forearc high elevation (> 2300 m) to the east (Fig. 7.1; Table 7.1) as well as by the steeper seafloor slope. The active fore-thrusts, which offset the most recent sedimentary unit and the older accreted material below, result from the thickening and shortening above the seamount's leading flank.

In addition to the active fore-thrusts, the bathymetry map (Fig. 7.8a) and seismic section (Fig. 7.8b) document a network of minor fault planes above the subducted seamount offshore eastern Java. These faults trend at an angle of ~45 ° with respect to the active thrusts (Fig. 7.8a). We interpret them as strike-slip faults resulting as an expression of the modified stress field in the immediate vicinity of the subducted seamount (Wang and Bilek, 2011). A similar fault pattern has been described for Bennett Knoll on the Hikurangi margin (Davidson et al., 2020). Our seismic line and the seafloor mapping cover only the eastern seamount flank (Fig. 7.8c), where the structure of the upper plate indicates a complex history of deformation, shortening and thickening of the accretionary wedge in a spatially and temporally evolving stress field around the subducting seamount. A symmetrical pattern including the combination of local strike-slip faults and larger scale thrust faults would also be expected on the seamount's western flank, where bathymetry data are lacking.

At the trailing side of a large-moderate size seamount (e.g., in BGR06_305), an oversteepened surface slope (8.3 °, Table 7.1) and a shallow basal dip (2.6 °, Fig. 7.6b) are observed. This geometry observation follows the prediction of the classic Coulomb wedge model, which implies a tendency for gravitational collapsing of the overriding plate since the taper geometry is over-critical due to the rotation by the seamount subduction at the trailing flank (Dahlen, 1984; Lallemand and Lepichon, 1987). Theoretically, the oversteepened surface slope and the shallow basal dip will result in a significant gravitation-driven extensional deformation all over the upper plate at the seamount's trailing edge, given the low strength of the megathrust (Gao and Wang, 2014). The gravity force overcomes the basal shear and leads to pervasive brittle/plastic yielding, and the state of the stress within such a wedge should have the same orientation everywhere (Dahlen, 1984). Evidence of such gravitational collapsing at the seamount's trailing side has been veri-

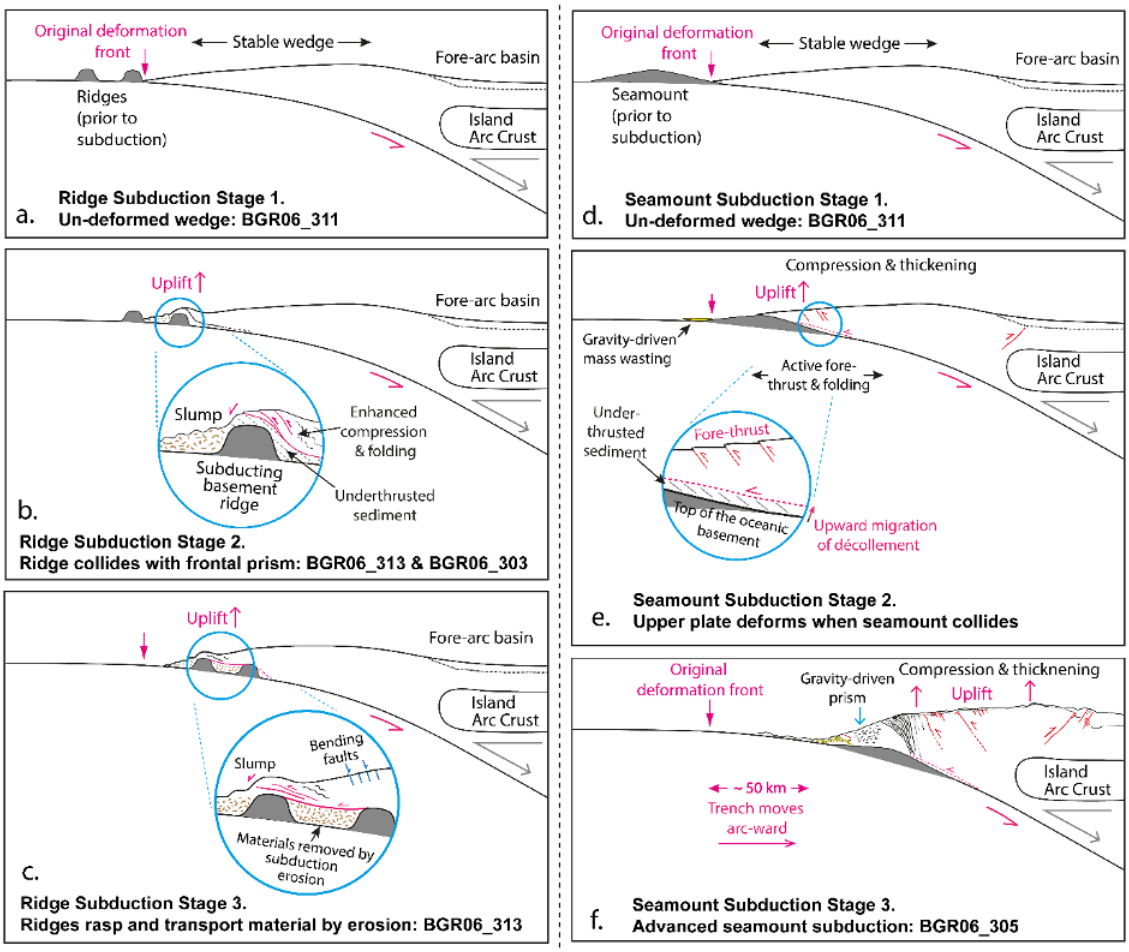


**Figure 7.9:** Conceptual sketch of oceanic relief/seamount subduction and associated upper plate deformation showing individual stages of a subducting ridge or seamount. a) Incipient ridge subduction underneath a stable accretionary wedge. b) Under-thrusting of the ridge acts as strong teeth and causes uplift and fracturing of the frontal prism. Fractured materials are deposited in the valley at the trailing side of the ridge. c) The slumping deposit are transported into greater depth as oceanic plate subducts. d) Incipient seamount subduction underneath a stable accretionary wedge. e) Seamount underthrusting causes uplift of the upper plate in front of the seamount. Please note the adjustment of the structural level of décollement in front of seamount and compression and shortening of the lower slope. f) Compression and uplift are compensated by fore-thrusts and folding on the seaward side of the prism and by back-thrusting at the transition to the forearc basin. Note that the long-term gravity-driven mass wasting in the wake of relief subduction results in a steep surface slope and a chaotic reflection pattern in the accretionary wedge.

fied in MCS profiles with subducting seamount in North-Ecuadorian margins (Fig. 4b in Marcaillou et al., 2016). However, a discrepancy between our geophysical observation and this concept exists. A dilemma emerges immediately: no widely distributed normal fault nor listric fault is observed at this over-steepened middle wedge. Instead, internal

structures of this steep wedge taper revealed in lines BGR06_305 and BGR06_303 show intense compressional signatures, like the chaotic and very fine-scale reflectors over the middle wedge at the seamount trailing side (e.g., in BGR06_305, Fig. 7.8e, km 12 - 30). Only minor normal faults are observed at the surface slope break (Fig. 7.8d, km 24 - 38).

Perhaps these geophysical observations may not be so paradoxical if we consider a continuous and progressive evolution of the upper plate rather than a transient snapshot of its 850 ka long-term deformation history (e.g., the seamount in BGR06_305 has subducted for 850 ka given a convergent rate of 67 mm/yr). On the one hand, compressional debris piles with chaotic reflection signatures are always a characteristic at the toe domain of a single submarine landslide, and the normal fault scarp is only observable at the landslide's headwall domain (Scarfì et al., 2020). On the other hand, this normal fault scarp at the slide's headwall will immediately be destructed and smeared by the next gravitational slide which will occur (Ruh et al., 2016) when the seamount subducts deeper. The topographic responses to these episodic slides are the normal faults scarps at the head wall, which are transient, re-constructed, and covered by numerous slide episodes over this seamount's 850 ka subduction history. In contrast, the compressional structural signature at the toe domain of the slide is perpetually preserved over time. Moreover, the upper plate's tectonic response and topographic expression by the subducting seamount are particularly significant when the seamount is in an early stage of collision close to the trench but will diminish progressively and eventually perish when the seamount reaches a greater depth (e.g., Fig. 4 e-h in Ruh et al., 2016). In the end, only minor surface responses (e.g., normal fault scarps) are preserved locally above the seamount's top, before the seamount is fully covered by overriding sediment sequences.

The seamounts and basement highs at the early stage of the subduction (e.g., Ridge A in BGR06_313 in this study, and seamount in the North-Ecuadorian margin, Marcaillou et al., 2016) may result in extensive normal faulting and gravitational collapse at their trailing edges, when the sediment does not completely bury the seamounts (Ruh et al., 2016). However, given the convergence rate of the plate margin in Java (67 mm/yr) and its crest distance to the trench (average 31 km), the seamount observed in BGR06_305 is not any more at its infant stage of collision. As a consequence of the long-term history of seamount subduction (850 ka) on line BGR06_305 resulting in a series of mass movements over the trailing edge, the stratigraphy above the trailing edge of the seamount is highly disrupted or completely destroyed, resulting in a chaotic reflection pattern dominated by short reflectors (Fig. 7.6g and 7.8e, km 12 to 30).

The subducting relief with a large aspect ratio (height/width ~0.2 to 0.3) as expressed e.g. in Ridges A and B on the Lombok profile (BGR06_313, Fig. 7.3b) are characterized by much steeper flanks than the larger subducting seamounts on the Java and Bali profiles

(BGR06_305 and BGR06_303). Deformation in response to the subduction of large aspect ratio features is expressed in intense folding ahead and above the ridge (e.g. Fig. 7.3a, km 9 - 17), documenting the uplift, deformation and compression of the sedimentary strata that was formerly composing the frontal prism. Ridge A in profile BGR06_313 shows a local slope of 27° at its trailing edge (Fig. 7.5a, km ~6), hosting slumps with chaotic reflection patterns (Fig. 7.5a, km 0 to 6). Comparable mass wasting is not observed on the Java and Bali lines (Fig. 7.6a, b). This observation indicates that the higher aspect ratio (height/width ~0.28 for Ridge A) of the moderate scale basement relief (width of Ridge A $<$ 10 km compared to tens of km for the subducting seamounts) results in enhanced gravitational collapse at the trailing edge. Furthermore, the relief on BGR06_313 is at an early stage of subduction compared to the seamounts offshore Java and Bali, which are observed at a greater depth so that some 'healing' of the lower slope may already have occurred.

In contrast to the three profiles to the west imaging oceanic relief subduction at large to moderate scales, the fourth line offshore Sumbawa (BGR06_311; Fig. 7.3a) shows no comparable subducting structures. Here, the trend of the top of the oceanic basement is only altered by plate-bending induced normal faults, resulting in a small-scale (1 - 2 km width) segmentation of the subducting oceanic crust with fault throws less than 150 m close to the trench to less than 600 m below the accretionary wedge (Fig. 7.3a). The décollement is able to develop as a spatially continuous feature above the subducting topography, and subducted sediment is observed between the décollement and the top of the oceanic crust (see below). Overall, this profile documents a history of sediment accretion and a stable surface slope of the accretionary wedge not disrupted by significant subducting oceanic basement relief.

### The evolution of the décollement

The subduction of different seafloor topography along the three western profiles (BGR06_305, BGR06_303, BGR06_313) modifies the structural level of the active décollement. In contrast, along the eastern profile BGR06_311, the décollement is spatially continuous and shows a reversed polarity (Fig. 7.3a) and negative reflection coefficient, resulting from a negative impedance contrast indicating juxtaposition of densified, accreted material to underthrusted sediment. The décollement marks the top of a 170 m thick unit of subducting sediment, smoothing the smaller scale undulations ($<$ 150 m) of the basement (Fig. 7.3a). This implies that lower plate topography is not in direct contact with the upper plate. The décollement follows the long-wavelength trend of the subducting slab, and does not substantially deviate from the top of the oceanic basement (Fig. 7.3a).

This pattern changes substantially along the neighbouring Lombok line (BGR06_313), where Ridges A and B cause undulations in the basement topography by more than 1.5 km in height over spatial width of less than 7 km (Fig. 7.3b). The décollement is clearly identified by its negative reflection coefficient (Fig. 7.3b), caused by the negative impedance contrast to the subducting sediment unit underneath. Landward of Ridge B (Fig. 7.3b) the décollement starts to diverge from the top of the oceanic crust (profile km 32), migrates upwards and follows a shallower trend. This effect is enhanced between Ridges A and B, where the décollement may be traced ~1.5 km above the top of the oceanic crust.

On line BGR06_303 offshore Bali, the subducted seamount produces undulations in the basement trend where the basement angle changes significantly over short distances from 1.8 ° to 8.9 ° (Fig. 7.6a). This induces a shallowing of the décollement landward of the leading edge of the subducted seamount (around profile km 45 - 65 in Fig. 7.6a). The décollement reflection amplitude is very weak beyond profile km 35 (Fig. 7.6a), but we deliberately chose not to apply a stronger gain control in order not to heavily manipulate the amplitudes. The décollement may be traced ~1.5 km above the top of the oceanic crust but deepens again on the trailing flank of the seamount, where it lies less than 500 m above the basement. Further towards the trench, where the basement topography is once more disrupted by a subducted ridge (Fig. 7.6a, km 5 - 10), the décollement again deviates from the oceanic crust starting at profile km 18 and dissects the seafloor ~8.5 km and ~12 km landward of the deformation front.

The Java profile (BGR06_305) images the largest seamount in our study, but the aspect ratio and hence the changes in subducting basement topography are smaller than on the other lines (Fig. 7.6b). At the leading edge of the seamount, the décollement trends ~1.2 km above the oceanic basement, and can unambiguously be identified by its negative, however weak, reflection coefficient here (Fig. 7.6b). Seaward of the seamount, the reflection coefficient of the décollement alternates between positive and negative values, reflecting the impedance contrast between the frontally accreted material in the frontal prism and the underthrust portion of the trench infill (Fig. 7.8e, km 15 - 20).

### 7.4.2 Subduction erosion and implications for wedge strength

#### Subduction erosion offshore Java-Lombok

The adjustment of the structural level of the décollement has important implications for the mass balance of the forearc. Where the décollement pinches out against subducting topographic features, this enhances localized subduction erosion by removing material from the base of the accretionary wedge (Ballance et al., 1989; Clift and Vannucchi, 2004;

Lallemand and Lepichon, 1987; Von Huene and Scholl, 1991). Ballance et al. (1989) documented the impact of subducting relief on the overriding plate, where the fracturing and thus weakening of arc upper plate rocks resulted in collapse into the grabens of the downthrusting basement. Commonly, geophysical evidence from multi-channel seismic data related to this process is rarely documented (von Huene et al., 2004), due to the limited depth resolution or insufficient horst height. In our study, profile BGR06_313 offshore Lombok images the trapping of material in the wake of ridge subduction resulting from high-stress physical abrasion (Figs. 7.3b and 7.5a, also refer to Fig. 4 in (Ballance et al., 1989), and refer to Fig. 3c, d in (Hilde, 1983)). The basement ridges (e.g., Ridge A offshore Lombok) feature a high aspect ratio and substantial height (> 1km, Table 7.2, Fig. 7.3b), causing fractures, uplift and compressional deformation of the accreted sediment when the ridge's leading flank collides with the tip of the upper plate. As the ridge subducts further, gravitational collapse and slumping at the trailing side disintegrates the accreted sequences (e.g., the under-thrusted sediment between distance km 9 to 21 seaward of Ridge B in Fig. 7.3b). The disintegrated material is deposited in the protected shadow behind the ridge, in the accommodation space of the graben to the next ridge further updip (Fig. 7.9a - c).

Intriguingly, the absolute height/offset of Ridges A and B (1300 – 1600 m) (Table 7.2, Fig. 7.3b) is larger than for any of the oceanic ridges (800 – 900 m) observed on the oceanic crust (Fig. 7.1c). We suggest that this effect is related to the oceanic plate bending as the basement scarps in the trench feature an intermediate offset value of 1000 to 1200 m (Fig. 7.5b).

The erosional impact of the large conical shape seamounts on lines BGR06_303 and BGR06_305, which feature a significantly lower aspect ratio than the ridges on line BGR06_313 (Table 7.1) is foremost documented in the re-entrant scars and embayments observed in the bathymetry data (Figs. 7.1 and 7.2). In addition to the material removal at the deformation front, Ballance et al. (1989) anticipated an elevated plate boundary in front of subducting seamounts, resulting in enhanced basal erosion. In our data, lines BGR06_303 and BGR06_305 document this deflection of the décollement which may clearly be discriminated from the top of the oceanic crust in front of the seamount (Fig. 7.6a, b). As a result, sediment subduction and subduction erosion along the Java-Lesser Sunda margin associated with seamount and ridge subduction remove significant volumes of upper plate material to greater depth (Scholl and von Huene, 2007).

#### Subduction erosion observed at other convergent margins

Similar observations as presented above are also documented in modern MCS surveys at other plate margins, including Costa Rica (Fig. 2 in Edwards et al., 2018) and Japan

(Fig. 1c in Chester et al., 2013), where the décollement steps up into the sediment layers in response to changing oceanic basement topography.

These observations are augmented by numerical modeling studies that reveal similar seamount-related basal erosion phenomena under specified boundary conditions. In the study of (Morgan and Bangs, 2017), stepping up of the décollement close to the subducting seamount only happens when weak horizons exist within accreting strata, and thus deeper strata are protected from vertical partitioning. Similar up-stepping of the décollement is also observed above a subducting seamount in the 3D modeling of (Ruh et al., 2016), and a weak upper plate, with an effective internal friction coefficient of 0.14 to 0.23, is predefined in all his models.

A weak upper plate is also testified and proved in Integrated Ocean Drilling Program (IODP) sample from Costa Rica and Japan. In Costa Rica, offshore the Osa Penisula, weak clay layers with an internal friction coefficient of 0.2, which is much lower than assumed in Byerlee's law (0.6 to 0.85) (Byerlee, 1978), are sampled in the IODP Exp 334 and examined by a shear-friction testing experiment (Namiki et al., 2014). During the Japan Trench Fast Drilling Project (JFAST), similar low shear strength ($< 0.2$) rocks near and above the décollement zone are substantiated by the friction experiment in all slipping velocity ranges (10 $\mu m s^{-1}$ to $3.5 m s^{-1}$) (Remitti et al., 2015; Ujiie et al., 2013).

Though drilling information is lacking for the Java margin, we still anticipate weak upper plate material from previous Coulomb wedge studies (Dahlen, 1984; Davis and von Huene, 1987; Kopp and Kukowski, 2003). Based on the proto-thrust geometry at the deformation front, the surface slope, and the basal dip measured from an MCS profile offshore western Java close to the Sunda Strait, (Kopp and Kukowski, 2003) derived a weak upper plate internal friction coefficient (0.29), a moderate upper plate fluid pressure ratio (0.46), and a resultant low effective strength of the upper plate of 0.13 in the accretionary wedge. Though the MCS profile in (Kopp and Kukowski, 2003) locates approximately 600 to 700 km west of this study, we would expect comparable physical properties of the frontal prism and accretionary wedge material as these two regions share a similar history and a sediment supply (McNeill et al., 2017). Such weak sedimentary rocks may thus facilitate the wearing and erosion of the upper plate material by the subduction of rigid oceanic basement scarps, and the up-stepping (migration) of the décollement in scenarios with seamount or ridge subduction.

## 7.5 Conclusion

1) From the bathymetry and MCS surveys in the eastern Java margin, distinct oceanic relief is observed: 1) on the oceanic seafloor prior to subduction, and 2) being subducted

underneath the overriding plate on the submerged plate interface. Along the margin strike, these oceanic basement highs feature a large diversity in scales and shapes, including large conical seamounts (diameter up to 40 km), high aspect ratio linear-shape ridges (height/width $> 0.25$), and oceanic plate bending normal faults with small offsets (vertical throw $< 150$ m).

2) The larger seamounts and linear ridges, breach the relatively thin sediment cover ($< 500$ m) on the oceanic crust. Upon collision with the upper plate and subsequent subduction, they deform and fracture the frontal prism and accretionary wedge, modify the seafloor level and surface slope, and permanently erode accreted material by transporting it to greater depth. Subduction erosion caused by underthrusting seamounts is manifested in the up-stepping of the décollement within the accretionary wedge on both the leading and trailing sides of the seamount.

3) In the accretionary wedge of the outer marine forearc, structural impacts from subducting seamounts and ridges share similar patterns in the MCS profiles and might share as well a scale-independent deformation mechanism. Enhanced compression, including active thrust-faulting and folding, is observed at the subducting relief's leading edges to compensate the change of the basal dip and the shortening at the seaward side of the wedge following the theoretical prediction from the Coulomb Wedge. In contrast, at the trailing edge of the relief, the overriding plate features a structureless reflection signature. This pattern likely results from numerous gravitational slumps at the relief's trailing side in its long-term subduction history until they are fully buried by the overriding sediment sequence.

4) Whether the different scales of oceanic relief will lead to a substantial structural response on the upper plate depends on whether or not the height of the relief is larger than the thickness of the pelagic and terrestrial sediment on the oceanic plate prior to subduction. For example, underneath the frontal part of the accretionary wedge offshore Sumbawa (BGR06_311) , small bending fault scarps ($<150$ m) are smoothed by the 170 m thick under-thrusting sediment. From bathymetry and subsurface observations, no indication of severe upper plate deformation by the oceanic bending fault scarps is observed off Sumbawa.

## Competing interest

The authors declare that they have no competing interests.

## Acknowledgments.

Y. Xia acknowledges funding from the China Scholarship Council (grant 201506400067). R/V SONNE cruise SO190 and the SINDBAD project were funded by the German Federal Ministry of Education and Research (BMBF) under grants 03G0190A and 03G0190B. The seismic data were processed with Schlumberger's Omega2 seismic processing suite OMEGA and Seismic Unix - open-source software package for seismic research and processing, Center for Wave Phenomena, Colorado School of Mines. Bathymetry and seismic images are plotted by the Generic Mapping Tools (GMT) and QGIS.

## Data Availability Statement.

Bathymetric data from *R/V SONNE* cruise SO190 can be requested through the German Bundesamt für Seeschifffahrt und Hydrographie (BSH; http://www.bsh.de). Seismic reflection lines BGR06_311, BGR06_313, BGR06_303, and BGR06_305 are available upon reasonable request.

## References

Abercrombie, R. E., Antolik, M., Felzer, K., & Ekstrom, G. (2001). The 1994 java tsunami earthquake: Slip over a subducting seamount. *Journal of Geophysical Research-Solid Earth*, *106*(B4), 6595–6607, https://doi.org/10.1029/2000jb900403.

Ballance, P. F., Scholl, D. W., Vallier, T. L., Stevenson, A. J., Ryan, H., & Herzer, R. H. (1989). Subduction of a late cretaceous seamount of the louisville ridge at the tonga trench: A model of normal and accelerated tectonic erosion. *Tectonics*, *8*(5), 953–962, https://doi.org/10.1029/TC008i005p00953.

Bangs, N. L. B., Gulick, S. P. S., & Shipley, T. H. (2006). Seamount subduction erosion in the nankai trough and its potential impact on the seismogenic zone. *Geology*, *34*(8), 701–704, https://doi.org/10.1130/G22451.1.

Barker, D. H. N., Henrys, S., Tontini, F. C., Barnes, P. M., Bassett, D., Todd, E., & Wallace, L. (2018). Geophysical constraints on the relationship between seamount subduction, slow slip, and tremor at the north hikurangi subduction zone, new zealand. *Geophysical Research Letters*, *45*(23), 12804–12813, https://doi.org/10.1029/2018gl080259.

Bell, R., Holden, C., Power, W., Wang, X., & Downes, G. (2014). Hikurangi margin tsunami earthquake generated by slow seismic rupture over a subducted seamount. *Earth and Planetary Science Letters*, *397*, 1–9, https://doi.org/10.1016/j.epsl.2014.04.005.

Bell, R., Sutherland, R., Barker, D. H. N., Henrys, S., Bannister, S., Wallace, L., & Beavan, J. (2010). Seismic reflection character of the hikurangi subduction interface, new zealand, in the region of repeated gisborne slow slip events. *Geophysical Journal International*, *180*(1), 34–48, https://doi.org/10.1111/j.1365-246X.2009.04401.x.

Bilek, S. L. (2007). Influence of subducting topography on earthquake rupture. *The Seismogenic Zone of Subduction Thrust Faults*, (pp. 123–146).

Bock, Y., Prawirodirdjo, L., Genrich, J., Stevens, C., McCaffrey, R., Subarya, C., Puntodewo, S., & Calais, E. (2003). Crustal motion in indonesia from global positioning system measurements. *Journal of Geophysical Research: Solid Earth*, *108*(B8), https://doi.org/10.1029/2001JB000324.

Bonnet, G., Agard, P., Angiboust, S., Fournier, M., & Omrani, J. (2019). No large earthquakes in fully exposed subducted seamount. *Geology*, *47*(5), 407–410, https://doi.org/10.1130/G45564.1.

Brune, S., Babeyko, A., Ladage, S., & Sobolev, S. V. (2010). Landslide tsunami hazard in the indonesian sunda arc. *Natural Hazards and Earth System Sciences*, *10*(3), 589–604, https://doi.org/10.5194/nhess-10-589-2010.

Byerlee, J. (1978). Friction of rocks. *Pure Appl. Geophys. PAGEOPH*, https://doi.org/10.1007/BF00876528.

Chesley, C., Naif, S., Key, K., & Bassett, D. (2021). Fluid-rich subducting topography generates anomalous forearc porosity. *Nature*, *595*(7866), 255–260, https://doi.org/10.1038/s41586-021-03619-8.

Chester, F. M., Rowe, C., Ujiie, K., Kirkpatrick, J., Regalla, C., Remitti, F., Moore, J. C., Toy, V., Wolfson-Schwehr, M., Bose, S., Kameda, J., Mori, J. J., Brodsky, E. E., Eguchi, N., Toczko, S., Scientist, E. ., & Scientist, E. T. (2013). Structure and composition of the plate-boundary slip zone for the 2011 tohoku-oki earthquake. *Science*, *342*(6163), 1208–1211, https://doi.org/10.1126/science.1243719.

Clift, P. & Vannucchi, P. (2004). Controls on tectonic accretion versus erosion in subduction zones: Implications for the origin and recycling of the continental crust. *Reviews of Geophysics*, *42*(2), https://doi.org/10.1029/2003rg000127.

Cloos, M. (1992). Thrust-type subduction-zone earthquakes and seamount asperities - a physical model for seismic rupture. *Geology*, *20*(7), 601–604, https://doi.org/10.1130/0091-7613(1992)020<0601:Ttszea>2.3.Co;2.

Cloos, M. & Shreve, R. L. (1996). Shear-zone thickness and the seismicity of chilean- and marianas-type subduction zones. *Geology*, *24*(2), 107–110, https://doi.org/10.1130/0091-7613(1996)024<0107:Sztats>2.3.Co;2.

Dahlen, F. A. (1984). Noncohesive critical coulomb wedges - an exact solution. *Journal of Geophysical Research*, *89*(Nb12), 125–133, https://doi.org/10.1029/JB089iB12p10125.

Davidson, S. R., Barnes, P. M., Pettinga, J. R., Nicol, A., Mountjoy, J. J., & Henrys, S. A. (2020). Conjugate strike-slip faulting across a subduction front driven by incipient seamount subduction. *Geology*, *48*(5), 493–498, https://doi.org/10.1130/G47154.1.

Davis, D. M. & von Huene, R. (1987). Inferences on sediment strength and fault friction from structures at the aleutian trench. *Geology*, *15*(6), 517–522, https://doi.org/10.1130/0091-7613(1987)15<517:IOSSAF>2.0.CO;2.

Dominguez, S., Lallemand, S. E., Malavieille, J., & von Huene, R. (1998). Upper plate deformation associated with seamount subduction. *Tectonophysics*, *293*(3-4), 207–224, https://doi.org/10.1016/S0040-1951(98)00086-9.

Edwards, J. H., Kluesner, J. W., Silver, E. A., Brodsky, E. E., Brothers, D. S., Bangs, N. L., Kirkpatrick, J. D., Wood, R., & Okamoto, K. (2018). Corrugated megathrust revealed offshore from costa rica. *Nature Geoscience*, *11*(3), 197–202, https://doi.org/10.1038/s41561-018-0061-4.

Gao, X. & Wang, K. (2014). Strength of stick-slip and creeping subduction megathrusts from heat flow observations. *Science*, *345*(6200), 1038–41, https://doi.org/10.1126/science.1255487.

Geersen, J., Ranero, C. R., Barckhausen, U., & Reichert, C. (2015). Subducting seamounts control interplate coupling and seismic rupture in the 2014 iquique earthquake area. *Nat Commun*, *6*, 8267, https://doi.org/10.1038/ncomms9267.

Hall, R. (2002). Cenozoic geological and plate tectonic evolution of se asia and the sw pacific: computer-based reconstructions, model and animations. *Journal of Asian earth sciences*, *20*(4), 353–431, https://doi.org/10.1016/S1367-9120(01)00069-4.

Hall, R., Smyth, H. R., Draut, A., Clift, P., & Scholl, D. (2008). Cenozoic arc processes in indonesia: Identification of the key influences on the stratigraphic record in active volcanic arcs. *Formation and applications of the sedimentary record in arc collision zones*, *436*, 27, https://doi.org/10.1130/2008.2436(03).

Hamilton, W. B. (1988). Plate tectonics and island arcs. *Geological Society of America Bulletin*, *100*(10), 1503–1527, https://doi.org/10.1130/0016-7606(1988)100<1503:PTAIA>2.3.CO;2.

Heine, C., Müller, R. D., Gaina, C., & Clift, P. (2004). Reconstructing the lost eastern tethys ocean basin: convergence history of the se asian margin and marine gateways. *Continent-Ocean Interactions Within East Asian Marginal Seas, Geophys. Monogr. Ser*, *149*, 37–54, https://doi.org/10.1029/149GM03.

Hilde, T. W. C. (1983). Sediment subduction versus accretion around the pacific. *Tectonophysics*, *99*(2-4), 381–397, https://doi.org/10.1016/0040-1951(83)90114-2.

Hoernle, K., Hauff, F., Werner, R., van den Bogaard, P., Gibbons, A., Conrad, S., & Müller, R. (2011). Origin of indian ocean seamount province by shallow recycling of continental lithosphere. *Nature Geoscience*, *4*(12), 883–887, https://doi.org/10.1038/ngeo1331.

Hühnerbach, V., Masson, D. G., Bohrmann, G., Bull, J., & Weinrebe, W. (2005). Deformation and submarine landsliding caused by seamount subduction beneath the costa rica continental margin—new insights from high-resolution sidescan sonar data. *Geological Society, London, Special Publications*, *244*(1), 195–205, https://doi.org/10.1144/GSL.SP.2005.244.01.12.

Karig, D., Moore, G., Curray, J., & Lawrence, M. (1980). Morphology and shallow structure of the lower trench slope off nias island, sunda arc. *Washington DC American Geophysical Union Geophysical Monograph Series*, *23*, 179–208.

Kirkpatrick, J. D., Edwards, J. H., Verdecchia, A., Kluesner, J. W., Harrington, R. M., & Silver, E. A. (2020). Subduction megathrust heterogeneity characterized from 3d seismic data. *Nature Geoscience*, *13*(5), 369–374, https://doi.org/10.1038/s41561-020-0562-9.

Kodaira, S., Takahashi, N., Nakanishi, A., Miura, S., & Kaneda, Y. (2000). Subducted seamount imaged in the rupture zone of the 1946 nankaido earthquake. *Science*, *289*(5476), 104–6, https://doi.org/10.1126/science.289.5476.104.

Kopp, H., Flueh, E. R., Petersen, C. J., Weinrebe, W., Wittwer, A., & Scientists, M. (2006). The java margin revisited: Evidence for subduction erosion off java. *Earth and Planetary Science Letters*, *242*(1-2), 130–142, https://doi.org/10.1016/j.epsl.2005.11.036.

Kopp, H., Hindle, D., Klaeschen, D., Oncken, O., Reichert, C., & Scholl, D. (2009). Anatomy of the western java plate interface from depth-migrated seismic images. *Earth and Planetary Science Letters*, *288*(3-4), 399–407, https://doi.org/10.1016/j.epsl.2009.09.043.

Kopp, H. & Kukowski, N. (2003). Backstop geometry and accretionary mechanics of the sunda margin. *Tectonics*, *22*(6), https://doi.org/10.1029/2002tc001420.

Kopp, H., Weinzierl, W., Becel, A., Charvis, P., Evain, M., Flueh, E. R., Gailler, A., Galve, A., Hirn, A., Kandilarov, A., Klaeschen, D., Laigle, M., Papenberg, C., Planert, L., Roux, E., Team, T., & Team, T. (2011). Deep structure of the central lesser antilles island arc: Relevance for the formation of continental crust. *Earth and Planetary Science Letters*, *304*(1-2), 121–134, https://doi.org/10.1016/j.epsl.2011.01.024.

Krabbenhöft, A., Weinrebe, R. W., Kopp, H., Flueh, E. R., Ladage, S., Papenberg, C., Planert, L., & Djajadihardja, Y. (2010). Bathymetry of the indonesian sunda margin-relating morphological features of the upper plate slopes to the location and extent of the seismogenic zone. *Natural Hazards and Earth System Sciences*, *10*(9), 1899–1911, https://doi.org/10.5194/nhess-10-1899-2010.

Lallemand, S., Culotta, R., & Von Huene, R. (1989). Subduction of the daiichi kashima seamount in the japan trench. *Tectonophysics*, *160*(1-4), 231–247.

Lallemand, S. & Lepichon, X. (1987). Coulomb wedge model applied to the subduction of seamounts in the japan trench. *Geology*, *15*(11), 1065–1069, https://doi.org/10.1130/0091-7613(1987)15<1065:Cwmatt>2.0.Co;2.

Laursen, J., Scholl, D. W., & von Huene, R. (2002). Neotectonic deformation of the central chile margin: Deepwater forearc basin formation in response to hot spot ridge and seamount subduction. *Tectonics*, *21*(5), 2–1, https://doi.org/10.1029/2001tc901023.

Lüschen, E., Müller, C., Kopp, H., Engels, M., Lutz, R., Planert, L., Shulgin, A., & Djajadihardja, Y. S. (2011). Structure, evolution and tectonic activity of the eastern sunda forearc, indonesia, from marine seismic investigations. *Tectonophysics*, *508*(1-4), 6–21, https://doi.org/10.1016/j.tecto.2010.06.008.

Marcaillou, B., Collot, J. Y., Ribodetti, A., d'Acremont, E., Mahamat, A. A., & Alvarado, A. (2016). Seamount subduction at the north-ecuadorian convergent margin: Effects on structures, inter-seismic coupling and seismogenesis. *Earth and Planetary Science Letters*, *433*, 146–158, https://doi.org/10.1016/j.epsl.2015.10.043.

Martinez-Loriente, S., Sallares, V., Ranero, C. R., Ruh, J. B., Barckhausen, U., Grevemeyer, I., & Bangs, N. (2019). Influence of incoming plate relief on overriding plate deformation and earthquake nucleation: Cocos ridge subduction (costa rica). *Tectonics*, *38*(12), 4360–4377, https://doi.org/10.1029/2019tc005586.

McNeill, L. C., Dugan, B., Backman, J., Pickering, K. T., Pouderoux, H. F., Henstock, T. J., Petronotis, K. E., Carter, A., Chemale Jr, F., Milliken, K. L., et al. (2017). Understanding himalayan erosion and the significance of the nicobar fan. *Earth and Planetary Science Letters*, *475*, 134–142, https://doi.org/10.1016/j.epsl.2017.07.019.

Moore, G., Curray, J., Moore, D., & Karig, D. (1980). Variations in geologic structure along the sunda fore arc, northeastern indian ocean. *Washington DC American Geophysical Union Geophysical Monograph Series*, *23*, 145–160, https://doi.org/10.1029/GM023p0145.

Moore, G. F., Curray, J. R., & Emmel, F. J. (1982). Sedimentation in the sunda trench and forearc region. *Geological Society, London, Special Publications*, *10*(1), 245–258, https://doi.org/10.1144/GSL.SP.1982.010.01.16.

Morgan, J. K. & Bangs, N. L. (2017). Recognizing seamount-forearc collisions at accretionary margins: Insights from discrete numerical simulations. *Geology*, *45*(7), 635–638, https://doi.org/10.1130/G38923.1.

Morton, E. A., Bilek, S. L., & Rowe, C. A. (2018). Newly detected earthquakes in the cascadia subduction zone linked to seamount subduction and deformed upper plate. *Geology*, *46*(11), 943–946, https://doi.org/10.1130/G45354.1.

Müller, R. D., Sdrolias, M., Gaina, C., & Roest, W. R. (2008). Age, spreading rates, and spreading asymmetry of the world's ocean crust. *Geochemistry, Geophysics, Geosystems*, *9*(4), https://doi.org/10.1029/2007gc001743.

Namiki, Y., Tsutsumi, A., Ujiie, K., & Kameda, J. (2014). Frictional properties of sediments entering the costa rica subduction zone offshore the osa peninsula: implications for fault slip in shallow subduction zones. *Earth, Planets and Space*, *66*(1), 1–8, https://doi.org/10.1186/1880-5981-66-72.

Planert, L., Kopp, H., Lueschen, E., Mueller, C., Flueh, E., Shulgin, A., Djajadihardja, Y., & Krabbenhöft, A. (2010). Lower plate structure and upper plate deformational segmentation at the sunda-banda arc transition, indonesia. *Journal of Geophysical Research: Solid Earth*, *115*(B8), https://doi.org/10.1029/2009JB006713.

Ranero, C. R. & von Huene, R. (2000). Subduction erosion along the middle america convergent margin. *Nature*, *404*(6779), 748–52, https://doi.org/10.1038/35008046.

Remitti, F., Smith, S., Mittempergher, S., Gualtieri, A., & Di Toro, G. (2015). Frictional properties of fault zone gouges from the j-fast drilling project (mw 9.0 2011 tohoku-oki earthquake). *Geophysical Research Letters*, *42*(8), 2691–2699, https://doi.org/10.1002/2015GL063507.

Ruh, J. B., Sallares, V., Ranero, C. R., & Gerya, T. (2016). Crustal deformation dynamics and stress evolution during seamount subduction: High-resolution 3-d numerical modeling. *Journal of Geophysical Research-Solid Earth*, *121*(9), 6880–6902, https://doi.org/10.1002/2016jb013250.

Scarfì, L., Langer, H., Messina, A., & Musumeci, C. (2020). Tectonic regimes inferred from clustering of focal mechanisms and their distribution in space: application to the central mediterranean area. *Journal of Geophysical Research: Solid Earth*, https://doi.org/10.1029/2020jb020519.

Scholl, D. W. & von Huene, R. (2007). Crustal recycling at modern subduction zones applied to the past—issues of growth and preservation of continental basement crust, mantle geochemistry, and supercontinent reconstruction. *Geological Society of America Memoirs*, *200*, 9–32, https://doi.org/10.1130/2007.1200(02).

Scholz, C. H. & Small, C. (1997). The effect of seamount subduction on seismic coupling. *Geology*, *25*(6), 487–490, https://doi.org/10.1130/0091-7613(1997)025<0487:Teosso>2.3.Co;2.

Seton, M., Müller, R. D., Zahirovic, S., Williams, S., Wright, N. M., Cannon, J., Whittaker, J. M., Matthews, K. J., & McGirr, R. (2020). A global data set of present-day oceanic crustal age and seafloor spreading parameters. *Geochemistry, Geophysics, Geosystems*, *21*(10), e2020GC009214, https://doi.org/10.1029/2020GC009214.

Shulgin, A., Kopp, H., Mueller, C., Planert, L., Lueschen, E., Flueh, E. R., & Djajadihardja, Y. (2011). Structural architecture of oceanic plateau subduction offshore eastern java and the potential implications for geohazards. *Geophysical Journal International*, *184*(1), 12–28, https://doi.org/10.1111/j.1365-246X.2010.04834.x.

Sun, T. H., Saffer, D., & Ellis, S. (2020a). Mechanical and hydrological effects of seamount subduction on megathrust stress and slip. *Nature Geoscience*, *13*(3), 249–+, https://doi.org/10.1038/s41561-020-0542-0.

Sun, T. H. Z., Ellis, S., & Saffer, D. M. (2020b). Coupled evolution of deformation, pore fluid pressure, and fluid flow in shallow subduction forearcs. *Journal of Geophysical Research-Solid Earth*, *125*(3), https://doi.org/10.1029/2019JB019101.

Timm, C., Bassett, D., Graham, I. J., Leybourne, M. I., De Ronde, C. E., Woodhead, J., Layton-Matthews, D., & Watts, A. B. (2013). Louisville seamount subduction and its implication on mantle flow beneath the central tonga–kermadec arc. *Nature communications*, *4*(1), 1–9, https://doi.org/10.1038/ncomms2702.

Todd, E. K., Schwartz, S. Y., Mochizuki, K., Wallace, L. M., Sheehan, A. F., Webb, S. C., Williams, C. A., Nakai, J., Yarce, J., Fry, B., et al. (2018). Earthquakes and tremor linked to seamount subduction during shallow slow slip at the hikurangi margin, new zealand. *Journal of Geophysical Research: Solid Earth*, *123*(8), 6769–6783, https://doi.org/10.1029/2018JB016136.

Tregoning, P., Brunner, F., Bock, Y., Puntodewo, S., McCaffrey, R., Genrich, J., Calais, E., Rais, J., & Subarya, C. (1994). First geodetic measurement of convergence across the java trench. *Geophysical Research Letters*, *21*(19), 2135–2138, https://doi.org/10.1029/94GL01856.

Trehu, A. M., Blakely, R. J., & Williams, M. C. (2012). Subducted seamounts and recent earthquakes beneath the central cascadia forearc. *Geology*, *40*(2), 103–106, https://doi.org/10.1130/G32460.1.

Ujiie, K., Tanaka, H., Saito, T., Tsutsumi, A., Mori, J. J., Kameda, J., Brodsky, E. E., Chester, F. M., Eguchi, N., Toczko, S., Expedition, & Scientists, T. (2013). Low coseismic shear stress on the tohoku-oki megathrust determined from laboratory experiments. *Science*, *342*(6163), 1211–4, https://doi.org/10.1126/science.1243485.

Van Rijsingen, E., Funiciello, F., Corbi, F., & Lallemand, S. (2019). Rough subducting seafloor reduces interseismic coupling and mega-earthquake occurrence: Insights from analogue models. *Geophysical Research Letters*, *46*(6), 3124–3132, https://doi.org/10.1029/2018GL081272.

von Huene, R., Ranero, C. R., & Vannucchi, P. (2004). Generic model of subduction erosion. *Geology*, *32*(10), 913–916, https://doi.org/10.1130/G20563.1.

Von Huene, R. & Scholl, D. W. (1991). Observations at convergent margins concerning sediment subduction, subduction erosion, and the growth of continental-crust. *Reviews of Geophysics*, *29*(3), 279–316, https://doi.org/10.1029/91rg00969.

Wang, K. L. & Bilek, S. L. (2011). Do subducting seamounts generate or stop large earthquakes? *Geology*, *39*(9), 819–822, https://doi.org/10.1130/G31856.1.

Wang, K. L. & Bilek, S. L. (2014). Invited review paper: Fault creep caused by subduction of rough seafloor relief. *Tectonophysics*, *610*, 1–24, https://doi.org/10.1016/j.tecto.2013.11.024.

Xia, Y. Y., Geersen, J., Klaeschen, D., Ma, B., Lange, D., Riedel, M., Schnabel, M., & Kopp, H. (2021). Marine forearc structure of eastern java and its role in the 1994 java tsunami earthquake. *Solid Earth*, *12*(11), 2467–2477, https://doi.org/10.5194/se-12-2467-2021.

Xia, Y. Y., Klaeschen, D., Kopp, H., & Schnabel, M. (2022). Reflection tomography by depth warping: a case study across the java trench. *Solid Earth*, *13*(2), 367–392, https://doi.org/10.5194/se-13-367-2022.

Yang, H., Liu, Y., & Lin, J. (2013). Geometrical effects of a subducted seamount on stopping megathrust ruptures. *Geophysical Research Letters*, *40*(10), 2011–2016, https://doi.org/10.1002/grl.50509.

## Supporting Information

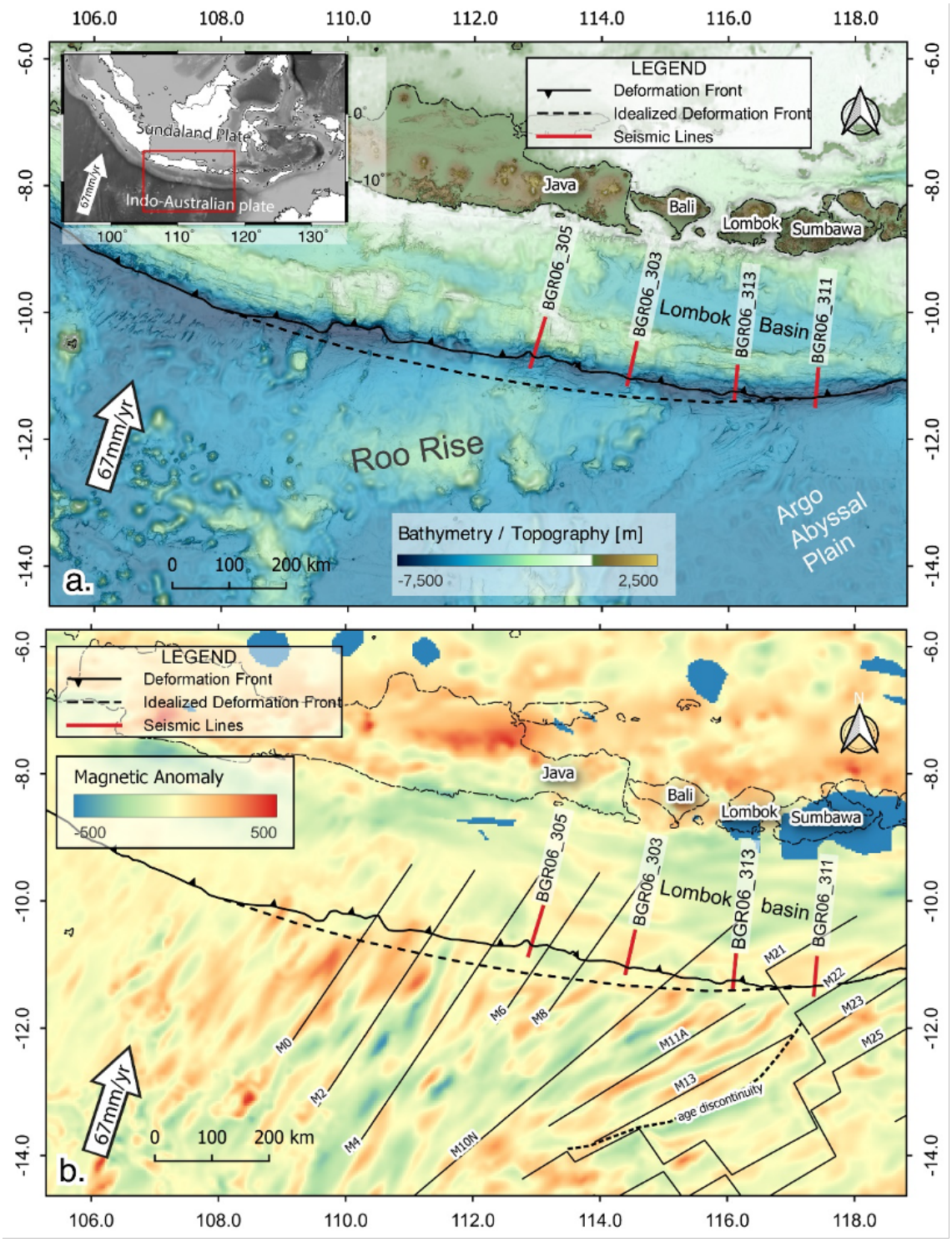


**Figure 7.10:** Regional tectonic setting and bathymetry of the study area (Caption next page).

**Figure 7.10:** a. Regional tectonic setting and bathymetry of the study area. Red lines indicate the location of the four MCS profiles. The deformation front is shown in a black line with triangle marks, and the undisturbed idealized trend of the deformation front is shown by the black dashed line. b. Satellite magnetic anomaly in the Java and Lesser Sunda regions. Red lines indicate the location of the four MCS profiles. The deformation front is shown in black line with triangles, and the undisturbed trend of the deformation front is shown by the black dashed line. Magnetic isochrons are indicated by black lines.

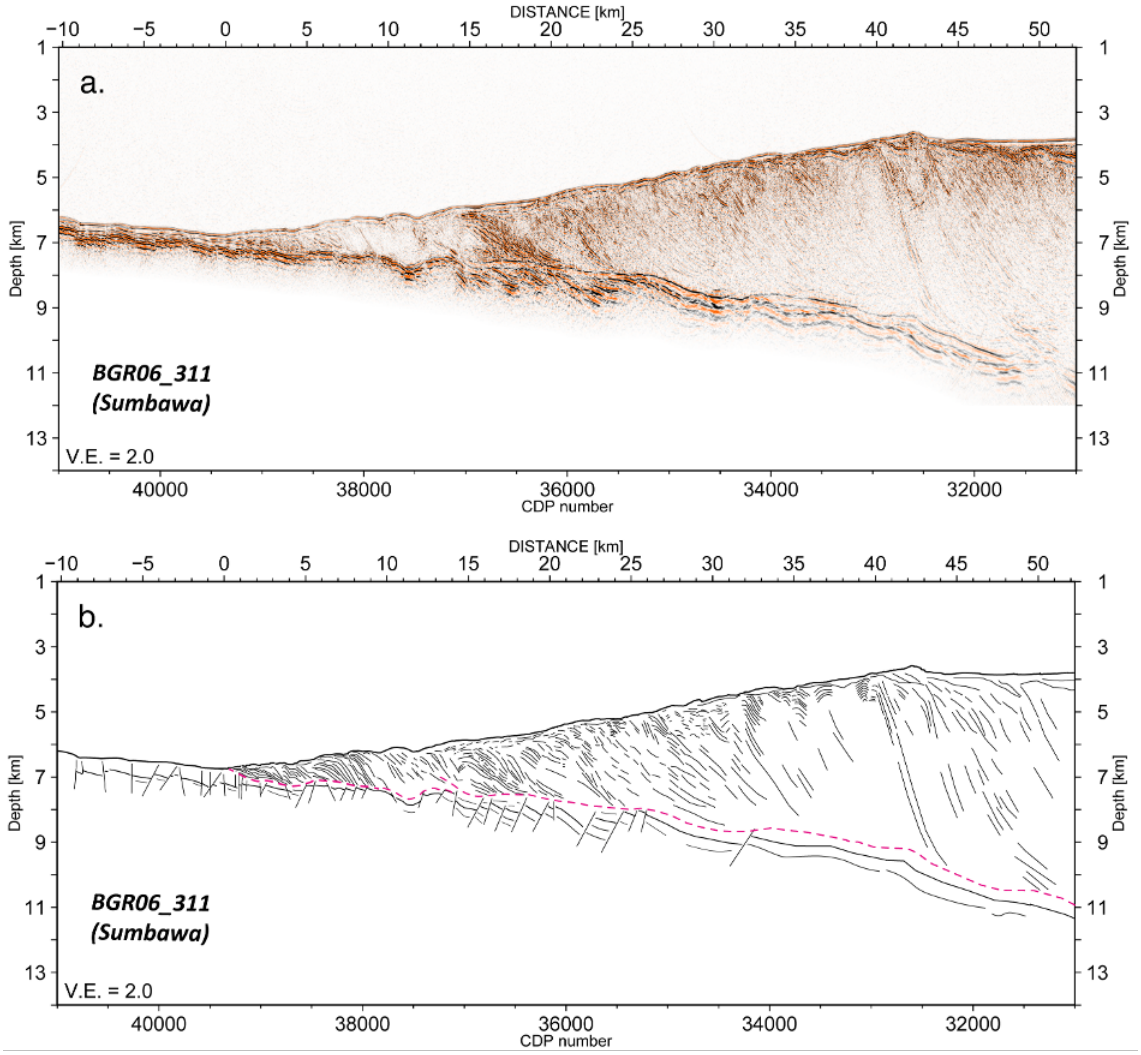


**Figure 7.11:** a. Uninterpreted depth section of BGR06_311. b. Line drawing of the seismic section.

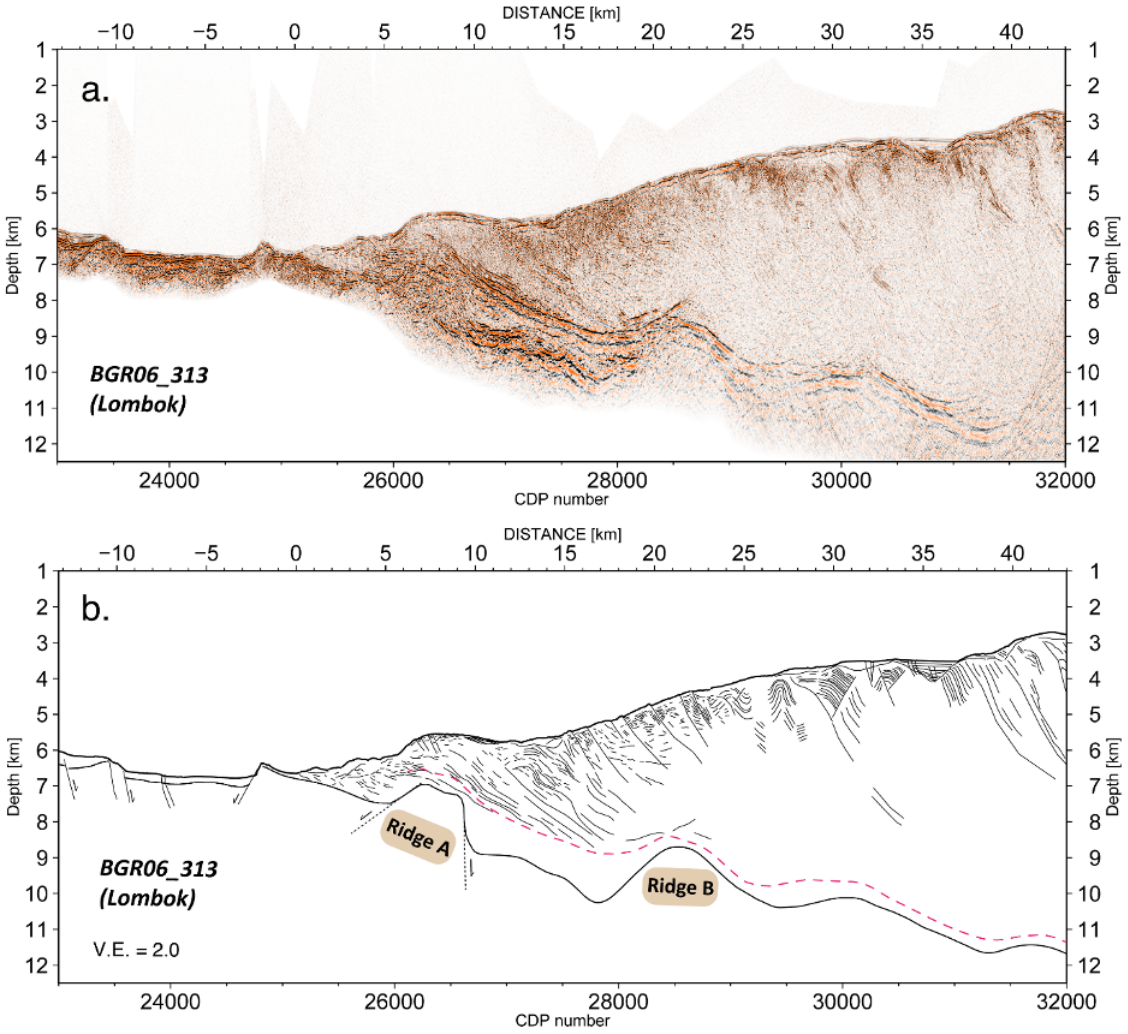


**Figure 7.12:** a. Uninterpreted depth section of BGR06_313. b. Line drawing of the seismic section.

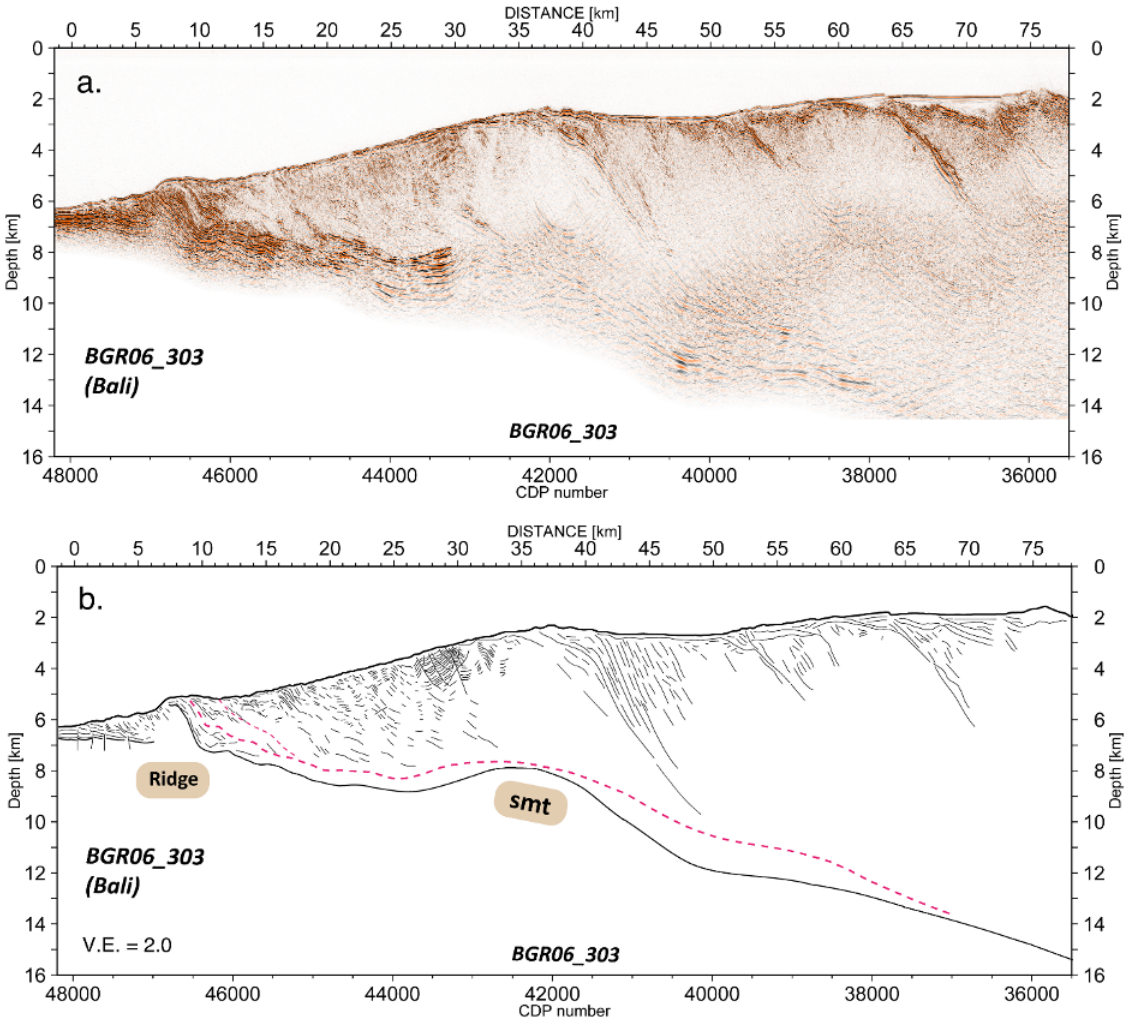


**Figure 7.13:** a. Uninterpreted depth section of BGR06_303. b. Line drawing of the seismic section.

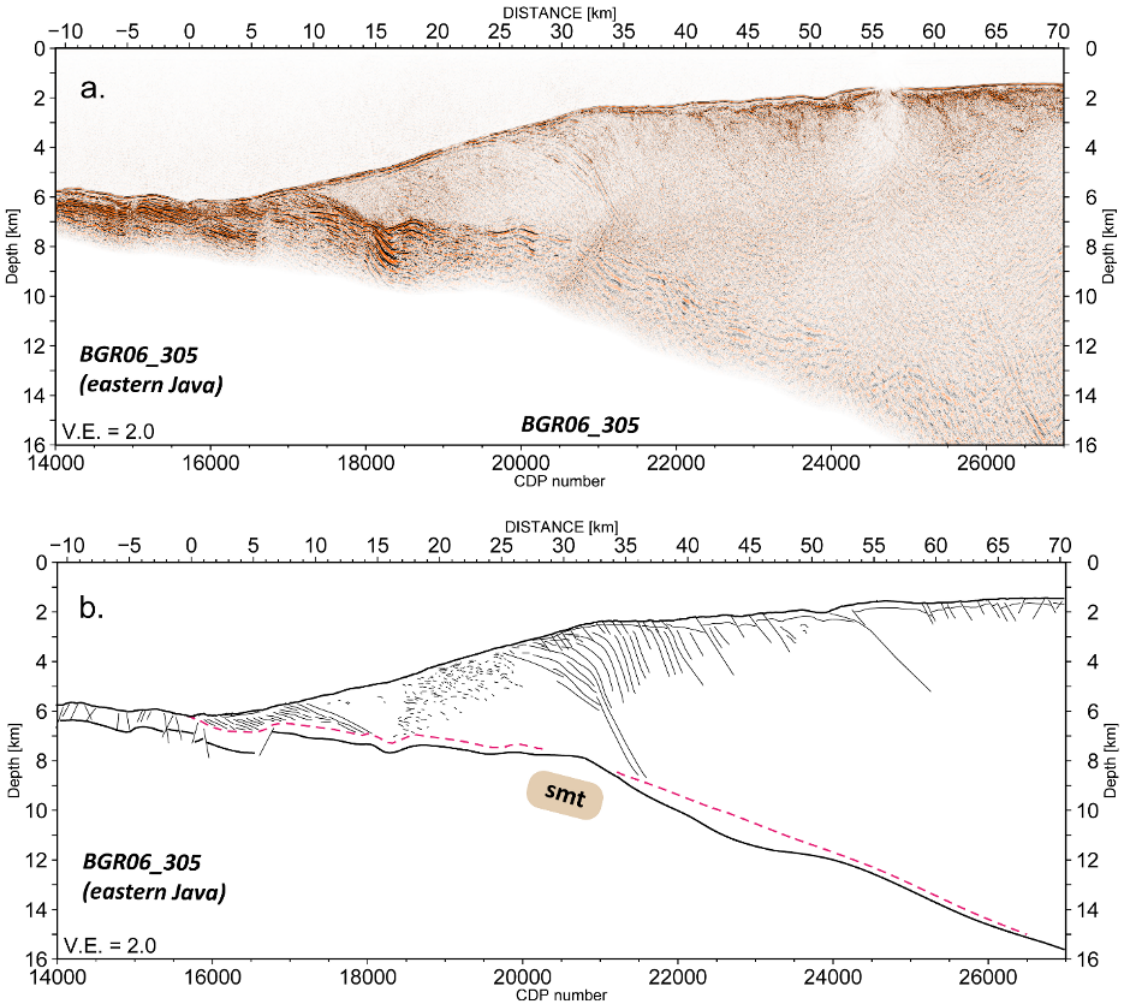


**Figure 7.14:** Uninterpreted depth section of BGR06_305. b. Line drawing of the seismic section.

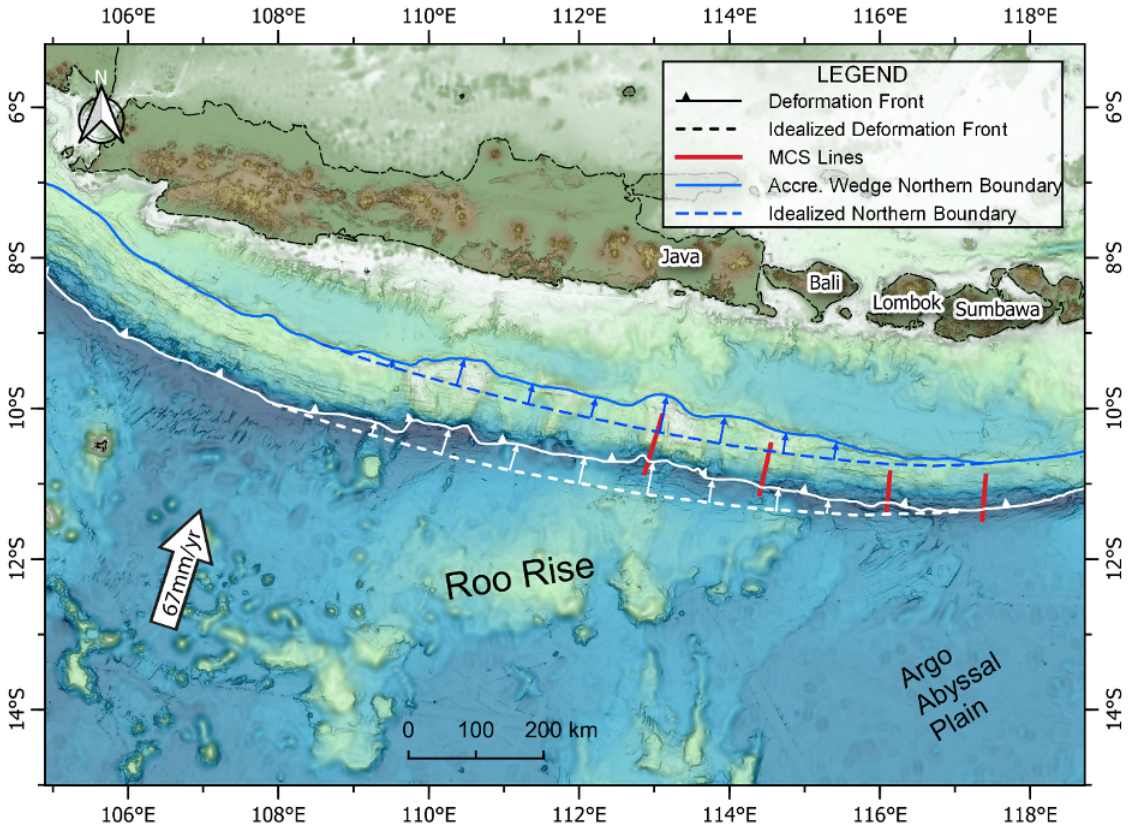


**Figure 7.15:** Bathymetry and topography map of the study area offshore Java and Lesser Sunda margin. Both the deformation front (marked in solid white line) and the northern boundary of the accretionary wedge (marked in solid blue line) deflected from their idealized trends (marked as a white dashed line and blue dashed line, respectively) in the arc-ward direction by maximum 50 km approximately over a broad region of 25,000 $km^2$ from 107.9 ° E to 117.1 ° E.

# 8 Conclusion and Outlook

## 8.1 Conclusion

The structural interpretation of the PSDM images was combined with other data sets (high-resolution bathymetry, OBS wide-angle velocity models, and seismicity) to characterize the Northern Chilean erosive margin. The main findings of our study suggest that:

**1)Megathrust reflectivity reveals the updip limit of the 2014 Iquique earthquake rupture**

Offshore Northern Chile, the 2014 $M_w$ 8.1 Iquique earthquake ruptured the plate boundary between 19.5 ° and 21 °S. We document a spatial correspondence between the rupture area and the seismic reflectivity of the plate boundary. North and updip of the rupture area, a coherent, highly reflective plate boundary indicates excess fluid pressure, which may prevent the accumulation of elastic strain. In contrast, the rupture area is characterized by the absence of plate boundary reflectivity, which suggests low fluid pressure that results in stress accumulation and thus controls the extent of earthquake rupture. This finding is described in chapter 3.

**2)The temperature of updip limit of the 2014 Iquique Ridge is around 100 - 150 °C**

The lower limit of the coherent and highly reflective plate boundary around 15 km depths in our profiles corresponds to a temperature of 100 – 150 °C. We interpreted the high reflectivity is mainly caused by dehydration of sedimentary smectite clays at temperatures below 150 °C. This finding is described in chapter 3.

**3)The ridge-related topography is currently subducting south of 20.5 °S**

We show that significant ridge-related topography is currently subducting south of 20.5 °S and that the combined effect of horst and graben subduction with subduction of Iquique ridge-related thickened and elevated crust causes an upward bulging of the entire upper

plate from the plate interface up to the seafloor as well as the presence of kilometer-scale anticlinal structures observed in multibeam bathymetric data that are approximately aligned with horsts seaward of the trench.. This finding is described in chapter 4.

**4)The subducting Iquique Ridge in our study area correlates to low interseismic coupling along the lowermost continental slope**

The subducting Iquique Ridge in our study area between 20.5 °S - 21 °S correlates to a region of low interseismic coupling along the lowermost continental slope. For comparison, the seismic line MC06 images a smoother plate interface, indicating less deformation of the outer wedge in the north of ~20.5 °S. This finding is described in chapter 4.

## 8.2 Outlook

The study presented here successfully identifies the properties of the updip limit and precise location of the subducting Iquique Ridge in Northern Chile. However, some unresolved issues continue to be concerned:

**1) The longer reflection of MC04 (north) and shorter reflection in the south lines**

The higher plate boundary fluid content at depths beyond 15 km to the north of the 2014 Iquique earthquake remains enigmatic, as shown in the reflectivity in Fig. 3.2. The reflectivity is longer both in the plate boundary and internal upper plate than in the southern downdip lines, we speculate that the strength of the upper plate and plate interface is weaker in the north area.

**2) The bulges and tilting reflections along the strike seismic profiles**

From the view of the strike lines (Fig. 3.3), we can find several tilting reflections from the plate interface to the continental basement and bulges at the updip edge of the Iquique earthquake. The origin of the structure is still unsolved, we speculate it results from the N-S compression in the Northern Chile margin forearc.

To solve these issues, the surveyed by long-term seafloor geodesy and heat flux observations, combined with drilling, may be helpful to study.

# List of Figures

# List of Tables

# 9 Acknowledgments

Over the course of my researching and writing this thesis, I would like to express my thanks to all those who have helped me.

I am incredibly grateful for my supervisors Prof. Dr. Heidrun Kopp for giving me an opportunity to study in GEOMAR and the excellent guidance and helpful comments for my manuscripts. I also would like to convey my heartfelt gratitude towards Dr. Dirk Kläschen. Many thanks for helping me in many technical aspects, valuable discussions and endless patient.

In addition, I would like to thank Dr. Jacob Geersen for his precious comments and questions on my papers. I am thankful to Dr. Jacob Geersen, Dr. Dietrich Lange, Dr. Dirk Kläschen, Prof. Dr. Ingo Grevemeyer, Dr. Eduardo Contreras-Reyes, Dr. Florian Petersen, Dr. Michael Riedel, Dr. Yueyang Xia, Prof. Dr. Anne M. Trehu and Prof. Dr. Heidrun Kopp, without their help, it would be much difficult for the publishing the first SCI paper in my life. I look forward to ongoing and future collaborations with you.

Many thanks to Jasmin Mögeltönder, Anne Völsch, and Julia Schätzel, who helped me greatly throughout the seven years at GEOMAR in dealing with all the paperwork and travel preparation. Thanks to Yueyang Xia, who shared past five years the office with me. Thank you for all the nice conversations, the good working climate, memorable vacations and discuss with him always inspire me a lot. I would also like to thank all current and past members of our laboratory for teaching basic experiments and their valuable friendship.

I would like to thank the China Scholarship Council and GEOMAR for financing my doctorate. A special thanks to my roommate, Quan Zu, who lived together with me for four years. I appreciate him taking good care of me when I had a cold.

Of cause, I would like to say thanks to my parents, Mr. Jianming Ma and Mrs. Caiping Zhou, my parents-in-law, Mr. Guohua Zhao and Mrs. Qing Shi, and all my families for their infinite support, advice, and backing me up in the doctorate Odyssey.

Finally, Mrs. Yue Zhao, my love for the whole life, thanks for your endless understanding, tolerance and patience. During these challenging global times, up to the time I wrote

this text, we have not seen each other for 80780400 seconds. Now it is 80780401 seconds, 80780402 seconds, etc. Every second that miss you are like passing a century. Although we are 8330 kilometers apart, my heart is always together with you. No matter how far we are separated, with you I made an agreement: I grasped your hand, together with you I was to grow old.

Everyone I've mentioned has helped me improve, grow, and become a better person. They also made me more curious about science and love Germany.

"**On and on stretched my road, long it was and far, I would go high and go low in this search that I made** — Yuan Qu <The Sadness of Separation>"